Probing the Higgs via pair production in the two W boson two photon channel at CMS:
Past, present, and future

by Abraham Tishelman-Charny

B.S. in Physics, Stony Brook University
M.S. in Physics, Northeastern University

A dissertation submitted to

The Faculty of
the College of Science of
Northeastern University
in partial fulfillment of the requirements
for the degree of Doctor of Philosophy

July 27, 2022

Dissertation Committee

Professor Toyoko Orimoto, Chair
Professor Emanuela Barberis
Professor James Halverson
Professor Darien Wood

1

Acknowledgements

I first would like to thank my advisor, Toyoko Orimoto. I am sincerely grateful to have had an advisor who has been on my side every step of the way during the course of my PhD, and who clearly prioritized my well-being above all else. Toyoko always enthusiastically encouraged me to follow my heart when it came to choosing research projects and activities, which led to me enjoying my research. I would not have had such a meaningful and fruitful PhD experience if it were not for her.

I would also like to thank the HH to WW$\gamma\gamma$ analysis team: Mingshui Chen, Peiran Li, Petr Mandrik, Badder Marzocchi, Fabio Monti, Ram Krishna Sharma, Sergei Slabospitskii, Junquan Tao, Joshuha Thomas-Wilsker, Chu Wang, and Jin Wang. One of the many fortunate circumstances which made my PhD experience special was the opportunity to lead a physics analysis working group. I am grateful to have had that opportunity, through which I learned from everybody in the group.

During my PhD, I was also very fortunate to be part of the wonderful CMS ECAL community. While I am grateful for all of the many people who I have learned from in this group, I would like to express special thanks to Giacomo Cucciati, David Petyt, and Davide Valsecchi. Giacomo was always incredibly kind and willing to thoroughly answer my countless questions about ECAL DAQ, and was a great partner in crime at ECAL Run Coordination. The experience I have gained working with David has been invaluable and an important part of my PhD. David was also willing to answer my endless questions, in this case about ECAL TPG, and always took the time to share his insightful perspective and feedback as the projects we worked on developed over time. Finally, whether it was through Italian lessons or ECAL trigger discussions, Davide and I always had *fun* with what we discussed. This was an absolutely essential aspect of our work. Keeping things fun kept us interested in collaborating over our multi-year projects.

I also want to thank Tanvi, Chad and Andrew for keeping me company while we were under lockdown during the pandemic. All of the meaningful conversations, support, silly jokes, and laughter kept me sane.

Finally, I want to thank my parents for encouraging me to pursue a PhD in the first place, and for believing in me more than I believed in myself.

Abstract of Dissertation

One of the few remaining parameters of the standard model (SM) of particle physics that has not yet been measured is the Higgs self-coupling. A measurement of this parameter would serve as a fundamental test of the SM, as its value has a direct effect on the shape of the Higgs potential, and any deviation of the measured Higgs self-coupling value from the SM prediction would have profound implications on physicists' collective understanding of the universe. This coupling is directly accessible via Higgs pair production, the production of two Higgs bosons in a single process, which is actively studied at the CMS experiment at the LHC. In this thesis, the first search by the CMS experiment for Higgs pair production in the WW$\gamma\gamma$ final state, performed using data collected at the LHC from 2016-2018 (Run 2), is presented. The dataset corresponds to a center-of-mass energy of 13 TeV, and an integrated luminosity of 138 fb^{-1}. The search results in an observed (expected) 95% confidence level (CL) upper limit on Higgs pair production in the gluon-fusion channel of 3.0 (1.7) pb, corresponding to about 97 (53) times the standard model prediction. Additionally, the analysis makes use of an Effective field theory (EFT) framework to obtain an observed (expected) constraint on the strength of the Higgs self-coupling of -25.9 (-14.5) to 24.1 (18.4) times its SM value. Within the same framework, constraints are also placed on purely beyond the standard model (BSM) scenarios. An observed (expected) constraint on the strength of the direct coupling of two Higgs bosons to two top quarks of -2.4 (-1.7) to 2.9 (2.2) is obtained at a 95% CL, and 95% CL upper limits are placed on twenty EFT benchmark scenarios ranging from 1.7 - 6.2 (1.0 - 3.9) pb. This thesis also includes a description of the experimental setup necessary for this analysis, comprising the LHC and CMS. A detailed description of the CMS Electromagnetic Calorimeter, crucial for the detection of these di-Higgs final states, is included along with its ongoing optimizations and operational plans for LHC Run 3. Additionally, the first Phase-II projection of Higgs pair production in the WW$\gamma\gamma$ and $\tau\tau\gamma\gamma$ final states at the future HL-LHC with the Phase-II upgraded CMS detector is included, where an expected significance of 0.22 σ is extracted.

Table of Contents

List of Figures

8

10

11

Chapter 1

Introduction

Through the study of particle physics, human beings are able to probe the fundamental building blocks of the very universe they inhabit. This field is rich in expertise. Firstly, particle physicists seeking to answer fundamental questions about the universe determine the experimental setups, namely the types of particle accelerators and detectors, that are required in order to attempt to answer these questions. Incredible efforts are then required of engineers and technicians to build these accelerators and detectors. Multi-year long data-taking periods then commence, warranting undying dedication from a multitude of accelerator and detector operations teams. The unprecedented amounts of data recorded by these particle detectors, and their associated simulations, then require state of the art computational tools and resources to be processed and analyzed in a reasonable time frame. Finally, novel statistical interpretations must then be invoked in order to infer results from the recorded data, in an attempt to answer the questions with which physicists began. This monumental effort requires expertise from scientists around the world, where CERN (Organisation Européenne pour la Recherche Nucléaire) is one of the main sites where these collaborators come together.

In 2012, the experimental discovery of the Higgs boson by the CMS (Compact Muon Solenoid) and ATLAS experiments at the CERN LHC (Large Hadron Collider) [1; 2; 3] marked a historic achievement for humanity. Physicists had finally experimentally verified the existence of the Higgs boson, a particle first theorized in the 1960s, and one that is central to the current framework of particle physics: The Standard Model (SM).

The SM is a quantum field theory describing the fundamental forces of nature and its constituent particles. It accounts for the electromagnetic, weak, and strong forces and in-

cludes particles classified as quarks, leptons, and bosons. The SM is consistent with the vast majority of experimental observations in particle physics, and continues to be widely used to this day when interpreting data. Additionally, it is often used as a basis from which extensions are made to new theories. In the SM, observable particles arise as excitations of their corresponding quantum fields. The Higgs field adds a potential energy term to the SM Lagrangian, and due to its shape and the requirement of a vacuum energy value, its mathematically described symmetry is spontaneously broken. This process is known as electroweak symmetry breaking, and is a crucial mechanism described by the SM as it explains the origin of mass for massive particles which interact with the Higgs field.

In the post Higgs-discovery era, physicists are aiming to further understand and characterize the Higgs boson, and by extension the electroweak symmetry breaking mechanism. A fundamental test of the SM is to measure the coupling strengths of the Higgs boson to massive SM particles, where many couplings have now been measured with precisions down to around 10% with respect to their SM predicted values. A coupling of particular interest which has not yet been precisely measured is the Higgs self-coupling. This coupling has a direct effect on the shape of the Higgs potential, and its magnitude is explicitly predicted by the SM. Based on this predicted value and the current measurements of the top quark mass and Higgs boson mass, it is predicted that the Higgs vacuum energy currently sits at a metastable minimum. This would mean there is a non-zero probability that the minimum of the Higgs potential can tunnel to a lower minimum, which would change the laws of physics as we know them. An experimental measurement of the Higgs self-coupling could have profound implications on physicists' understanding of the universe: It may confirm the predictions of the SM, or it may refute the SM entirely and prompt physicists to make sense of this in a way that is in agreement with all previous observations.

Through the study of Higgs pair production, the production of two Higgs bosons in a single process, the Higgs self-coupling is directly accessible. Additionally, through the use of an Effective Field Theory (EFT) framework, a wide model-independent search for

physics beyond the standard model (BSM) through searches of Higgs pair production can be performed. Due to destructive interference between its two leading order (LO) processes, non-resonant Higgs pair production has a low production cross section, meaning that the combination of many di-Higgs final states will be necessary in order to maximize the chances for observation, and obtain as precise a measurement as possible of the Higgs self-coupling. In order to search for this relatively small signal and include a new search channel, a search for Higgs pair production by the CMS experiment in the $WW\gamma\gamma$ channel was performed. This channel benefits from the sensitive $H\to\gamma\gamma$ process which provides a narrow, distinguishable signature. The $H\to WW$ leg of the decay contributes a relatively large branching ratio among Higgs boson decay processes of about 22%, increasing the expected yields of the di-Higgs process. Because the W boson can decay both leptonically and hadronically, the $H\to WW$ and by extension the $HH\to WW\gamma\gamma$ process has three possible final states: The Fully-Hadronic, Semi-Leptonic, and Fully-Leptonic final states, corresponding to 0, 1, and 2 leptonically decaying W-bosons respectively.

During Run 2 of the LHC (2016-18), about 138 fb^{-1} of data was recorded by the CMS detector from proton-proton collisions at a center-of-mass energy of $\sqrt{s} = 13$ TeV. Using this dataset, the first search for Higgs pair production in the $WW\gamma\gamma$ final state by the CMS experiment was performed. The CMS ECAL (Electromagnetic Calorimeter) was vital for this analysis, as it is the sole sub-detector of CMS that can directly detect photons which leave a trace of the sensitive $H\to\gamma\gamma$ signature in all three final states of this di-Higgs channel. It is additionally crucial for the detection of electrons, present in two of the three $WW\gamma\gamma$ final states.

In order to potentially improve the sensitivity of this analysis and similar analyses using the CMS dataset to be collected during Run 3 of the LHC beginning in 2022, existing CMS ECAL features have been optimized and new features have been investigated. During the commissioning period of the CMS ECAL for Run 3, the performance of the CMS ECAL operations teams will be crucial for the detector's successful operation and its commissioning

of these features.

Additionally, it is important to estimate the expected sensitivity of this analysis and similar analyses using data to be collected by the upgraded CMS detector during the running period of the future High Luminosity LHC, in order to gauge the prospects of these future physics analyses. This is done through projection studies, the first of which in the WW$\gamma\gamma$ and $\tau\tau\gamma\gamma$ di-Higgs final states has been performed by the CMS collaboration.

This thesis is organized as follows: Chapter 2 will describe the theoretical background which comprises our current understanding of particle physics, and inherently motivates experimental analyses. Chapter 3 will describe the experimental setup: The Large Hadron Collider and the CMS detector. Chapter 4 makes up the "Past" portion of this thesis, and will describe the first search by the CMS collaboration for Higgs pair production in the two W-boson and two-photon final state. Chapter 5 makes up the "Present" portion of this thesis, and will describe the ongoing efforts to optimize the CMS Electromagnetic Calorimeter for Run 3, a crucial subdetector for detecting photon and electron signatures of the HH→WW$\gamma\gamma$ process. This chapter will also include a description of the roles of the various CMS ECAL operations teams. Chapter 6 makes up the "Future" portion of this thesis, and will describe the first sensitivity projection of the search for Higgs pair production in the WW$\gamma\gamma$ and $\tau\tau\gamma\gamma$ final states at the future High Luminosity LHC with the upgraded CMS detector. Finally, Chapter 7 will summarize the full content of the thesis, and highlight the importance of making the most of the data taken in the past while simultaneously optimizing the quality of the data taken during the present, and investigating the potential prospects for physics analysis using data to be taken in the future.

Chapter 2

Theoretical background

The history of particle physics encompasses a slew of discoveries of fundamental particles and force mediators that describe the matter and interactions of the universe. While much has been theorized and experimentally verified, the story of particle physics is far from over. As we progress, theoretical and experimental results will continue to influence other with the goal of understanding the nature of the universe. In this chapter, the current theoretical foundation of particle physics will be described in order to motivate the experimental setup and physics analyses later described in this thesis.

This chapter is structured as follows: The most successful theoretical model of particle physics to date, the standard model, will be described in Section 2.1. In Section 2.2, the Higgs boson and its corresponding electroweak symmetry breaking mechanism will be described. Finally, Section 2.3 will describe the process of Higgs pair production.

2.1   The Standard Model

The standard model (SM) is a quantum field theory which defines a set of quantum fields, whose excitations correspond to observable particles, and describes how they interact. The SM is considered one of the most successful and widely encompassing physical theories to date, as it is consistent with most of the phenomena observed in particle and nuclear physics experiment, and therefore forms a bedrock of understanding of the nature of the universe. The SM defines a quantum field for each type of particle, where the particles include force mediating gauge bosons, a scalar boson, and fermions making up massive material.

The difference between these two classes of particles is as follows: Bosons obey Bose-Einstein statistics, meaning many of them in a given system can simultaneously exist in

the same quantum state, while fermions obey Fermi-Dirac statistics, under which no two fermions within a system can exist in the same quantum state. The particles described by the standard model are depicted in Fig 2.1.

Standard Model of Elementary Particles

	three generations of matter (fermions)			interactions / force carriers (bosons)	
	I	**II**	**III**		

QUARKS

mass charge spin	≃2.2 MeV/c² ⅔ ½ **u** up	≃1.28 GeV/c² ⅔ ½ **c** charm	≃173.1 GeV/c² ⅔ ½ **t** top	0 0 1 **g** gluon	≃124.97 GeV/c² 0 0 **H** higgs
	≃4.7 MeV/c² −⅓ ½ **d** down	≃96 MeV/c² −⅓ ½ **s** strange	≃4.18 GeV/c² −⅓ ½ **b** bottom	0 0 1 **γ** photon	

LEPTONS

	≃0.511 MeV/c² −1 ½ **e** electron	≃105.66 MeV/c² −1 ½ **μ** muon	≃1.7768 GeV/c² −1 ½ **τ** tau	≃91.19 GeV/c² 0 1 **Z** Z boson	
	<1.0 eV/c² 0 ½ **ν_e** electron neutrino	<0.17 MeV/c² 0 ½ **ν_μ** muon neutrino	<18.2 MeV/c² 0 ½ **ν_τ** tau neutrino	≃80.39 GeV/c² ±1 1 **W** W boson	

GAUGE BOSONS / VECTOR BOSONS

SCALAR BOSONS

Figure 2.1: Particles described by the Standard Model

An important feature of the SM lagrangian is its invariance under the product group shown in Equation 2.1.

$$SU(3)_C \times SU(2)_W \times U(1)_Y \tag{2.1}$$

The invariance of the SM lagrangian under these gauge groups corresponds to the conservation of color charge, weak isospin, and hypercharge. In addition, these gauge groups correspond to three fundamental forces: The electromagnetic force mediated by the photon (U(1)), the weak force mediated by the $W^{\pm}$ and Z bosons (SU(2)), and the strong force mediated by the gluon (SU(3)). A known fourth fundamental force of nature, the gravitational force, is not described by the standard model. The absence of the gravitational force in the standard model is a sign that while the SM explains the majority of observations, it is an incomplete description of the fundamental particles and interactions of the universe.

2.1.1 Particles

The SM predicts the existence of particles, which manifest in observation as excitations of their corresponding quantum fields. The particles are classified as fermions described in Section 2.1.1.1, and bosons described in Section 2.1.1.2.

2.1.1.1 Fermions

Fermions are defined as particles which obey Fermi-Dirac statistics, meaning that no two fermions in a quantum system can occupy the same quantum state. At a macroscopic scale, this can be qualitatively thought of as the impossibility for two pieces of matter to go through each other. At a microscopic scale, one implication of Fermi-Dirac statistics is that as an atom gains more electrons, they must occupy "shells" at higher energy states, as lower energy states may already be occupied by existing electrons.

The two types of fermions are quarks and leptons, each of which has three generations, increasing in mass with each generation. The quarks are composed of up and down (1st generation), charm and strange (2nd generation), and top and bottom quarks (3rd generation).

When describing particle masses, the base unit used is the electronvolt (eV), where 1 eV corresponds to the amount of kinetic energy gained by an electron when accelerated from rest across one volt of electric potential in a vacuum. The six SM quarks have a large mass range spanning a few MeV up to 173 GeV (current mass measurement of the top quark), and account for the quantum numbers of hadrons. A common instance of quarks is the composition of the most common hadrons we see around us: Protons (neutrons) have three valence quarks: two up (down) quarks and one down (up) quark.

In the SM, quarks are predicted to be confined, meaning they cannot exist freely and must always be in a bound state with other particles. This means when quarks are produced in experiment, such as from particle collisions, these quarks immediately form pairs with quarks from the QCD vacuum. This process continues with subsequent quarks, leading to the detection of a jet of hadronic activity rather than a single quark. This phenomenon is called hadronization, and is shown in Figure 2.2. This phenomenon is constantly seen at hadron colliders, and is a fundamental handle for detecting quarks and gluons.
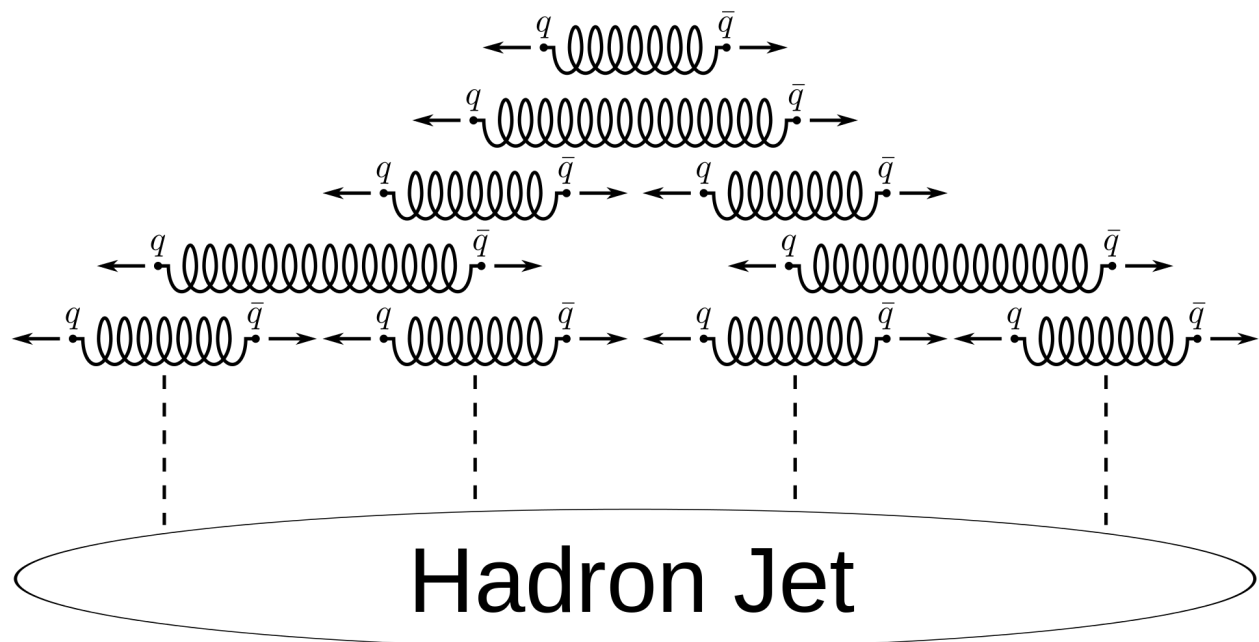
Figure 2.2: Diagram of quark hadronization

The three generations of leptons are the electron, muon, and tau, each with a corre-

sponding flavour of neutrino. Electrons are present in atoms, as they exist in quantum states surrounding the atomic nucleus comprised of neutrons and protons.

While electrons, muons, and taus have mass, in the SM there is no mechanism by which neutrinos gain mass. However, experimental measurements of neutrino oscillations have observed non-zero differences between the squared masses of different neutrino flavors, implying that neutrinos have mass. This is further evidence that the SM is incomplete.

All leptons also have an associated anti particle, which posses the same traits as its corresponding particle but with a negated electric charge.

2.1.1.2 Bosons

Bosons are defined as particles which obey Bose-Einstein statistics. The SM predicts five bosons, namely the gluon, photon, Z boson, W boson and Higgs boson.

Gluons are responsible for mediating the strong force, the mechanism which keeps protons in a bound state by binding their valence and sea quarks. The energy stored in this binding of quarks via gluons accounts for most of the mass of the proton.

The photon is a massless boson which mediates the electromagnetic force between charged particles. It is also the particle corresponding what we see as light: Electromagnetic radiation, which at certain frequencies is visible to the human eye.

The W and Z bosons mediate the weak force, and were experimentally discovered by the UA1 and UA2 experiments at CERN in 1983.

The quantum field corresponding to the Higgs boson plays the special role of providing the mechanism by which massive fermions and bosons obtain their mass.

2.1.2 Forces

While predicting the existence of fermions and bosons, the SM also predicts three types of interactions between these particles: The strong, weak, and electromagnetic interactions.

2.1.2.1   The strong interaction

The strong force is mediated by the gluon, and is the force by which gluons and quarks inter-act. This type of interaction is called Quantum Chromodynamics (QCD), and corresponds to the SU(3) gauge symmetry in the SM, for which color charge is the conserved quantity.

This force is crucial to our qualitative conception of matter, as it is responsible for the binding of quarks into protons and neutrons, as well as the binding of protons and neutrons into stable molecules.

2.1.2.2   The weak interaction

The weak force is a fundamental force mediated by the $W^{\pm}$ and Z bosons, and corresponds to the SU(2) gauge symmetry of the SM, whose conserved quantity is weak isospin.

A fundamental concept in particle and nuclear physics is that of decay: Unstable particles tend to decay towards a more favorable energy state, in which they are transformed into subsequent "daughter" particles, and the weak force is the mechanism by which radioactive decays occur. A common decay known as beta decay, the process by which a neutron decays into a proton, does so via the decay of one of its valence quarks to the opposite signed quark. A Feynman diagram illustrating this is shown in Figure 2.3.
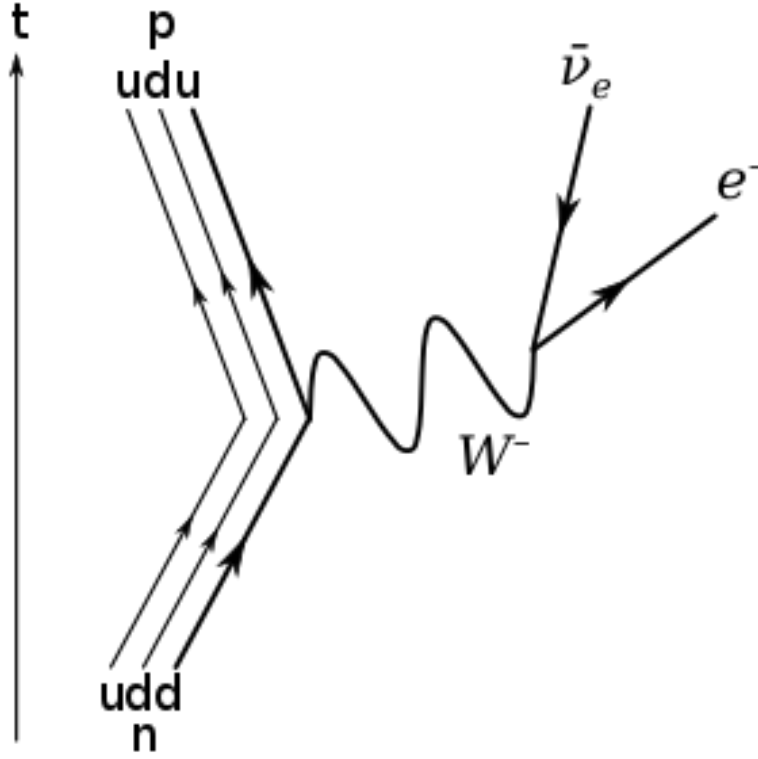
Figure 2.3: Feynman diagram of β decay.

In this interaction, the down-flavoured valence quark of a neutron (d) spontaneously decays into an up quark via the emission of a W boson. This W boson then subsequently decays into an electron and an anti-electron neutrino, leaving a traceable signature. This is known as the lepton decay mode of the W boson, and is one signature through which physicists can search for the W boson in particle collisions.

2.1.2.3   The electromagnetic interaction

The electromagnetic interaction is mediated by the photon, a spin 1 gauge boson. The conserved quantity in the SM through this interaction is hypercharge, corresponding to the U(1) gauge symmetry in the SM, illustrated in Equation 2.2.

$$\phi \to \phi' = e^{i\alpha}\phi \tag{2.2}$$

Where ϕ represents a scalar field, and α represents a constant. Under this transformation the SM lagrangian is invariant.

The photon interacts with all electromagnetically charged particles, which includes quarks, massive leptons, and the W boson. An example interaction, that of the repulsion of two electrons via the electromagnetic force, is shown in the form of a Feynman diagram in Figure 2.4.
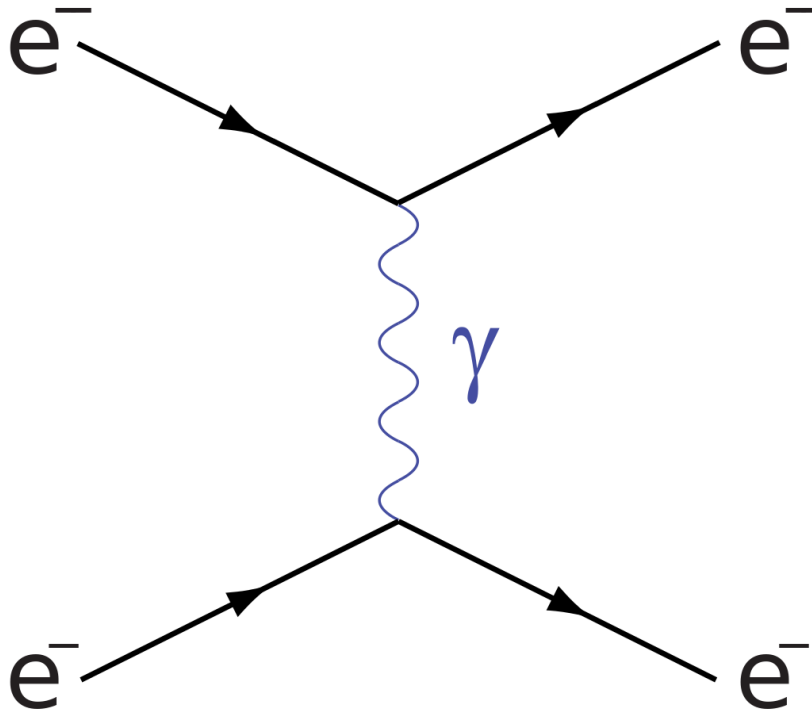
Figure 2.4: Feynman diagram of the electromagnetic interaction between two electrons.

2.2 The higgs boson and electroweak symmetry breaking

While the electromagnetic and weak forces can be defined individually, and act separately at low energy scales, at the electroweak energy scale of about 246 GeV, they are unified into

a single force called the electroweak force. This energy scale is convenient for describing the potential energy term from the Higgs boson, and the subsequent spontaneous breaking of its symmetry.

The Higgs potential term of the SM lagrangian looks as shown in Equation 2.3.

$$V(\Phi) = -\frac{\mu^2}{2}|\Phi|^2 + \frac{\lambda}{4}|\Phi|^4 \tag{2.3}$$

The shape of the higgs potential is shown in Figure 2.5, in a two dimensional phase space made up of the real and imaginary parts of the field Φ.
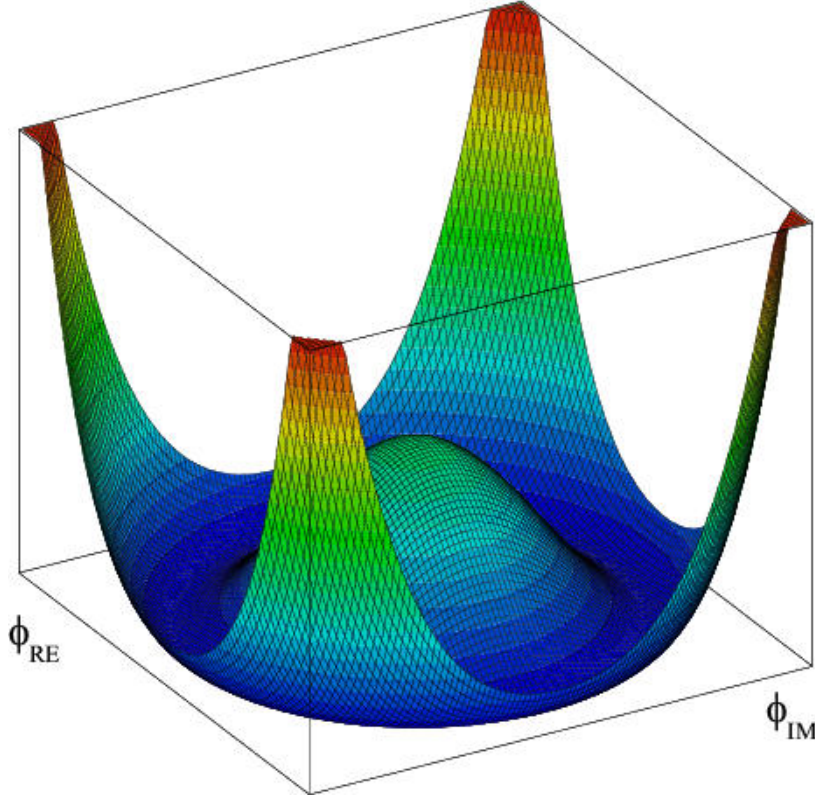
Figure 2.5: Shape of the Higgs potential

A minimum energy value, or vacuum expectation value (VEV), must be taken by the higgs potential. Due to the shape of the higgs potential, an infinite number of points in the two dimensional phase space made up by the real and imaginary parts of the field Φ lie on a

circle which all take on the same value of the Higgs potential. This means that a choice must be made as to which point is taken for the VEV, which leads to a spontaneous breaking of this symmetry.

After electroweak symmetry breaking, additional terms are added to the lagrangian including mass terms for the known massive particles, and terms which determine the shape of the Higgs potential, shown in Equation 2.4.

$$V \quad = \quad \frac{m_H^2}{2}H^2 + \lambda_3 v H^3 + \frac{\lambda_4}{4}H^4, \quad \lambda_3 = \lambda_4 = \lambda_{HHH} = \frac{m_H^2}{2v^2} \tag{2.4}$$

Thus, the shape of the higgs potential depends on the coupling strength values of a Higgs to two Higgs (the tri-linear coupling H^3), and of two Higgs to two Higgs (the quartic Higgs coupling H^4). The values of these couplings are predicted by the SM in terms of the Higgs boson mass and VEV, and based on experimental measurements the higgs self-coupling is predicted to be 0.13 by the SM.

Based on its predicated shape and the current measurements of the top quark mass and Higgs boson mass, the type of stability in which the Higgs VEV is predicted to sit is shown in Figure 2.6.
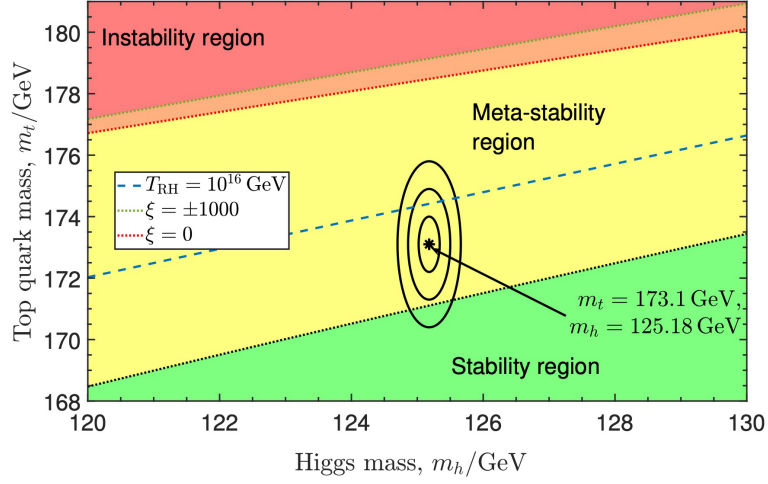
Figure 2.6: Higgs VEV stability as a function of top quark mass and Higs mass

Based on current measurements of the top quark mass and Higgs boson mass, the Higgs VEV is predicted to sit at a meta-stable minimum, as depicted in Figure 2.7.
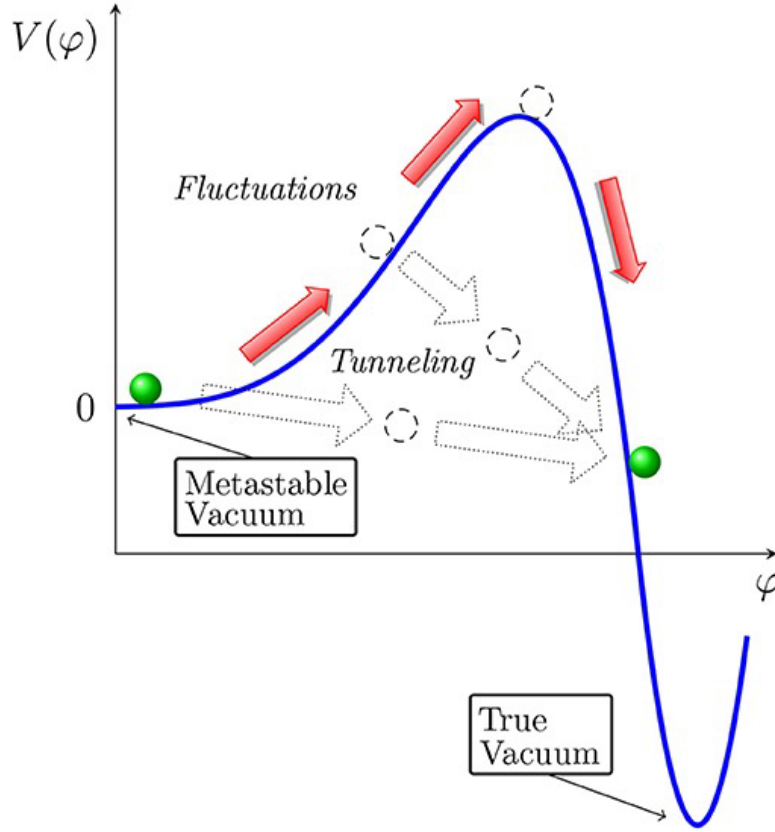
Figure 2.7: Depiction of a metastable Higgs VEV.

This allows for a non-zero probability of the Higgs minimum to shift to a lower, global minimum value, through the process of quantum tunnelling. A shift of the minimum of this sort would completely change the laws of physics as we understand them.

As this is the prediction made by the SM based on the current top quark and Higgs boson mass measurements, it is crucial to be able to compare this to experiment. This implies that an experimental measurement of the shape of the Higgs potential, accessible via its tri-linear and quartic couplings, would provide a fundamental test of the SM.

2.3 Higgs pair production

A process through which the Higgs self-coupling can be directly accessed is Higgs pair production, the production of two Higgs bosons in a single process. The access of this coupling can allow for a measurement of its value, meaning that physics analyses of Higgs pair production can allow physicsts to provide experimental input into the shape of the Higgs potential. This comparison would be fundamental, and could have profound implications: This measurement may agree with the SM, or it may disagree and prompt physicists to consider how to reconcile the SM with their current observations.

The two Feynman diagrams at leading order (LO) which have the largest impact on the production likelihood of Higgs pair production in the gluon-gluon fusion production mode are shown in Figure 2.8.

(a) Triangle diagram   (b) Box diagram
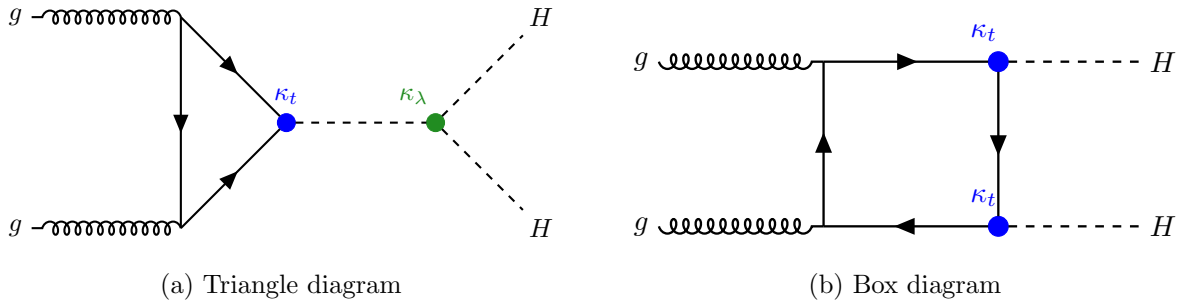
Figure 2.8: Leading order Higgs pair production Feynman diagrams in the gluon-gluon fusion production channel.

These diagrams are referred to as the "triangle" and "box" diagrams, where the triangle diagram is sensitive to both the Higgs self-coupling and top yukawa coupling (the coupling of the Higgs boson to two top quarks), while the box diagram is sensitive only to the top yukawa coupling. These diagrams destructively interfere in the computation of the process' matrix element, leading to a low production cross section. The contributions and interference of these two diagrams as a function of di-Higgs invariant mass for a center-of-mass energy of proton-proton collisions equal to $\sqrt{s} = 14 TeV$ is shown in Figure 2.9.
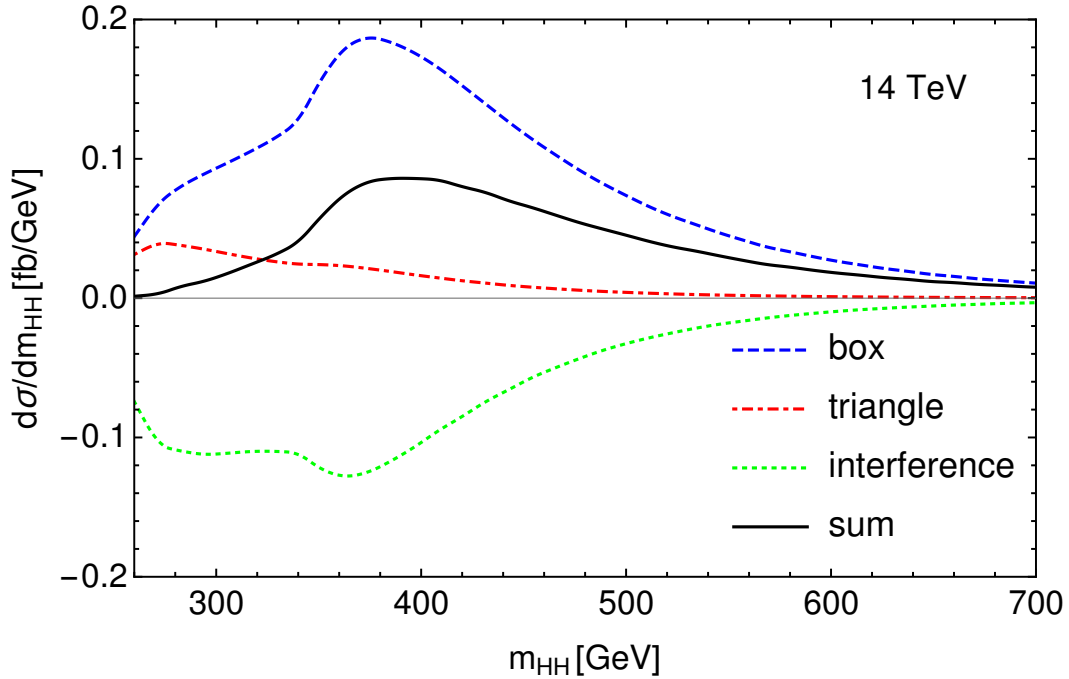
Figure 2.9: Contribution to HH production cross section as a function of di-Higgs system invariant mass, for the triangle and box diagrams and their interference term.

Taking the higher order Feynman diagrams into account, including at next to leading order (NLO) and next-to-next-to leading order (NNLO), a more precise value of the di-Higgs production cross section is computed as a function of center of mass energy for different production modes, and is shown in Figure 2.10.
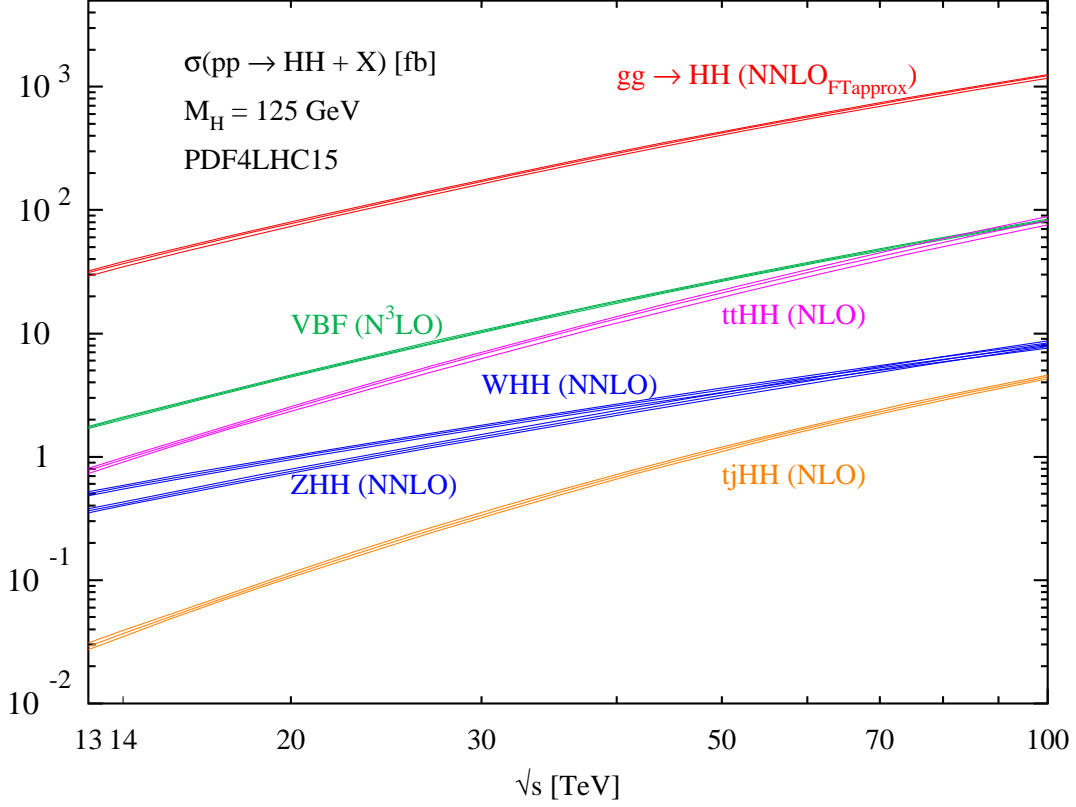
Figure 2.10: Higgs pair production cross sections for different production modes, as a function of center of mass energy.

For proton-proton collisions at center-of-mass energies between 13-100 TeV, the dominant production mode of Higgs pair production is gluon-gluon fusion. For most of this energy spectrum, the next most sensitive production mode is Vector Boson fusion, roughly a factor of 20 less likely. Theoretical productions of Higgs pair production cross section, and physics processes in general, are extremely important for motivating the types of particle colliders and detectors to be built in the future. This allows the matching of a desired physics program with colliders and experiments expected to be capable of producing and detecting these expected physics signatures, in order to answer physicists' questions.

Chapter 3

Experimental Setup: The LHC and the CMS Detector

From the theoretical background described in the previous chapter, we know what type of physics we expect to see given an initial set of conditions. In order to test the consistency of this theory and search for its expected signatures in order to answer fundamental questions, we require an experimental setup designed to produce and study these physical interactions.

This chapter is divided into two sections: Section 3.1 will describe the Large Hadron Collider, and Section 3.2 will describe the Compact Muon Solenoid detector.

3.1   The Large Hadron Collider

The Large Hadron Collider is a particle accelerator located about 100 meters underground, straddling the border of France and Switzerland. It is the largest machine ever built, and an aerial view is shown in Fig 3.1, including the positions of the major experiments it delivers collisions to: The ALICE, ATLAS, CMS, and LHCb detectors. Its construction took place from 1998 to 2008, with the intention of building a machine which can produce proton-proton collisions at a center of mass energy not yet achieved, where part of its physics program was to experimentally discover the Higgs boson, and enhance the ability to test a variety of beyond the standard model (BSM) theories.
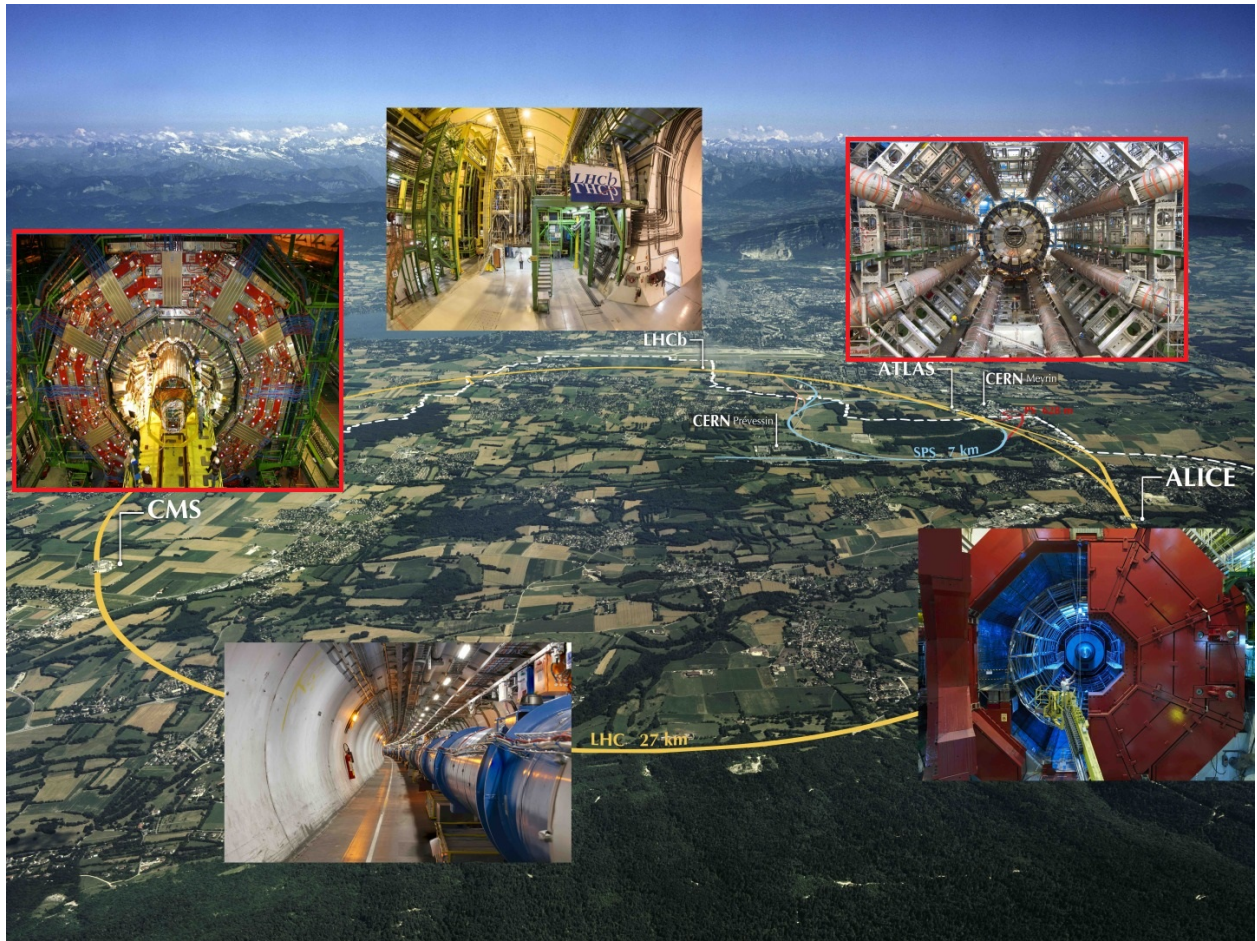
Figure 3.1: The geographical location of the Large Hadron Collider (yellow solid), relative to the French-Swiss border (white dashed) and LHC experiments (white labels)

The LHC is the final acceleration stage in a complex of linear and circular accelerators, all of which are depicted in Figure 3.2.
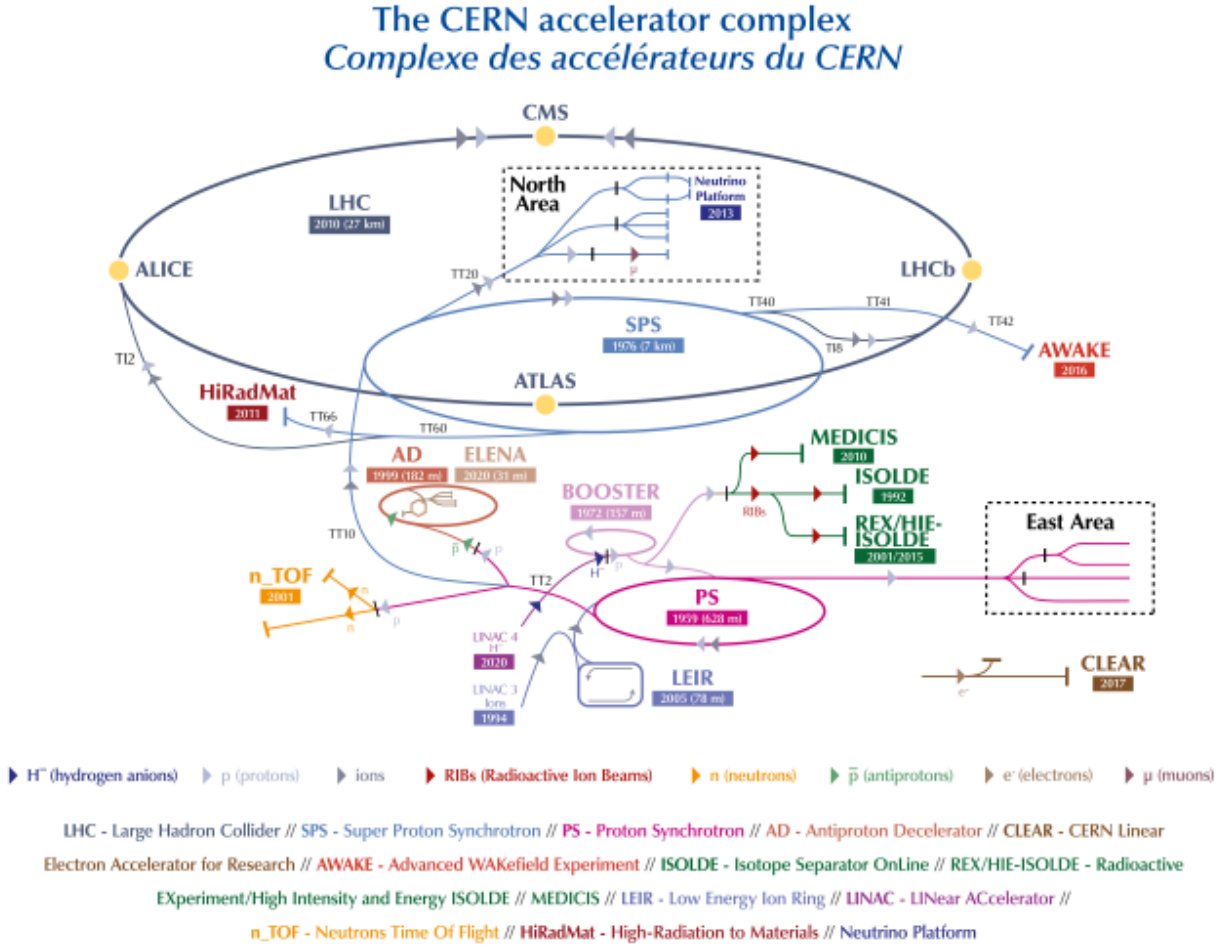
Figure 3.2: CERN accelerator complex

Proton-proton collisions are a useful basis for performing a variety of particle physics analyses, as with a high enough initial energy, all of the SM fermions and bosons can be produced. As the mass of the proton is small compared to that of other SM particles such as the W and Z bosons (about 1/90th) or the Higgs boson (about 1/125th the mass), particle accelerators are used in order to increase the energy of the protons such that this energy can be converted into these more massive particles. Also as seen in the theoretical background chapter, higher center-of-mass energies can lead to higher likelihoods of producing rare processes, such as Higgs pair production.

In Figure 3.3, the long term schedule of the LHC is shown. It should be noted that this

schedule is always subject to change, as unforeseen circumstances may come up during this long time period.
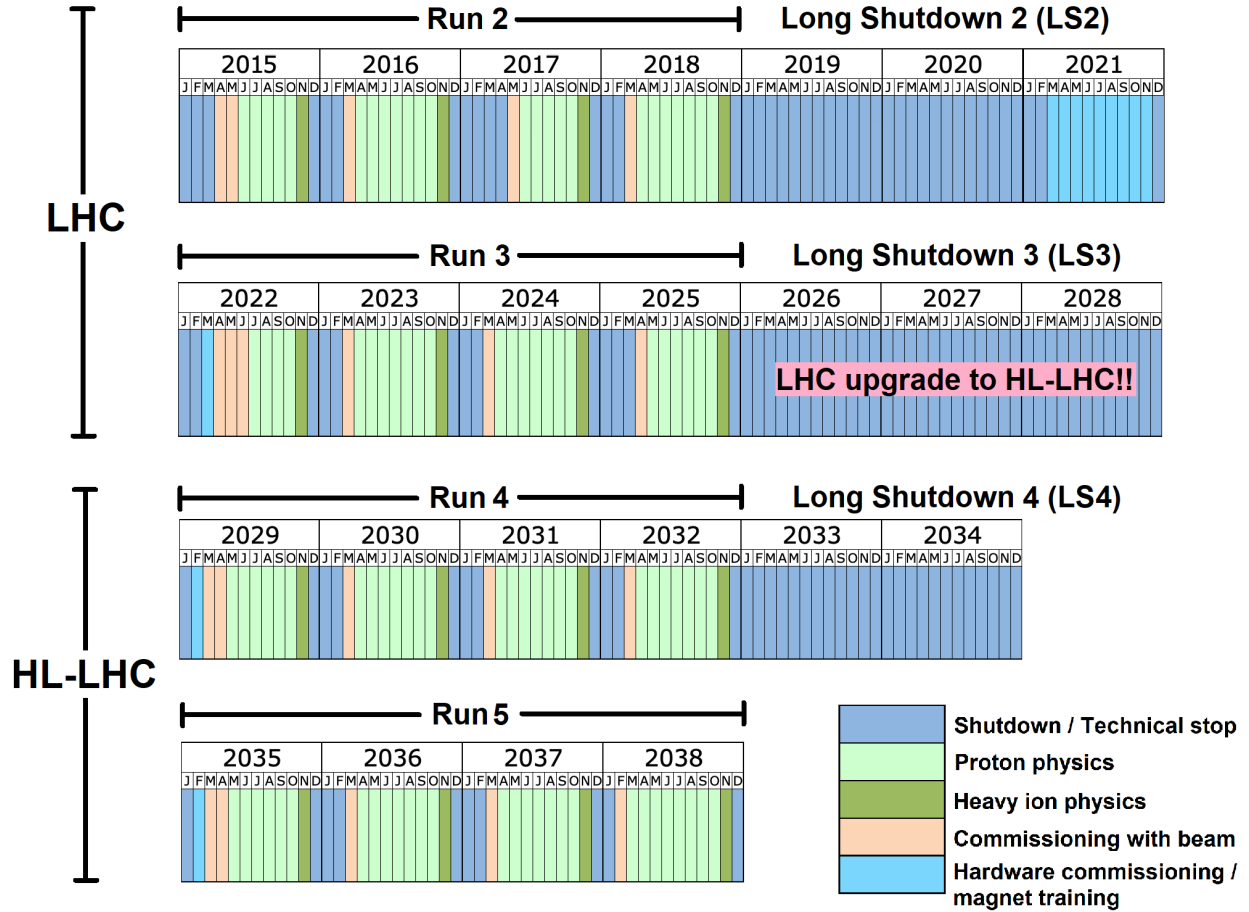
Figure 3.3: LHC long term schedule

3.1.1 Run 2

Run 2 of the LHC took place from 2015-2018 as shown in Figure 3.3, where very little data was delivered to the experiments in 2015, and therefore the vast majority of Run 2 analyses include data collected from 2016-2018.

In order to prepare proton-proton collisions with a high center of mass energy and instantaneous luminosity, during LHC Run 2 the CERN accelerator complex began with a source of H_2, a hydrogen gas. This H_2 gas was injected into a cavity in the presence of an electric

field in order to strip it of its electrons, yielding a pure proton source. These protons were then sent to LINAC 2 (Linear Accelerator 2) to perform an initial acceleration of protons to an energy of 50 MeV. The proton beam then enters the Proton Synchrotron Booster, where they are further accelerated to 1.4 GeV for injection into the Proton Synchrotron, where the beam is further accelerated to 26 GeV. The penultimate stop in the proton beams' acceleration journey is the Super Proton Synchrotron (SPS). In SPS, proton are accelerated up to 450 GeV each and are then injected into the LHC. It is in the LHC where the proton beams, during Run 2, were accelerated up to 6.5 TeV each corresponding to a center of mass energy of 13 TeV, then a world record.

Each stage of acceleration is performed thanks to a variety of superconducting magnets and radio-frequency cavities, with additional magnets used to focus the beams.

During LHC Run 2, the LHC delivered about 156 fb^{-1} of proton-proton collisions to the CMS and ATLAS experiments, with a average number of simultaneous collision interactions, known as pile-up, around 36.

3.1.2   Run 3

Run 3 of the LHC is expected to last from 2022-2025, as shown in Figure 3.3. During LHC Run 3, the acceleration stages will generally be the same as during LHC Run 2, but with the replacement of LINAC 2 in favor of LINAC 4.

On July 5th 2022, the LHC delivered its first "stable beam" collisions at a new world record center-of-mass energy: 13.6 TeV, corresponding to beam energies of 6.8 TeV each, displayed on the LHC monitor shown in Figure 3.4.
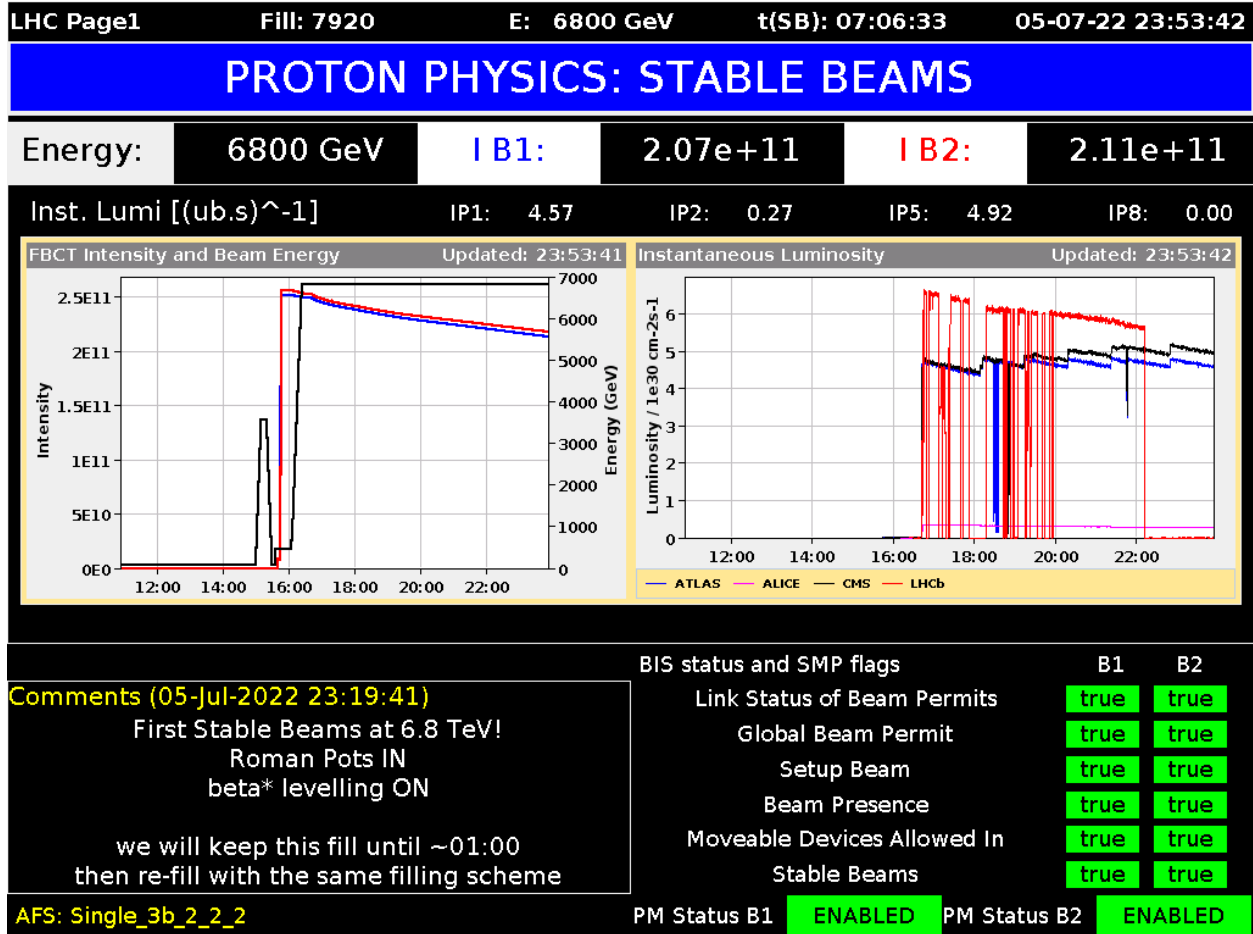
Figure 3.4: LHC monitor during the first stable beams collisions at $\sqrt{s} = 13.6$ TeV

This marked the official start of LHC Run 3. The LHC will spend July 2022 increasing the number of proton bunches in the machine, and starting around the end of July 2022 and early August 2022, will have a full machine of proton bunches in order to provide high intensity collisions to the experiments so that large amounts of data can be recorded.

During LHC Run 3, it is expected that the average pileup will be around 55 simultaneous interactions per bunch crossing, and early estimates of total integrated luminosity are about double that delivered during Run 2. Due to this increase in pileup and total radiation dose to the detectors, it will be important to continue to optimize the LHC detectors during Run 3 to ensure quality data is taken.

3.1.3 The High-Luminosity LHC

At the end of LHC Run 3, the LHC will enter Long Shutdown 3 (LS3), during which the LHC will be upgraded to the High Luminosity LHC (HL-LHC). The HL-LHC is then planned to deliver record amounts of collisions data to the experiments over Runs 4 and 5 between the years 2029-2038, as shown in Figure 3.3.

The sensitivity and uncertainty of a plethora of physics analyses is driven by the yields, or number of events, of the analyzed dataset. Increasing the number of events of the available data to be used for analysis is one of the main motivations for upgrading the LHC, allowing for a higher integrated luminosity which will lead to more sensitive BSM searches, and more precise SM measurements.

The HL-LHC expects to deliver an unprecedented 3000 fb^{-1} to the main LHC experiments, which will make up about 90% of the experiments' total datasets. A visualization of the integrated luminosity to be delivered by the LHC and HL-LHC over time, with a slightly shifted timeline, is shown in Figure 3.5.
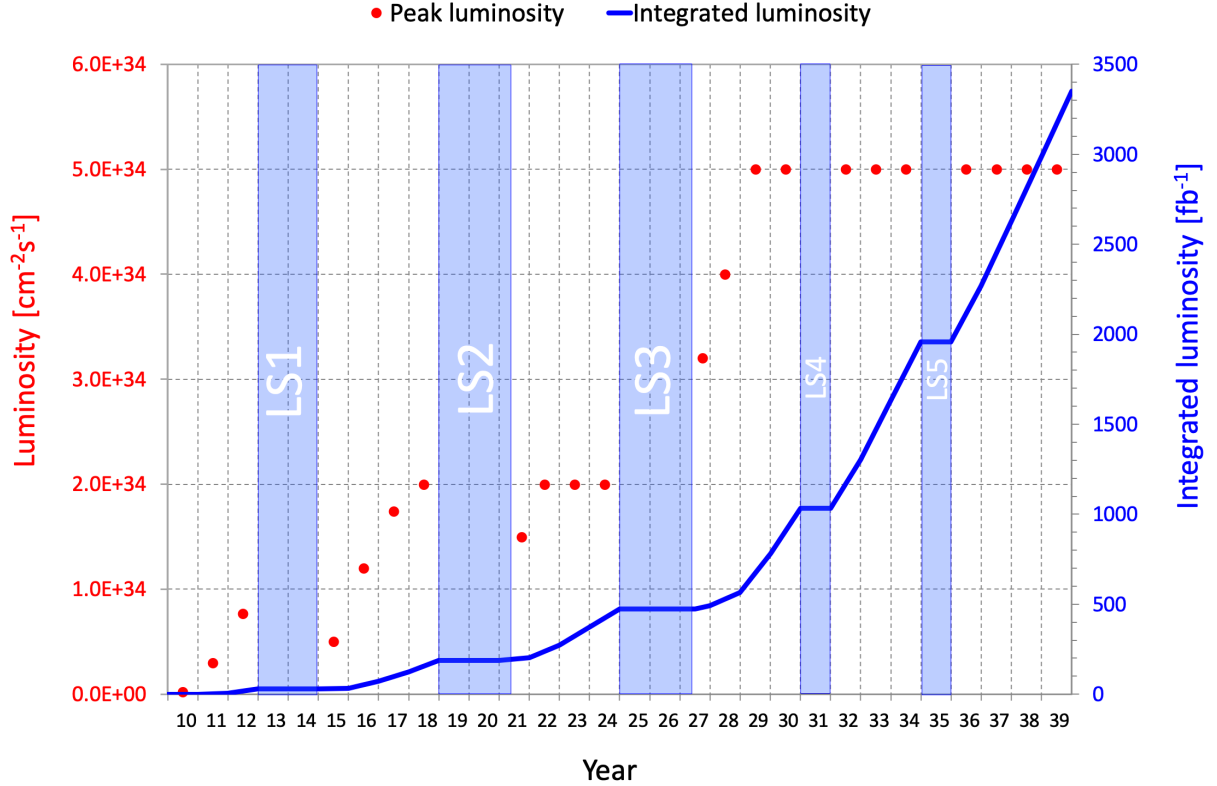
Figure 3.5: LHC and HL-LHC expected integrated luminosity over time

While the upgraded HL-LHC will deliver extremely large datasets to the experiments, this will also lead to very challenging data-taking conditions: One aspect will be the increased pileup which will be produced during HL-LHC collisions, expected to increase from about 55 simultaneous interactions during Run 3 data-taking, to about 140 during HL-LHC. This means that while more interesting signal-like interactions may occur during this data-taking period, there will be many more less-interesting background interactions which will need to be separated from signal interactions. Additionally, during this period detectors will receive a very large amount of radiation which will degrade their sub-detectors. In order to deal with the increase in pileup and radiation, the LHC experiments plan to implement major upgrades so that they can collect high quality data during HL-LHC in order to extend their BSM reaches and SM measurement precisions.

3.2 The CMS detector

The Compact Muon Solenoid (CMS) is a general purpose particle detector located at one of the main interaction points of the LHC. CMS began operation at the start of the LHC in 2009, and collected data delivered by the LHC during LHC Runs 1 (2010-12) and 2 (2015-18). CMS has just recently completed its commissioning phase and started recording data as a part of LHC Run 3, which officially began in July 2022. CMS resides in an underground cavern (UXC), shown in Figure 3.6.
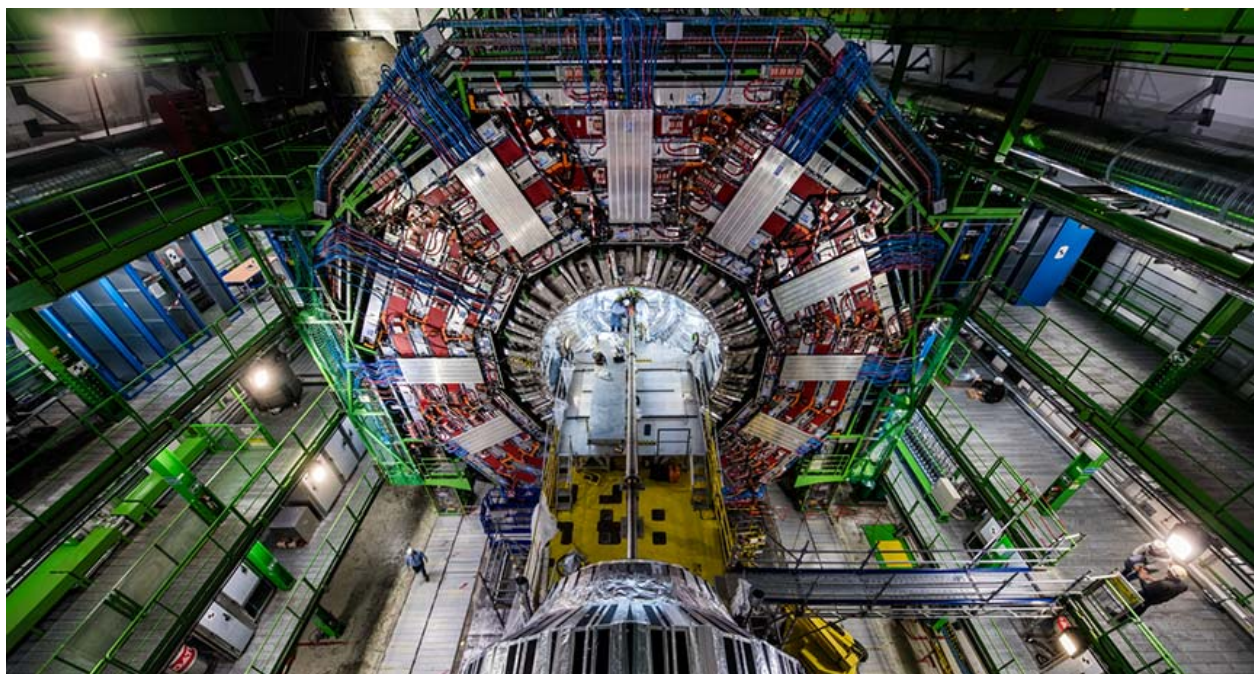
Figure 3.6: The Compact Muon Solenoid

CMS is designed as a hermetic layered structure made of different technologies in order to detect different particles coming from proton-proton and heavy ion collisions delivered by the LHC. A slice of the CMS detector and its different technologies, and the different particles detected, is shown in Figure 3.7.
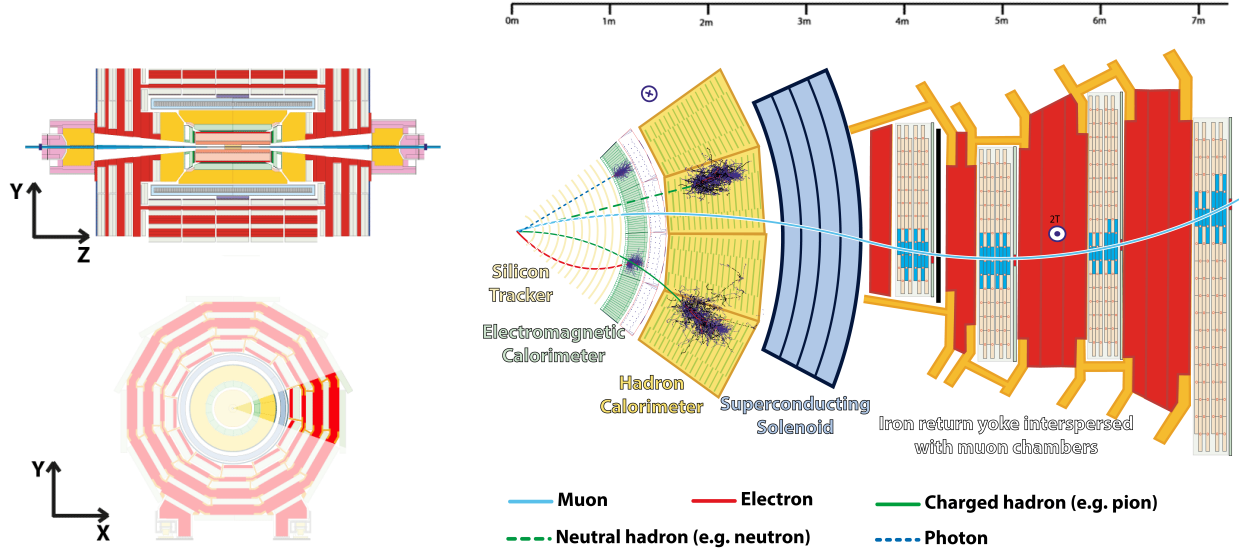
Figure 3.7: CMS detector technologies and particles detected.

3.2.1 Tracker

The CMS tracker is the innermost layer of CMS, and is composed of silicon pixel and strip trackers. The main purpose of the tracker is to detect tracks left by electrically charged particles. These tracks are used to measure particle momentum, corresponding to the track's radius. Additionally, the tracker is used to identify the sign of the particle's charge, and is crucial for identifying the vertex of hard interactions from LHC collisions. The tracker is the most sensitive of the CMS sub-detectors, and is subject to the brunt of radiation produced by LHC collisions.

3.2.1.1 Pixel tracker

The innermost layer of the CMS detector, and first layer of the CMS tracker, is the pixel tracker. This pixel tracker is composed of silicon sensors, of which there were initially about 65 million individual pixel readout channels in 2016. After the first full year of Run 2 data taking in 2016, the pixel detector was upgraded to the Phase-I pixel detector [4] in order to maintain performance following the upgrade of the LHC during the first Long Shutdown

43

(LS1) from 2013-14, from which an instantaneous luminosity larger than the original pixel detector design was produced. The Phase-I pixel detector was installed during the 2016 Year End Technical Stop (YETS), which lasted from December 2016 to April 2017. After its installation, the Phase-I pixel detector, now containing about 124 million individual channels, was used during the 2017 and 2018 data-taking periods of Run 2.

The pixel tracker is composed of the Barrel (BPIX) and Forward (FPIX) pixel detectors, which result in a combined pseudorapidity region for particle detection of $|\eta| < 2.5$. A layout of the Phase-I pixel detector, and a comparison to the original design, is shown in Figure 3.8.
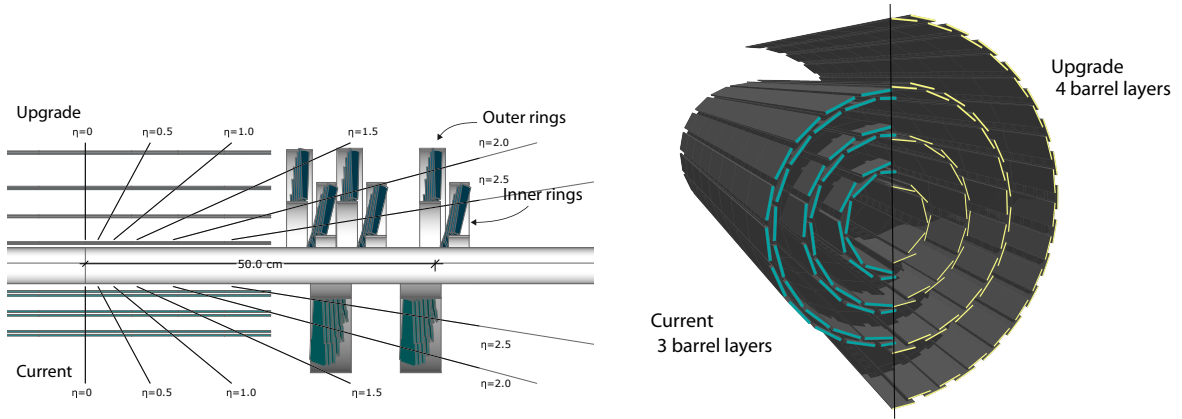
Figure 3.8: The Phase-I CMS pixel detector ("Upgrade"), compared to its original design ("Current").

It can be seen that the main additions to the original CMS pixel detector are the addition of a layer in BPIX, and the addition of several disks in FPIX. Half of the BPIX system during production is shown in Figure 3.9. In this image, the four half-circles concentric to the center of the image correspond to the four layers, L1-4.

44
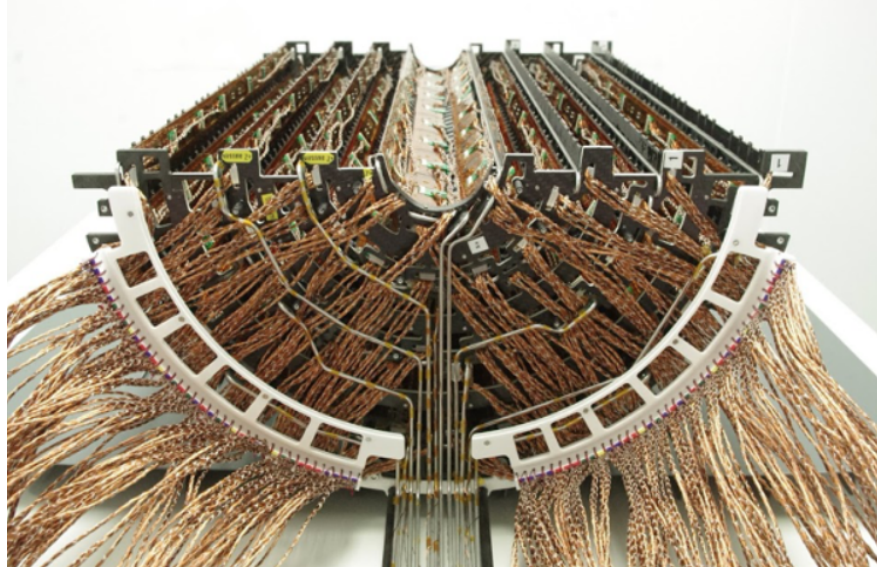
Figure 3.9: Half of the Phase-I BPIX.

The Phase-I pixel detector was able to deliver its expected performance, as shown in Figure 3.10.
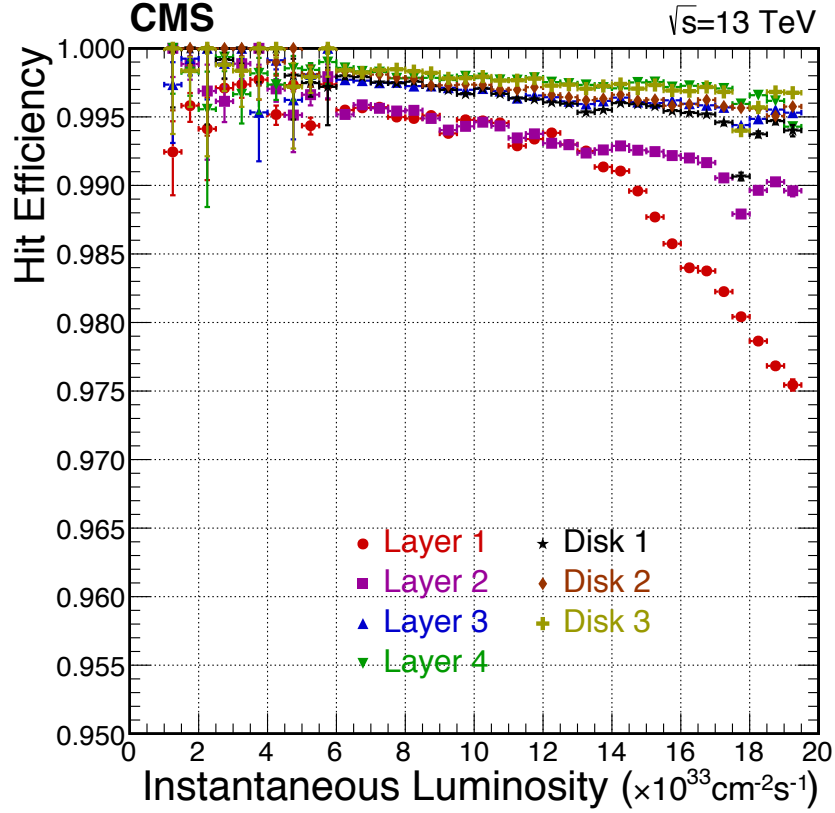
Figure 3.10: Pixel hit efficiency during 2018.

The hit efficiency is shown as a function of different instantaneous luminosities during the 2018 data-taking year of Run 2, where higher values correspond to a higher number of simultaneous interactions, and therefore harsher data-taking conditions. Hit efficiency is defined as the probability that a cluster of pixel hits corresponds to an extrapolated track. Layers 1-3 of BPIX, and the entire FPIX were able to maintain hit efficiencies around 99% even for large instantaneous luminosity values of $2*10^{34}\mathrm{cm}^{-2}\mathrm{s}^{-1}$. Additionally, the L1 hit efficiency, which suffers the most from the harsh data-taking conditions at it is closest to the interaction region, begins to drop around $1.4*10^{34}\mathrm{cm}^{-2}\mathrm{s}^{-1}$ down to about 97.5% at $2\mathrm{cm}10^{34-2}\mathrm{s}^{-1}$. However, this performance is greater than what would have been expected from the original pixel tracker which ran during 2016.

This is an example of a detector upgrade which was unforeseen but deemed necessary to

implement, in response to the data-taking conditions presented to CMS based on collisions delivered by the LHC.

3.2.1.2   Strip tracker

The second layer of the CMS detector, and outer portion of the CMS tracker, is the strip tracker. A view of one quarter of the Phase I strip tracker used during Run 2 can be seen in Figure 3.11.
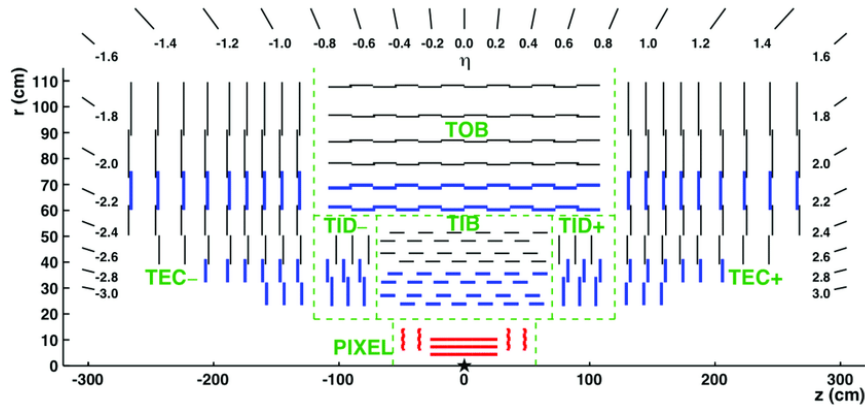
Figure 3.11: A view of half of the CMS strip detector in the r-z plane of CMS.

The CMS strip tracker is composed of 15,148 silicon sensors which are spread over several partitions to cover different regions around the collision point: The Tracker Outer Barrel (TOB), Tracker Inner Barrel (TIB), Tracker Inner Disks (TID) with a plus and minus side, and Tracker Endcaps (TEC) which have modules on the plus and minus side. As shown in the diagram, the strip tracker surrounds the pixel tracker described in Section 3.2.1.1.

The strip tracker performs the same task as the pixel tracker, namely recording hits from electromagnetically charged particles in order to track their movement - a vital task for measuring particle p_T, identifying interaction vertices, and identifying jets from quark/gluon hadronization. The pixel and strip measurements are combined in order to obtain more accurate track measurements.

During Run 2, the strip tracker maintained an excellent signal over noise ratio, and held

a very stable percentage of problematic channels during Run 2, shown in Figure 3.12.

(a) 2017 Signal over noise of TIB

(b) Run 2 problematic channel fraction
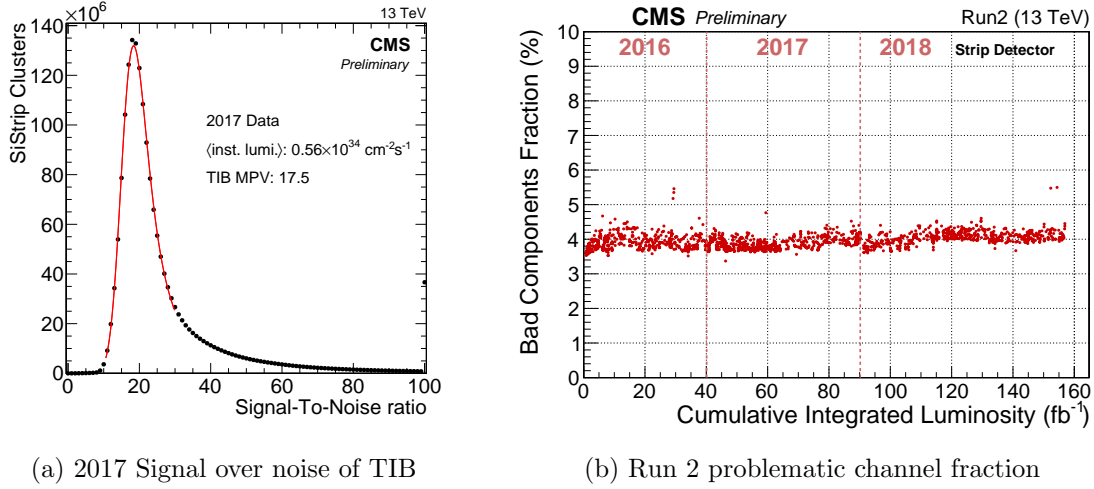
Figure 3.12: Run 2 strip tracker performance.

In 2017, TIB had an excellent MPV (Most probable value) of 17.5 as a signal-to-noise ratio, indicating good signal detection in the strip tracker partition closest to the CMS interaction point. Additionally, over the course of Run 2 operations the percentage of bad components remain stable at about 4% even after receiving the full Run 2 intergrated luminosity, highlighting the robustness of the detector.

3.2.2 Calorimeters

The two calorimeters contained within the CMS detector are the Electromagnetic Calorimeter (ECAL), and the Hadronic Calorimeter (HCAL). A description of ECAL is provided in Section 3.2.2.1, and a description of HCAL is provided in Section 3.2.2.2.

3.2.2.1 The Electromagnetic Calorimeter

The CMS ECAL is a homogeneous crystal calorimeter composed of 75,848 $PbWO_4$ (lead tungstate) crystals that measures the energy of photons and electrons with high precision. The ECAL is composed of a barrel (EB) containing 61,200 crystals and covering the pseudo-

rapidity η region $|\eta| < 1.479$, and two endcaps (EE) containing 14,648 crystals and extending the coverage up to $|\eta| = 3$. Accurately measuring the energy and position information of electrons and photons is vital for an extensive array of physics analyses, in particular the decays of the Higgs boson in the two photon and ZZ to 4 leptons channels, considered the "golden channels" in the experimental discovery of the Higgs boson. The ECAL is supported by an additional subsystem called the ECAL Preshower (ES), located in front of each ECAL endcap. ES is composed of lead and silicon sensors, and is meant to improve two-photon separation, i.e. determine whether photons came from pion decays rather than from Higgs boson, or other interesting decays. The layout and geometry of the CMS ECAL and ES are shown in Figures 3.13 and 3.14. Images of the EB and half of an EE endcap are shown in Figure 3.15.
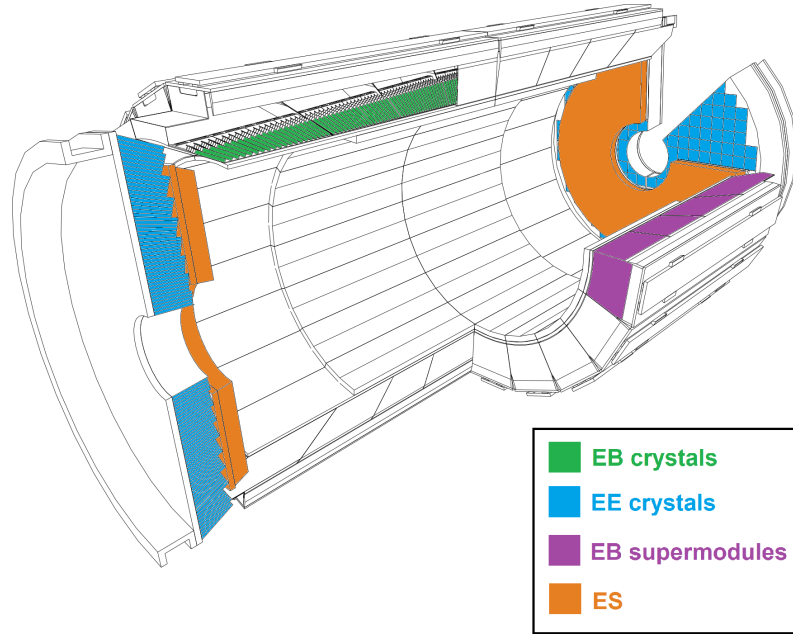
Figure 3.13: CMS ECAL and ES partitions.
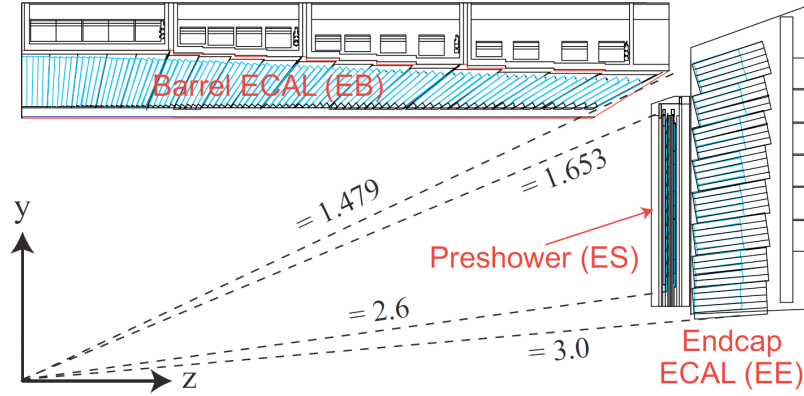
Figure 3.14: Geometric coverage of the CMS ECAL and ES.

(a) ECAL barrel
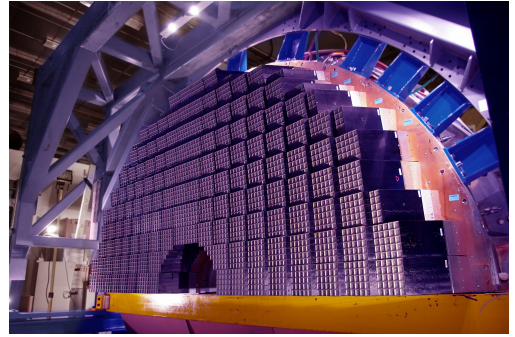
(b) Half of an ECAL endcap

Figure 3.15: Images of the CMS ECAL.

The basis of detection at ECAL is an electromagnetic shower. As a high energy electron or photon approaches ECAL, the electron will emit a photon as bremsstrahlung radiation, and the photon will pair produce to an electron-positron pair in the presence of massive detector material. The resulting photons, electrons, and positrons from this initial process will then perform the same types of processes as a cascade of particles is produced in the ECAL crystals. This is shown as a diagram in Fig. 3.16 for a photon initiating a shower, Fig. 3.17 for an electron initiating a shower, and is visualized as a simulation in Fig. 3.18.
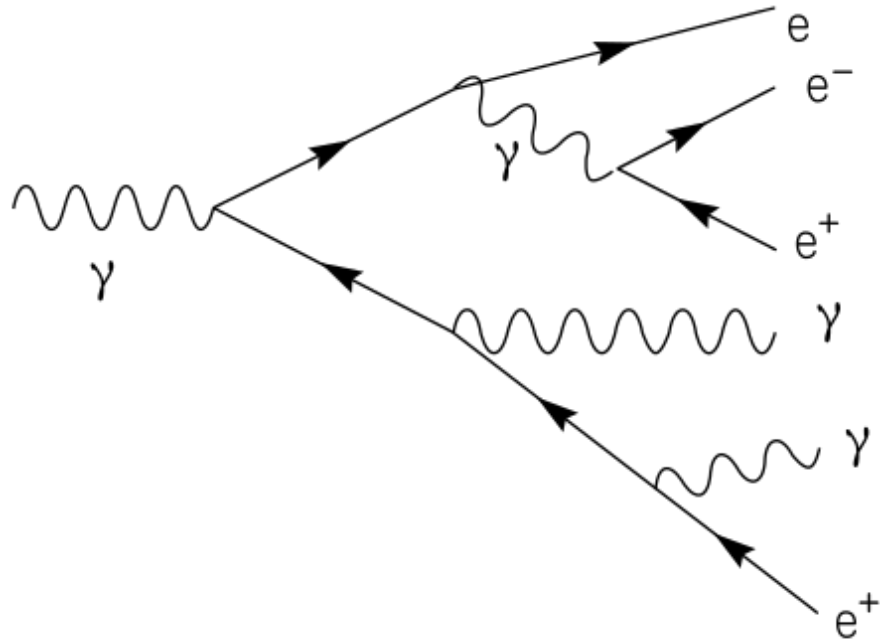
Figure 3.16: Diagram form of a photon initiating an electromagnetic shower via pair production of an electron-positron pair.
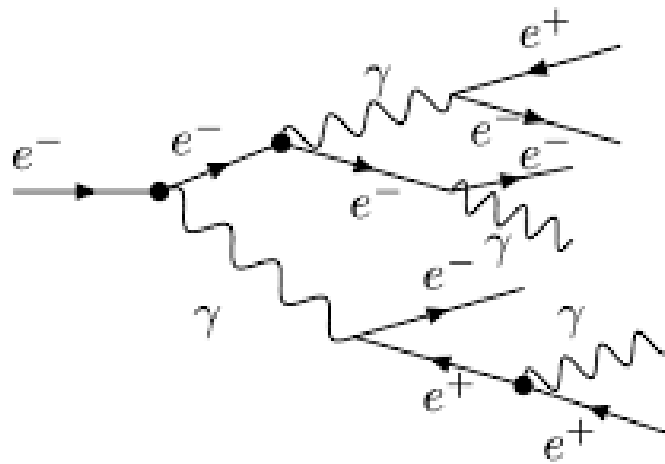
Figure 3.17: Diagram form of an electron initiating an electromagnetic shower via bremsstrahlung radiation.
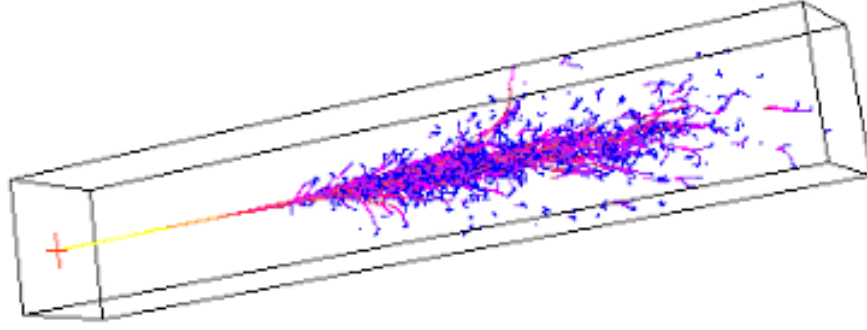
Figure 3.18: Simulated electromagnetic shower inside a material.

In ECAL, this EM shower leads to scintillation in its lead tungstate crystals, producing light that is read by photodetectors on the back of the crystals. The EB uses APDs (avalanche photodiodes), and the endcaps use VPTs (vacuum phototriodes) to convert scintillation light into an electrical signal. Digitized samples of ECAL are taken every 25 ns, and through a series of calibrations, the samples can be converted into an energy in GeV. An image of an EE crystal with its attached VPT is shown in Figure 3.19.

Figure 3.19: EE crystal with its attached VPT.

3.2.2.2 The Hadronic Calorimeter

The CMS hadronic calorimeter is a sampling calorimeter composed of plastic scintillator and brass, whose purpose is to measure the energies of hadrons. This measurement is crucial

for detecting clusters of hadronic energy, which can be matched with regions of high track activity in the identification of jets.

A diagram of the HCAL layout during the start of Run 2 is shown in Figure 3.20.
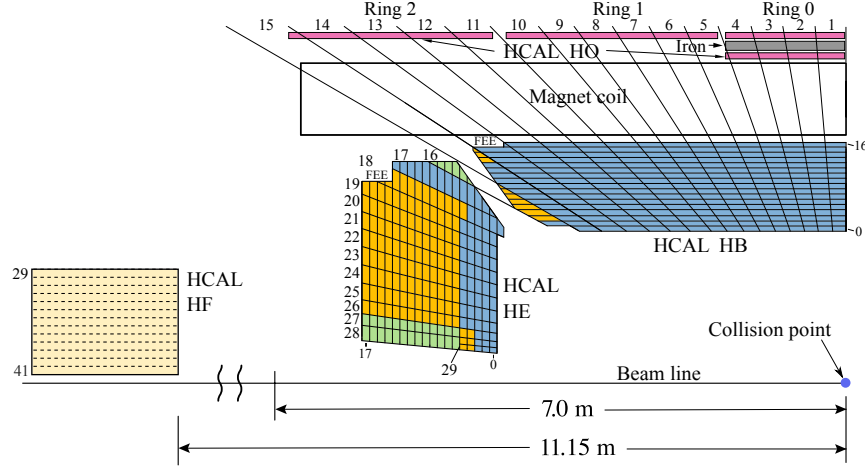
Figure 3.20: CMS HCAL layout in 2016

The HCAL is composed of a hadron barrel (HB), hadron endcap (HE), hadron outer (HO), and hadron forward (HF) sections. HB (HE) has a pseudorapidity coverage of $|\eta| < 1.3$ ($1.3 < |\eta| < 3.0$). HO provides additional measurements in the barrel range, and the HCAL is complimented by HF which extends the angular coverage up to about $|\eta| = 5$. This is very useful, for example, for detecting high pseudorapidity jets originating from Vector Boson Fusion (VBF) quarks, allowing for the detection of an additional production mode for many physics signatures.

During Run 2, HE was upgraded via a replacement of its HPD (Hybrid Photodetectors) in favor of SiPMs (Silicon PhotoMultipliers). In addition, HF was upgraded in order to improve its PMT (Photomultiplier Tubes) in order to better distinguish false signals resulting from cherenkov light, from direct PMT hits from high energy muons.

3.2.3 Solenoid magnet

The central feature of the Compact Muon Solenoid is a superconducting solenoid magnet with a 6m internal diameter, providing an internal magnetic field of 3.8 T - it is the most powerful solenoid magnet on earth. An image of the solenoid magnet placed within the CMS detector is shown in Figure 3.21.

Figure 3.21: The in-progress CMS detector, with the central solenoid magnet visible.

The CMS solenoid magnet plays the dual purpose of producing a magnetic field both in the inner and outer detector, in the outer detector thanks to the ferromagnetic material composition of the CMS outer steel flux return yokes, while also acting as the main support unit to sustain the massive weight of CMS. The magnetic field strength across the inner and outer detector are shown in Figure 3.22.
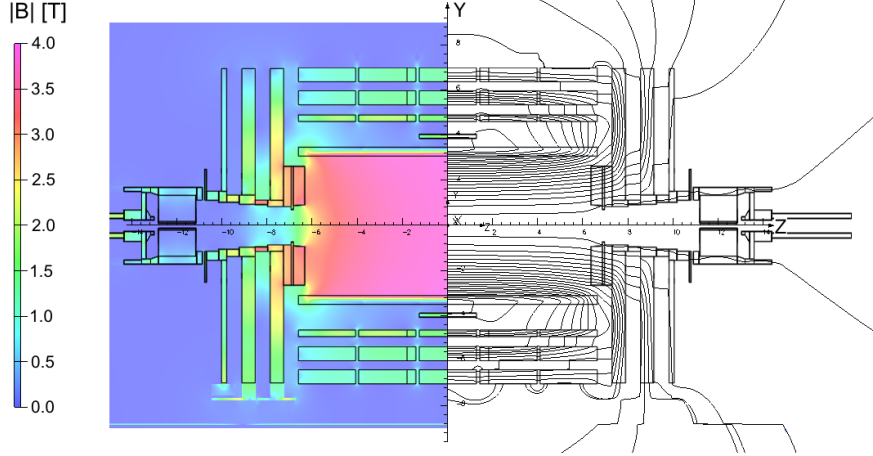
Figure 3.22: CMS magnetic field produced by the solenoid magnetic and steel flux return yoke.

Having a strong magnetic field in the inner tracker region is crucial for the measurements of charged particle tracks and momentum measurement. Additionally, because particles produced in LHC collisions are moving near the speed of light as they traverse the CMS tracker, they spend a finite amount of time in the tracker region, and the stronger the magnetic field in the region the more likely the particle can be "bent" allowing the a high transverse momentum measurement. In particular, the presence of a strong magnetic field to measure the tracks of high p_T particles is of high interest as these particles are more likely to have come from interesting hard interactions, such as those producing a massive particle.

A magnetic field is also produced in the outer CMS detector, which is crucial for the measurement of muon tracks by the CMS muon system.

3.2.4 Muon system

During Run 2, the muon system of CMS was composed of three sub-detectors whose information was combined in order to optimize muon reconstruction. These three sub-detectors are the Cathode Strip Chambers, the Resistive Plate Chambers, and the Drift Tubes described in Sections 3.2.4.1, 3.2.4.2 and 3.2.4.3 respectively. During LS2, the installation of a new muon system called the Gas Electron Multiplier (GEM) was completed in order to

improve muon identification through the addition of additional measurements. This new sub-detector is currently being commissioning for LHC Run 3. A diagram including all CMS muon subsystems, as of the beginning of LHC Run 3, is shown in Figure 3.23.
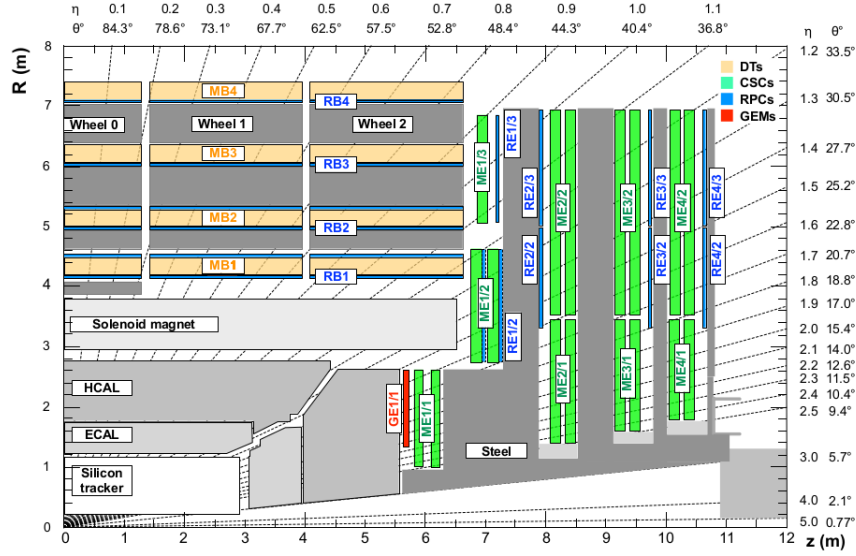
Figure 3.23: CMS muon system at the start of LHC Run 3.

3.2.4.1   Cathode Strip Chambers

The CMS Cathode Strip Chambers (CSC) are a group of 540 gas ionization chambers located in the CMS endcaps. The CSC cavities are filled with a gas mixture composed of Ar, CO_2 and CF_4, and detect muons via ionization of this gas mixture. A diagram showing a CSC and its mechanism for muon detection is shown in Figure 3.24.
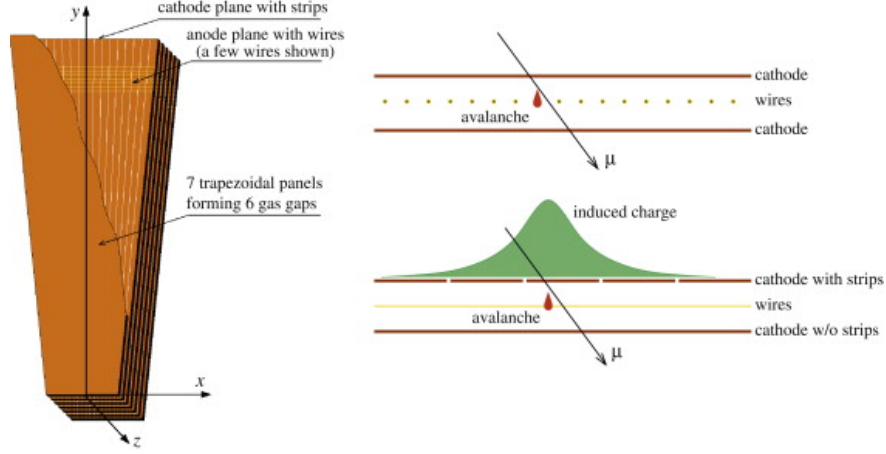
Figure 3.24: Muon detection in the CMS CSCs

When an energetic muon from an LHC collision strikes a CSC, it knocks the electrons off of the atoms making up the CSC gas mixture. These electrons are forced to the anodes (positive ions forced to the cathodes) due to the presence of an electric potential, which produces an avalanche of electrons and thus a net charge.

The CSCs performed extremely well during Run 2, with an average segment reconstruction efficiency around 97%, shown for the 2016 data taking year in Figure 3.25.
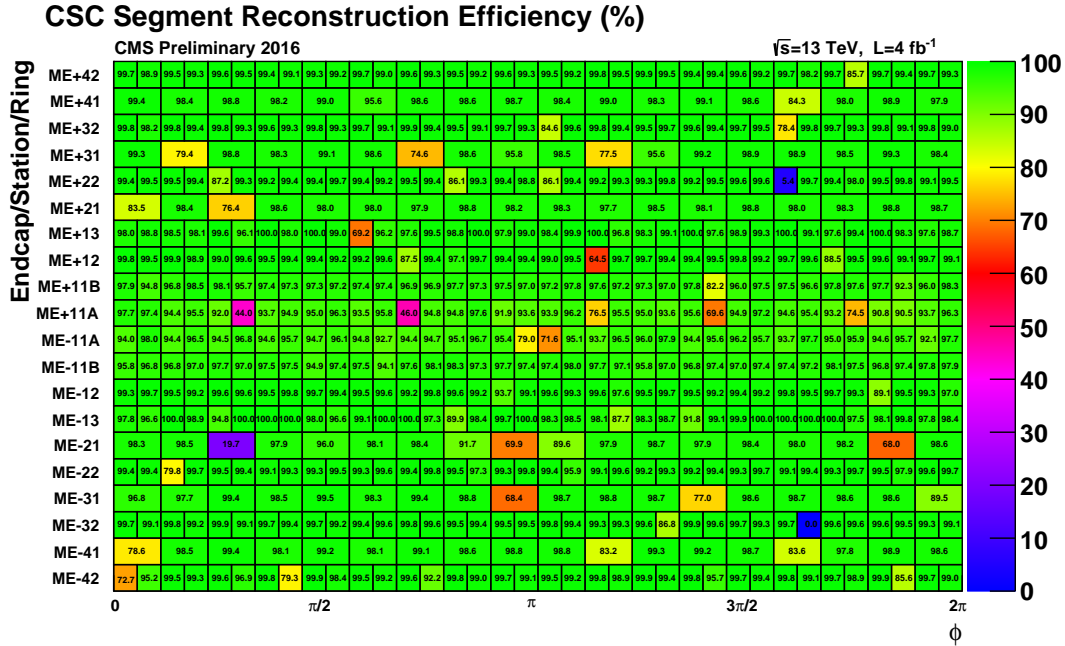
Figure 3.25: 2016 CSC segment reconstruction efficiency.

3.2.4.2 Resistive Plate Chambers

The CMS Resistive Plate Chambers (RPCs) are a group of 1056 chambers placed in both the CMS barrel and endcap sections for muon detection, filled with a gas mixture of $C_2H_2F_4$, C_4H_{10} and SF_6. In a fashion similar to the CSCs, the RPCs detect muons via direct ionization of its gaseous mixture. The layout of an RPC module is shown in Figure 3.26.
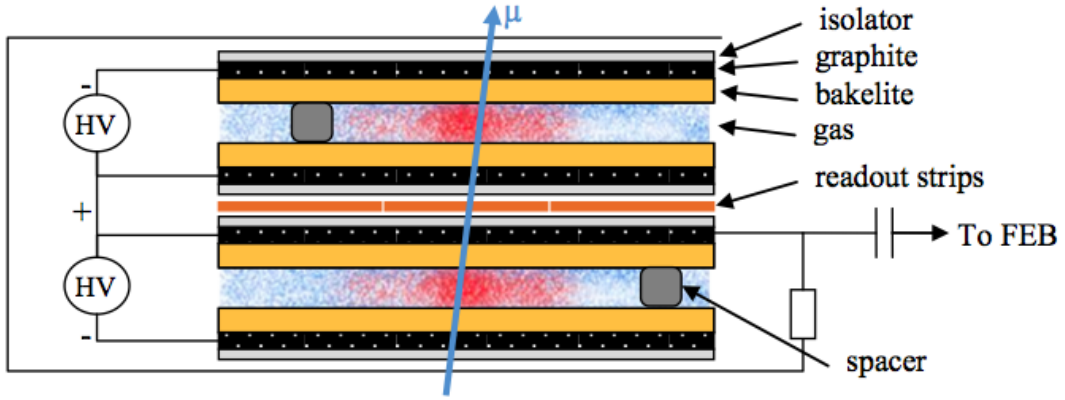
Figure 3.26: RPC schematic.

The idea behind the geometry of an RPC chamber is to have readout strips in the center, with gaseous chambers located on either side.

Like the CSCs, throughout Run 2 the RPCs maintained excellent hit efficiency, as shown separately for the barrel and endcap portions in Figures 3.27 and 3.28.
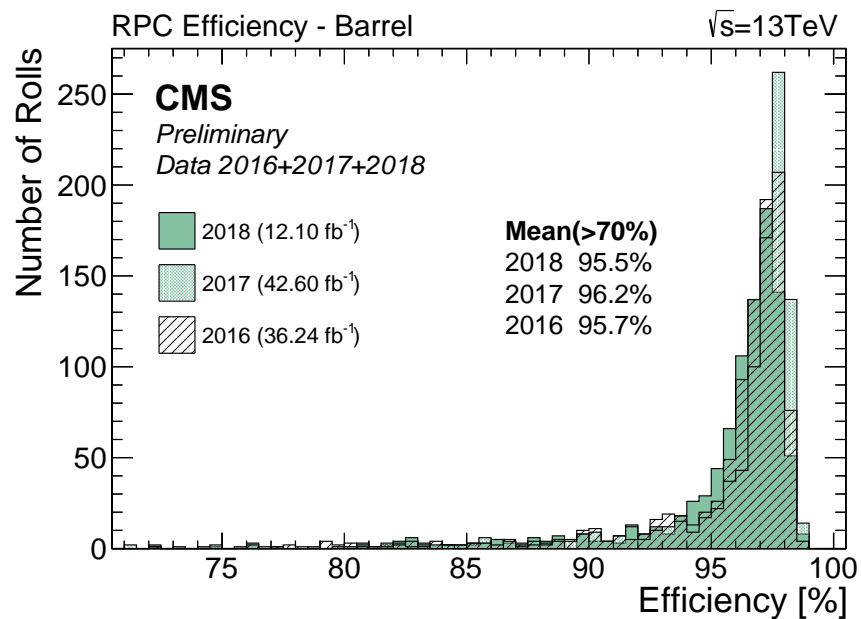
Figure 3.27: RPC barrel efficiency during LHC Run 2.
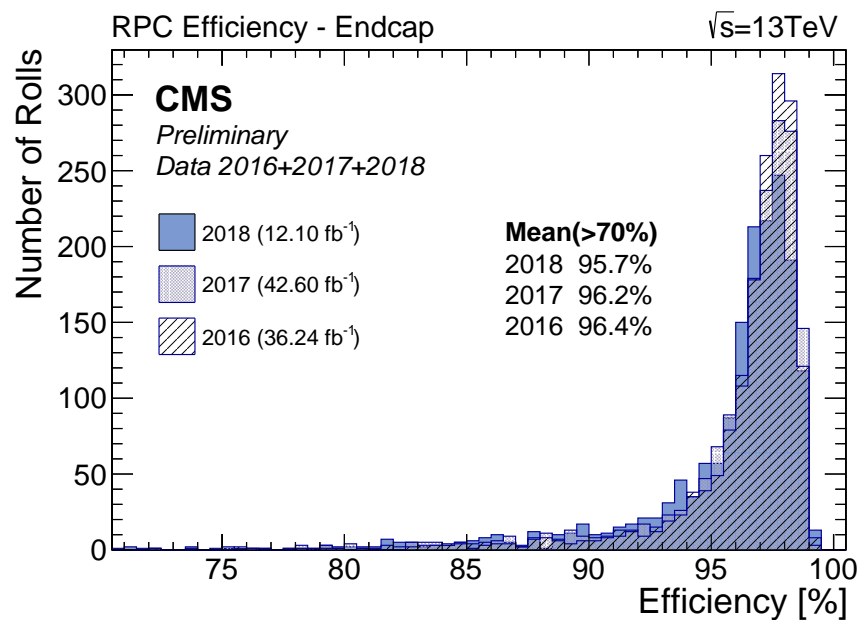
Figure 3.28: RPC endcap efficiency during LHC Run 2.

3.2.4.3 Drift Tubes

The Drift Tubes (DTs) are a CMS muon system located exclusively in the barrel portion of CMS. They function in a similar way to the CSCs and RPCs, as they detect muons via the direct ionization of a gaseous mixture. A diagram of a DT is shown in Figure 3.29.
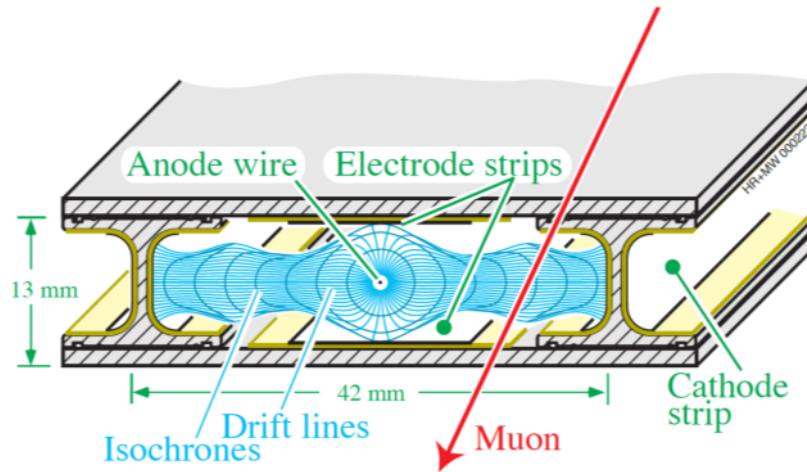
Figure 3.29: Drift tube diagram

3.2.5 Trigger system

During LHC Run 2, and at the start of Run 3, the LHC provides collisions to CMS at a rate of 40 MHz due to the spacing between bunches of protons. It is not feasible for the CMS detector to save recorded information from all collisions, as the on-detector electronics buffers would fill and halt the incoming flow of data. Additionally, this would lead to a very large amount of required offline storage space.

In order to reduce the rate of data saved by the detector, CMS employs a two tiered trigger system in order to pre-select interesting physics events at the hardware level.. The first level, the Level 1 (L1) trigger, reduces the rate of data stored to 100 kHz. The second level, the High Level Trigger (HLT) further reduces this rate to 1 kHz.

3.2.5.1   Level 1 Trigger

The CMS L1 trigger makes an initial judgement on the incoming data in order to determine if a physics event is worth keeping or not. The inputs into the CMS L1 are Trigger Primitives (TP) formed by individual subsystems, and the output is a decision on whether or not to save data for further processing. A diagram of the CMS Level-1 trigger is shown in Figure 3.30 [5].
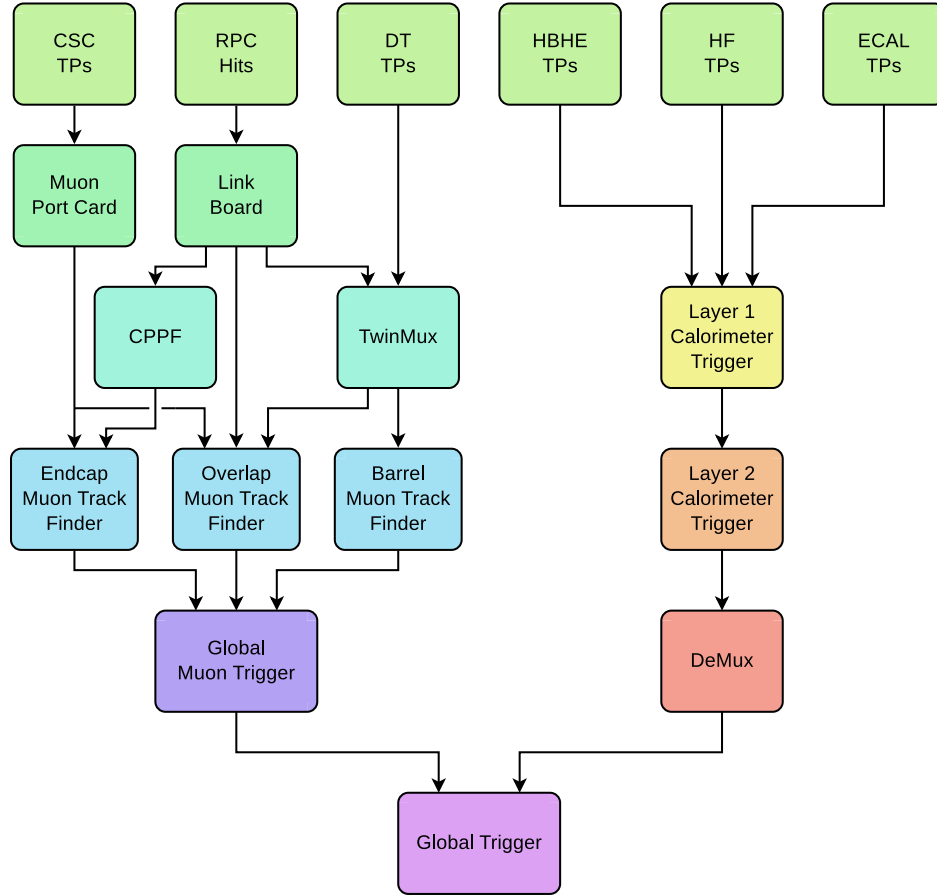
Figure 3.30: The CMS Level-1 Trigger

It is imperative that Level-1 decisions are made in a timely fashion, quickly enough such that the on-detector electronics buffers do not fill. If this were to occur, the flow of incoming data would be halted and CMS would begin to lose events. It is for this reason that a latency of ≈ 4 μs is imposed as the maximum time limit for L1 to make a decision on whether or not

to further process data from a bunch crossing (BX).

During this ≈4 μs, TPs from the muon systems are input to the muon L1 algorithms: The EMTF (Endcap muon track finder), OMTF (Overlap muon track finder) and BMTF (Barrel muon track finder). These respective track finding algorithms make use of the multiple CMS muon sub-system information, and their outputs are all input to the Global Muon Trigger in order to build L1 muon objects. At the same time, the ECAL and HCAL TPs are input to the calorimeter layers: Calorimeter layers 1 and 2, which are responsible for producing L1 objects of the remaining physics objects of interest: EGamma (Electron or photon), jet, and tau objects.

For a given event, this will result in a set of L1 objects. To determine whether or not an event passes the L1 trigger through a Level-1 accept (L1A), it is checked whether at least one of the Level-1 menu seeds meets the requirements of the event's L1 objects. If this is the case, an L1A is sent to the CMS sub-detectors in order to notify them to send the TP information stored in their on-detector electronics buffers to the central DAQ (Data acquisition) system for further processing at the HLT. It is for this reason that an appropriate level-1 menu must be designed based on the expected collisions delivered to CMS, and physics program the detector would like to pursue.

During Run 2 and at the start of Run 3, the goal of the L1 trigger was to reduced the data-taking rate from 40 MHz to 100 kHz.

A major update to the L1 trigger for CMS envisioned to be implemented for the Phase-II CMS detector, which will operate during the HL-LHC, is the addition of tracker information for making L1 decisions. This has the potentially to make L1 decisions based on a variety of additional physics signatures, including based on displaced vertices from b-quarks, potentially leading to much purer CMS datasets.

3.2.5.2 High Level Trigger

After the L1 trigger makes an initial decision on which events recorded by CMS are interesting and warrant further inspection, reducing the data-taking rate from a maximum of 40 MHz to 100 kHz, events are passed to the HLT (High level trigger) to make a final decision on whether or not an event is saved at CMS. The HLT is a computing farm located above the CMS control room, which performs a reconstruction similar to the standard offline CMS event reconstruction on events passing the L1 trigger, and during Run 2 reduced the trigger rate from 100 kHz to 1 kHz for permanent storage. An image of the HLT computing farm is shown in Figure 3.31.

Figure 3.31: CMS HLT computing farm (2010)

During LS2, the CMS HLT began implementing the use of Graphical Processing Units (GPUs) in conjunction with CPUs (Central processing units) in order to decrease the time required to reconstruct physics events. The potential gain could be very useful for CMS, as if HLT processing time is decreased one would have more "time budget" to allocate to reconstruction, potentially allowing for more complex reconstruction, and to that end a purer

dataset saved by the HLT farm. The CMS HLT is currently running with a combination of CPUs and GPUs, and has successfully commissioned this version of reconstruction for the start of LHC Run 3.

Chapter 4

Past: Search for Higgs boson pair production in the WW$\gamma\gamma$ final state with the Run 2 dataset

As mentioned in Chapter 1, the experimental discovery of a particle consistent with the SM Higgs boson by the CMS and ATLAS experiments at the CERN LHC in 2012 marked a milestone moment in the history of particle physics. After having verified the existence of this particle, physicists have sought to further their understanding of the Higgs boson and the underlying electroweak symmetry breaking process. Additionally, the Higgs boson is widely explored as a potential bridge to physics beyond the standard model (BSM).

Through the investigation of Higgs pair production, the production of two Higgs bosons in a single process introduced in Section 2.3, physicists can both test SM predictions and search for BSM. On the SM front, investigating Higgs pair production allows for a fundamental test as the shape of the Higgs potential in the SM Lagrangian depends on the Higgs self-coupling value described in Section 2.2, which can be directly accessed via Higgs pair production. A precise measurement of this coupling would provide the first experimental insight into the shape of the Higgs potential, which can have profound implications on the understanding of our world, for example by providing evidence that the Higgs vaccum expectation value sits at a meta-stable minimum consistent with the SM prediction. Alternatively, a measurement which is not consistent with this SM prediction could hint to physics beyond the standard model [6].

The main LO processes which contribute the most to the di-Higgs production cross section destructively interfere, leading to a low production cross section of about 31.05 fb at a center

of mass of $\sqrt{s} = 13$ TeV, previously explained in Section 2.3.

In order to search for this relatively small signal, a search is performed in the WW$\gamma\gamma$ channel. This final state benefits from the sensitive $H \to \gamma\gamma$ process which provides a narrow, distinguishable signature. Additionally, the $H \to WW$ leg of the decay contributes a relatively large branching ratio among Higgs boson decays of about 22%. Because the W boson can decay both leptonically (W$\to \ell\nu$) and hadronically (W$\to$qq), the $H \to WW$ and by extension the $HH \to WW\gamma\gamma$ process has three possible final states: The fully-hadronic (FH), semi-leptonic (SL), and fully-leptonic (FL) final states, corresponding to 0, 1, and 2 leptonically decaying W-bosons respectively, whose Feynman diagrams are shown in Figure 4.1.

(a) Semi-Leptonic   (b) Fully-Hadronic   (c) Fully-Leptonic
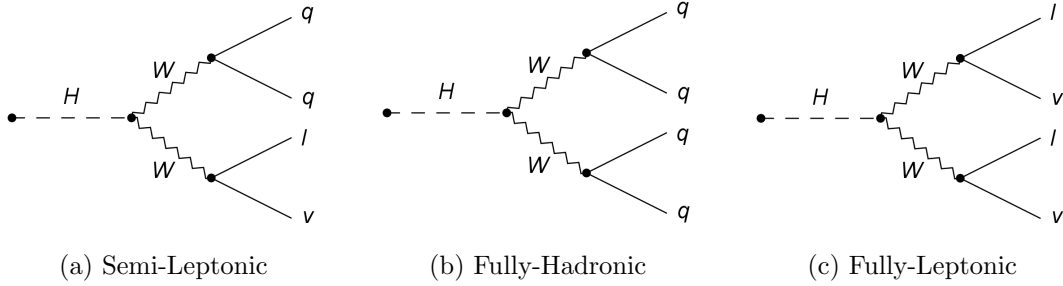
Figure 4.1: The three decay modes of H$\to$ WW.

These three final states can be identified in data and simulation with separate selections and categorizations, and their corresponding signal and background models can be simultaneously fit to data in order to improve the overall analysis sensitivity towards di-Higgs production. Due to the expected overlap between the FH WW$\gamma\gamma$, FH ZZ$\gamma\gamma$, and bb$\gamma\gamma$ di-Higgs final states, an attempt is made to remove as much FH ZZ$\gamma\gamma$ and bb$\gamma\gamma$ as possible. Any residual yields from these non-WW$\gamma\gamma$ final states are considered as signal in the analysis when building simulation templates.

In addition to the prediction of SM di-Higgs, several BSM models predict the existence of real and virtual heavy particles that can couple to a pair of Higgs bosons [7; 8; 9; 10; 11]. These can lead to the appearance of a resonant contribution to the invariant mass of the

HH system, or to a significant modification of Higgs boson pair production through virtual processes. As no direct searches for BSM particles have resulted in discoveries at the LHC, we choose to parameterize these possible effects at LHC energy scales using an Effective field theory (EFT) approach [7; 12]. The effects are parametrized either as modifications to the SM couplings, or as contact interactions. In the SM coupling modifications, possible new resonances contribute through loop diagrams whereas the contact interaction is a way of describing a process where the mediator has a mass far above the momentum transfer in the event and therefore can be both via a triangular virtual loop or resonant production. The interpretations of this analysis include the purely SM interpretation, an EFT interpretation leading to scans of modified SM and purely BSM lagrangian coupling constants, and a search for 20 EFT benchmarks corresponding to points which are collectively largely representative of the explored 5-dimensional EFT phase space [12; 13; 14].

This is the first search for Higgs pair production in the WW$\gamma\gamma$ final state performed by the CMS experiment, and is performed using pp collisions at $\sqrt{s} = 13$ TeV. The data sample corresponds to an integrated luminosity of 138 fb^{-1} collected with the CMS detector at the CERN LHC during Run 2 (2016-18). A search in the SL WW$\gamma\gamma$ final state was performed by the ATLAS experiment using data collected at the LHC in 2016, where a cut-based analysis was performed to obtain an observed (expected) upper limit on SM di-Higgs production of 7.7 (5.4) pb at a 95% confidence level [15].

The structure of this chapter is as follows: The overall strategy of the analysis is described in Section 4.1. A description of the EFT parameterization and benchmarks is provided in Section 4.2. The data samples and simulated events are described in Section 4.3. The reconstruction of particles as detector objects is described in Section 4.4. Event selection criteria and categorization are described in Section 4.5. The method of signal and background modelling using simulation and data is described in Section 4.6. A description of the systematic uncertainties of the analysis is presented in Section 4.7. The results of the analysis are described in Section 4.8, and a summary is provided in Section 4.9.

4.1 Strategy

In most searches for physical processes in particle physics data, a simulation template is formed and is then fit to data in a given signal region in order to determine if the expected physical process in present in the data. Typically the signal region is a single variable, or set of variables where more signal than background is expected. In this analysis, the signal region used to fit the simulation template to data is the diphoton invariant mass, in the window $115 < m_{\gamma\gamma} < 135$. This region is chosen due to the expectation that the H$\rightarrow \gamma\gamma$ leg of the HH$\rightarrow$WW$\gamma\gamma$ process should provide a peak in this region.

There are two background signatures present in this analysis: A resonant background from the single Higgs to $\gamma\gamma$ process, and a continuum background formed by a combination of background processes which do not contain a prompt diphoton. An illustration of the signal and background signatures is shown in Figure 4.2.
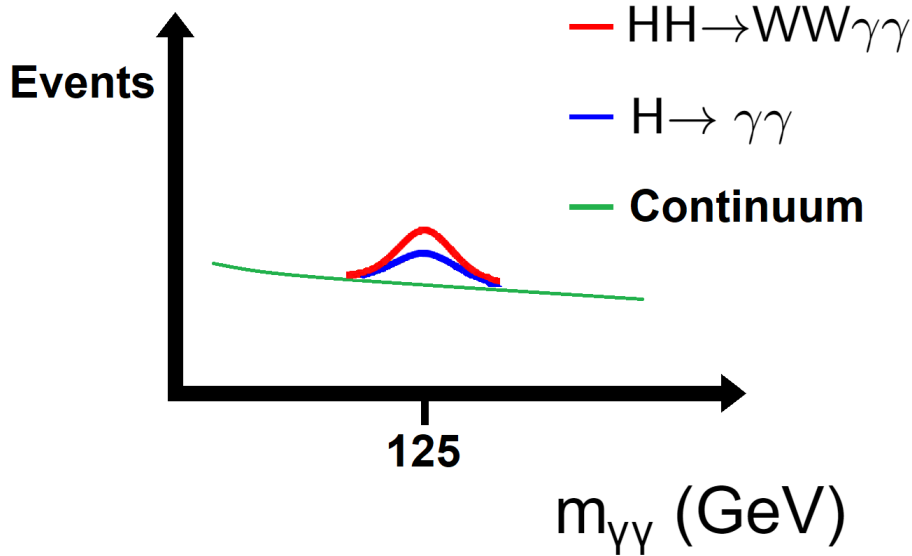
Figure 4.2: Analysis signal and background signatures.

In order to optimize the sensitivity of this analysis, a DNN (Deep Neural Network) is employed for the Semi-Leptonic final state, as it is expected to be the most sensitive channel

due to the increase in branching ratio from the hadronic W decay, but with the benefit of maintaining a clean signature due to the presence of a lepton. A multiclass DNN is trained in order to separate the SM di-Higgs signal from background processes, while a binary parametric DNN is used to differentiate 20 EFT benchmark scenarios from background processes.

The FH channel also uses a DNN in order to optimize sensitivity, in this case by separating FH HH signal from backgrounds. In the FH channel, there is a significant overlap with the $HH \rightarrow$ bb$\gamma\gamma$ final state, so two binary DNNs are trained: The first binary DNN separates the FH WW$\gamma\gamma$ process from all backgrounds, and is used for categorization. To reduce the overlap of bb$\gamma\gamma$ events between the bb$\gamma\gamma$ and WW$\gamma\gamma$ phase spaces, another binary DNN is trained that separates bb$\gamma\gamma$ from all backgrounds. The bb$\gamma\gamma$ training score is used as a "bb$\gamma\gamma$ killer", where a selection is applied on its value to reduce the contamination of bb$\gamma\gamma$ events in the WW$\gamma\gamma$ phase space, while preserving the majority of WW$\gamma\gamma$ signal events.

For the Fully-Leptonic channel, a cut based strategy is used due to a lack of number of events necessary to perform an MVA (Multivariate analysis) training.

It is imperative to apply orthogonal selections to data and simulation events in order to avoid including the same events in multiple background categories. This is done via the event's number of leptons, where each lepton must pass a common set of selections applied for all final state tags. After a set of lepton objects is selected for each data or simulation event, events fall into the FH category if they contain exactly zero leptons, the SL category if they contain exactly one lepton and the FL category if they contain exactly two leptons.

Further event selections are made for the three final state categories, but by requiring an orthogonal separation of the number of leptons, it is guaranteed no one event can fall into more than one category. Thus, a simultaneous fit of background and signal models to data in different final state categories can be performed in order to obtain a final result which benefits from a combination of the physics signatures of all three final states. This is also summarised in the flow chart shown in Figure 4.3.
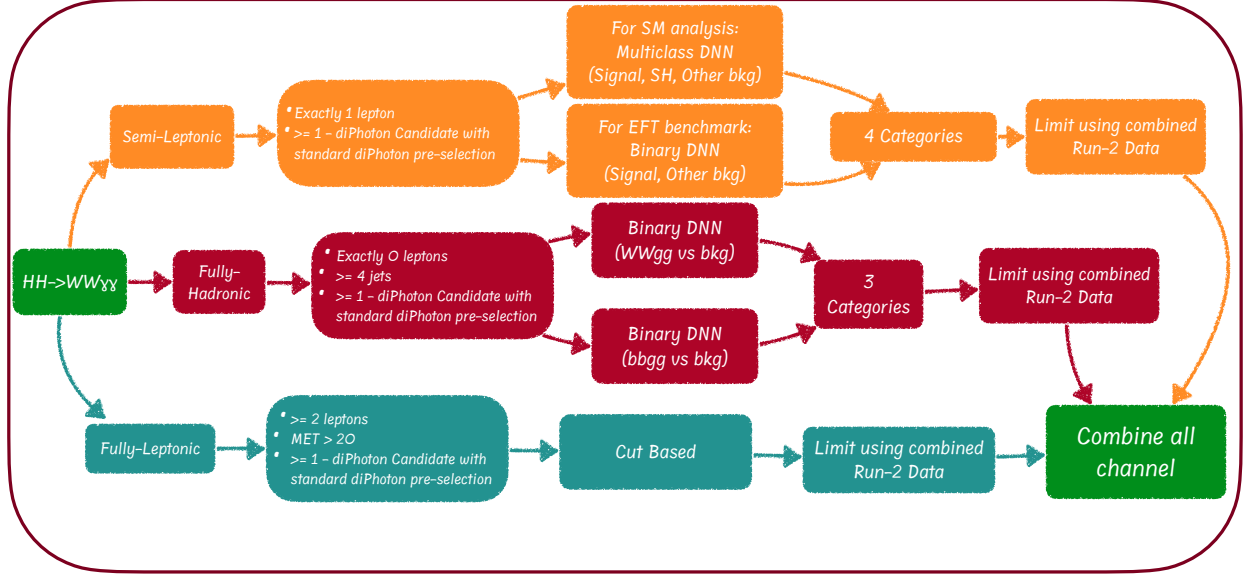
Figure 4.3: $HH \to WW\gamma\gamma$ Analysis flow chart

Signal and background models are constructed independently for each year of data and MC (2016, 2017 and 2018) and combined to produce signal and background models to fit to the LHC Run 2 dataset. Results are obtained by performing a simultaneous likelihood fit to the invariant diphoton distribution, $m_{\gamma\gamma}$, among all categories. This procedure is performed in order to extract 95% CL upper limits on di-Higgs production within the context of the SM interpretation. Additionally, through the use of an EFT lagrangian, various simulation templates are fit to data and a linear combination of EFT samples results in the scan of two EFT parameters, and upper limits are extracted on 20 EFT benchmark scenarios.

4.2 EFT description

As di-Higgs in the WW$\gamma\gamma$ final state is predicted in the SM, a search for its SM signature is performed. In order to increase the breadth of the search, the analysis is extended to a search for a variety of EFT scenarios predicting the HH→WW$\gamma\gamma$ process with varying cross sections. This extension branches from the SM, where the Higgs potential before spontaneous symmetry breaking reads as shown in Equation 4.1, where Φ is an $SU(2)$ doublet scalar field, and ϕ is the real part of its neutral component, equal to $v + H$, where v is the field's vacuum expectation value.

$$V(\Phi) = -\frac{\mu^2}{2} |\Phi|^2 + \frac{\lambda}{4} |\Phi|^4 \tag{4.1}$$

Requiring there be a minimum value of this potential leads to the relations shown in Equation 4.2.

$$\lambda = \frac{m_H^2}{2v^2}, \quad \mu^2 = \frac{m_H^2}{2}, \quad m_H^2 = \frac{\partial^2 V}{\partial \phi^2} \tag{4.2}$$

These relations include a determination of the structure of the Higgs self-coupling, λ, as a value depending on the Higgs mass m_H and Higgs vacuum expectation value (VEV) v. After spontaneous symmetry breaking, the leading terms of the Higgs potential look as shown in Equation 4.3.

$$V = \frac{m_H^2}{2} H^2 + \lambda_3 v H^3 + \frac{\lambda_4}{4} H^4, \quad \lambda_3 = \lambda_4 = \lambda_{HHH} = \frac{m_H^2}{2v^2} \tag{4.3}$$

Experimentally measuring λ_{HHH} is a crucial test of the SM electroweak symmetry break-

ing mechanism, in order to compare the experimentally measured value to its SM predictions. Modifications of the Higgs self-coupling coupling (λ_{HHH}) can only be directly accessed via Higgs pair production, making this analysis a good use-case to search for possible BSM effects on the structure of the Higgs self-coupling.

In this analysis, the effective Lagrangian [7; 12] used to describe Higgs pair production is shown in Equation 4.4, with its parameters' mathematical definitions shown in Equation 4.5, and corresponding SM and BSM Feynman diagrams shown in Figure 4.4.

$$\mathcal{L}_{BSM} = -\kappa_\lambda \lambda_{HHH}^{SM} v H^3 - \frac{m_t}{v}(\kappa_t H + \frac{c_2}{v}H^2)(\bar{t}_L t_R + h.c.) + \frac{\alpha_S}{12\pi v}(c_g H - \frac{c_{2g}}{2v}H^2)G_{\mu\nu}^a G^{a,\mu\nu} \quad (4.4)$$

$$\kappa_\lambda = \frac{\lambda_{HHH}}{\lambda_{HHH}^{SM}}, \quad \lambda_{HHH}^{SM} = \frac{m_H^2}{2v^2}, \quad \kappa_t = \frac{y_t}{y_t^{SM}}, \quad y_t^{SM} = \frac{\sqrt{2}m_t^2}{v} \quad (4.5)$$
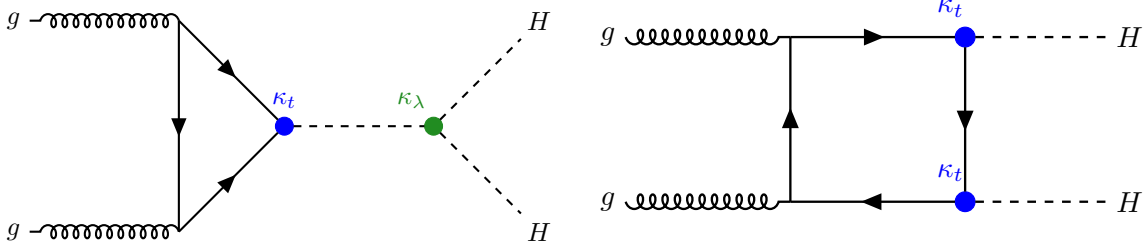
(a) SM-like processes
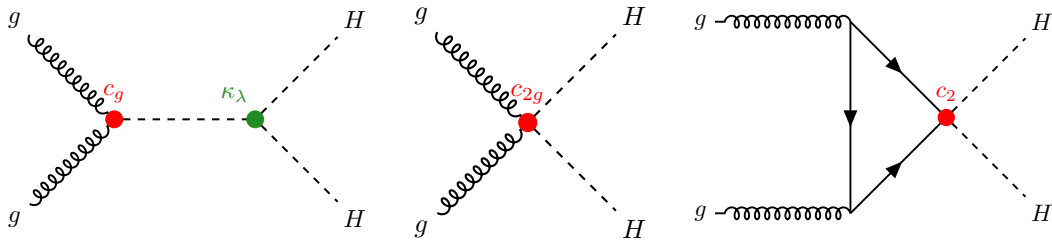
(b) Pure BSM processes

Figure 4.4: Feynman diagrams for leading-order Higgs boson pair production via gluon fusion

Qualitatively, each of these variables are defined as follows:

- $G^a_{\mu\nu} = \partial_\mu G^a_\nu - \partial_\nu G^a_\mu + f^{abc} G^b_\mu G^c_\nu$ is the gluon field strength tensor.

- f^{abc} is the totally anti-symmetric $SU(3)$ structure tensor.

- κ_λ is a measure of the deviation of the Higgs boson self-coupling from its SM expectation λ^{SM}_{HHH}. For example, $\kappa_\lambda = 2$ corresponds to a self-coupling with twice the strength as the SM expectation.

- κ_t is a measure of the deviation of the coupling of a single Higgs boson and two top quarks, called the top Yukawa coupling, from its SM expectation y^{SM}_t. For example, $\kappa_t = 2$ corresponds to a top Yukawa coupling with twice the strength as the SM expectation.

- c_2 is the strength of a purely BSM coupling between two Higgs bosons and two top quarks. In the SM this coupling strength equals zero, as the dimension of this added lagrangian term would be non-renormalizable.

- c_g is the strength of a purely BSM coupling between one Higgs boson and two gluons. In the SM this coupling strength equals zero, corresponding to the fact that gluons are massless in the SM.

- c_{2g} is the strength of a purely BSM coupling between two Higgs bosons and two gluons. In the SM this coupling strength equals zero, corresponding to the fact that gluons are massless in the SM.

In order to simplify the search of HH models across the entire 5-dimensional phase space and avoid the need to generate simulated events for a large number of points in the 5-dimensional EFT space, a reweighting technique is employed, a set of benchmark EFT points is searched for, and scans of multiple EFT parameters are performed. Within this lagrangian formalization, the differential cross section of of gluon-gluon fusion induced Higgs boson pair production, σ_{HH}, can be expressed as a polynomial in terms of the EFT model parameters using generator-level information on the HH system as shown in Equation 4.6.

$$\frac{d^2\sigma}{dm_{HH}d|\cos\theta^*|} = \sum A_i(m_{HH}, |\cos\theta^*|)\, c_i \tag{4.6}$$

where c_i represents the combinations of couplings defined in [13], and $A_i(m_{HH}, |\cos\theta^*|)$ are known coefficient values. Equation 4.6 is used to extract per event weights, which are normalized by equation 4.7, where σ_i (σ_f) is the cross section of the initial (final) benchmark point when reweighting i → f. This allows one to reweight any HH sample at NLO to any other HH sample at NLO precision. In this analysis, this is used to reweight from a set of generated HH samples at NLO to any point in the 5-dimensional EFT phase space [16; 13]. Additionally, when performing DNN trainings in the SL and FH final states, signal samples generated at LO are reweighted to the SM at NLO using this technique in order to provide a larger number of signal events for training.

$$w(m_{HH}, |\cos\theta^*|) = \frac{d\sigma_f(m_{HH}, |\cos\theta^*|)}{d\sigma_i(m_{HH}, |\cos\theta^*|)} \cdot \frac{\sigma_i}{\sigma_f} \tag{4.7}$$

With this technique, twenty benchmark scenarios considered in this analysis, chosen as they are largely representative of different kinematic regions of the 5-dimensional EFT phase space [12; 13; 14], are produced via a reweighting of four generated simulation samples at NLO ($\kappa_\lambda = [0, 1, 2.45, 5]$) and are shown in Table 4.1.

In addition, by considering a linear combination of the four generated simulation samples weighted to their corresponding contribution to arbitrary κ_λ and c_2 signal hypotheses, scans of these two parameters can be performed in order to constrain their values. The κ_λ parameter also affects the Higgs boson branching ratios and the single Higgs production cross sections because of next-to-leading (NLO) electroweak corrections [17; 18], taken into account when scanning over κ_λ values.

Benchmark	κ_λ	κ_t	c_2	c_g	c_{2g}
SM	1.0	1.0	0.0	0.0	0.0
1	7.5	1.0	-1.0	0.0	0.0
2	1.0	1.0	0.5	-0.8	0.6
3	1.0	1.0	-1.5	0.0	-0.8
4	-3.5	1.5	-3.0	0.0	0.0
5	1.0	1.0	0.0	0.8	-1
6	2.4	1.0	0.0	0.2	-0.2
7	5.0	1.0	0.0	0.2	-0.2
8	15.0	1.0	0.0	-1	1
9	1.0	1.0	1.0	-0.6	0.6
10	10.0	1.5	-1.0	0.0	0.0
11	2.4	1.0	0.0	1	-1
12	15.0	1.0	1.0	0.0	0.0
8a	1.0	1.0	0.5	$\frac{0.8}{3}$	0.0
1b	3.94	0.94	$\frac{-1}{3}$	0.75	-1
2b	6.84	0.61	$\frac{1}{3}$	0.0	1.0
3b	2.21	1.05	$\frac{-1}{3}$	0.75	-1.5
4b	2.79	0.61	$\frac{1}{3}$	-0.75	-0.5
5b	3.95	1.17	$\frac{-1}{3}$	0.25	1.5
6b	5.68	0.83	$\frac{1}{3}$	-0.75	-1.0
7b	-0.10	0.94	1.0	0.25	0.5

Table 4.1: Parameter values of the 20 EFT benchmarks and the Standard Model.

4.3 Samples

In order to perform the analysis, datasets collected with the CMS detector from 2016-18 are used, as well as a slew of simulation samples in order to optimize the analysis strategy for the desired HH→WW$\gamma\gamma$ physics signature, and perform statistical inferences by fitting simulation to data in order to extract the analysis' final results.

In this Section, the CMS data samples used will be described in Section 4.3.1, the simulated signal samples will be described in Section 4.3.2, the simulated background samples will be described in Section 4.3.3, and the corresponding simulation hadronization and detector response will be described in Section 4.3.4.

4.3.1 Data

The analyzed data correspond to a total integrated luminosity of 138 fb^{-1} and were collected during Run 2 at the LHC from 2016 to 2018. In order to select events which may come from the HH→WW$\gamma\gamma$ process, events with highly energetic photons are selected in order to tag the H→ $\gamma\gamma$ leg of the HH process.

Events are selected using double-photon triggers with thresholds on the leading (subleading) photon transverse momentum (p_{T}) of $p_T^\gamma > 30$ (18) GeV for the data collected during 2016 and $p_T^\gamma > 30$ (22) GeV for 2017 and 2018. In addition, loose calorimetric identification requirements [19], based on the shape of the electromagnetic shower, the isolation of the photon candidate, and the ratio between the hadronic and electromagnetic energy deposit of the shower, are imposed on the photon candidates at the trigger level.

The HLT paths applied to events from these datasets are:

HLT_Diphoton30_18_R9Id_OR_IsoCaloId_AND_HE_R9Id_Mass90 (2016 data)

HLT_Diphoton30_22_R9Id_OR_IsoCaloId_AND_HE_R9Id_Mass90 (2017 and 2018 data)

HLT_Diphoton30_22_R9Id_OR_IsoCaloId_AND_HE_R9Id_Mass95 (2017 and 2018 data)

Datasets expected to contain events with two photons are used in order to obtain events containing the $H \to \gamma\gamma$ process, and further selections are applied to identify events that also contain the $H \to WW$ process.

4.3.2 Signal simulation

Di-Higgs signal Monte-Carlo (simulation) samples in the gluon-gluon fusion production mode are generated using POWHEG v2 [20; 21; 22; 23] at NLO in QCD including the full top quark mass dependence for four different sets of $(\kappa_\lambda, \kappa_t)$ parameter values: $(1, 1)$, $(2.45, 1)$, $(5, 1)$ and $(0, 1)$, where these parameters are defined in section 4.2. In addition, 12 EFT benchmark samples in a five-dimensional EFT model space are generated at LO [12] using MadGraph, where the EFT coupling parameter values are defined in the rows labelled 1-12 of Tab. 4.1.

A combination of the four NLO signal simulation samples, in which the EFT parameters are varied as $(\kappa_\lambda, \kappa_t) = (1, 1)$, $(2.45, 1)$, $(5, 1)$ and $(0, 1)$, is reweighted using an analytic formula derived in [16; 13]. The analytic formula is shown in Eq.4.6. The signal hypotheses to which this combination of NLO samples is reweighted to are defined as the 20 benchmark scenarios (1-12 [12], 8a [13], 1b-7b [14]), shown in Tab. 4.1.

A possible way to improve this analysis in the future would be to include the VBF production mode of HH in the signal definition, and include a dedicated VBF tagging category in order to improve the overall analysis sensitivity. While this may not have a significant impact on the final result due to its low production cross section, it may be able to improve the sensitivity of the analysis on order of $\approx 5\%$.

4.3.3 Background simulation

The analysis is affected by backgrounds from single Higgs boson production and by non-resonant backgrounds which manifest as a continuum in the $m_{\gamma\gamma}$ spectrum. Monte Carlo event generators were used for the simulation of the background from SM single Higgs boson

production, including gluon gluon fusion (ggH), associated production with a Z or W boson (VH), associated production with a top quark pair (ttH) simulated at NLO in QCD precision using MadGraph5_aMCatNLO [24; 25] with the FxFx merging scheme [26], and vector-boson fusion (VBF H) using POWHEG v2 [20; 21].

The continuum background contribution from SM processes with multiple photons is estimated using data-driven methods described in Sec. 4.6.3. In the SL and FH final states, MVA methods are employed which use background MC for training. The continuum background MC includes γ+jets modeled with the PYTHIA 8 [27] generator, $\gamma\gamma$+jets modeled with the SHERPA v.2.2.1 generator [28], $0, 1, 2\gamma + W$+jets, $t\bar{t}$, and $t\bar{t}W$ modeled using MadGraph5_aMCatNLO [24; 25; 26].

4.3.4   Hadronization and detector response

The PYTHIA 8 [27] package is used for parton showering, hadronization, and the underlying event simulation of all signal and background samples (with the exception of $1, 2\gamma$+jets MC from SHERPA v.2.2.1), with parameters set by the CUETP8M1 tune [29] (2016 data taking period) and the CP5 tune [30] (2017 and 2018 data taking periods). Parton distribution functions (PDFs) are taken from the NNPDF3.0 set [31]. The response of the CMS detector is modeled using the Geant4 package [32]. The simulated events include additional pp interactions within the same or nearby bunch crossings (pileup), generated using Pythia and overlaid on the MC events using event weights so that the distribution of the number of collisions matches the data.

4.4 Objects

When processing the CMS data and simulated physics samples described in Section 4.3, a particle flow (PF) [33] algorithm is used in order to define objects from real or simulated CMS detector information. Objects corresponding to the following particles are utilized in the analysis: Photons, electrons, muons, and "jets" resulting from hadronized quarks or gluons. In addition, a special object called "MET" (Missing transverse momentum) is utilized in order to tag events which may contain particles which evade detection such as neutrinos.

The same object definitions are used for all WW$\gamma\gamma$ final state categories when reconstructing objects from both data and simulation events.

In this section, the choice and reconstruction of the following objects is described: Vertex choice in Section 4.4.1, photons in Section 4.4.2, electron and muons in Section 4.4.3, jets in Section 4.4.4 and MET in Section 4.4.5. Finally, the yields and efficiencies of the signal and background processes in this analysis after the selections described in this section are described in Section 4.4.6.

4.4.1 Vertex

Because there can be many simultaneous interactions in a given CMS event due to the large number of protons in colliding LHC protons bunches, many interactions points may be reconstructed. In order to identify the vertex corresponding to the highest energy interaction of the proton-proton collisions, called the "hard interaction", the vertex which has the highest sum of p_T^2 is chosen as the point from which photons are reconstructed and from which jets are taken. This is chosen as in the WW$\gamma\gamma$ processes, high p_T tracks from the WW decay products are expected, namely from leptons and jets.

In Figure 4.5, the probability of choosing a vertex with a z-position along the colliding axis within $|dZ|$ of the z-position of the generator level vertex is shown for the 2017 SM

at NLO semi-leptonic signal sample. It is shown from the first few points that the selected
reconstructed vertex has an absolute z position within 0.1cm of the z position of the generator
vertex for more than 99% of events. This indicates that the choice of the vertex with the
highest sum of p_T^2 is an appropriate choice for the HH→WW$\gamma\gamma$ process.
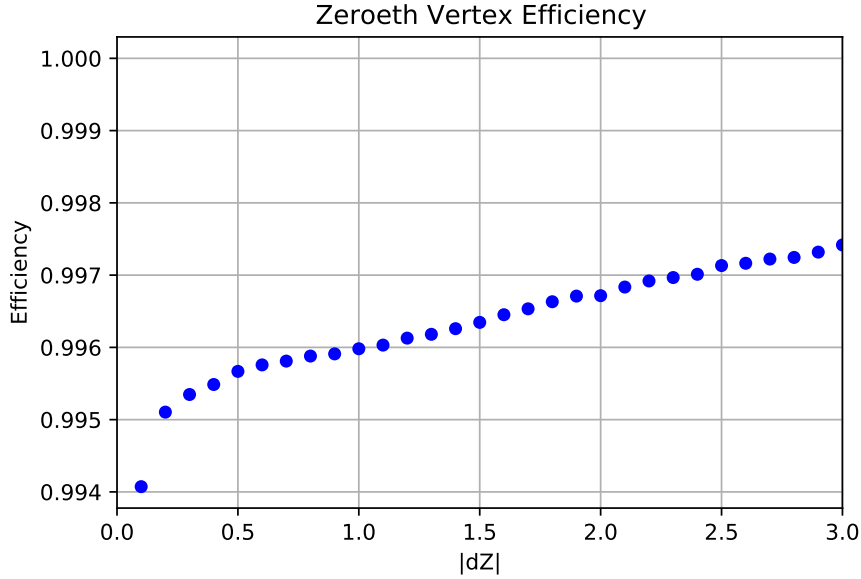
Figure 4.5: Efficiency vs $|dZ|$ for the Semi-Leptonic Signal

4.4.2   Photons

Photons used in this analysis are selected from the PF set of photon candidates. The energy
of each photon candidate is estimated from the Supercluster (SC), which includes deposits
from the many particles comprising the electromagnetic shower. In some cases, photons will
interact with detector material upstream of the ECAL and produce an electron-positron pair;
these are known as "converted" photons. Converted photons will also deposit energy in the
ECAL preshower detector (ES), which is included in the SC energy estimate. A correction is
then made to this SC energy using a multivariate regression technique [19]. After that, data
and MC are brought into agreement by applying additional scale and smearing corrections
to the photon energies. Once the photon energy has been established, a set of preselection

criteria is applied to obtain the final set of photons considered in the analysis. One of these criteria is a requirement placed on the output score of the photon identification BDT, which is trained to reduce the contamination from other objects which mimic real photons.

All data events are required to have fired the high-level trigger (HLT) double photon paths and pass diphoton preselections. Simulated events are only required to pass diphoton preselections, defined to be tighter than the HLT dataset requirements.

The HLT trigger paths used in this analysis are defined in Section 4.3.1, and require the presence of two isolated photons with one photon p_{T} higher than 30 GeV and the other one with a p_{T} of at least 18 GeV for 2016 or 22 GeV for 2017 and 2018 in order to keep the bandwidth of the HLT at sustainable levels. The trigger efficiency of each year is measured using data collected at the LHC by CMS and is applied to simulation samples. Higgs candidates with diphoton decays are then built from pairs of photon candidates.

Photon candidates are subject to a pre-selection that imposes requirements on photon kinematics, hadronic leakage, and shower shape. The pre-selection is designed to be slightly more stringent than the trigger requirements, where the pre-selection cuts are summarized in Table 4.2. The shower shape and isolation variables in simulation are corrected with a chained quantile regression method [34] based on studies of $Z \rightarrow e^{+}e^{-}$ events. Each variable is corrected with a separately trained boosted decision tree (BDT), taking the photon kinematic properties, per-event energy density, and the previously corrected features as inputs to ensure that correlations between the inputs are preserved and closer to those in data. This correction method also improves the modeling of the photon identification (photon ID) discriminant in MC simulation with respect to the previous CMS H $\rightarrow \gamma\gamma$ results [19]. A multivariate identification method, based on photon shower-shape, isoaltion and kinematic variables, is used to separate H $\rightarrow \gamma\gamma$ signal from background photons (photon ID). A very loose requirement on the photon ID score above -0.9 is applied as a further selection, which eliminates a very significant amount of non-prompt photons while keeping almost 100% of prompt photons. Each photon candidate is required to satisfy the "conversion-safe"

electron-veto, which aims to reject photon objects which may have been reconstructed from real electrons.

Additionally, both photons must pass either $R_9 > 0.8$, $Iso_{ch,had} < 20$ GeV, or $Iso_{ch,had}/$ $p_T < 0.3$ if their p_T is above 14 GeV and H/E is below 0.15. R_9 is defined as the energy sum of the 3×3 crystal matrix centered on the most energetic crystal in a given ECAL supercluster, divided by the energy of the supercluster, and H / E represents the ratio of hadronic energy to electromagnetic energy.

Table 4.2: List of photon preselection requirements.

	H/E	$\sigma_{i\eta i\eta}$	R_9	Iso_{ph}	Iso_{track}
EB; R9> 0.85	<0.08	–	>0.5	–	–
EB; R9≤0.85	<0.08	<0.015	>0.5	< 4.0	< 6.0
EE; R9>0.90	<0.08	–	>0.8	–	–
EE; R9≤0.90	<0.08	<0.035	>0.8	< 4.0	< 6.0

Preselection efficiencies and the loose photon ID cut efficiency are determined from data using $Z \to e^+e^-$ events with the tag and probe method. By definition the tag and probe technique using $Z \to e^+e^-$ does not allow for the measurement of the electron-veto efficiency, which instead is measured independently using $Z \to \mu^+\mu^-\gamma$ events. The scale factors, defined as the ratio of efficiency in data to efficiency in simulation, are used to correct the signal efficiency in simulated signal samples and the uncertainties are propagated to the expected signal yields.

Each event is required to have at least one diphoton candidate constructed with respect to the zeroth vertex that passes the preselections described above. The largest-p_T photon (leading) is required to have $p_T > 35$ GeV and the second largest (subleading) is required to have $p_T > 25$ GeV. These photons must also pass a loose selection on a dedicated $H \to \gamma\gamma$ photon ID shown in Table 4.3.

Finally, the events with the invariant mass of two photons within $100 < m_{\gamma\gamma} < 180$ GeV, are selected for the signal extraction.

	Leading Photon	Subleading Photon
Photon ID	-0.9	-0.9

Table 4.3: Additional photon object selections

4.4.3 Leptons

In this analysis, electron and muon objects are considered, and the analysis remains agnostic to tau leptons, as they are neither tagged nor rejected. Because the number of leptons is used as a handle of orthogonality between the three final state categories, it is necessary that all final state categories apply the same lepton selections. A possible way to improve this analysis in the future would be to include the tagging of tau leptons, which may be present in the leptonic WW$\gamma\gamma$ final states.

For electrons and muons, ID MVA outputs are utilized in order to identify leptons with different balances of sensitivity and yields. Additionally, isolation criteria is defined and utilized in order to quantify how isolated leptons are from other objects. The decision of which electron ID, muon ID and muon isolation to select comes from comparing the ratio of signal yields after preselections and subsequent lepton selections for the two final state categories containing leptons: the semi-leptonic and fully-leptonic final states. This figure is checked when applying a loose cut based electron ID with a tight Muon ID and isolation, versus applying a medium MVA based electron ID with a medium Muon ID and isolation. Comparing the ratios between sets of lepton selections allows one to observe which categories lose the most signal due to the corresponding lepton selections. The relative yields are shown in Table 4.4.

In the Fully-Hadronic final state category, events are required to contain exactly zero leptons. This means that the choice of lepton selection can impact the FH yields, as it may change whether an event has zero leptons or not. The ratio of FH signal yield between the two sets of lepton IDs and ISOs is found to be 0.947, where about 5% of signal events are

Category	SL_e	SL_μ	FL_{ee}	$FL_{\mu\mu}$	$FL_{e\mu}$	$FL_{\mu e}$
Loose Electron, Tight Muon	0.16	0.20	0.018	0.053	0.038	0.037
Medium Electron, Medium Muon	0.023	0.228	0.0006	0.062	0.0067	0.005
Ratio	0.14375	1.14	0.0333	1.17	0.176	0.135

Table 4.4: Ratio of signal yields after preselections and $p_\mathrm{T}/m_{\gamma\gamma}$ cuts over the addition of lepton requirements, and the ratio between the two pairs of lepton requirements. In this analysis, the selections in the top row are used (Loose electron, tight muon), while the other two rows are produced in order to determine the ideal combination of lepton selections to use.

lost when using medium MVA based electron ID and medium Muon ID and ISO.

Exactly one lepton is required to pass selections in the SL (Semi-Leptonic) category, therefore for this check the yields for this process are split into the SL_e (Semi-Leptonic electron) and SL_μ (Semi-Leptonic muon) subcategories. For the FL (Fully-Leptonic) category, it is required that exactly two leptons pass the common set of lepton selections, and therefore for the purpose of this check, this process is split into four sub-categories corresponding to the flavours of the leading two leptons.

Applying a medium MVA based electron ID reduced subcategory yields containing electrons by factors of 0.14375, 0.0333, 0.176 and 0.135, while subcategories containing a muon change by factors of 1.14, 1.17, 0.176 and 0.135. While a slight gain is obtained from loosing the muon ID and isolation, most signal events are rejected from tightening electron ID, especially in the di-electron FL subcategory whose ratio of selected events to pre-selected events is reduced by a factor of about 30.

Because a DNN method is applied in the Semi-Leptonic final state, it is desirable to use looser selections in order to keep more events to input for training. In the Fully-Leptonic analysis, as the expected yield is already low, it is desirable to preserve signal while also maintaining enough events in the data sideband regions to perform a data driven background fit. For muon subcategories, as the yields are not affected drastically by tightening the muon ID and isolation from medium to tight, these selections are determined desirable in order to

tag muons with greater purity.

Therefore, all electrons are required to pass a loose cut based ID, and muons are required to pass a Tight ID and posses a relative PF isolation value in a cone of $\Delta R < 0.4$ less than 0.15, as defined in Eq. 4.8. This is required for all three final state categories.

4.4.3.1 Electrons

All PF Electrons considered must pass a group of selections in order to consistitue a high p_T electron that may have come from a leptonically decaying W boson. Each electron is required to pass the selections in Table 4.5. Scale factors corresponding to loose cut based electron ID are applied as a multiplicative factor to the central event weight to account for the discrepancy in data / MC electron ID assignment.

In addition to a loose electron ID, electron candidates are required to have $p_T > 10$ GeV, and a pseudorapidity in the range $(0 < |\eta| < 1.4442)$ or $(1.566 < |\eta| < 2.5)$ in order to remain in the CMS tracker region and avoid the ECAL overlap region. Furthermore, a distance parameter value $(\Delta R = \sqrt{(\Delta\eta)^2 + (\Delta\phi)^2})$ greater than 0.4 is required between each electron candidate and each of the two photon candidates from the event's highest p_T diphoton in order to select isolated electron candidates. A distance parameter value of less than 0.4 is also required between the electron candidate's track and ECAL supercluster position, and a distance parameter value with each jet candidate > 0.4 is required. Finally, the invariant mass of the electron with each photon candidate in the event's highest p_T diphoton candidate must be at least 5 GeV greater or less than the Z boson mass in order to avoid selecting events coming from Z→ee decays.

Variable	Selection
p_T [GeV]	> 10
$|\eta|$	$(0 < |\eta| < 1.4442)$ or $(1.566 < |\eta| < 2.5)$
ID	Loose Cut Based
$\Delta R(e^-, \gamma)$	> 0.4
$\Delta R(e^-, jet)$	> 0.4
$\Delta R(track_{e^-}, SC_{e^-})$	< 0.4
$|m_{e^-\gamma}$ - 91.187| [GeV]	> 5

Table 4.5: Electron object requirements

4.4.3.2 Muons

Selections are applied to all muon objects with the aim of identifying a muon coming from a leptonically decaying W boson. Each muon object is required to pass the selections in Table 4.6. In addition to a tight Muon ID, muon candidates are required to have $p_T > 10$ GeV, a pseudorapidity in the range ($|\eta| < 2.4$) to remain in the CMS tracker region, a distance parameter value with each photon candidate > 0.4, a distance parameter value with each jet candidate > 0.4, and an isolation < 0.15, as defined in Eq. 4.8, in order to select isolated muon candidates, where sumPUPt is the summed transverse momentum of charged particles not from the primary vertex.

Variable	Selection
p_T [GeV]	> 10
$|\eta|$	< 2.4
ID	Tight
$\Delta R(\mu, \gamma)$	> 0.4
$\Delta R(\mu, jet)$	> 0.4
I_μ	< 0.15

Table 4.6: Muon object requirements

Scale factors for each year corresponding to the applied tight muon ID are applied to the event weight for each lepton passing all Muon selections, in order to improve the agreement between data and simulation.

$$I_\mu = \frac{(sumChargedHadronPt + max(0, sumNeutralHadronEt + sumPhotonEt - \frac{sumPUPt}{2}))}{p_T^\mu}$$

(4.8)

4.4.4 Jets

Jets are constructed using the anti-k_T clustering method with a distance parameter of 0.4, classifying them as "AK4 jets". The selections applied on jets are shown in Table 4.7. Jet candidates are required to have $p_T > 25$ GeV, an absolute value of pseudorapidity < 2.4, are required to pass a loose PU Jet ID in order to avoid reconstructing jets from pileup interactions, a distance parameter value > 0.4 between the jet candidate and each photon candidate from the diphoton candidate, and a distance parameter > 0.4 with any electron and muon candidates which pass the previously defined electron and muon selections. Jet corrections applied include jet energy corrections and a jet energy regression.

Variable	Selection
p_T [GeV]	> 25
$|\eta|$	< 2.4
ID	Tight
PU Jet ID	Loose
$\Delta R(j, \gamma_l)$	> 0.4
$\Delta R(j, \gamma_{sl})$	> 0.4
$\Delta R(j, e^-)$	> 0.4
$\Delta R(j, \mu)$	> 0.4

Table 4.7: Jet requirements

In addition, jets from the hadronization of bottom quarks are tagged using a Deep Neural Network (DNN) that takes secondary vertices and PF candidates as inputs [35]. The output of this DNN is referred to as the b-tagging score. In the Semi-Leptonic and Fully-Hadronic categories, the b-tagging score is input as a training variable in Deep Neural Network trainings, and therefore no selection is applied before training. In the Fully-Leptonic category, medium b-tagging working points for the years 2016, 2017 and 2018 are applied to all jets. This decision is based on the event yields of the 2017 HH SM NLO signals, and of the associated production of H$\to \gamma\gamma$ with a pair of top quarks process (ttH), a prominent b-quark background in the WW$\gamma\gamma$ phase space due to b-quarks coming from the t$\to$bW decay.

For each event, an event is considered b-vetoed if it contains at least one jet with a b-tagging score greater than a given threshold. The value of this threshold was scanned from 0 to 1, using the b-tagging score, and the ratio of process yields with and without a b-veto applied are shown for the WW$\gamma\gamma$ signal and the ttH background process in Figure 4.6, and a ratio of the two is shown in Figure 4.7, where the three vertical lines represent the Loose, Medium and Tight working points as defined by the CMS Jet-Met physics object

group (POG).

(a) WW$\gamma\gamma$ Signal

(b) ttH
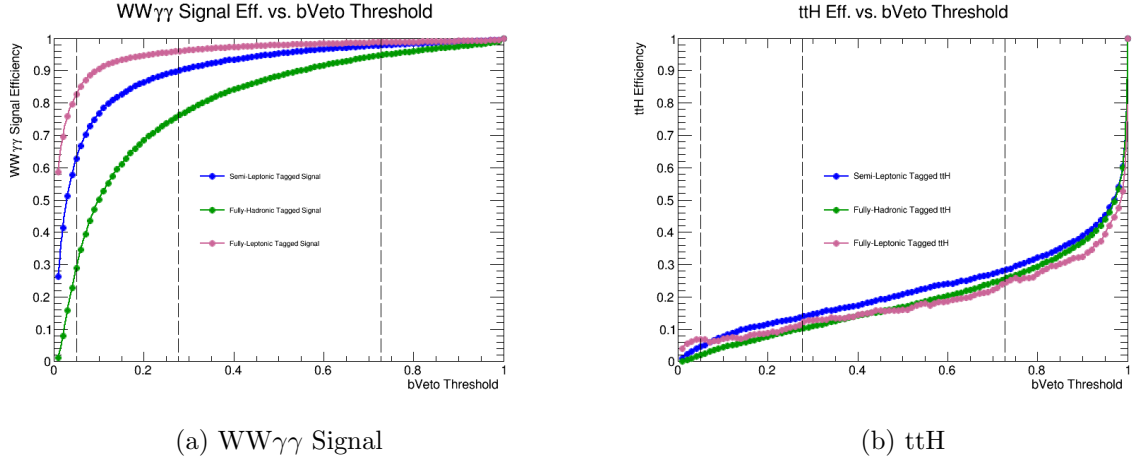
Figure 4.6: 2017 Signal and ttH background signal yields, relative to signal yield with no bVeto, vs. bVeto threshold
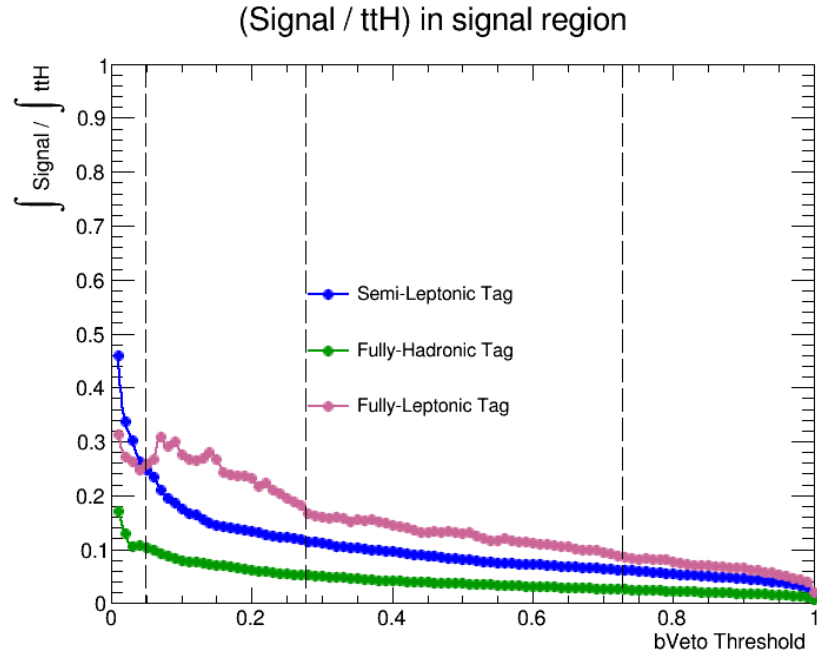
Figure 4.7: Ratio of ttH signal region events over WW$\gamma\gamma$ signal events in signal region vs. bVeto threshold

The signal efficiency curves look as expected for the three final states: The Fully-Leptonic final state is overall the most efficient because there are no quarks in its signal, Semi-Leptonic

89

comes next as it contains two quarks in its signal, and the Fully-Hadronic signal is the least efficient overall as it contains four quarks in its signal, and therefore is the most likely to contain a jet with a higher b score due to high values of important b-tagging variables such as p_T. The ttH signal events as categorized by the three WW$\gamma\gamma$ categories have similar efficiencies among the three categories, with about 75% of events rejected from vetoing an event with at least one tightly b-tagged jet.

For the Semi-Leptonic and Fully-Hadronic final state categories, no b-veto is applied but rather is used as an input variable into DNN trainings. In order to properly reshape the MC b-tagging score distribution, a btag-reshape scale factor is applied to these event weights for each jet passing event selections.

For the Fully-Leptonic final state category, the medium b-tagging score working point is applied as only about 5% of signal is rejected, while about 85% of ttH background is rejected. Events falling into the fully-leptonic category are vetoed if they contain at least one jet with a b-tagging score greater than the medium working point.

The decision to apply a loose PU Jet ID to all jets with p_T below 50 GeV comes from comparing the Fully-Hadronic final state category signal and data yields in the data sideband (defined as $[100 < m_{\gamma\gamma} < 115]$ or $[135 < m_{\gamma\gamma} < 180$ GeV$]$) when applying different PU Jet IDs. This category requires at least four jets, so applying different PU Jet ID requirements on all jets results in different yields, as shown in Figure 4.8, with yields summarized in Table 4.8.

(a) Data Sidebands   (b) Signal Region
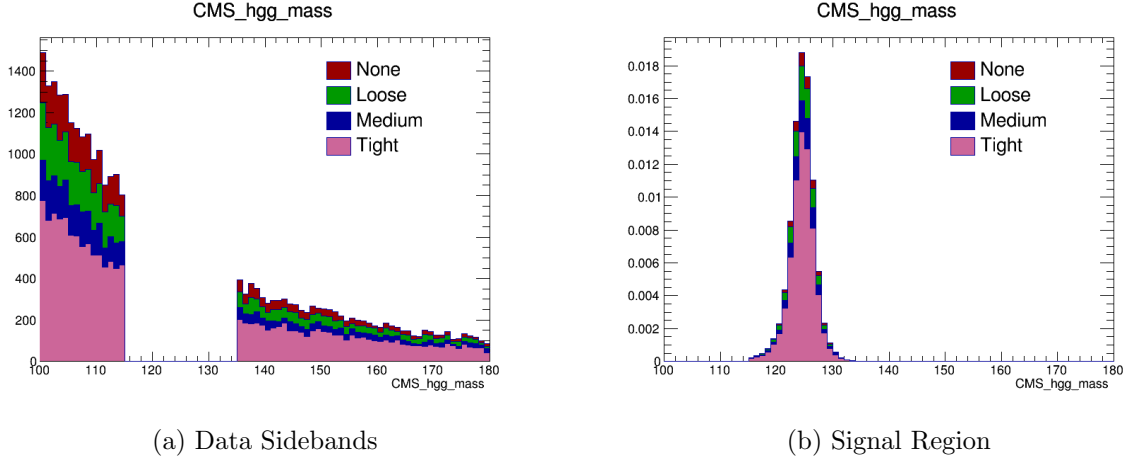
Figure 4.8: 2017 Data (Signal) diphoton mass distributions in the sideband (signal) region for the Fully-Hadronic tagged category.

PUJet ID	Data Sidebands	Signal Region	Data Ratio to None	Signal Ratio to None	$\frac{S}{\sqrt{B}}$
None	25940	0.09015	1	1	1
Loose	22119	0.08625	0.853	0.957	1.036
Medium	17418	0.07644	0.672	0.848	1.035
Tight	14001	0.06707	0.540	0.744	1.012

Table 4.8: Number of data events in data sidebands and 2017 SM NLO Fully-Hadronic events in signal region, and relevant ratios.

If it is assumed that the relative change in dataside band events is roughly proportional to the relative change of data events in the signal region (defined as $115 < m_{\gamma\gamma} < 135$ GeV), an estimated signal region $\frac{S}{\sqrt{B}}$ can be computed and is found to be maximized in the case of applying a Loose PU Jet ID. A similar value is obtained when applying Medium PUJetID, but considering they are within 0.1% of each other at the trade-off of a loss of about 10% of signal, it is optimal to apply a loose PU Jet ID for the Fully-Hadronic final state. As the Semi-Leptonic and Fully-Leptonic final state categories do not explicitly select on jet number, and the loose PU Jet ID has a high efficiency and should therefore not affect the Semi-Leptonic and Fully-Leptonic final states noticeably, all jets are required to pass the Loose PU Jet ID.

4.4.5 MET

The missing transverse momentum vector $\vec{p}_T^{\text{miss}}$ (sometimes referred to as "MET") is defined as the projection onto the plane perpendicular to the beam axis of the negative vector sum of the momenta of all reconstructed PF objects in an event. Its magnitude is referred to as p_T^{miss}. This variable is of importance when identifying events which may contain a neutrino coming from a leptonic W decay, as neutrinos escape the CMS detector undetected.

In the Semi-Leptonic final state, MET is used as an input variable in the DNN training. In the Fully-Hadronic final state, MET is not used. In the Fully-Leptonic final state, a selection of 20 GeV is required for MET. Corrections applied include an XY correction and MET filters, where the MET filters applied to Data and MC for all three years are shown in Table 4.9 in order to remove events which are flagged as bad due to various reasons including large HCAL noise, dead ECAL channels. For Data there is one additional MET filter applied: `Flag_eeBadScFilter`, corresponding to events tagged as having poor ECAL endcap super clusters.

MET Filters
`Flag_goodVertices`
`Flag_globalSuperTightHalo2016Filter`
`Flag_HBHENoiseFilter`
`Flag_HBHENoiseIsoFilter`
`Flag_EcalDeadCellTriggerPrimitiveFilter`
`Flag_BadPFMuonFilter`

Table 4.9: MET filters applied to Data and MC for all three years of data taking and detector conditions.

4.4.6 Preselection yields

In this section, the yields and efficiencies of each 2017 signal and background MC process described in Section 4.3 are shown before and after all object selections and final state preselections are applied in order to understand the major background processes to be targeted in each final state's subsequent selections.

Preselections are defined as the common object and event selections described in the above subsections, in addition to the orthogonality selection applied for each final state: Events in the Semi-leptonic category are required to have exactly one lepton passing the common lepton selections, events in the Fully-hadronic category are required to have at least four jets and exactly zero leptons passing the common jet and lepton selections, and events in the Fully-leptonic category are required to have exactly 2 leptons passing the common lepton selections.

The yields and process efficiencies before and after each final state's pre-selections are shown in Tables 4.10, 4.12 and 4.14 below. Additionally, the individual contribution of each MC sample with respect to the total MC yield for a given set of selections (Before preselection, Semi-leptonic preselections, Fully-hadronic preselections or Fully-Leptonic preselections) are shown in Tables 4.11 and 4.13. Note that processes with an absolute number of simulated events less than 1000 (less than 100 in the fully-leptonic final category) are given a null value or only an efficiency is reported, as their low number of events implies that their corresponding processes would have a poor simulated description and potentially a large statistical uncertainty.

MC Sample	Before preselection	SL (efficiency)	FH (efficiency)	FL (efficiency)
$\gamma\gamma$+jets	302977.6194	542.4641 (0.179%)	6246.9949 (2.062%)	2.7749 (0.001%)
THQ_ctcvcp	3.4592	0.5789 (16.735%)	1.0579 (30.582%)	0.0012 (0.034%)
TTGG_0Jets	44.0507	10.9847 (24.936%)	25.6024 (58.12%)	0.1487 (0.338%)
TTGJets_TuneCP5	765.4892	154.6684 (20.205%)	402.1377 (52.533%)	(<0.2%)
ttWJets	5.0469	($\approx$21%)	2.8337 (56.147%)	(<0.1%)
GJet	830909.3171	1061.0649 (0.002%)	2466.3582 (0.002%)	(<0.001%)
QCD	1653618.4935	(<0.001%)	(<0.001%)	(<0.001%)
TTJets	23.5628	3.3477 (81.397%)	18.8106 (55.121%)	(<2%)
W1Jet	5838.2419	245.2825 (0.329%)	(<0.5%)	(<0.5%)
W2Jets	5589.4864	352.6322 (0.343%)	204.2186 (0.232%)	(<0.5%)
Total	2812863.3417	2371.0234 (0.0008%)	9368.014 (0.0033%)	2.9248 (0.0%)

Table 4.10: 2017 Continuum Background MC before and after preselections for each final state, and process efficiency. Note that for processes with less than 1000 unweighted MC events after a selection (100 for the fully-leptonic preselections), a null value or only efficiency is shown.

MC Sample	Before preselection	SL	FH	FL
$\gamma\gamma$+jets	10.7711%	22.8789%	66.6843%	94.8755%
THQ_ctcvcp	0.0001%	0.0244%	0.0113%	0.0397%
TTGG_0Jets	0.0016%	0.4633%	0.2733%	5.0849%
TTGJets_TuneCP5	0.0272%	6.5233%	4.2927%	-%
ttWJets	0.0002%	-%	0.0302%	-%
GJet	29.5396%	44.7513%	26.3274%	-%
QCD	58.7877%	-%	-%	-%
TTJets	0.0008%	0.1412%	0.2008%	-%
W1Jet	0.2076%	10.345%	-%	-%
W2Jets	0.1987%	14.8726%	2.18%	-%
Total	100%	100%	100%	100%

Table 4.11: Contribution w.r.t total 2017 Continuum Background MC for various phase spaces: Before and after preselections for each final state. Note that for processes with less than 1000 unweighted MC events after a selection (100 for the fully-leptonic preselections), a null value is shown.

MC Sample	Before preselection	SL (efficiency)	FH (efficiency)	FL (efficiency)
GluGluHToGG	2226.7151	2.5556 (0.115%)	18.3933 (0.826%)	- (-%)
ttHJetToGG	23.8639	5.9022 (24.733%)	14.4288 (60.463%)	0.0545 (0.228%)
VBFHToGG	158.1456	0.3712 (0.235%)	1.0675 (0.675%)	- (-%)
VHToGG	85.5536	10.0542 (11.752%)	4.4384 (5.188%)	0.0832 (0.097%)
Total MC	2494.2782	18.8832 (0.0076%)	38.328 (0.0154%)	0.1377 (0.0001%)

Table 4.12: 2017 Single Higgs MC before and after preselections for each final state, and process efficiency. Note that for processes with less than 100 unweighted MC events after a selection, a null value is shown.

MC Sample	Before preselection	SL	FH	FL
GluGluHToGG	89.3%	13.5%	48%	-%
ttHJetToGG	0.96%	31.3%	37.6%	39.6%
VBFHToGG	6.34%	2.0%	2.8%	-%
VHToGG	3.43%	53%	11.6%	60.4%
Total	100%	100%	100%	100%

Table 4.13: Contribution w.r.t total 2017 Single Higgs MC for various phase spaces: Before and after preselections for each final state. Note that for processes with less than 1000 unweighted MC events after a selection (100 for the fully-leptonic preselections), a null value is shown.

MC Sample	Before preselection	SL (efficiency)	FH (efficiency)	FL (efficiency)
Semi-leptonic HH$\to WW\gamma\gamma$	0.3042	0.1044 (34.306%)	- (-%)	- (-%)
Fully-hadronic HH$\to WW\gamma\gamma$	0.3012	- (-%)	0.0966 (32.07%)	- (-%)
Fully-leptonic HH$\to WW\gamma\gamma$	0.0741	- (-%)	- (-%)	0.0098 (13.214%)

Table 4.14: 2017 HH MC before and after preselections for each final state, and process efficiency. Note that for processes with less than 100 unweighted MC events after a selection, a null value is shown.

The tables show that among the continuum background MC processes, the fully-leptonic final state has a very low absolute number of simulation events after pre-selections and requiring exactly two leptons passing the common lepton selections. This was a core reason for the decision to perform a cut-based analysis for this final state, as there are not nearly enough MC events in order to perform a reasonable MVA based analysis. In the fully-hadronic final state, where a large QCD multi-jet background is expected, there is a low absolute number of simulation events from QCD MC, prompting the use of a data-driven estimate of QCD. For all three final states, the non-resonant diphoton + jets process acts as a major background.

The single higgs resonant background tables indicate that, as expected, different single higgs processes have larger background contaminations among the different WW$\gamma\gamma$ final states due to their different process topologies. However, for all final states the ttH process has a relatively high efficiency due to the presence of two top quarks which decay into bbWW in the majority of cases.

Finally, it is seen in the HH selection table that the semi-leptonic and fully-hadronic signal processes have similar signal efficiencies and yields after pre-selections. This may be due to their relatively high branching ratios compared to the FL final state.

4.5   Selections and Categorization

After implementing the object reconstruction defined in Section 4.4, each final state performs additional selection and categorization techniques specific to its final state topology.

For all three final states, the distribution of signal events has a peak in the diphoton invariant mass, $m_{\gamma\gamma}$, distribution around the mass of the Higgs boson (125 GeV). The analysis strategy is therefore based on defining regions of phase space sensitive to the diphoton mass peak around 125 GeV containing as many HH events as possible, while minimizing the yields of the continuum background and resonant single Higgs backgrounds. However, because each WW$\gamma\gamma$ final state has its own signal topology, dominant background processes and absolute number of simulation events, each final state employs a separate strategy for further selections and categorization techniques after the pre-selections defined in Section 4.4.

This section is organized as follows: In Section 4.5.1, the semi-leptonic final state selections and categorization, including the use of multiple DNNs, will be described. In Section 4.5.2, the fully-hadronic final state selections and categorization, which also make use of DNN methods will be described. Finally, in Section 4.5.3 the fully-leptonic final state selections will be described.

4.5.1   Semi-Leptonic

Events fall into the Semi-Leptonic analysis category if they contain at least one pre-selected diphoton as described in Section 4.4.2, and contain exactly one lepton passing the common lepton selections described in Section 4.4.3. The Semi-Leptonic channel is expected to be the most sensitive of the three WW$\gamma\gamma$ channels due to the combination of a relatively large $W \rightarrow qq$ branching ratio of $\approx 67\%$, and the presence of a clean, highly energetic lepton from the $W \rightarrow \ell\nu$ decay leg.

The four NLO generated Semi-Leptonic signal events corresponding to the points $\kappa_\lambda = [0, 1 \text{ (SM)}, 2.45, 5]$, and a set of samples coming from a reweighting of these four samples to

the points $3D3$ ($\kappa_\lambda = 0$, $\kappa_t = 1.0$, $c_{ttHH} = 1.0$), $c_{ttHH} = 3$, and $c_{ttHH} = 0.35$ are categorized with a multi-class DNN, where c_{ttHH} represents the coupling strength of two top quarks to two Higgs bosons. These corresponding simulation templates are used to model the Semi-Leptonic HH final state for the SM hypothesis, and to perform scans of the κ_λ and c_2 EFT parameters.

The four generated NLO samples are reweighted to the 20 EFT benchmarks, and categorized using a parametric DNN which includes the EFT benchmark scenario number as a training variable. The resulting categorized simulation templates are used to model the semi-leptonic HH final state for these 20 scenarios.

4.5.1.1   Standard Model: Multiclass Deep Neural Network

For a general description of Deep Neural Networks, see Appendix A.

In the Semi-Leptonic category, in order to separate the di-Higgs signal from the expected single Higgs boson and continuum backgrounds, a multiclass deep neural network is trained to identify these three types of processes separately, in order to identify regions of phase space with a maximal number of HH events, but a minimal number of single H and continuum background events. Because the single higgs and continuum background processes are markedly different due to the expectation of a resonant H signal vs. a falling continuum background, as shown in Figure 4.2, it is more logical to define these two processes separately in a DNN training rather than defining them as the same type of background.

The samples used for training and labeled as signal are the 12 LO benchmark samples, as well as the LO SM benchmark, where all thirteen simulation samples include 2017 detector conditions for reconstruction. When training on these samples, the reweighting procedure described in Section 4.2 is applied to reweight these LO EFT benchmark and SM sample to the SM process at NLO, in order to train the network to identify the SM at NLO HH signal. In deriving these weights, NLO samples are reweighted following [13], and LO samples are reweighted following an analytic parameterization as a function of σ_{HH} and $|\cos\theta^*|$ which

extends beyond $m_{HH} = 1050$ GeV, and the ratio of the two is taken and normalized by Equation 4.7, yielding an event by event weight. These event weights scale the per-event training loss in order to assign more training importance to events which must be weighted up in order to match SM NLO.

The ratio of a few of the DNN's input variable distributions between the sum of reweighted 13 LO benchmarks (12 + SM at LO), and the 2017 SM at NLO signal are shown in Figures 4.9 and 4.10, and the rest are shown in Appendix B.

(a) Scaled Leading Photon p_{T} (b) Scaled subleading photon p_{T}
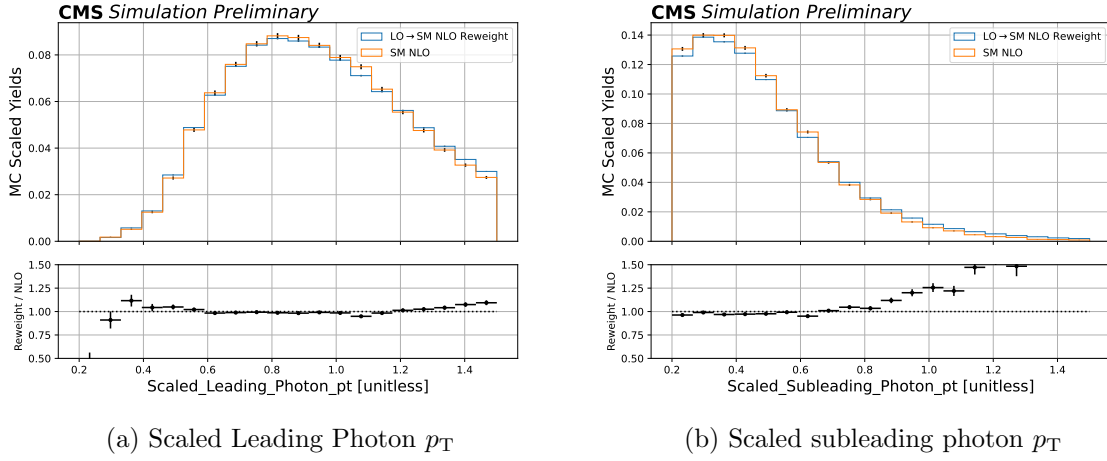
Figure 4.9: Scaled leading and subleading photon p_{T}.

(a) Lepton p_T (b) MET
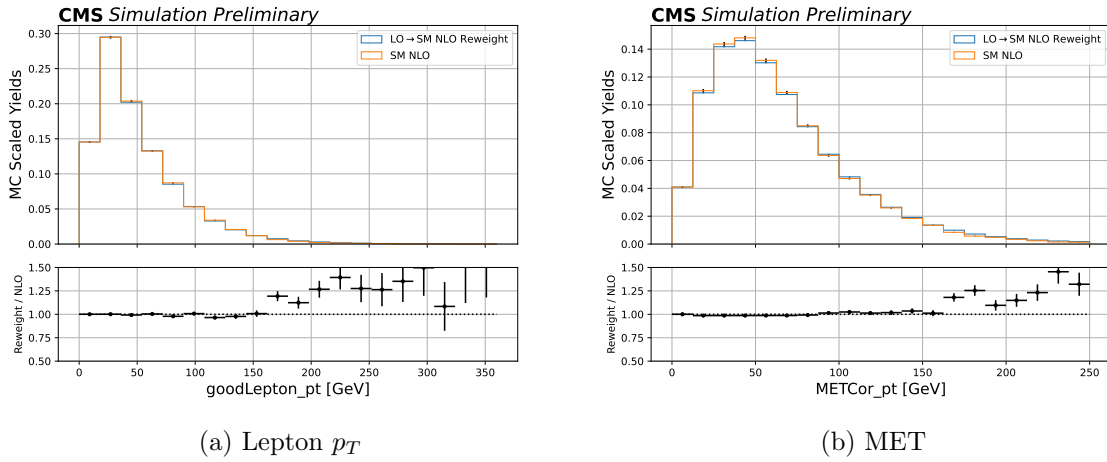
Figure 4.10: Lepton p_{T} and MET

There is good agreement overall, indicating that training on these events and including the LO to NLO event reweighting in the training via loss scaling trains a network geared towards identifying the SM and NLO signal.

The samples used for training and labeled as single Higgs processes are the associated production of a Higgs boson with a vector boson (VH), and with a top quark pair (ttH), where the Higgs decays to $\gamma\gamma$ in both cases.

The samples used for training and labeled as continuum background were chosen based on the background MC processes which have at least 1000 absolute events after the semi-leptonic pre-selections, such that there is no large statistical uncertainty on these process descriptions.

Events used to train the network are required to contain at least one diphoton candidate passing the common diphoton selections described in Section 4.4.2, and contain exactly one lepton passing the common lepton selections in Section 4.4.3.

Due to the class imbalance in the datasets, events are re-weighted with a per-class "class weight", such that after applying this weight, the effective number of events in both classes is the same. In deriving each class weight, a class's weighted MC yield is scaled to the unweighted HH yield of 866,833. This ensures that the network focuses on categorizing all three classes with equal importance. The unweighted and weighted yields, and class weights of all training events which have only diphoton pre-selections applied and the requirement of exactly one lepton passing the common lepton selections, are shown in Table 4.15. Note that in Table 4.15, HH events are not normalized to cross section and branching ratio, as this is not necessary because all weighted yields are reweighted to a common target, and therefore what is relevant are the relative yields.

Class	Unweighted Yield	Weighted Yield	Class Weight	Class Weight * Weighted Yield
HH	866833	2.232871	388214	866833
H	78108	1.057757	819501	866833
Continuum Background	61408	16104	53.8278	866833

Table 4.15: Unweighted and weighted yields, and class weights applied during Semi-Leptonic DNN training, without data sideband scale. Weighted class yields are reweighted by class weights to the unweighted HH yield.

The features used as input to the semi-leptonic channel DNN can be found in Table 4.16.

Table 4.16: Input features used to train semi-leptonic channel DNN.

Feature	Description
Leading Photon p_T / $m_{\gamma\gamma}$	Transverse momentum of the photon with the highest transverse momentum out of the selected photons, scaled to diphoton mass.
Leading Photon η	Pseudorapidity of the photon with the highest transverse momentum out of the selected photons
Leading Photon ϕ	Direction in the transverse plane of the photon with the highest transverse momentum out of the selected photons
Leading Photon E / $m_{\gamma\gamma}$	Energy of the photon with the highest transverse momentum out of the selected photons, scaled to diphoton mass.
Leading Photon MVA	Photon MVA score of the photon with the highest transverse momentum out of the selected photons
Subleading Photon p_T / $m_{\gamma\gamma}$	Transverse momentum of the photon with the second highest transverse momentum out of the selected photons, scaled to diphoton mass.
Subleading Photon η	Pseudorapidity of the photon with the second highest transverse momentum out of the selected photons
Subleading Photon ϕ	Direction in the transverse plane of the photon with the second highest transverse momentum out of the selected photons
Subleading Photon E / $m_{\gamma\gamma}$	Energy of the photon with the second highest transverse momentum out of the selected photons, scaled to diphoton mass.
Subleading Photon MVA	Photon MVA score of the photon with the second highest transverse momentum out of the selected photons
Jet Multiplicity	Number of selected jets in the event (flavour inclusive)
Leading Jet p_T	Transverse momentum of the jet with the highest transverse momentum out of the selected jets
Leading Jet η	Pseudorapidity of the jet with the highest transverse momentum out of the selected jets
Leading Jet ϕ	Direction in the transverse plane of the jet with the highest transverse momentum out of the selected jets
Leading Jet E	Energy of the jet with the highest transverse momentum out of the selected jets
Leading Jet DeepJet Score	DeepJet b-tag discriminator score of the jet with the highest transverse momentum out of the selected jets
Subleading Jet p_T	Transverse momentum of the jet with the second highest transverse momentum out of the selected jets
Subleading Jet η	Pseudorapidity of the jet with the second highest transverse momentum out of the selected jets
Subleading Jet ϕ	Direction in the transverse plane of the jet with the second highest transverse momentum out of the selected jets
Subleading Jet E	Energy of the jet with the second highest transverse momentum out of the selected jets
Subleading Jet DeepJet Score	DeepJet b-tag discriminator score of the jet with the second highest transverse momentum out of the selected jets
Lepton p_T	Transverse momentum of the selected lepton
Lepton η	Pseudorapidity of the selected lepton
Lepton ϕ	Direction in the transverse plane of the selected lepton
Lepton E	Energy of the selected lepton
MET	The missing transverse energy
M_T(l, MET)	The transverse mass of the selected lepton and MET
$m_{j_0 j_1}$	The invariant mass of the leading and subleading jets

To determine the level of optimization of the network towards CMS data by training on MC, the data-MC ratio is checked for input features in the data sideband region after the

semi-leptonic preselections are applied. Disagreements are seen between data and MC in the data sideband ($100 < m_{\gamma\gamma} < 115$ or $135 < m_{\gamma\gamma} < 180$ GeV), as shown for various input features shown in Figures 4.11a, 4.12a, 4.13a, 4.14a, 4.15a, and 4.16a. In order to improve data/MC agreement so that the input features of the DNN are closer to a representation of the data in order to train a DNN more optimally, a 6-dimensional kinematic reweighting is performed.

A per-event weight, called a kinematic weight, is computed as the ratio between data and background MC from the $m_{\gamma\gamma}$ sideband region (Note that data events in the signal region, $115 < m_{\gamma\gamma} < 135$ GeV, are not used at all when deriving the kinematic weights). The variables Leading Jet p_{T}, Subleading Jet p_{T}, Lepton p_{T}, Leading Photon p_{T} over $m_{\gamma\gamma}$, Subleading Photon p_{T} over $m_{\gamma\gamma}$, and MET are used to calculate this per-event weight, as they correspond to quantities related to the semi-leptonic WW$\gamma\gamma$ final state particles. During the derivation of the weights, 5 bins are used for each variable. The range of each bin is selected in an automatic way such that there are the same number of data events in each bin. When the number of data events in a bin is lower than 20, the kinematic weight is set to 1. Otherwise, the weight is set equal to the ratio (data entries)/(MC entries). After the kinematic weights are derived, a fiducial selection is made removing all events which have $|w_{MC} * w_k| > 10$, where w_{MC} is the nominal MC weight computed from cross section, luminosity, PU weight, scale factors and GEN weights, and w_k represents the per event kinematic weight. This fiducial selection removes events with very large weights which heavily impact the DNN training in a non-desirable way.

The data/MC after applying the per-event kinematic weights, in the data sideband ($100 < m_{\gamma\gamma} < 115$ or $135 < m_{\gamma\gamma} < 180$ GeV) and before any evaluation of the DNN, are shown in Figures 4.11b, 4.12b, 4.13b, 4.14b, 4.15b, 4.16b. It can be seen that the application of the kinematic weights improves the data/MC agreement, especially in very high yield bins. It can also be seen that after applying the kinematic reweighting there is no introduction of extremely large statistical uncertainties or fluctuations, indicating that there is a sufficient

amount of data and MC events in deriving the kinematic weights.
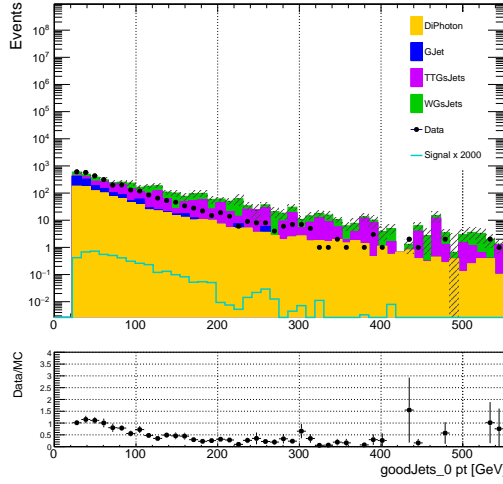
(a) Before kinematic reweighting applied
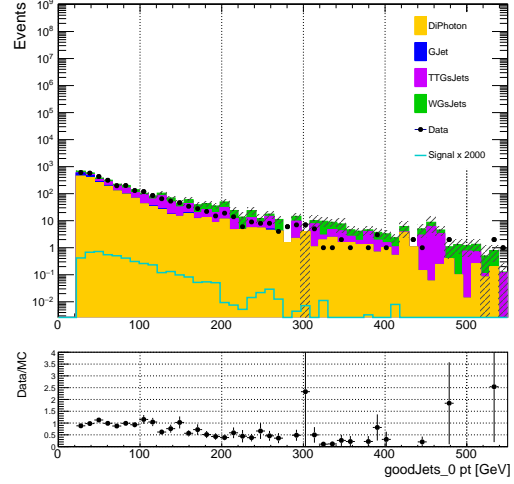
(b) After kinematic reweighting applied

Figure 4.11: Leading jet p_T before and after kinematic reweighting (before any DNN evaluation), in the data sideband ($100 < m_{\gamma\gamma} < 115$ or $135 < m_{\gamma\gamma} < 180$ GeV)
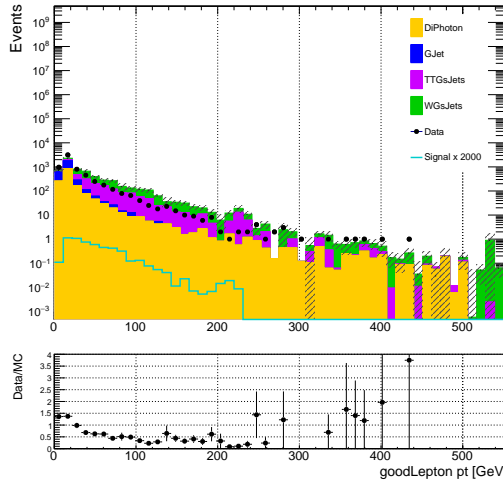
(a) Before kinematic reweighting applied
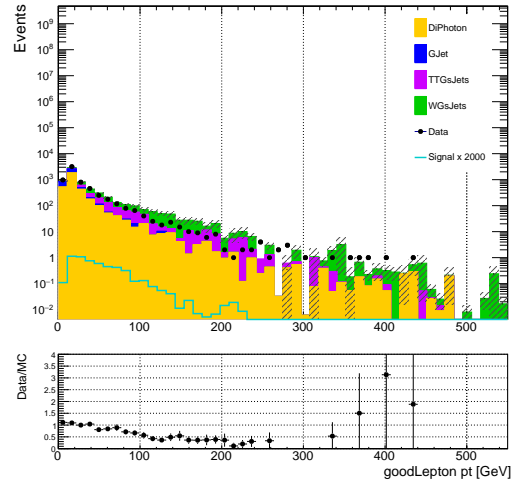
(b) After kinematic reweighting applied

Figure 4.12: Lepton p_T before and after kinematic reweighting (before any DNN evaluation), in the data sideband ($100 < m_{\gamma\gamma} < 115$ or $135 < m_{\gamma\gamma} < 180$ GeV)
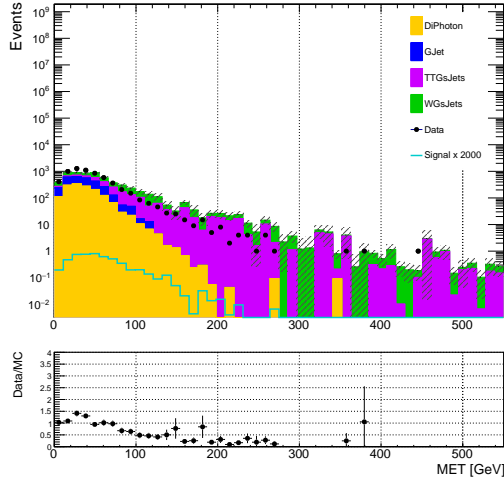
(a) Before kinematic reweighting applied
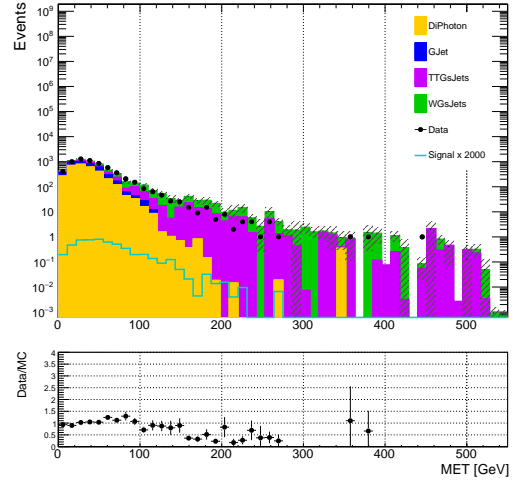
(b) After kinematic reweighting applied

Figure 4.13: MET before and after kinematic reweighting (before any DNN evaluation), in the data sideband ($100 < m_{\gamma\gamma} < 115$ or $135 < m_{\gamma\gamma} < 180$ GeV)
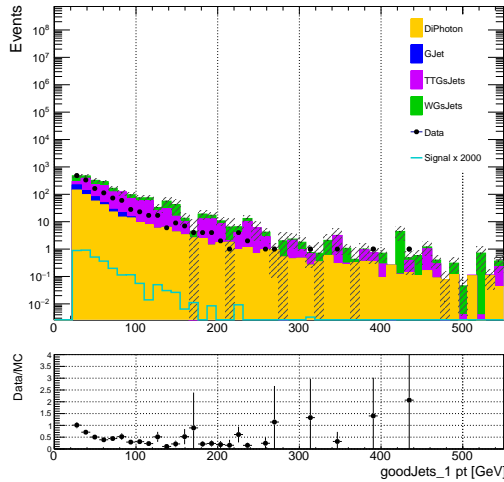
(a) Before kinematic reweighting applied
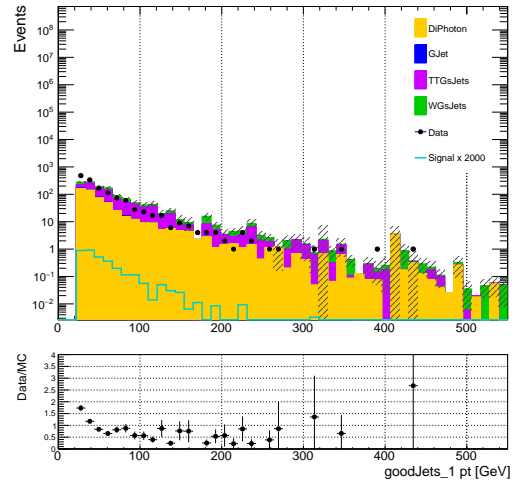
(b) After kinematic reweighting applied

Figure 4.14: Subleading jet p_{T} before and after kinematic reweighting (before any DNN evaluation), in the data sideband ($100 < m_{\gamma\gamma} < 115$ or $135 < m_{\gamma\gamma} < 180$ GeV)
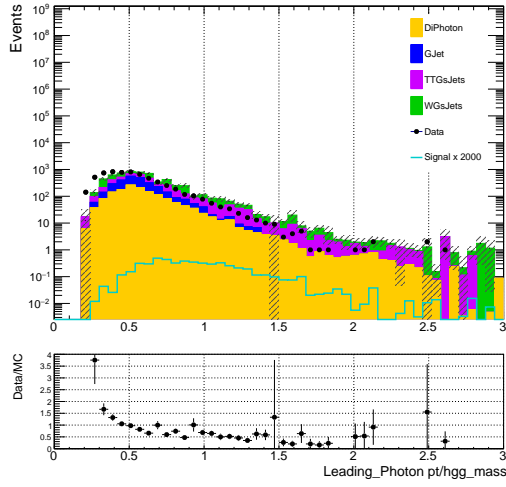
(a) Before kinematic reweighting applied
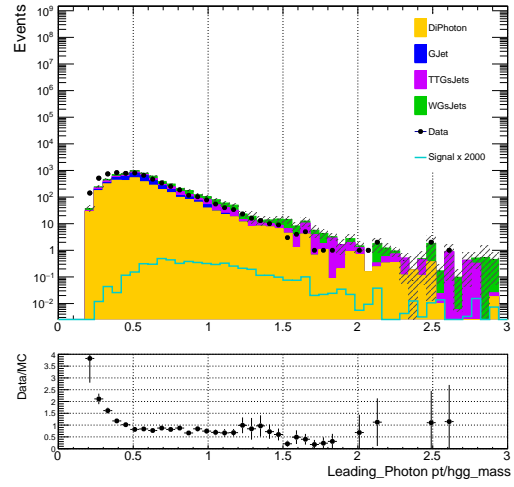
(b) After kinematic reweighting applied

Figure 4.15: Leading photon p_T over $m_{\gamma\gamma}$ before and after kinematic reweighting (before any DNN evaluation), in the data sideband ($100 < m_{\gamma\gamma} < 115$ or $135 < m_{\gamma\gamma} < 180$ GeV)
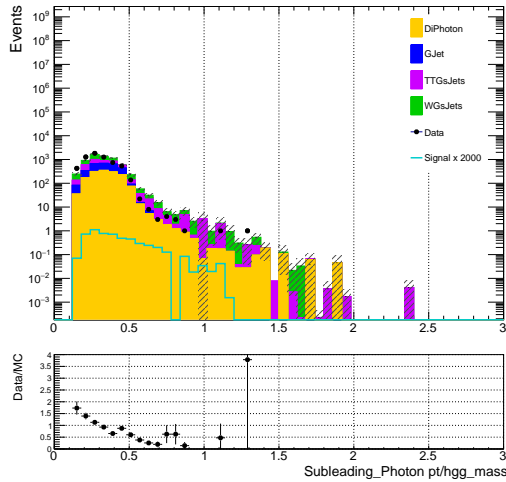
(a) Before kinematic reweighting applied
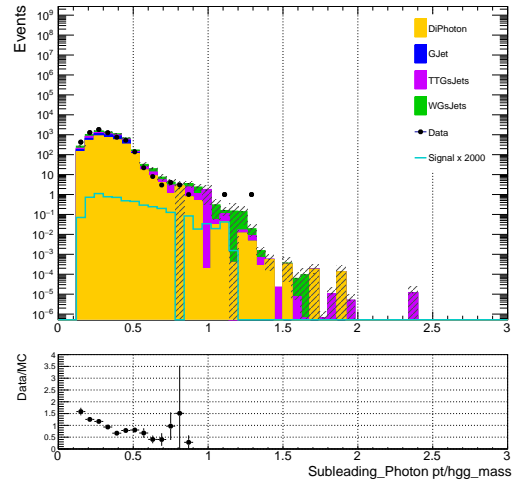
(b) After kinematic reweighting applied

Figure 4.16: Subleading photon p_T over $m_{\gamma\gamma}$ before and after kinematic reweighting (before any DNN evaluation), in the data sideband ($100 < m_{\gamma\gamma} < 115$ or $135 < m_{\gamma\gamma} < 180$ GeV)

The MultiClass DNN outputs three DNN scores, each with a range 0-1 and corresponding to the likelihood that an event falls into each of the three classes, which sum to one. This means that if an event has a high HH class DNN score, the sum of the H and continuum background DNN scores must be small. Because of this constraint, only the output HH class DNN score is used in the analysis for categorization as it has a known correlation to the output H and continuum background DNN scores.

The DNN training results in the ROC (Receiver operating curve) shown in Figure 4.18, and normalized DNN scores for the three classes shown in Figure 4.19.

A possible way to improve this analysis in the future would be to make use of the H and continuum background DNN scores, for instance in order to define control regions with high H and continuum background but low HH yields. These could potentially be included in the simultaneous fit to data in order to decrease the statistical uncertainty, and improve the modelling of the single Higgs templates in the signal region.

Due to the non-linearity of deep neural network models, understanding the relative importance of the input features is non-trivial. In this analysis, we evaluate the relative importance by evaluating Shapley values [36] for each feature. The Shapley value is the average of the marginal contribution of a feature's value to the prediction, across all possible coalitions of features. Specifically, it is calculated by taking the difference in the value of the prediction with and without a given feature (the marginal contribution). This is repeated for all possible combinations of the other input features and the average value of the marginal contributions is taken as the Shapely value. It is important to note that the Shapley value is the average contribution of a feature value to the prediction in the different coalitions of features and not the difference in prediction with and without the feature in the model. It is also worth noting that coalitions of features can be formed without the complete list of input features. When this happens, in order to evaluate the network the missing feature(s) value is randomised in order to obtain a prediction. The relative importance of the input features can be found in Figure 4.17, for the HH class DNN score. The variables are ranked

from highest to lowest in order of their discriminatory power per class. The leading importance variables all correspond to quantities from the final state topology of the semi-leptonic $WW\gamma\gamma$ process, namely two photons, one lepton, two jets and a neutrino.

(a) All Shapley scores

(b) Average Shapley score magnitudes
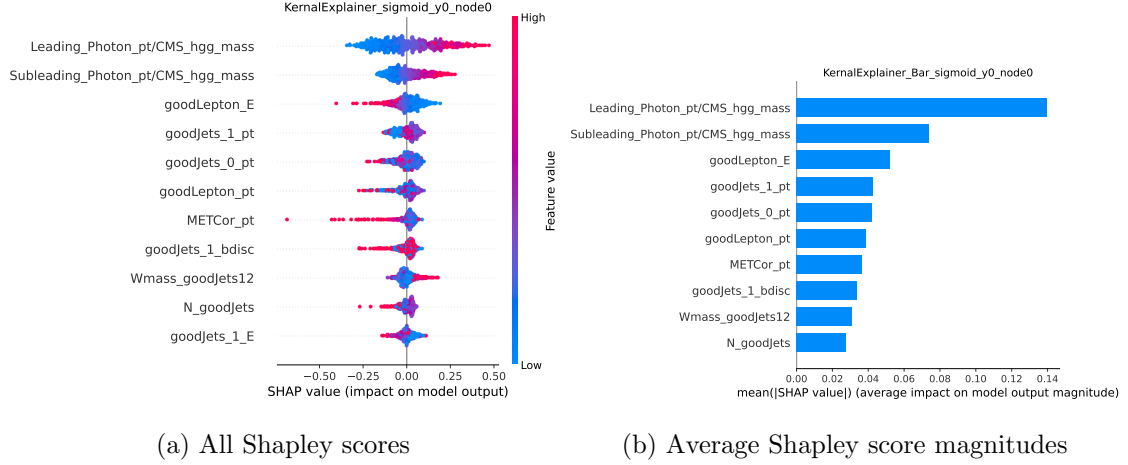
Figure 4.17: Semi-leptonic channel DNN input feature ranking according to Shapely values in the HH class
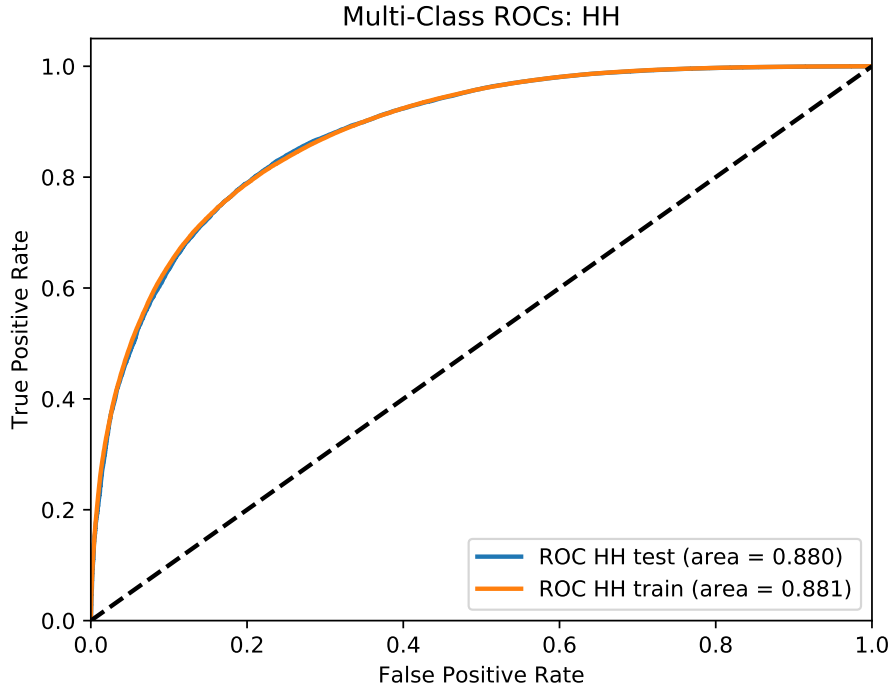
Figure 4.18: Semi-Leptonic DNN ROC curve for training and test data: HH Class
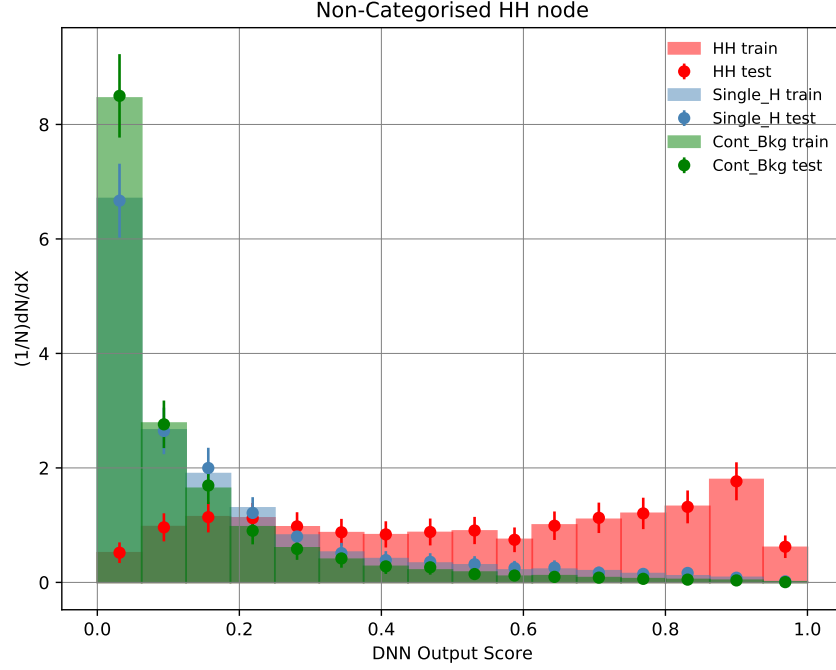
Figure 4.19: Normalized HH DNN score distributions for the three semileptonic DNN nodes, shown for training and test events.

Events with a DNN score less than 0.1 are removed and not used for categorization, nor in any background or signal modelling, as this region is largely background dominant.

In order to qualitatively understand the level of optimization of the DNN in identifying data events with MC, the data / MC ratio comparison of events with a DNN score greater than 0.1 are shown for the leading importance input variables in Figures 4.20 and 4.21. It should be noted that any disagreement between data and MC will lead to a sub-optimal network, but will not introduce any bias in the final result extraction, as MC is only used for selection and categorization optimization.

Table 4.17 shows the post-selection yields, including a selection on the output DNN score of > 0.1, for all of the simulated samples used in this analysis, both the absolute number and the corresponding yield accounting for proper MC scaling.

The correlation plot of all input features can also be found in Figure 4.22 and is used

to check if any correlations are present between input training variables. In particular it can be seen there is less than 2% correlation between all input variables and reconstructed diphoton mass, "CMS_hgg_mass", indicating that a bias in diphoton mass distributions is not expected. Note that the diphoton mass variable is only included in the correlation matrix in order to ensure the DNN does not train on any input features correlated to the signal region, as the diphoton mass is not included in the training.

An additional check is performed to ensure the resulting DNN does not shape the diphoton mass, outlined in Appendix C. No evident shaping is seen, and therefore no bias is expected from the DNN. In addition, a check is performed in a dedicated control region to demonstrate that a large difference in data and MC acceptance is not expected to be introduced by the DNN, and that the DNN behaves as expected on its target signal topology. This check is shown in Appendix D.

(a) Scaled Leading Photon p_T (b) Scaled Subleading Photon p_T
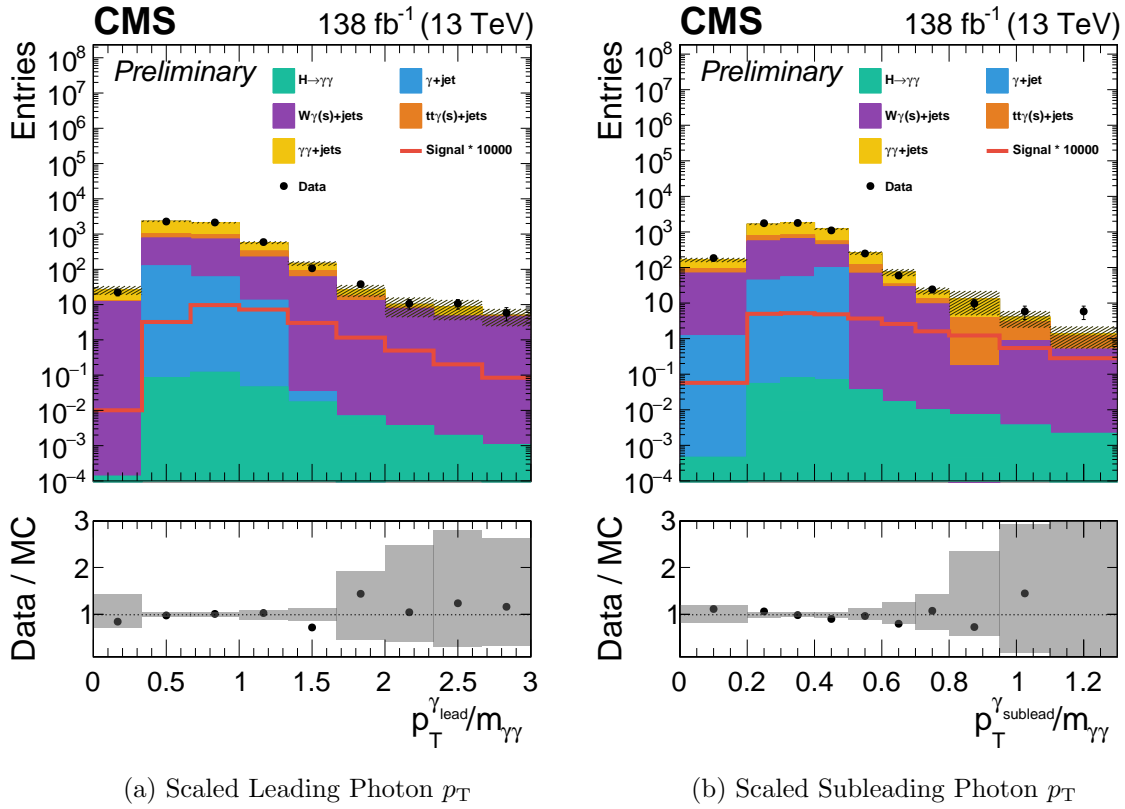
Figure 4.20: Data/MC ratio of semi-leptonic channel input features in full mass region

(a) Lepton energy

(b) Leading jet p_{T}
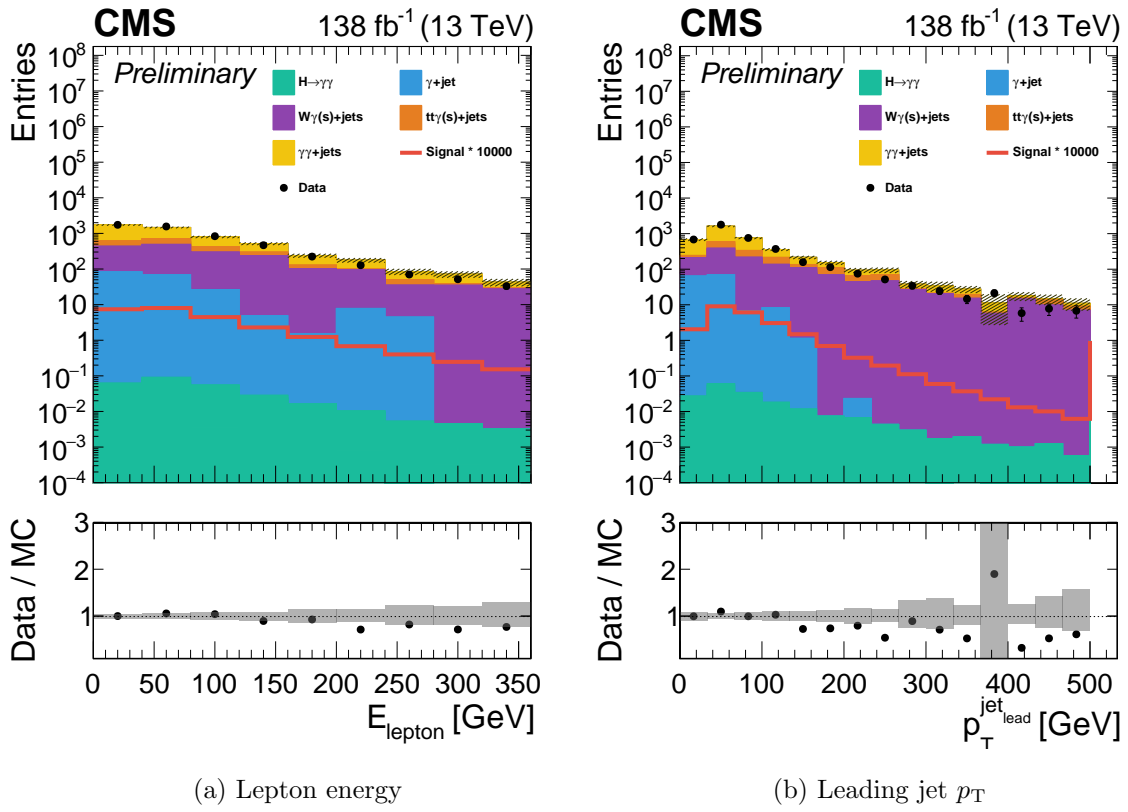
Figure 4.21: Data/MC ratio of semi-leptonic channel input features in full mass region

MC Sample	Unweighted	Weighted
DiPhoJetsBox_MGG-80toInf	5108	581.97343
GJet_40toInf	110	48.26491
tt$\gamma\gamma$+0Jets	4633	17.01703
ttγ+Jets	1564	52.52178
tt+Jets	288	51.77128
W1Jets_pT_150-250	1298	64.88303
W1Jets_pT_250-400	341	7.42416
W1Jets_pT_400-inf	217	1.80622
W1Jets_pT_50-150	23	13.60197
W2Jets_pT_150-250	1612	60.29933
W2Jets_pT_250-400	777	12.25016
W2Jets_pT_400-inf	531	3.05085
W2Jets_pT_50-150	59	27.52279
WGGJets	360	132.12192
WGJJToLNu_EWK_QCD	140	30.91906
ttWJets	74	0.5721

Table 4.17: Unweighted and weighted training MC yields in the $m_{\gamma\gamma}$ sideband region, including semi-leptonic training pre-selections and only events with a DNN output score > 0.1.

The output DNN score comparison between the data and MC is shown in Figure 4.23. In this comparison, events with a DNN score less than 0.1 are removed as they are not used in categorization or signal modeling.

Finally, the output DNN score for data events in the sidebands and signal events in the signal region are shown in Figure 4.24, not including events with a DNN score less than 0.1 as they are not used in the analysis. Each signal histogram is normalized to an integral of 1,

Figure 4.22: Pairwise Spearman's correlation (monotonic relationships) between semileptonic channel DNN input features.

Input Feature Correlations
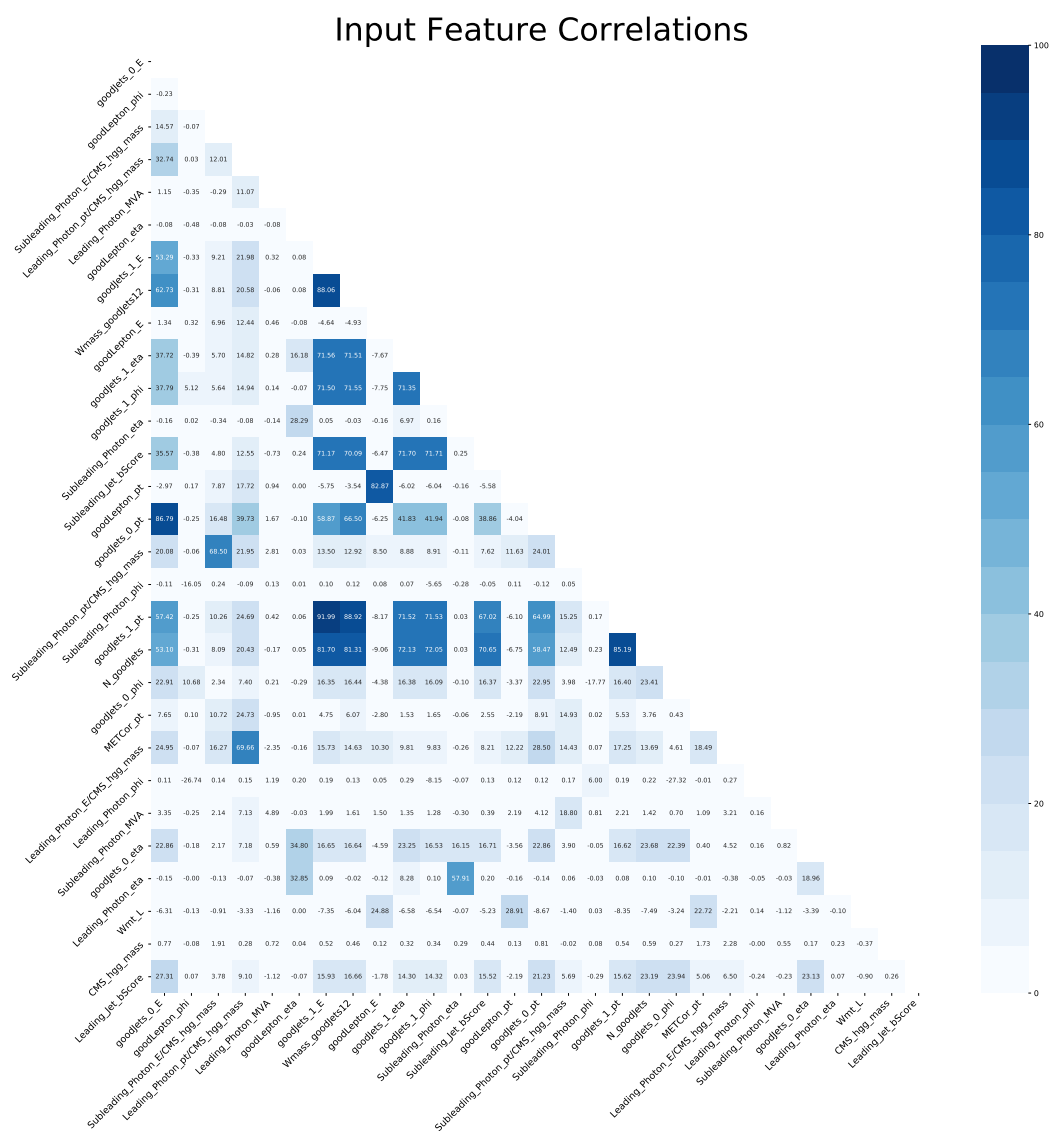
and each data histogram is normalized to the luminosity of the 2018 dataset. It can be seen that the shapes are very similar per year, and that there is no clear systematic difference when applying the 2017-only trained DNN on 2016 and 2018 data and signal events. The data histograms are shown in log scale in order to highlight that there are similar DNN score shapes per year which appear similar within statistical uncertainty, in particular in the high DNN score region which is the most signal sensitive region.
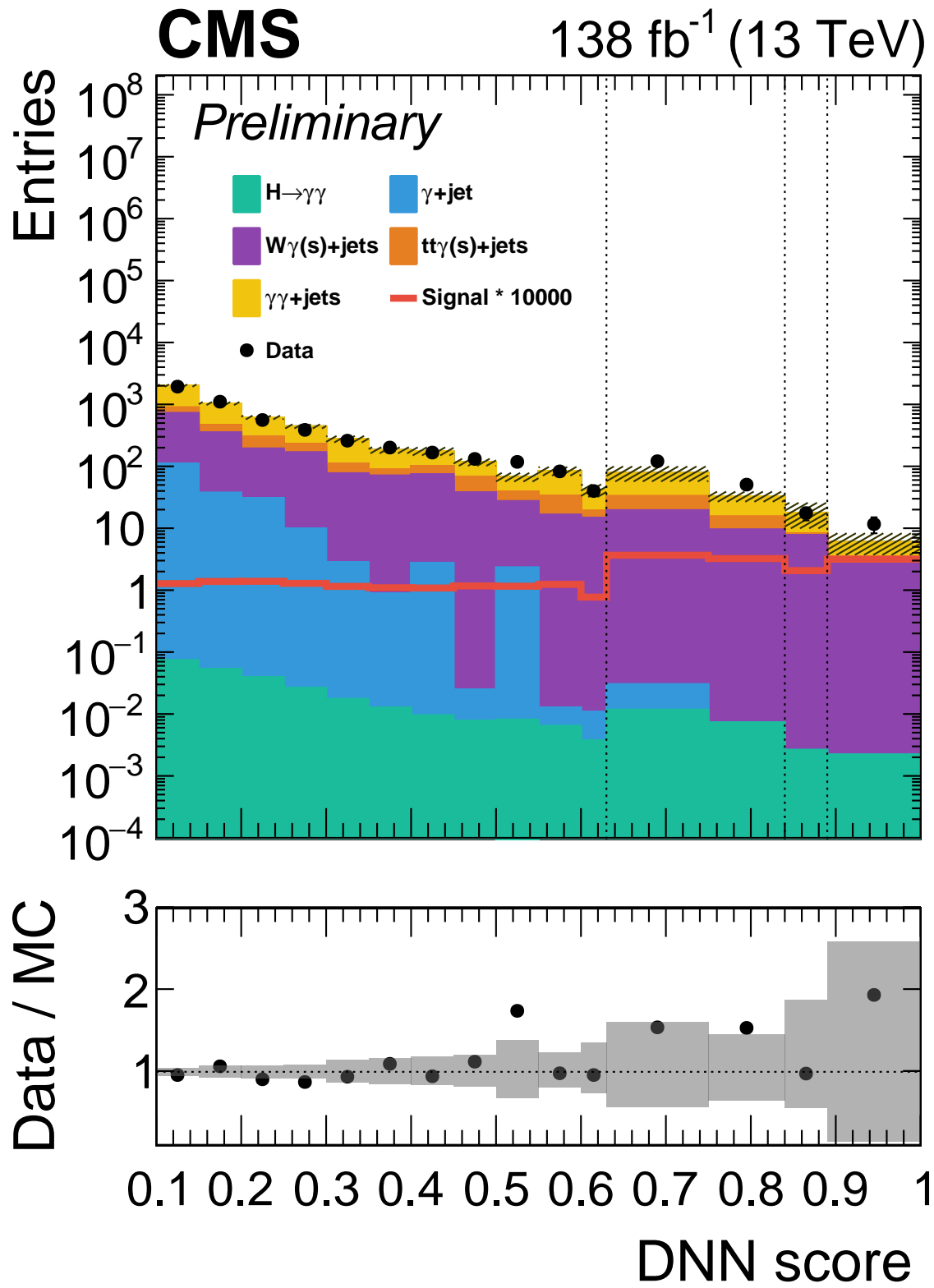
Figure 4.23: DNN output score between data and MC, using Run 2 dataset and 2017 MC scaled to Run 2 lumi.
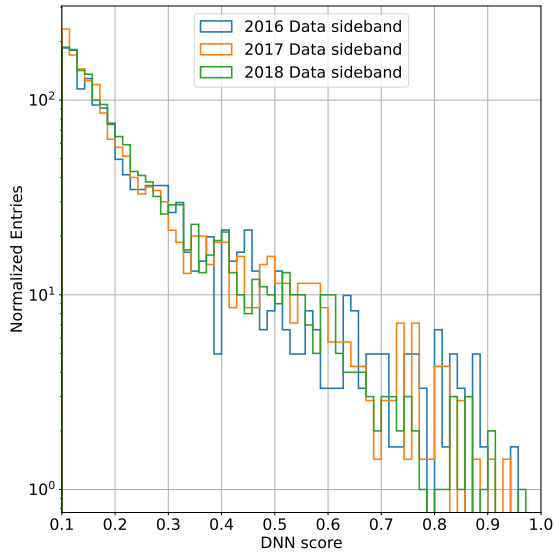
(a) Data in data sideband, each year scaled to 2018 luminosity
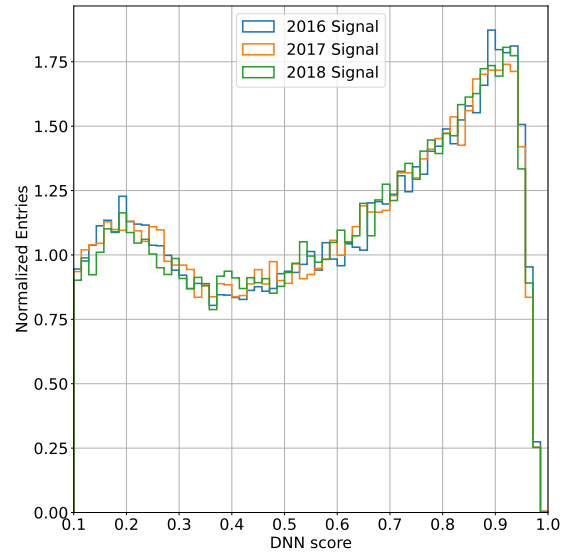
(b) Signal in signal region, each histogram normalized to an integral of 1

Figure 4.24: DNN output score of data events in the sideband region (a), and HH simulation events in the signal region (b), for each separate year.

4.5.1.2 Standard Model: Categorization

After computing a DNN output score for each event, events are placed into categories based on their DNN score in order to maximize the sensitivity of the DNN categorization. The optimization of categories is done using the output HH class DNN score only, as it has a known correlation to the H and continuum background DNN scores. If an event has a large HH class DNN score, by construction it must have small H and continuum background DNN output scores. Sensitivity is maximized by systematically determining the ideal position of category boundaries in terms of DNN score in order to maximize total significance, a proxy of the result of the asymptotic limits method to be applied during extraction of final results via fitting of the background models to the data.

This categorization is done using signal and background MC in the signal region, and therefore is maximally optimial for data when data and MC fully agree in the dataside bands. After scaling MC in the sidebands to the integral of data in the sidebands, a non-optimal data-MC agreement is found. In order to correct for this disagreement, a per-bin reweighting of the DNN score is performed. The reweighting is performed using the Run 2 dataset and 2017 MC, with MC appropriately scaled to cross section, luminosity, PU reweight and any CMS POG (Physics object groups) recommended scale factors. Each DNN score bin weight is computed as the ratio of data to MC in the sideband region. The event weight is then applied to MC in the sideband and signal region events. It should be noted that this reweighting is used only to optimize analysis categories, and is not used for the evaluation of any final results.

During category optimization, generally a finner binning of the DNN score distributions leads to a greater significance. However, small bin widths can cause statistical fluctuations which bias categorization, as a very high (low) yield bin would improve (reduce) a potential category's significance drastically, thus biasing the categorization. To ensure that the effect of statistical fluctuations is reduced in the categorization procedure, a smoothing of the background distributions is performed.

The smoothing procedure is performed on background MC in the signal and side-band region. The smoothing procedure ensures that statistical fluctuations in the shape of the DNN scores have a negligible impact on the categorization procedure.

An optimal categorization of events based on the DNN discriminant variable is extracted by computing total significance among categories, varying the number of categories, number of equally sized bins, and definition of the signal region. A simultaneous optimization of category boundaries is performed, and the case which yields the greatest significance is chosen as the final categorization. Total significance is defined as the quadtratic sum of category significance, where category significance is defined by Equation 4.9 (Equation 96 in [37]), where S and B are the number of weighted signal (HH events) and background (Single H + continuum background) events in the category, respectively. Events with a score of less than 0.1 are not used for categorization.

$$\sqrt{2((S + B)ln(1 + \frac{S}{B}) - S)} \tag{4.9}$$

The optimal category boundaries for a given number of categories, equally sized bins and signal region window are chosen by computing total significance for every possible position of category boundaries given the number of bins and categories. A simultaneous optimization of category boundaries is performed. The category boundary positions which yield the greatest total significance are defined as the optimal category boundaries for the given number of categories, bins and signal region window.

The number of categories is varied from 1-5, and the number of equally sized bins is varied among: [10, 20, 30, 40, 50, 60, 70, 80, 90, 100, 110, 120, 130, 140, 150, 160, 170, 180, 190, 380, 760, 1520]. When computing significance values for category optimization, a signal region definition of 122 to 128 GeV is used as this is the experimental resolution: A range centered around the expected higgs mass with a width $\approx \pm$ 1-2 times the expected signal width, known a-posteriori from analytic fitting.

The optimal categorization was chosen based on the 90 bin case, in which category

boundaries are simultaneously optimized among 90 equally sized bins of width (1/90) from output DNN scores of 0.1 to 1.

A very small increase in total significance is obtained when increasing from four to five total categories, as seen in Figure 4.25, in both the case where significance is computed with Equation 4.9 and S / $\sqrt{B}$. In addition, the category boundary for the most sensitive category remains constant. Therefore, the choice is made to classify events into four categories. The category boundaries, number of signal events, number of background events and significance for the N category case where N ranges from 1-5 are shown in Tables 4.18, 4.19, 4.20, 4.21 and 4.22, where the final categorization is that shown in Table 4.21. The HH yields in these tables, denoted by 'S', are properly scaled to the cross section and branching ratio of the Semi-Leptonic final state of HH→WW$\gamma\gamma$. The MC modeling the backgound in the signal region comes from the continuum background MC which is smoothed before use in the category optimization. Each MC process is scaled to its cross section and branching ratio, as well as the kinematic weight with its fiducial selection, the removal of events with an absolute value of weight times kinematic weight > 10.

CatN	DNN Min	DNN Max	S	B_{SR}	$Data_{Sideband}$	Significance
0	0.89	1.0	0.03568	0.81037	8.0	0.03935

Table 4.18: Semi-Leptonic DNN Category Boundaries and yields in signal region for 1 Categories

CatN	DNN Min	DNN Max	S	B_{SR}	$Data_{Sideband}$	Significance
0	0.89	1.0	0.03568	0.81037	8.0	0.03935
1	0.1	0.89	0.23129	511.65079	3580.0	0.01022

Table 4.19: Semi-Leptonic DNN Category Boundaries and yields in signal region for 2 Categories

CatN	DNN Min	DNN Max	S	B_{SR}	$Data_{Sideband}$	Significance
0	0.89	1.0	0.03568	0.81037	8.0	0.03935
1	0.64	0.89	0.09449	16.43561	114.0	0.02329
2	0.1	0.64	0.1368	495.21518	3466.0	0.00615

Table 4.20: Semi-Leptonic DNN Category Boundaries and yields in signal region for 3 Categories

CatN	DNN Min	DNN Max	S	B_{SR}	$Data_{Sideband}$	Significance
0	0.89	1.0	0.03568	0.81037	8.0	0.03935
1	0.84	0.89	0.02267	1.84053	12.0	0.01668
2	0.63	0.84	0.07483	15.73924	111.0	0.01885
3	0.1	0.63	0.13379	494.07101	3457.0	0.00602

Table 4.21: Semi-Leptonic DNN Category Boundaries and yields in signal region for 4 Categories

CatN	DNN Min	DNN Max	S	B_{SR}	$Data_{Sideband}$	Significance
0	0.89	1.0	0.03568	0.81037	8.0	0.03935
1	0.84	0.89	0.02267	1.84053	12.0	0.01668
2	0.64	0.84	0.07182	14.59508	102.0	0.01878
3	0.25	0.64	0.0964	157.99225	974.0	0.00767
4	0.1	0.25	0.0404	337.22293	2492.0	0.0022

Table 4.22: Semi-Leptonic DNN Category Boundaries and yields in signal region for 5 Categories
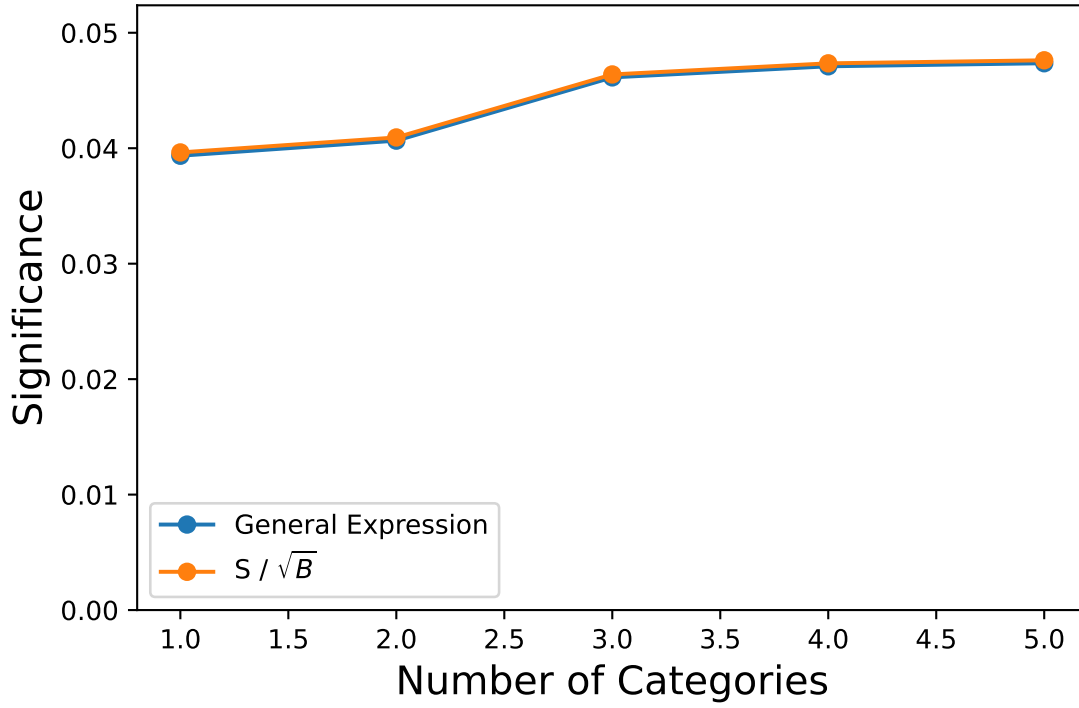
Figure 4.25: Total significance vs. number of categories in DNN categorization optimization, using either Equation 4.9 or S / $\sqrt{B}$ to compute each category's significance, with total significance computed as category significances summed in quadrature. S is the number of weighted HH events, and B is the weghted number of MC events modeling the continuum background in the signal region plus the number of weighted single H events. Also shown in Table 4.23

NCategories	Total Significance with Eq 4.9	$\frac{S}{\sqrt{B}}$
1	0.03935	0.039635
2	0.040656	0.040933
3	0.046135	0.04639
4	0.047095	0.047352
5	0.04736	0.047616

Table 4.23: Significance values using two equations for significance

4.5.1.3   EFT Benchmarks: Parametric Binary Deep Neural Network

To categorize events from the 20 EFT benchmarks in the Semi-Leptonic final state, a parametric binary DNN is used. The DNN is trained using 2017 signal and background samples, and is evaluated on 2016, 2017 and 2018 signal samples for analytic fitting and on Run 2 data to be used for categorization and data-driven background modeling. Models of the 20 EFT benchmarks are obtained by reweighting the combination of four NLO samples to each benchmark at NLO precision. The 20 EFT benchmark samples are combined and considered together as signal. The network is then trained on a labelled dataset with the 20 EFT HH processes as the signal, and various background process labelled as background.

In addition to the training variables used for the multiclass DNN, the node number ranging from 1-20 is input as a feature into the DNN, allowing one to produce an output score for any EFT benchmark hypothesis. This is essentially a way to produce 20 MVA scores in a given training, which is much more convenient than running 20 individual trainings.

The same training pre-selections are applied in this case as for the multi-class DNN, and the same category boundary optimization procedure is followed.

4.5.2 Fully-Hadronic

Data and simulation events fall into the Fully-hadronic category if they contain at least 4 jets satisfying the conditions described in Section 4.4.4, and at least one diphoton candidate satisfying the selections described in Section 4.4.2. To maintain categorical orthogonality with the Semi-leptonic and Fully-leptonic final states, events in the Fully-hadronic category are required to have exactly zero leptons passing the selections described in Section 4.4.3.

Because the invariant mass resolution of two jets is not expected to be precise enough to separate W-boson and Z-boson events, the Fully-Hadronic $HH \to ZZ\gamma\gamma$ channel is expected to overlap with the Fully-hadronic $HH \to WW\gamma\gamma$ channel. In addition, the HH→bb$\gamma\gamma$ process is difficult to distinguish from the Fully-hadronic HH→VV$\gamma\gamma$ signatures. In order to optimize this final state analysis for the Fully-hadronic WW$\gamma\gamma$ final state, a dedicated "bb$\gamma\gamma$ killer" DNN is trained to differentiate HH→bb$\gamma\gamma$ from all backgrounds. After the removal of these additional final states, any remaining events are included in the signal definition. Therefore, in the final signal definition, $HH \to ZZ\gamma\gamma \to qqqq\gamma\gamma$, $HH \to bb\gamma\gamma$ and $HH \to WW\gamma\gamma \to qqqq\gamma\gamma$ are included. Thus, the Fully-Hadronic signal corresponds to $HH \to (WW + ZZ + bb)\gamma\gamma$.

4.5.2.1 DNN for Fully-Hadronic Channel

As mentioned in Section 4.1, a DNN approach must be taken for the Fully-hadronic final state to optimize sensitivity, while simultaneously minimizing contamination from the $HH \to (bb + ZZ)\gamma\gamma$ processes. To this end, two binary trainings are performed as follows:

- **WW$\gamma\gamma$ identifier**: Trained for the separation of signal ($HH \to WW\gamma\gamma$) and backgrounds listed in Tab. 4.24).

- **bb$\gamma\gamma$ killer**: Trained in order to obtain a discriminant to use for reducing the contamination of bb$\gamma\gamma$. For this training, bb$\gamma\gamma$ is considered signal, and the MC listed in Tab. 4.24, with the addition of the WW$\gamma\gamma$ process, are considered background.

MC Samples
DiPhoJetsBox_MGG-80toInf
GJet_40toInf $\Rightarrow$ Data-Driven QCD
HT-binned QCD $\Rightarrow$ Data-Driven QCD
tt$\gamma\gamma$+0Jets
ttγ+Jets

Table 4.24: MC list for Fully-Hadronic

4.5.2.2 WW$\gamma\gamma$ identifier

This binary DNN training is used for the separation of di-Higgs (WW$\gamma\gamma$) signal w.r.t. background. The backgrounds used for the Fully-Hadronic training is shown in Tab. 4.24.

From the list of background considered in Tab. 4.24, QCD simulation suffers from a very low number of events, so a data-driven approach is considered for estimating the QCD. The considered data-driven approach estimates QCD and γ+jets simultaneously. This is described in sec. 4.5.2.5.

This DNN is trained using 2017 signal and background MC, and is evaluated on the signal and data of each data-taking year. The sum of three EFT benchmark simulation samples generated at LO (nodes 1, 2 and 3 as defined in Table 4.1) is considered as signal in MC training, and is reweighted to the SM HH signal and NLO as was done in the Semi-leptonic case. The dominant background processes, namely $\gamma\gamma$+jets and QCD are used as background for training the network.

In order to produced a data-driven estimate of QCD+γjet, data events in the sideband with an additional selection on photon ID of $<$ -0.7 is applied to the leading and subleading photons. Therefore, events used for the Fully-hadronic DNN training are required to have a photon ID score $>$ -0.7.

The features used as input to the Fully-Hadronic channel DNN can be found in Tab. 4.25 and Tab. 4.26.

The data/MC agreement is shown for a few leading importance input features, after the

Feature	Description
Leading Photon pT / $m_{\gamma\gamma}$	pT of the photon with the highest transverse momentum out of the selected photons, scaled to diphoton mass.
Subleading Photon pT / $m_{\gamma\gamma}$	pT of the photon with the second highest transverse momentum out of the selected photons, scaled to diphoton mass.
Leading Photon ϕ	Direction in the transverse plane of the photon with the highest transverse momentum out of the selected photons
Subleading Photon ϕ	Direction in the transverse plane of the photon with the second highest transverse momentum out of the selected photons
Leading Photon η	Direction in the transverse plane of the photon with the highest transverse momentum out of the selected photons
Subleading Photon η	Direction in the transverse plane of the photon with the second highest transverse momentum out of the selected photons
max Photon ID	The maximum value of the photon MVA score out of the two selected photons.
min Photon ID	The minimum value of the photon MVA score out of the two selected photons.
$\Delta\phi(\gamma\gamma)$	Azimuthal separation between the two selection photon candidates
$\Delta R(\gamma\gamma)$	Separation between two photons in the transverse plane
Jet Multiplicity	Number of selected jets in the event (flavour inclusive)
Sum two max bScores	Sum of two highest b-score jets out of all available good jets
Leading Jet p_T	Transverse momentum of the jet with the highest transverse momentum out of the selected jets
Leading Jet η	Rapidity of the jet with the highest transverse momentum out of the selected jets
Leading Jet ϕ	Phi of the jet with the highest transverse momentum out of the selected jets
Leading Jet E	Energy of the jet with the highest transverse momentum out of the selected jets
Leading Jet DeepJet Score	DeepJet b-tag discriminator score of the jet with the highest transverse momentum out of the selected jets
Subleading Jet p_T	Transverse momentum of the jet with the second highest transverse momentum out of the selected jets
Subleading Jet η	Rapidity of the jet with the second highest transverse momentum out of the selected jets
Subleading Jet ϕ	Phi of the jet with the second highest transverse momentum out of the selected jets
Subleading Jet E	Energy of the jet with the second highest transverse momentum out of the selected jets
Subleading Jet DeepJet Score	DeepJet b-tag discriminator score of the jet with the second highest transverse momentum out of the selected jets

Table 4.25: Input features used to train Fully-Hadronic channel DNN.

Feature	Description
Second Subleading Jet p_T	Transverse momentum of the jet with the third highest transverse momentum out of the selected jets
Second Subleading Jet η	Rapidity of the jet with the third highest transverse momentum out of the selected jets
Second Subleading Jet ϕ	Phi of the jet with the third highest transverse momentum out of the selected jets
Second Subleading Jet E	Energy of the jet with the third highest transverse momentum out of the selected jets
Second Subleading Jet DeepJet Score	DeepJet b-tag discriminator score of the jet with the third highest transverse momentum out of the selected jets
Third Subleading Jet p_T	Transverse momentum of the jet with the fourth highest transverse momentum out of the selected jets
Third Subleading Jet η	Rapidity of the jet with the fourth highest transverse momentum out of the selected jets
Third Subleading Jet ϕ	Phi of the jet with the fourth highest transverse momentum out of the selected jets
Third Subleading Jet E	Energy of the jet with the fourth highest transverse momentum out of the selected jets
Third Subleading Jet DeepJet Score	DeepJet b-tag discriminator score of the jet with the fourth highest transverse momentum out of the selected jets
$\Delta\phi(HH)$	Azimuthal separation between the two selection Higgs candidates
$\Delta R(HH)$	Separation between two Higgs in the transverse plane
$min(\Delta R(g_k, j_l))$	minimum separation between the selected jet and photon candidate
$max(\Delta R(g_k, j_l))$	maximum separation between the selected jet and photon candidate
$min(\Delta R(j_k, j_l))$	minimum separation between the jet candidates
$max(\Delta R(j_k, j_l))$	maximum separation between the jet candidates
costhetastar	The angle between the parton collision axis z and the $pp \to H_1 H_2$ decay axis z', both defined in the $H_1 H_2$ system rest frame
costheta1	Angle between the direction of the W-boson (W_1) from the $H_1 \to W_1 W_2$ and the direction opposite the $H_1 H_2$ in the H_1 rest frame.
costheta2	Angle between the direction of the W-boson (W_2) from the $H_2 \to \gamma\gamma$ and the direction opposite the $H_1 H_2$ in the H_2 rest frame.
Phi	Angle between the decay planes of the two Z-system in the $H_1 H_2$ rest frame
Phi1	Angle between the zz' plane and the plane of the $H_1 \to \gamma\gamma$ decay in the $H_1 H_2$ rest frame
W1 pT	pT of vector sum of two leading jets
W1 η	rapidity of vector sum of two leading jets
W1 mass	Invariant mass of vector sum of two leading jets
W2 pT	pT of vector sum of 3rd and 4th leading jets
W2 η	rapidity of vector sum of 3rd and 4th leading jets
W2 mass	Invariant mass of vector sum of 3rd and 4th leading jets
WW pT	pT of vector sum of first four leading jets
WW η	rapidity of vector sum of first four leading jets
WW mass	Invariant mass of vector sum of first four leading jets

Table 4.26: Input features used to train Fully-Hadronic channel DNN.

removal of events with a DNN score < 0.1, in Figures 4.26 and 4.27.
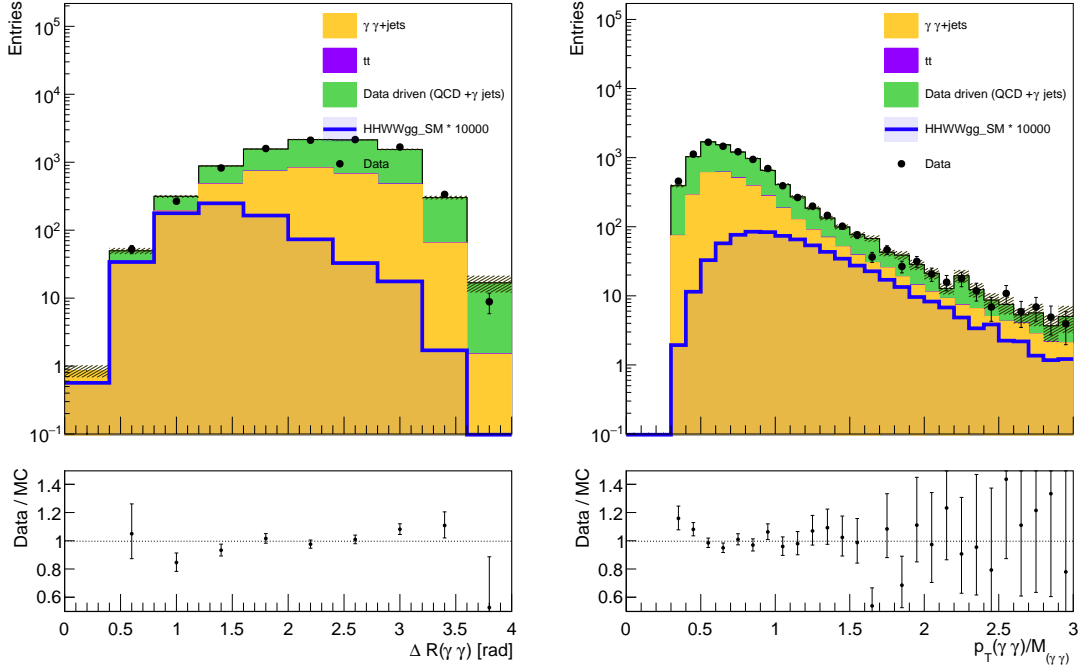
Figure 4.26: Data/MC comparison of a fully-hadronic leading DNN input feature (left) and second leading DNN input feature (right).

The output ROC curve from the training is shown in Fig. 4.28.

As the curves are similar, this indicates no sign of over-training. Additionally, the output score of signal and background for training and testing shows no overtraining signature, as shown in Fig. 4.29.

In addition, a check is performed in a dedicated control region to demonstrate that a large difference in data and MC acceptance is not expected to be introduced by the $WW\gamma\gamma$ identifier DNN, and that the DNN behaves as expected on its signal topology. This check is shown in Appendix D.

4.5.2.3   bb$\gamma\gamma$ killer

This binary DNN training is used as a bb$\gamma\gamma$ killer. The objective of this DNN is to output a bb$\gamma\gamma$ killer score to use as a discriminant to use for the removal of bb$\gamma\gamma$ events from
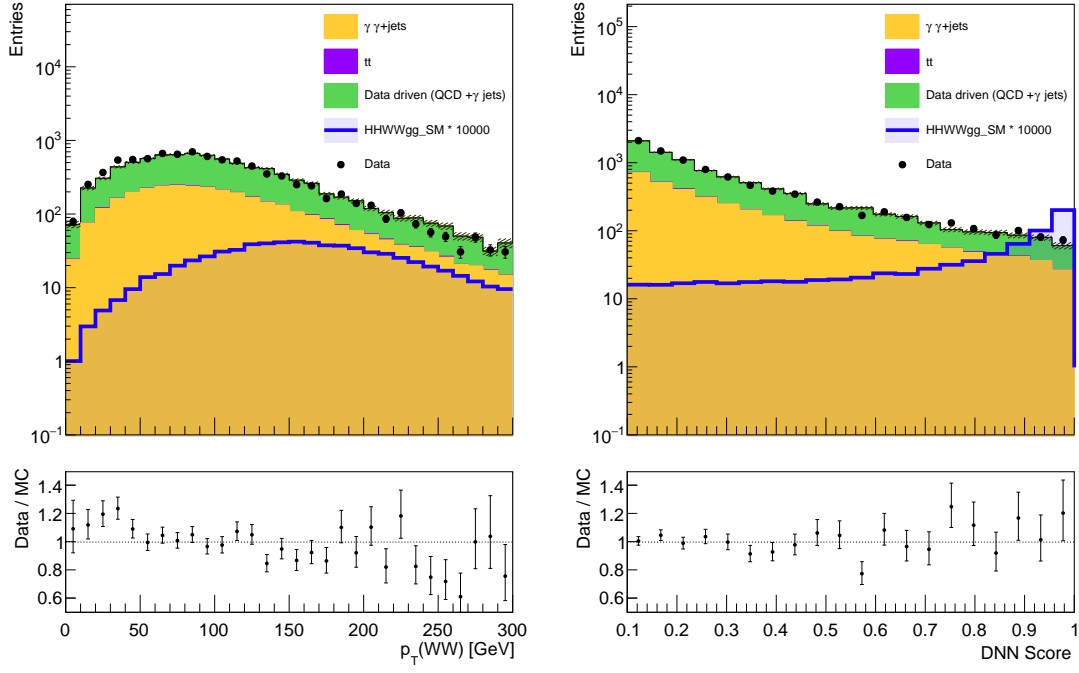
Figure 4.27: Data/MC comparison of a fully-hadronic third leading DNN input feature and DNN score.
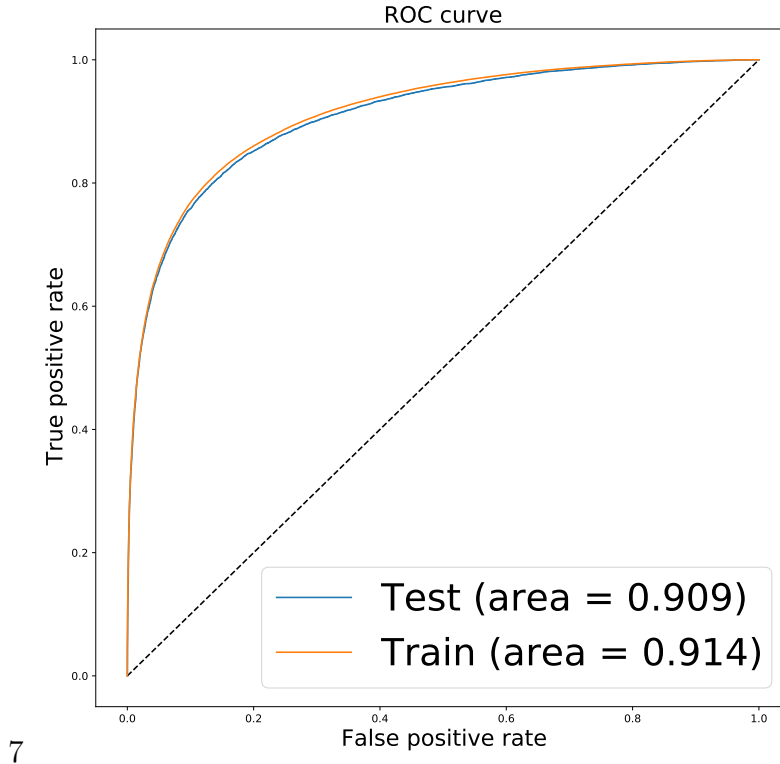
Figure 4.28: ROC curve for WW$\gamma\gamma$ identifier Fully-Hadronic DNN
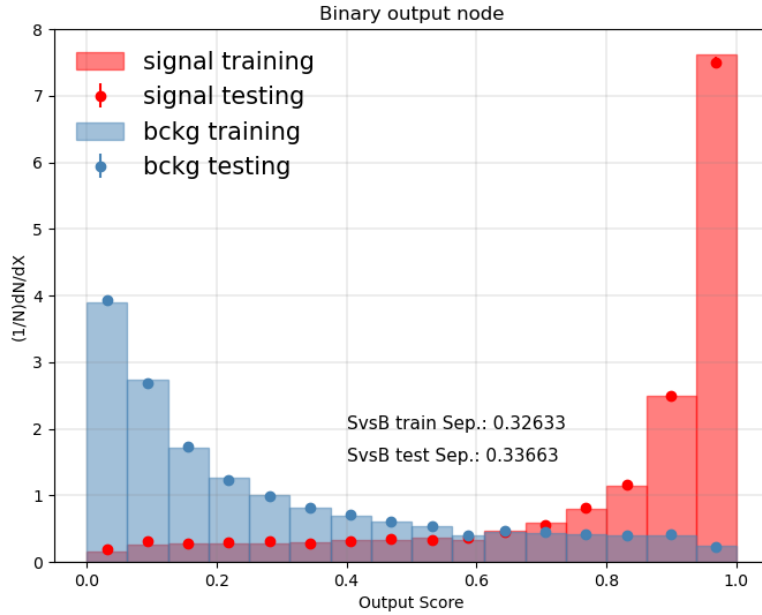
Figure 4.29: Output score of Fully-Hadronic DNN WW$\gamma\gamma$ identifier training

the WW$\gamma\gamma$ phase-space. This is trained considering a bb$\gamma\gamma$ simulation sample as signal. The list of background used consists of all background mentioned in Tab. 4.24 along with the Fully-hadronic WW$\gamma\gamma$ simulation sample. Other details for this training including the events selections, list of input variables and DNN architecture remain the same as for the WW$\gamma\gamma$ identifier described in Section 4.5.2.1.

The output ROC curve of this training is shown in Fig. 4.30. As the curves are similar for both the training and test datasets, this indicates that there is no overtraining. Additionally, the output score of signal and background for training and testing shows no overtraining signature, as shown in Fig. 4.31.
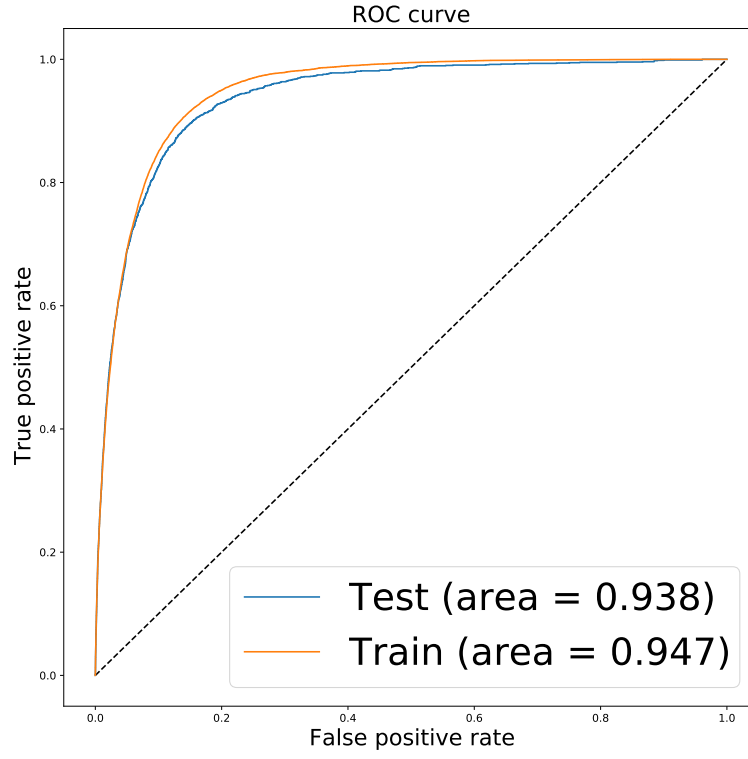
Figure 4.30: ROC curve for Fully-Hadronic DNN bb$\gamma\gamma$ killer
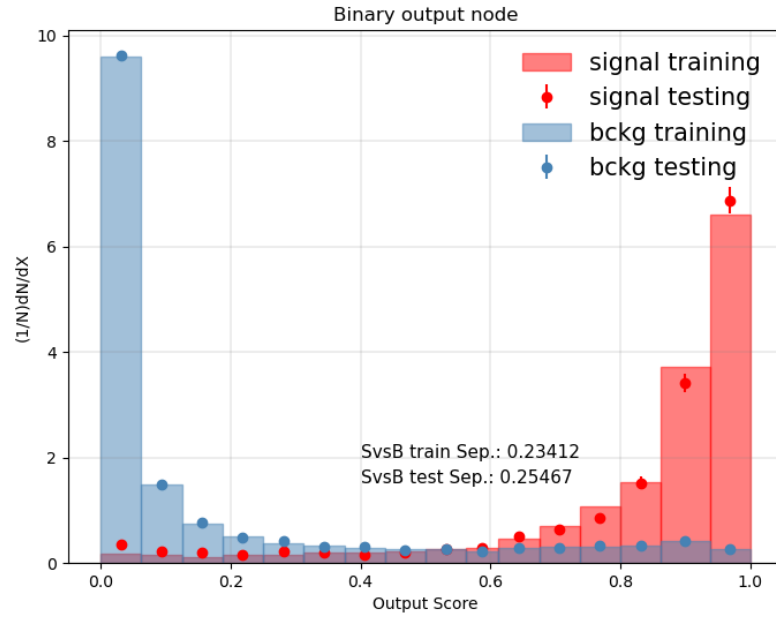
Figure 4.31: Output score of Fully-Hadronic DNN bb$\gamma\gamma$ killer training

4.5.2.4 Categorization

Events falling into the Fully-hadronic category are categorized in a similar fasion as described in Section 4.5.1.2 for the Semi-leptonic channel, but with the addition of a selection on the bb$\gamma\gamma$ killer score.

The expected signal region yields background processes, simulated with MC, and HH signal, both scaled to the Run 2 luminosity of 137 fb^{-1} (the estimated luminosity value at the time of training), are shown in Figure 4.32 for the WW$\gamma\gamma$ identifier score.
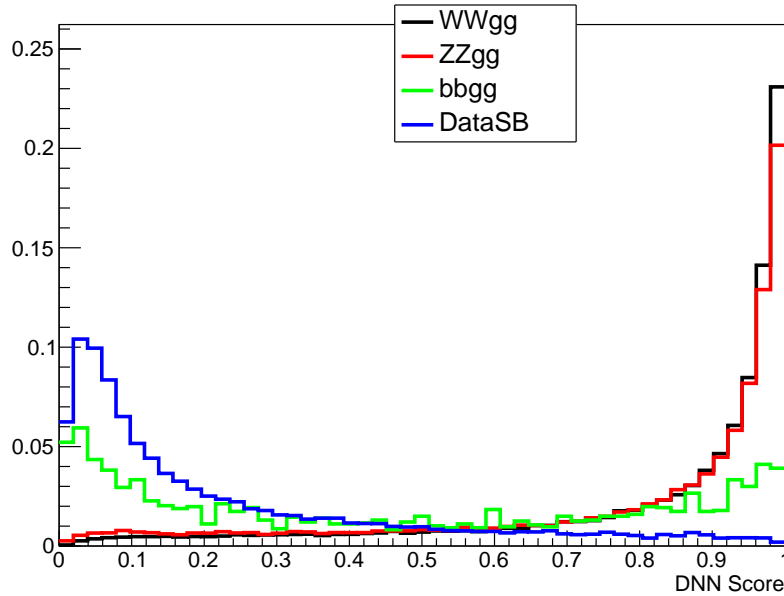
Figure 4.32: Fully-Hadronic output score for signal and background. All distributions are normalized to unity.

These distributions are used for significance computations.

In performing the categorization, the same method is followed as for the semi-leptonic final state described in Section 4.5.1.2. The result of smoothing of the MC in the signal region is shown in Fig. 4.33.

The optimal categorization was chosen based on the 380 bin case, in which category boundaries are simultaneously optimized among 380 equally sized bins of width (1/380) from output WW$\gamma\gamma$ identifier DNN scores of 0.1 to 1. It was also found that a signal region
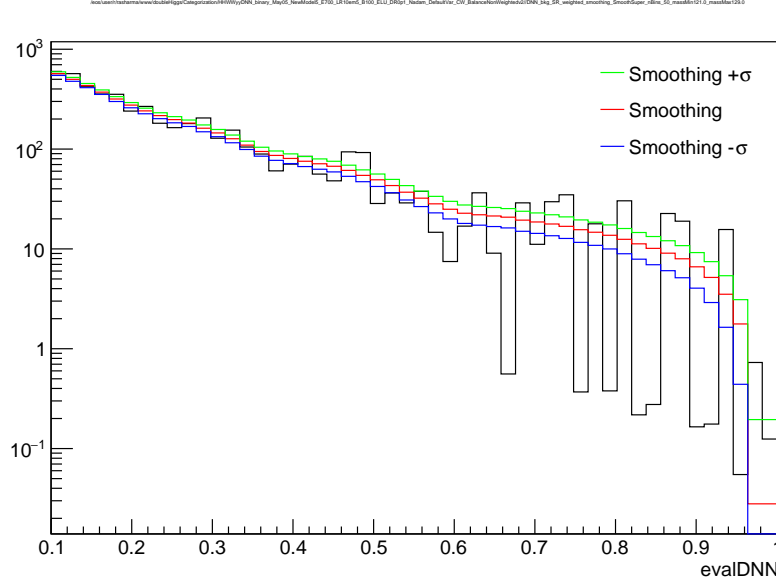
Figure 4.33: Result of background smoothing for Fully-Hadronic channel.

definition of 120 to 130 GeV in the di-photon mass region returns the greatest significance with number of bins and categories held constant, a hint that choosing optimal category boundaries based on this definition may return the most sensitive result. The category boundaries, yields and significance values are summarized in Tab. 4.27 for the case of four categories, the final choice on number of categories for optimization.

After categorizing based on the WW$\gamma\gamma$ identifier to maximize signal efficiency, events are required to have a bb$\gamma\gamma$ killer score less than 0.6 in order to remove the majority of bb$\gamma\gamma$ events.

CatN	DNN Min	DNN Max	S	B_{SR}	$Data_{Sideband}$	Significance
0	0.983	1.0	0.03373	0.101421	24.0	0.03373
1	0.969	0.983	0.04398	4.684672	55.0	0.02029
2	0.893	0.969	0.13746	53.51282	384.0	0.01878
3	0.1	0.893	0.30157	5979.241	27390.0	0.00390

Table 4.27: Fully-Hadronic DNN Category Boundaries and yields in signal region for 4 Categories

4.5.2.5   Data Driven QCD and γjet

For this final state category, a data-driven QCD+γjet estimation is performed in a control region where one photon candidate fails the requirement of photon ID > -0.7, previously used and described in [38].

4.5.3 Fully-Leptonic

For events to fall into the FL analysis category, they must contain exactly two oppositely charged leptons (e^+e^-, $\mu^+\mu^-$, $e^\pm\mu^\mp$). The leading p_T lepton is required to have $p_\mathrm{T} > 20$ GeV, the subleading lepton is required to have $p_\mathrm{T} > 10 GeV$, and a distance parameter between the two leading p_T leptons > 0.4 is required. Events are rejected from this category if the event contains a third lepton with $p_\mathrm{T} > 10$ GeV in order to avoid saving events with three high energy leptons, as only two are expected from this process. In order to identify events with missing transverse momentum due to the two neutrinos from the leptonically decaying W-bosons, events are required to have $p_T^{miss} > 20$ GeV. Furthermore, the diphoton candidate in this final state is required to have $p_\mathrm{T} > 91$ GeV, and the invariant mass between each electron candidate and photon candidate is required to be at least 5 GeV different from the invariant Z boson mass to avoid saving Z$\rightarrow \ell\ell$ events. The invariant mass from the two leading leptons is required to be < 80 GeV or > 100 GeV in order to suppress VH(H$\rightarrow \gamma\gamma$) events, as shown in Fig 4.34. In addition, events containing at least one jet with a b-tagging score greater than a medium working point are removed. The reason a b-veto is applied in this final state and not for the SL and FH final states is because this final state applies a cut-based selection, and therefore we choose to apply a b-veto as part of the final selections.

The $p_T^{\gamma\gamma}$ selection was chosen to optimize $\frac{S}{\sqrt{B}}$ while also preserving enough events for a meaningful background fit. The significance plot is shown in Fig. 4.34 (a). Working points were identified from this plot for which limits are computed, and a study is performed to determine if the data-driven background model fit introduces a bias in the signal region. The results from these checks are shown in Table 4.28.

A selection on diphoton p_T of 91 GeV is chosen as it returns the greatest significance among the tested working points, which passed a check on the bias of data-driven background modelling with a low number of data-sideband events. The $|m_{e\gamma} - m_Z| > 5$ GeV selection was chosen as it was previously used in the Run 2 CMS ttH(H$\rightarrow \gamma\gamma$) analysis [39]. This is

$p_T^{\gamma\gamma}$ (GeV)	Run2 $N_{sidebands}$	$\frac{S}{\sqrt{B}}$
91	10	2.80
97	8	3.05
100	7	3.21
104	6	3.39

Table 4.28: Fully-Leptonic significance for four $p_T^{\gamma\gamma}$ workpoints

aimed at rejecting Z Boson events while preserving background yields. As shown in Fig 4.34 (b), the m_{ll} selection is applied to suppress VH backgrounds. This selection rejects ≈90% of VH events while preserving ≈99% of Fully-Leptonic HH signal events.
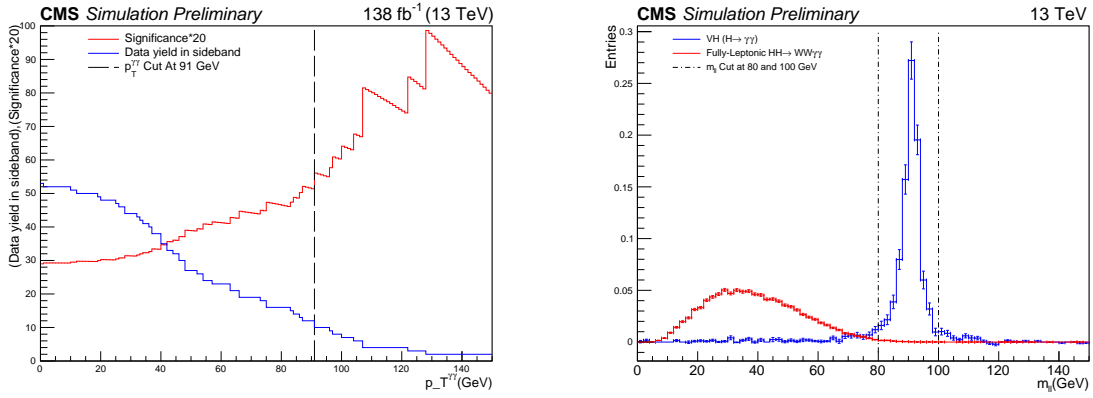

Figure 4.34: For fully leptonic channel: (a) Significance scan of di-photon p_T cut, the black dashed line is the final cut value:$p_T > 91$ GeV . (b) m_{ll} distribution comparison between signal and VH events, the signal and VH have been normalized to 1, and the two dashed lines are the final cuts at di-Lepton mass: $m_{ll} < 80$GeV or $m_{ll} > 100$ GeV .

4.6   Signal and background modelling

In order to model the di-Higgs signal process, and single higgs resonant background processes in the signal region, $115 < m_{\gamma\gamma} < 135$ GeV, simulated events in each analysis category are combined to construct $m_{\gamma\gamma}$ shapes. To define a template for each HH and H process in each analysis category, the same strategy is followed: A sum of 1-5 Gaussian functions is fit to the histogram of diphoton mass entries.

Because the continuum background in the signal region is expected to follow a falling shape continuous with the data sidebands, data events in the data sidebands are fit to a falling analytic function in order to model the continuum background.

4.6.1   di-Higgs Signal

Signal models are formed by an analytic fit of gaussians of polynomic order 1-5, determined by an F-Test, to the $m_{\gamma\gamma}$ region. First an F-test is performed in order to determine the order to determine the order of the gaussian fit, and then the parameters that best fit the signal model $m_{\gamma\gamma}$ bins is found. This is done separately for each year (2016, 2017, 2018) and each analysis category.

Signal model fits are shown for the two highest DNN score Semi-Leptonic categories in Figure 4.35.

For the Fully-Hadronic category, the remaining bb$\gamma\gamma$ and fully-hadronic ZZ$\gamma\gamma$ yields after the minimization of contamination in the WW$\gamma\gamma$ phase space are considered HH signal in this category when extracting upper limits the di-Higgs cross section. Signal model fits are shown for the Fully-Hadronic WW, ZZ, and bb$\gamma\gamma$ categories in Figures 4.36a, 4.36b, and 4.37a respectively. These signal models are combined before fitting to data in the Fully-Hadronic categories.

For the fully-leptonic final state, after applying the object and event selections described in Sections 4.4 and 4.5.3, a signal fit model is produced using the remaining events. The
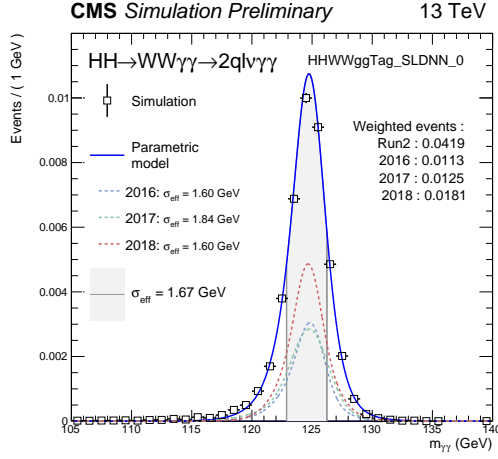
(a) DNN Category 0
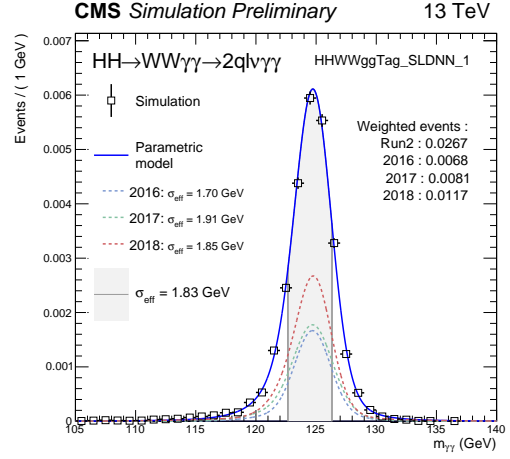
(b) DNN Category 1

Figure 4.35: Semi-Leptonic signal models for all three years and the Run 2 combination, in the two highest DNN score categories.
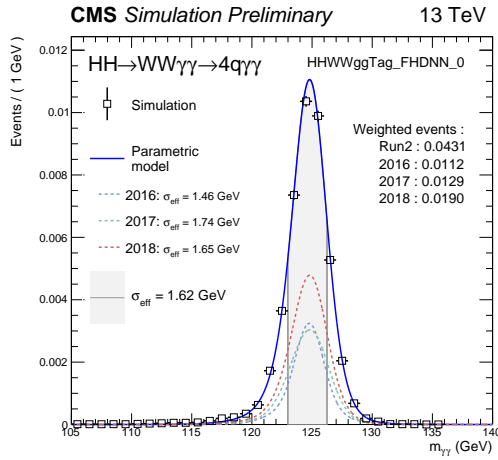
(a) WW$\gamma\gamma$ signal model
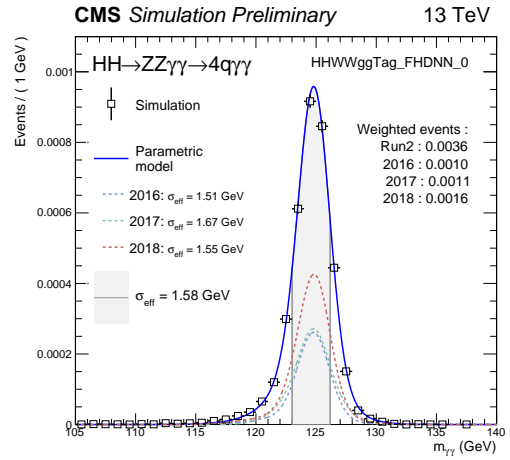
(b) ZZ$\gamma\gamma$ signal model

Figure 4.36: Fully-Hadronic HH models for all three years and the Run 2 combination in the highest DNN score Fully-hadronic category.

signal model is shown in Figure 4.37b.
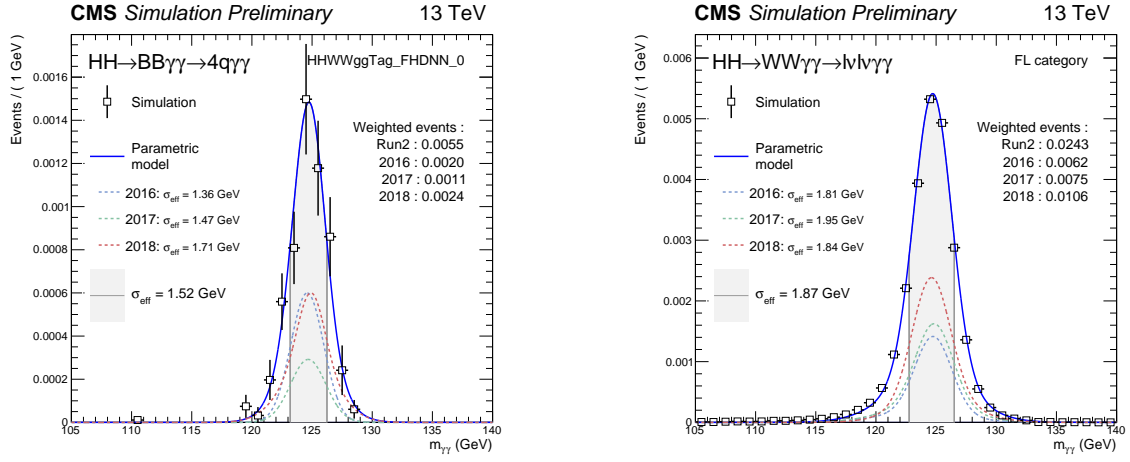
(a) Fully-Hadronic bbγγ signal models for all three years and the Run 2 combination in the highest DNN score Fully-hadronic category.

(b) Fully-Leptonic signal models for all three years and the Run 2 combination

Figure 4.37: Fully-Hadronic HH→bbγγ and Fully-leptonic signal models for all three years and the Run 2 combination.

For all categories, the total number of signal events increases by year as expected due to the increase in integrated luminosity per year.

4.6.2 Single Higgs Background

There are expected resonant background processes present in the signal region, $115 < m_{\gamma\gamma} < 135$, due to $H \to \gamma\gamma$ processes, which cannot be modeled with a data-driven method using data sideband events. These backgrounds are modeled with MC in the same fashion as the $HH \to WW\gamma\gamma$ signals in Section 4.6.1. Examples of some Single Higgs models in the Semi-leptonic, Fully-hadronic and Fully-leptonic categories can be seen in Figures 4.38, 4.39, and 4.40. Note that the ggH and VBFH single higgs signals are not provided for the Fully-Leptonic final state, as their contributions are either zero due to the absence of any signal events passing the Fully-Leptonic selections, or are extremely low and can not be reasonably fit to an analytic model.

(a) VHToGG

(b) ttHJetToGG

Figure 4.38: Semi-Leptonic DNN Category 0 Single Higgs Models

(a) ggH

(b) VBFH

Figure 4.39: Fully-Hadronic single higgs models in the highest DNN score category.

(a) VHToGG

(b) ttHJetToGG

Figure 4.40: Fully-Leptonic Single Higgs Models

4.6.3 Continuum Background

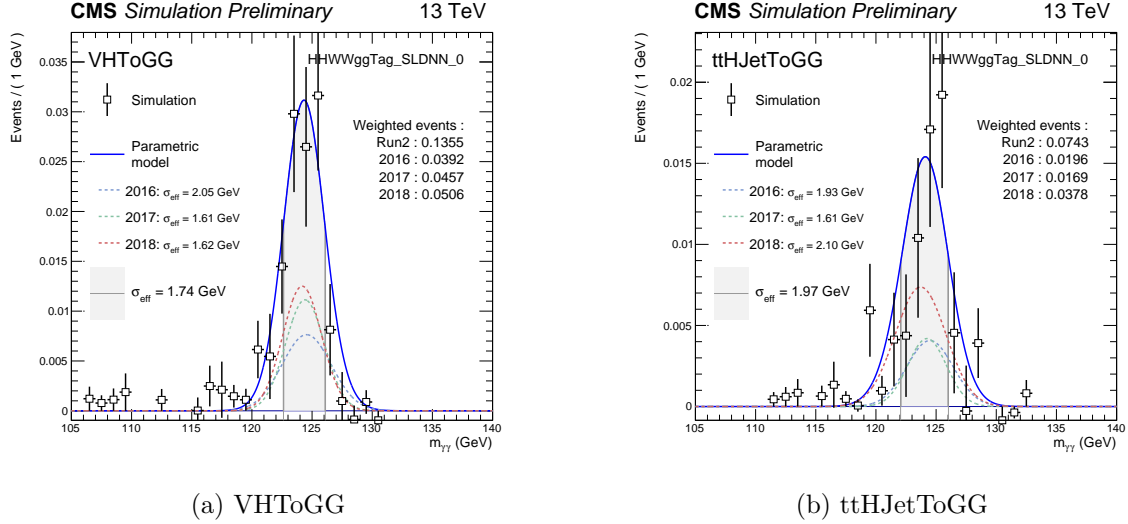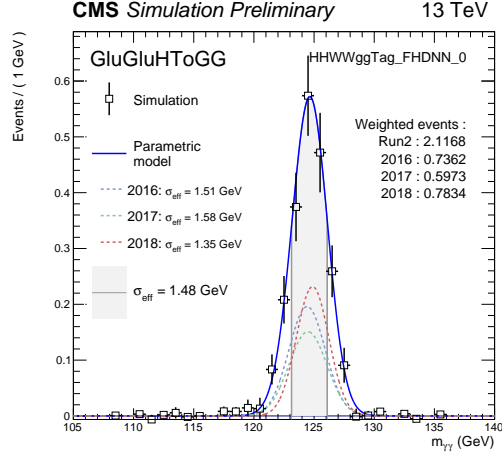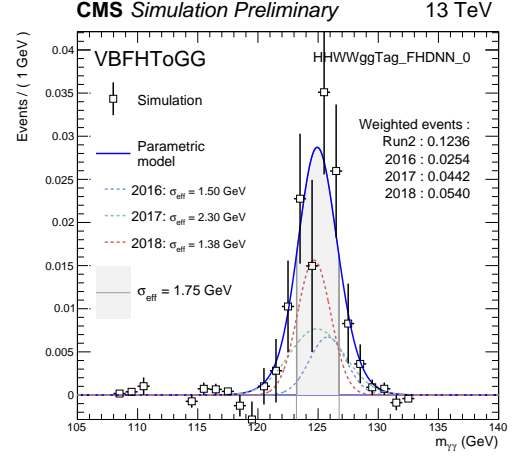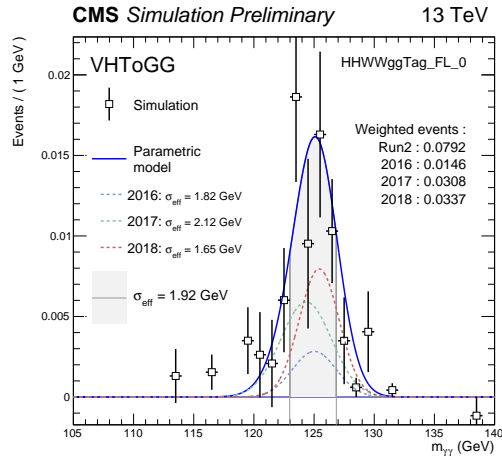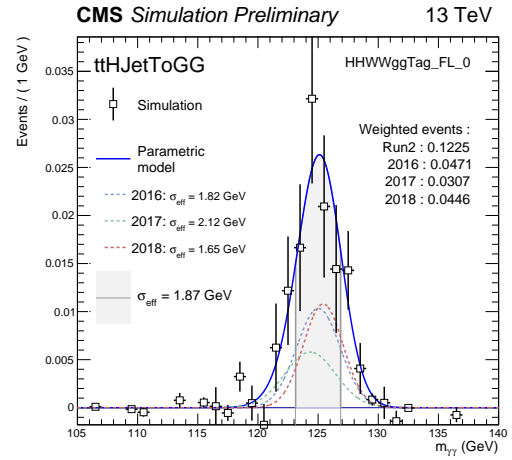A data-driven background model is produced for each category using the data sidebands: events in the regions $100 < m_{\gamma\gamma} < 115$ and $135 < m_{\gamma\gamma} < 180$. The aim of this is to model the continuum background. After the selections and categorizations of each final state category are applied to the 2016, 2017, and 2018 datasets, analytic functions are fit to the resulting $m_{\gamma\gamma}$ distributions in the data sidebands for each analysis category. These are later combined with their corresponding single Higgs models in order to obtain a full background model. As with the signal fitting, an F-Test is performed first in order to determine the most appropriate analytic function to fit to the data sidebands. Bernstein, laurent, exponential, and powerlaw function families are considered as candidates to fit the data. The fit is then performed with the fit function shape determined from the F-Test. In the Semi-Leptonic background fitting, the three data taking years are merged together before ftest and fitting are performed. The ftests and S + B fits for the Semi-Leptonic channel, where the HH signal model is scaled to the resulting simultaneous best fit to data in all WW$\gamma\gamma$ categories, are shown in Figures 4.41, 4.42, 4.43 and 4.44. The f-tests and fits for the Fully-Hadronic category is shown in Figures 4.45. For the Fully-Leptonic category only, due to a low number of sideband events per year, a single full Run2 continuum background model is produced by summing the three years of sideband data before performing an f-Test and producing a fit model, where uncertainty is obtained via the envelope method, which can be seen in Figure 4.49. A best fit function is chosen by treating the choice of function as a discrete nuisance parameter. An uncertainty is then assigned to the chosen fit function based on a combination of the likelihoods of all attempted fit functions. This method is described in Ref. [40]. Note that in the lower panel plots for all data-driven background fit plots, the quantity shown is the data with the single Higgs and continuum background components subtracted.

The resulting combined fit of the background + signal models to the data, where the signal strength of the HH models are varied to best fit the data, are shown in Figure 4.50
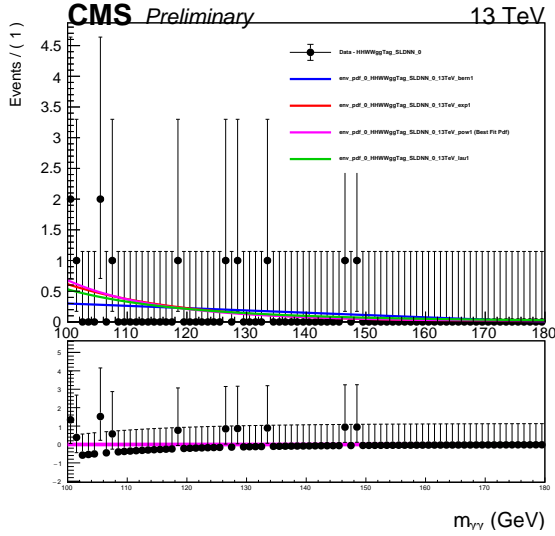
(a) fTest
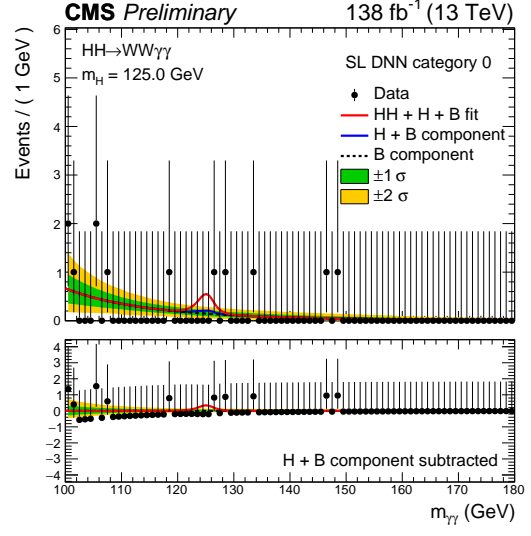
(b) Fit with uncertainty

Figure 4.41: Semi-Leptonic data-driven background model for Run 2 data, DNN Category 0

(a) fTest
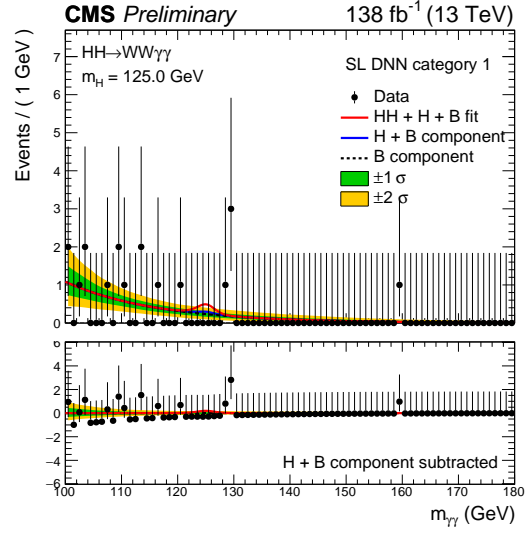
(b) Fit with uncertainty

Figure 4.42: Semi-Leptonic data-driven background model for Run 2 data, DNN Category 1

(a) fTest
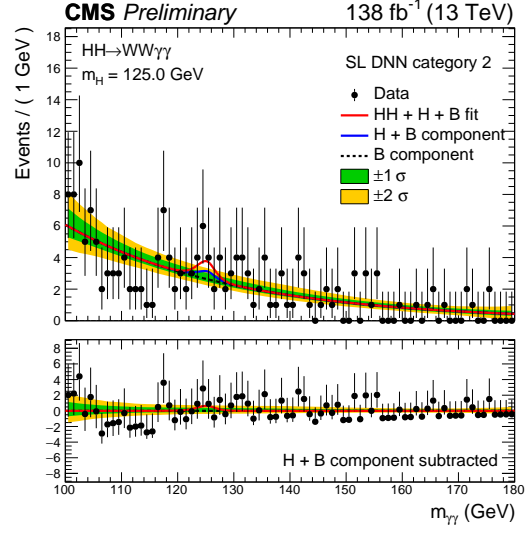
(b) Fit with uncertainty

Figure 4.43: Semi-Leptonic data-driven background model for Run 2 data, DNN Category 2
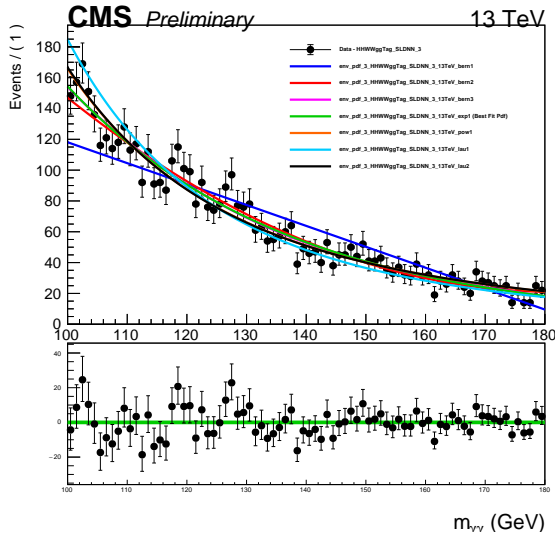
(a) fTest
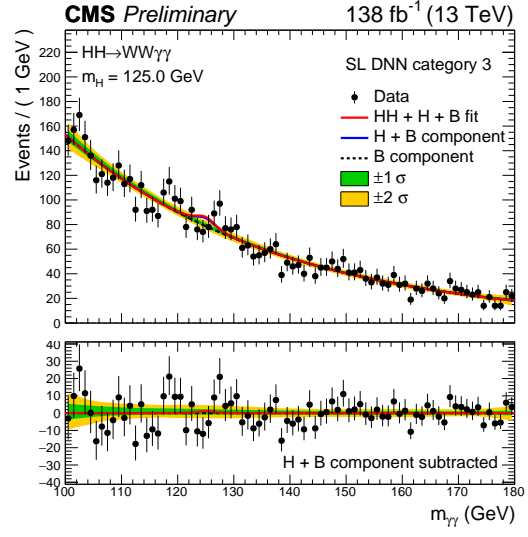
(b) Fit with uncertainty

Figure 4.44: Semi-Leptonic data-driven background model for Run 2 data, DNN Category 3
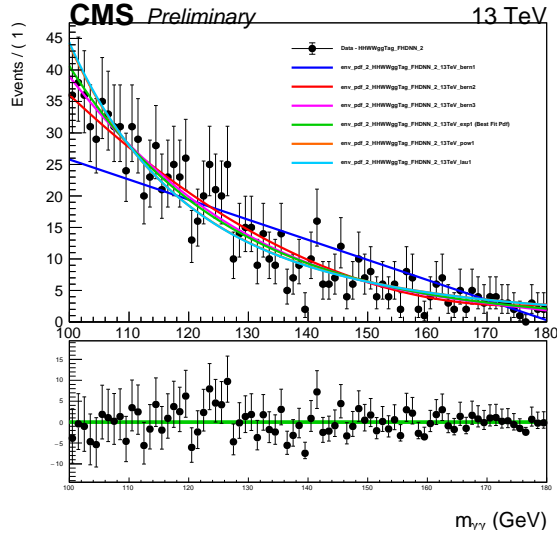
(a) fTest, DNN Category 2
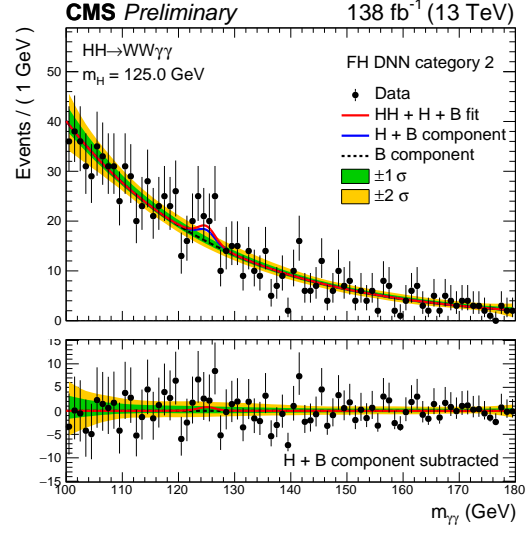
(b) Background Fit, DNN Category 2

Figure 4.45: Fully-Hadronic data-driven background models for Run 2 data
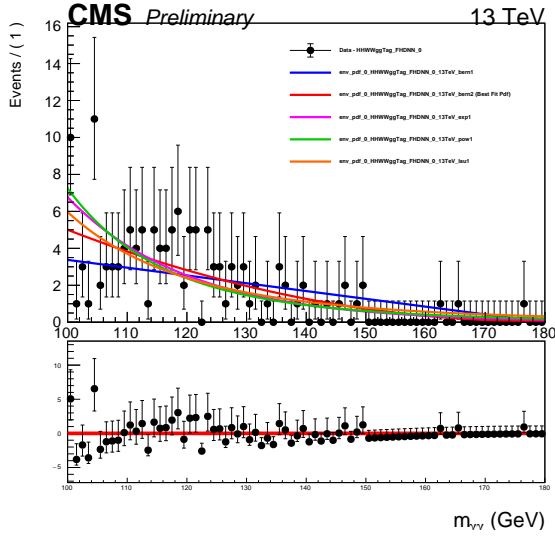
(a) fTest, DNN category 0
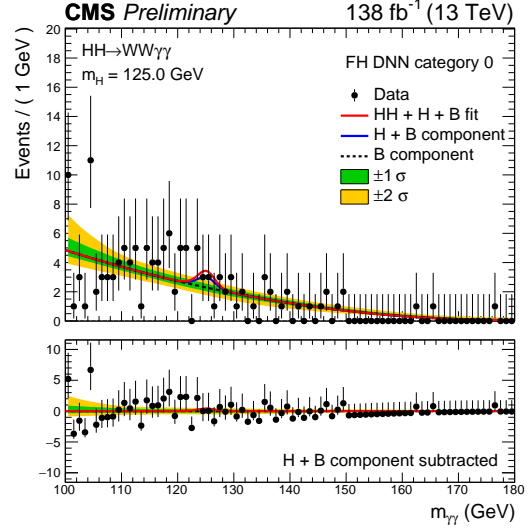
(b) B + S fit to data, category 0

Figure 4.46: Fully-Hadronic data-driven background and simulation models
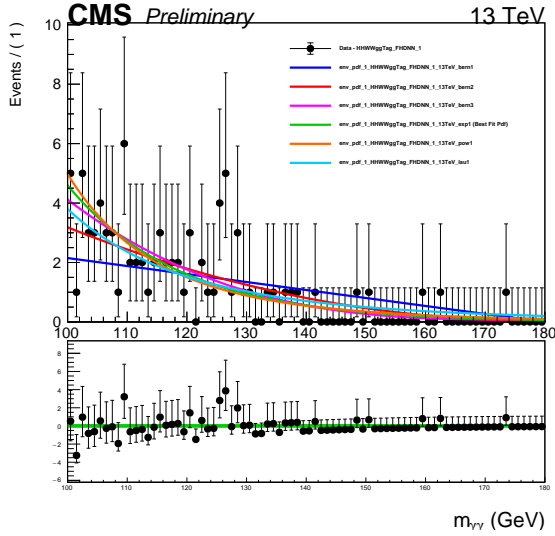
(a) fTest, DNN category 1
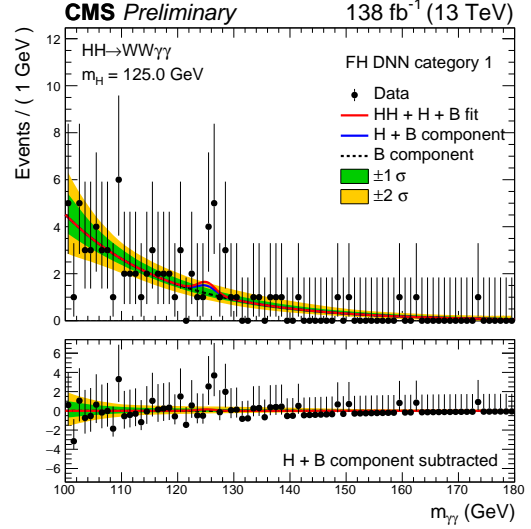
(b) B + S fit to data, category 1

Figure 4.47: Fully-Hadronic data-driven background and simulation models
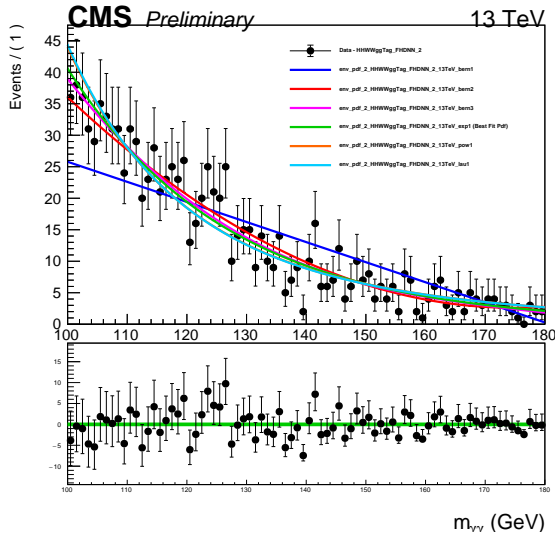
(a) fTest, DNN category 2
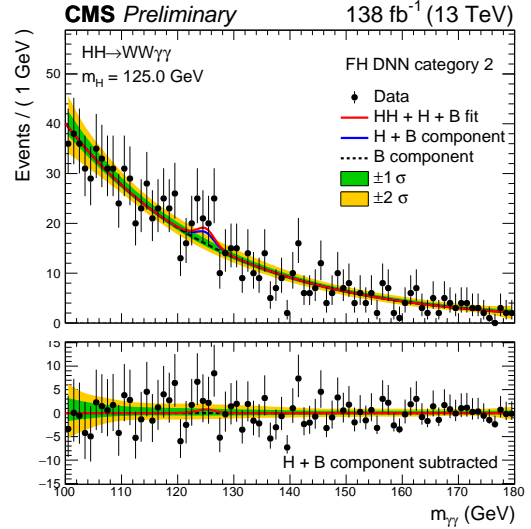
(b) B + S fit to data, category 2

Figure 4.48: Fully-Hadronic data-driven background and simulation models
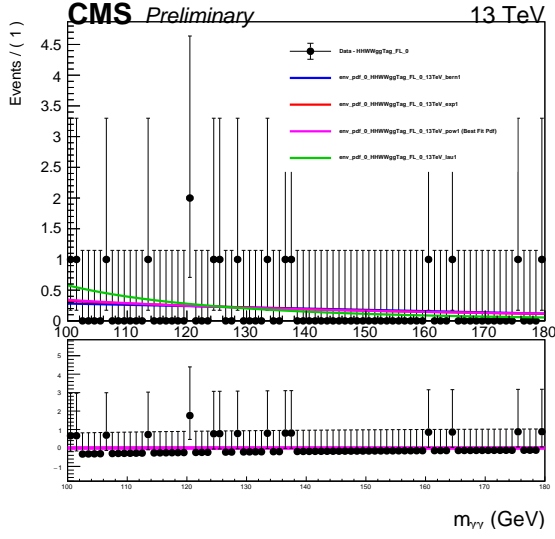
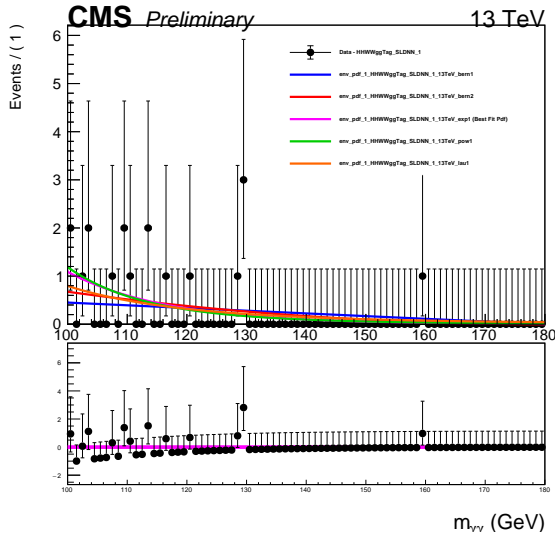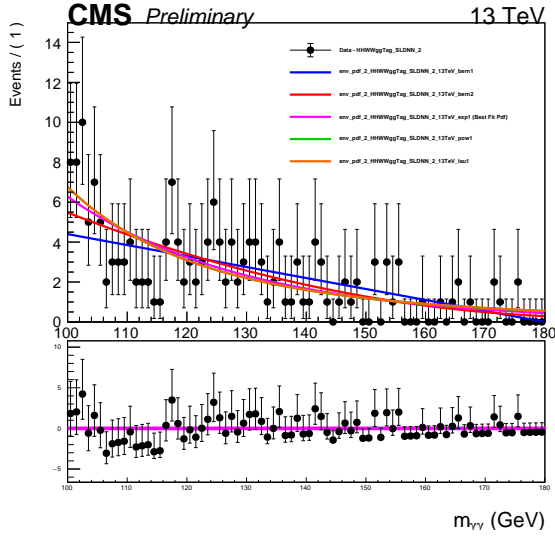(a) fTest
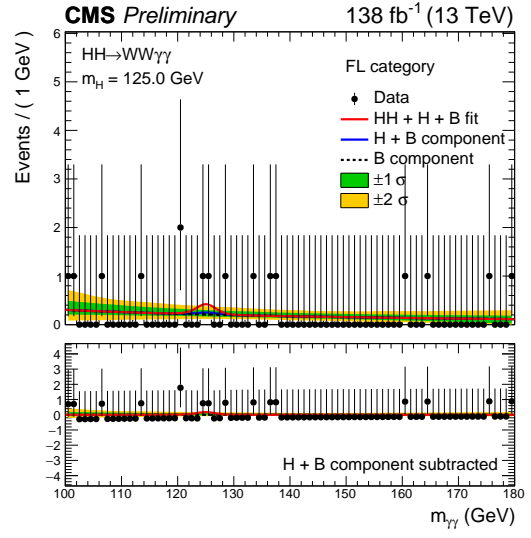
(b) Fit with uncertainty

Figure 4.49: Fully-Leptonic data-driven background model for Run 2 data

where each analysis category's contribution is weighted by its signal to background yield ratio.
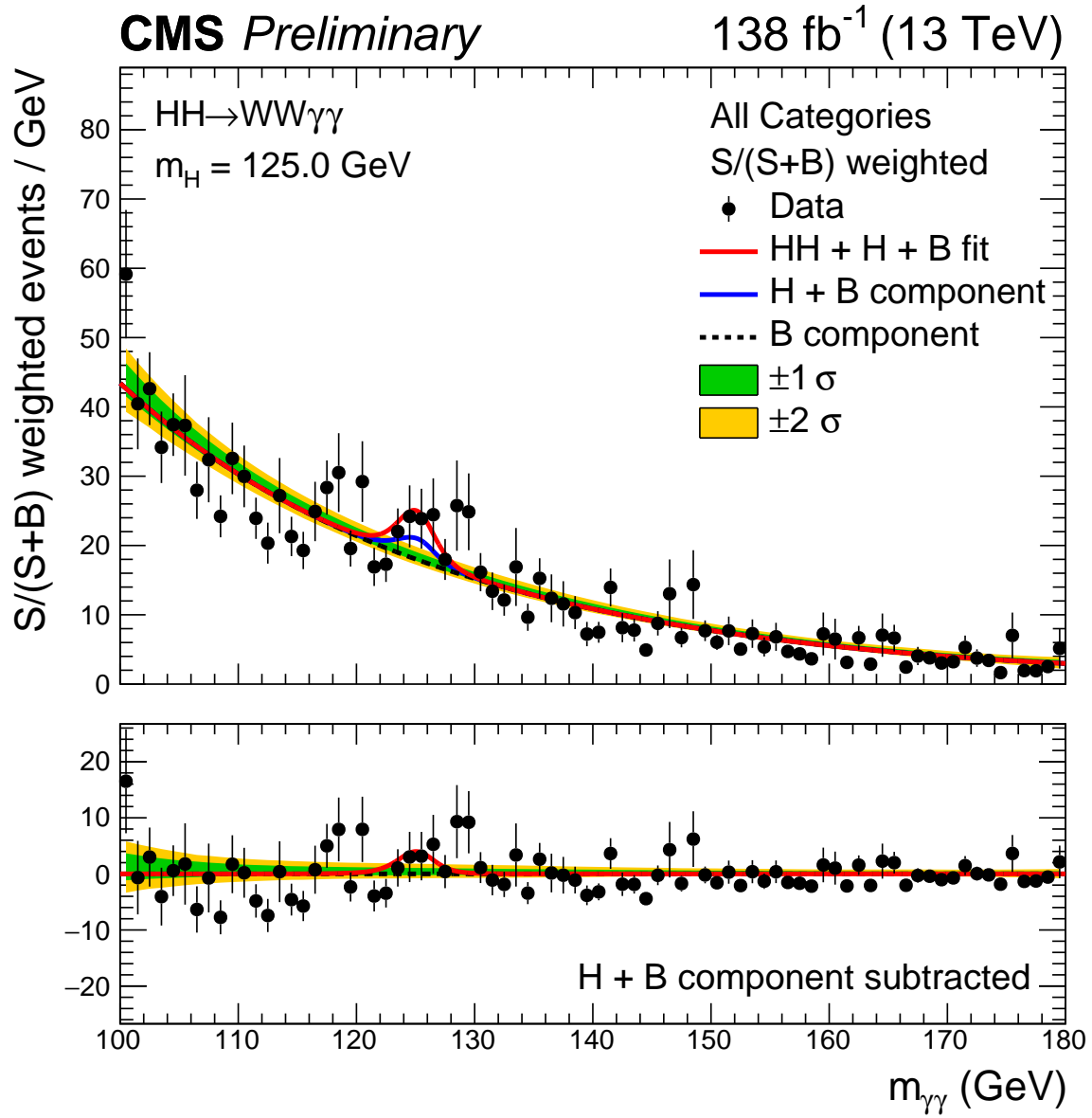
Figure 4.50: Combined signal + background model fit to Run 2 data, weighted per category by S / S+B

4.7   Systematic uncertainties

This analysis takes into account systematic uncertainties from theoretical and experimental sources. The uncertainties on the signal and on the single Higgs backgrounds are modeled as scale or shape uncertainties. The scale uncertainties affect the yield of the processes and are treated as log-normal uncertainties, while the shape uncertainties are modeled as variations of the $m_{\gamma\gamma}$ shape of the processes, i.e. the peak position or the width. The systematic uncertainty associated with the data-driven estimate of the continuum background is accounted for via the discrete profiling method. Given the small number of expected signal events compared to the backgrounds, the effect of the systematics uncertainties on the final results is expected to be small compared to the statistical ones. In case a systematic uncertainty affects processes in different channels, it is considered fully correlated across those channels. The following sources of systematic uncertainties are considered:

1. **Theoretical uncertainties on the HH cross section**: The combined uncertainty on the QCD scale and on the top mass is taken into account, considering also its dependence from the value of κ_λ. For the SM signal this uncertainty amounts to $-23/+6\%$. The combined uncertainty on the PDF modeling and on the strong coupling constant is also considered with a value of 3% [41].

2. **Theoretical uncertainties on the single Higgs cross sections**: Process-dependent uncertainties related to the QCD scale, the PDF modeling, and the strong coupling constant are taken into account for the ggH, ttH, VBF H, and VH processes.

3. **Theoretical uncertainties on the Higgs boson branching ratios**: Such uncertainties are considered for both the single and the double Higgs processes. The considered uncertainties on the $H \to \gamma\gamma$, $H \to VV$, and $H \to bb$ branching ratios are approximately 2%, 1.5%, and 1.2%, respectively.

4. **Integrated luminosity**: A scale uncertainty is defined according to the luminosity measurements performed by the CMS experiment [42; 43; 44].

5. **Trigger**: The trigger efficiency is measured from data with a tag and probe procedure using $Z \to ee$ events. The related uncertainty is uncorrelated between the three data taking years. An additional considered source of uncertainty is related to inefficiencies of the ECAL L1 trigger at $|\eta| > 2$ experienced during 2016 and 2017. This is modeled as a purely rate-changing uncertainty.

6. **Electron and muon reconstruction, identification and isolation efficiency**: These efficiencies are evaluated in data and simulation with tag-and-probe techniques using Drell-Yan events [45; 46]. Scale factors are derived and applied to the simulated events to improve the agreement of the efficiencies between simulation and data. The related uncertainty is purely rate-changing and uncorrelated between the three data taking years.

7. **Photon identification**: The efficiency of the pre-selection on the photon identification MVA score is estimated in data and simulation with a tag-and-probe technique using Drell-Yan events. Scale factors are applied to correct for the difference between the data and the simulation. The related uncertainty is purely rate-changing and uncorrelated between the three data taking years.

8. **Photon shower shape**: Corrections for the imperfect modeling of the photon shower shape (and isolation) variables in simulation are applied to improve the agreement with the data. The impact of this uncertainty is estimated from the difference of the photon energy scale before and after the correction. This is modeled as a shape uncertainty which is correlated between the three years of the data taking.

9. **Photon energy scale and resolution**: Corrections for the difference of the photon energy scale and resolution between data and simulation are derived using $Z \to ee$

events, with electron-photon differences accounted for as a systematic uncertainty. This uncertainty is uncorrelated between the three years of the data taking.

10. **Jet energy scale and resolution**: Corrections for the differences in the measured jet energies between data and simulation are applied [47]. The impact of the corresponding uncertainties on the signal yield is evaluated by varying the corrected jets four-momentum within their respective per-jet uncertainties and propagating the effect to the final result. Several sources of uncertainty are considered, each with a specific level of correlation among the three years of data taking.

11. **B-tagging**: The difference in the b-tagging score distribution between data and simulation is corrected for with a reweight of the simulated events dependent on the jet p_T, $|\eta|$, and flavor [35]. The corresponding uncertainty is purely rate-changing and uncorrelated between the three years of data taking.

In this analysis, the uncertainties with the largest impact on the expected results are the theoretical uncertainties. One can find the uncertainties with the leading impacts on the expected upper limits on signal strengths in Appendix B.1. Note that while a leading systematic impact is "HighR9EBPhi", this is set to a conservative uncertainty by definition. The systematic uncertainties due to a finite number of events in Monte Carlo samples for the HH signal are neglected.

4.8 Results

The SM hypothesis tested in this analysis is the existence of the SM non-resonant di-Higgs process, probed via the WW$\gamma\gamma$ phase space. Additionally, BSM hypotheses are tested in the context of the EFT framework described in Section 4.2, including a di-Higgs process whose production cross section is altered due to the modification of the di-Higgs self-coupling, coupling of two Higgs bosons to two top quarks, and a group of 20 EFT benchmark nodes corresponding to modifications of κ_λ, κ_t, c_2, c_g, c_{2g} defined in Tab. 4.1.

Expected (observed) results are obtained by performing a simultaneous likelihood fit of the signal and background templates to Asimov (observed) data, in categories defined by selections from a multiclassifier DNN in the SL final state, a combination of two binary DNN's in the FH final state, and a group of cut based selections in the FL final state. For the κ_λ scan, the same categorization methods are used as for the SM case, but applied to three HH simulated samples corresponding to $\kappa_\lambda = [1, 2.45, 5]$, where a weighted linear combination and shape interpolation of the three is made in order to estimate the expected yield and shape for κ_λ hypotheses between -30 and 30. The effects of anomalous κ_λ values on the Higgs boson branching ratios and on the single Higgs cross sections are taken into account using the modeling provided in Ref. [17] and [18].

For the c_2 scan, a similar approach is taken but with the use of 6 EFT signal models obtained via a reweighting of 4 NLO samples. The 20 EFT benchmark node results are extracted in categories defined based on a parametric DNN in the SL final state, and a reweighting of SM MC events for the FH and FL final states.

As it is not possible to observe evidence of an SM HH signal given the sensitivity of the analysis on the available dataset, a modified frequentist method CL_s [48; 49] is used to calculate 95% confidence-level (CL_s) exclusion limits with the asymptotic approximation [50]. This method is applied in order to determine the upper limit on the production cross section of each signal hypothesis. Each upper limit is extracted by positively scaling the

corresponding HH signal model until it is incompatibile with the background-only hypothesis (expected), or data (observed), at a 95% CL_s.

Combining the SL results with the FL and FH WW$\gamma\gamma$ (+ZZ$\gamma\gamma$+bb$\gamma\gamma$ for fully hadronic case) channels leads to the combined Run 2 results shown in Table 4.29.

	Observed limit	-2σ	-1σ	Expected Limit	$+1\sigma$	$+2\sigma$
Fully-Leptonic	280	81	120	190	330	550
Fully-Hadronic	310	70	98	140	230	350
Semi-Leptonic	71	30	42	64	110	170
Combination	97	25	35	53	86	130

Table 4.29: Full Run2 Combination results, including SL, FL and FH categories, on $\frac{\sigma(HH)}{\sigma_{SM}(HH)}$, assuming an NLO standard model cross section of about 31.05 fb. Results have been rounded to two significant figures.

A combined median value of 97 (53 expected) times the NLO approximation of the standard model gluon gluon HH cross section is obtained, considering a standard model cross section of 31.05 fb.

The combined κ_λ scan is shown in Figure 4.52b, with each category and the combined median limit values shown in Figure 4.52a. Note that the theory prediction line, drawn in red, represents the predicted HH cross section value for a certain value of κ_λ.

As shown in Figure 4.52b, an observed (expected) constraint on the Higgs self-coupling of about -26 (-14) to 24 (18) times its standard model value is obtained at a 95% CL.

The combined c_2 scan is shown in Figure 4.53b, with each category and the combined median limit values shown in Figure 4.53a. Note that the theory prediction line, drawn in red, represents the predicted HH cross section value for a certain value of c_2.

As shown in Figure 4.53b, an observed (expected) constraint on the coupling constant magnitude of two top quarks to two Higgs bosons of about -2.4 (-1.8) to 2.9 (2.2) is extracted at a 95% CL.

Finally, the observed (expected) upper limits on the production cross section of the 20 EFT benchmark scenarios defined in Tab. 4.1 are shown separately for each WW$\gamma\gamma$ final

state in Figure 4.54, and in the combined case in Fig.4.55, where the combined results range from 1.7 - 6.2 (1.0 - 3.9) pb.
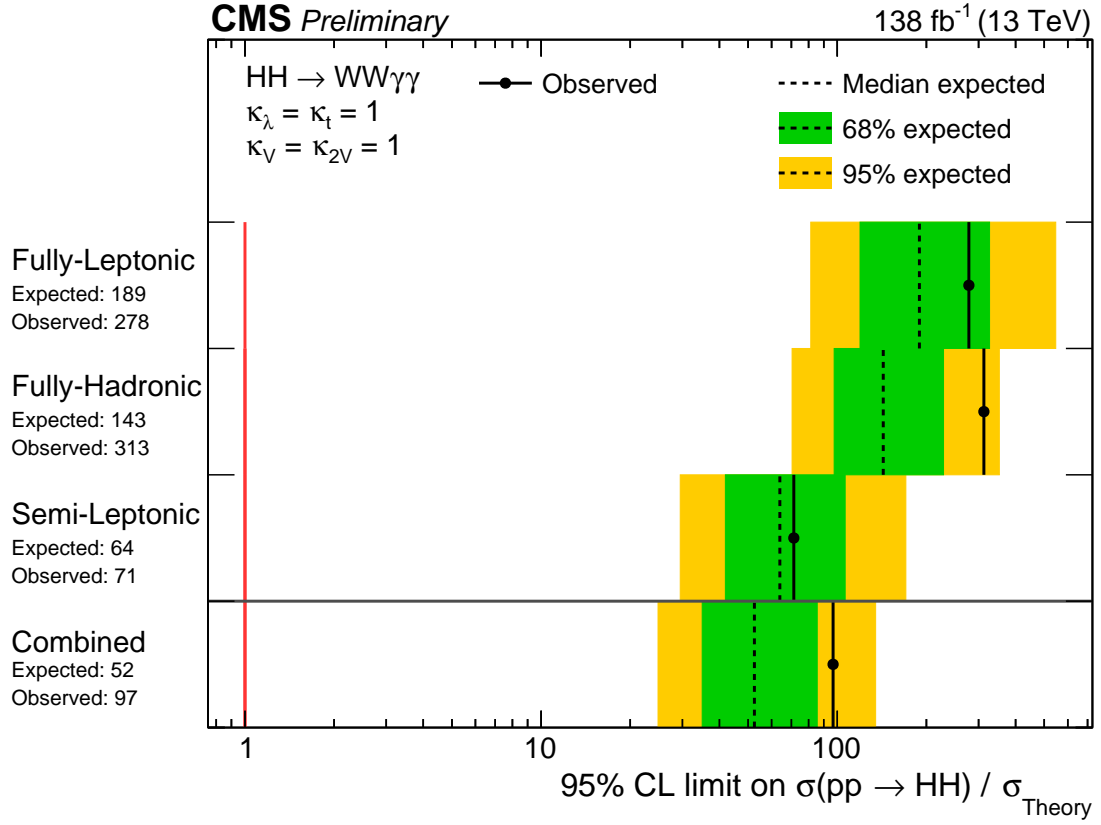
Figure 4.51: Run 2 95% CL_s limits on HH gluon gluon fusion production with respect to $\sigma_{SM}^{NLO} \approx 31.05$fb. Note that the red line at one corresponds to the SM prediciton.
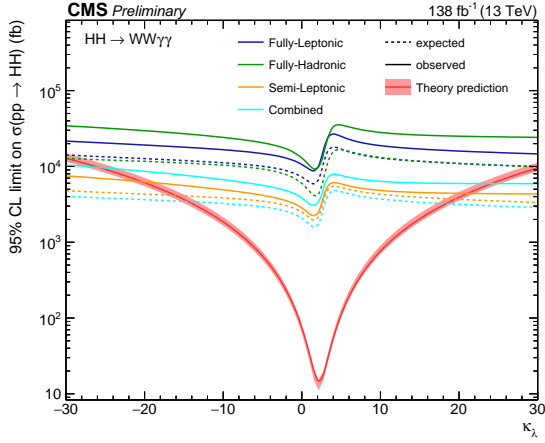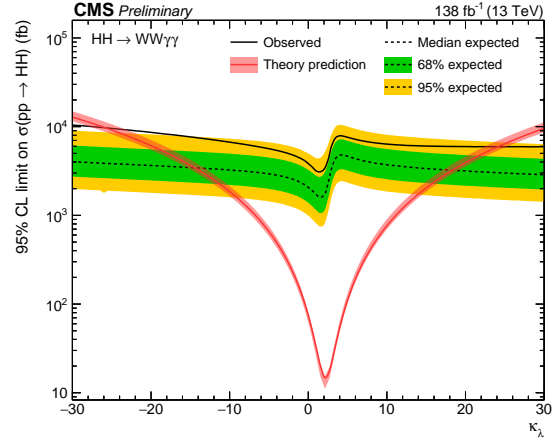
(a) Per channel

(b) Combined

Figure 4.52: 95% CL_s upper limit scan of κ_λ hypotheses from -30 to 30. Note that the red curves correspond to theoretical cross section predictions for each given κ_λ hypothesis.
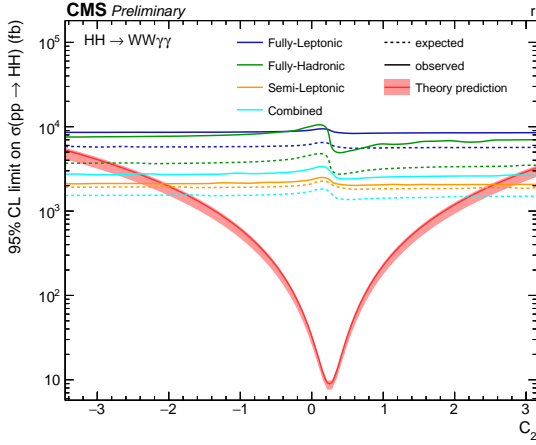
(a) Per channel
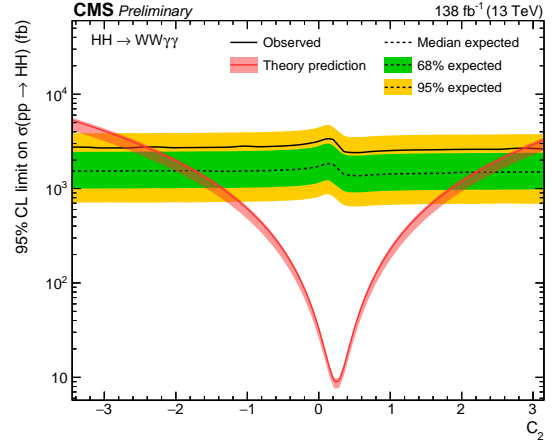
(b) Combined

Figure 4.53: 95% CL_s upper limit scan of c_2 hypotheses from -3 to 3. Note that the red curves correspond to theoretical cross section predictions for each given c_2 hypothesis.
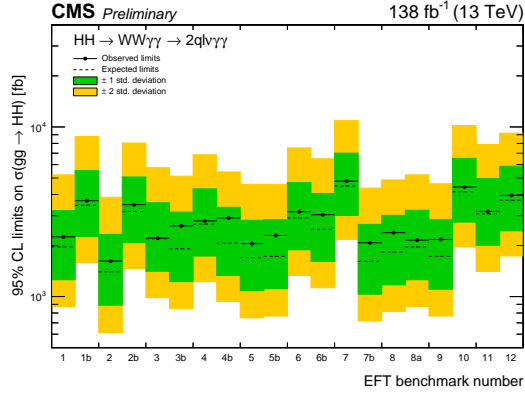
(a) Semi-Leptonic channel
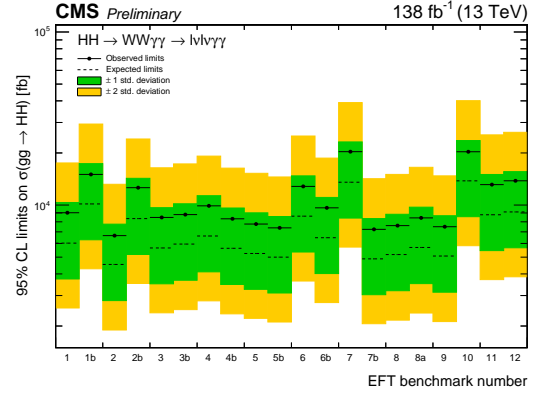
(b) Fully-Leptonic channel
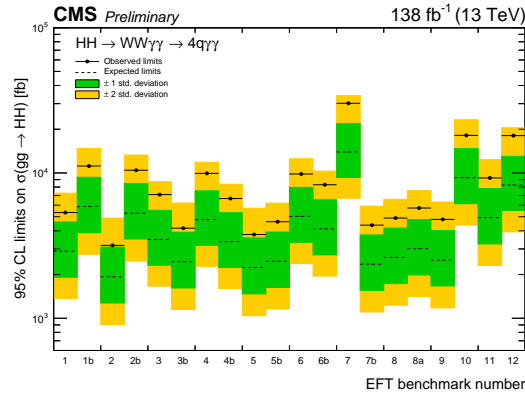
(c) Fully-Hadronic channel

Figure 4.54: Run 2 95% CL limits on HH gluon gluon fusion production for different non-resonant benchmark models defined in Table 4.1.
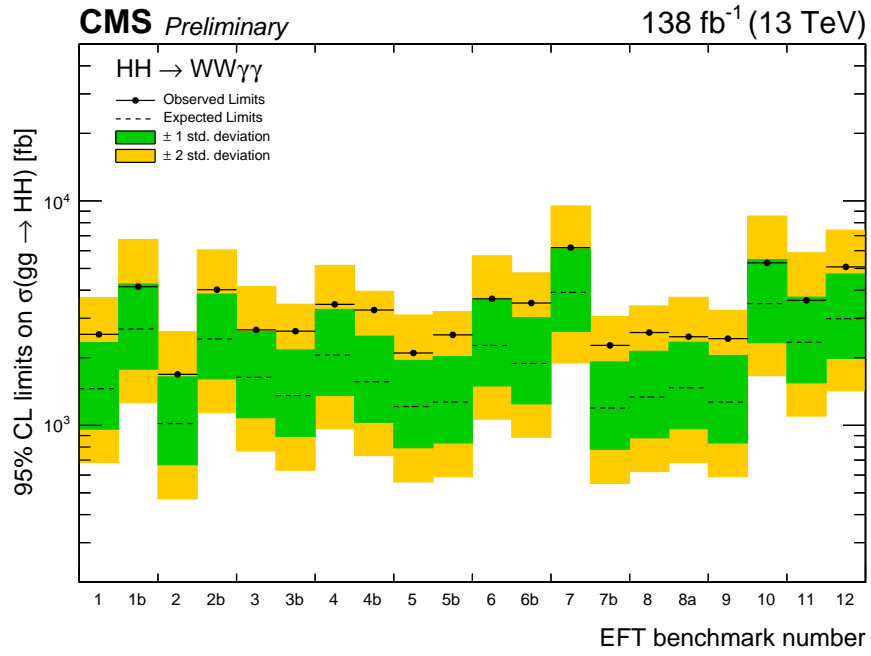
Figure 4.55: Run 2 95% CL_s limits on HH gluon gluon fusion production for different nonresonant benchmark models defined in Table 4.1.

4.9　Summary

The first search for Higgs pair production in the WW$\gamma\gamma$ final state performed by the CMS collaboration has been presented. The analysis makes use of data collected with the CMS detector between 2016 and 2018 corresponding to an integrated luminosity of 138 fb^{-1}, from proton-proton collisions at a center-of-mass energy of 13 TeV. Combining all final state categories, which makes use of all three WW decay modes, results in an observed (expected) 95% CL_s upper limit on the di-Higgs production cross-section of 3.0 (1.7) pb, corresponding to about 97 (53) times the standard model prediction. Scans of modified SM and purely BSM coupling parameters in an EFT framework result in an observed (expected) constraint on the Higgs self-coupling of -25.9 (-14.5) to 24.1 (18.4) times its standard model value, and a constraint on the magnitude of the direct coupling of two top quarks to two Higgs bosons of -2.4 (-1.7) to 2.9 (2.2) at a 95% CL_s. Additionally, observed (expected) 95% CL_s upper limits are placed on twenty EFT benchmark scenarios ranging from 1.7 - 6.2 (1.0 - 3.9) pb.

Chapter 5

Present: ECAL trigger optimization and commissioning for Run 3

While a search for Higgs pair production in the two W boson, two photon state has been performed with the LHC Run 2 dataset, it is important for CMS to continue optimizing its data-taking algorithms in order to improve this and other analysis sensitivities that will use the LHC Run 3 dataset. During LS2, the CMS ECAL trigger algorithms used during Run 2 were further developed and optimized. Additionally, there have been ongoing investigations and testing of new features of the CMS ECAL trigger for Run 3. In order for the CMS ECAL to properly operate and test these new features, a variety of operations teams are required.

This Chapter is organized as follows: In Section 5.1, the method of ECAL Trigger Primitive Generation as input to the CMS L1 trigger, and a re-optimization of its energy reconstruction algorithm for Run 3 will be described. In Section 5.2, the development and commissioning of a new ECAL feature known as "Double Weights", targeting deployment during Run 3, will be described. In Section 5.3, the various ECAL operations teams and their responsibilities, vital for the successful commissioning and operation of the CMS ECAL for Run 3, will be described.

5.1 Trigger primitive generation

ECAL provides an input to the CMS Level-1 trigger in the form of trigger primitives. It is one of several inputs to the CMS Level-1 trigger, as shown in Figure 3.30. This section is structured as follows: Section 5.1.1 will describe the composition of ECAL trigger primitives,

and section 5.1.2 will describe a re-optimization of ECAL TP generation, known as PU optimized weights.

5.1.1 ECAL trigger primitives

ECAL TPs are one of three inputs into the Layer 1 Calorimeter Trigger, shown in Figure 3.30. The basic building blocks of ECAL TPs, with the Phase-I electronics used during LHC data-taking, are "strips" composed of 5 crystals each in EB, and 1-5 crystals in EE. Every 25 ns, a digitized sample is taken of ECAL signals in every crystal, shown in Figure 5.1. During data taking, this leads to a constant stream of values measured in ADC (analog to digital converter) counts. These values are linearized to account for different gains that may be set in different amplifiers, summed within a strip. For each set of 10 linearized strip samples, a digital filter made of a set of 10 FIR (Finite impulse response) weights is multiplied by their corresponding sample values and summed to obtain a transverse energy (E_T) value, shown in Equation 5.1. In this equation, S_i represents digitized sample "i", where "i" can range from 0-10 for the 10 digitized samples taken from an ECAL pulse from 0-225ns. Additionally, w_i represents the FIR weight assigned to sample "i", which is pre-determined for each ECAL strip. A requirement on the FIR weights is that they sum to zero, in order to include a dynamic pedestal subtraction, also shown in Equation 5.1. This is performed for every subsequent set of 10 samples, with the window of 10 samples shifting 25ns forward each time, leading to a constant stream of E_T values. Additionally, a peak finder is then applied to strip sums in order to determine which BX (Bunch crossing) in a predefined window of BXs has the greatest calculated E_T value. Strip energies are then summed to form trigger towers (5 strips in EB, 1-5 strips in EE), for which TPs are formed. An ECAL TP is an E_T value of a trigger tower at a given BX, with up to two feature bits. One feature bit is the fine grain bit, and is used to distinguish EM signals from jets. In EB TPs, a bit is also reserved for the rejection on anomalous signals termed "spikes". When a BX has a TP created, the other BXs in the window are not eligible to have a TP formed. Non-zero TPs are sent to

TCC (Trigger concentrator card) boards for further processing and time alignment before being sent to the L1 trigger. A schematic showing this process and computation of strip E_T is shown in Figure 5.2.
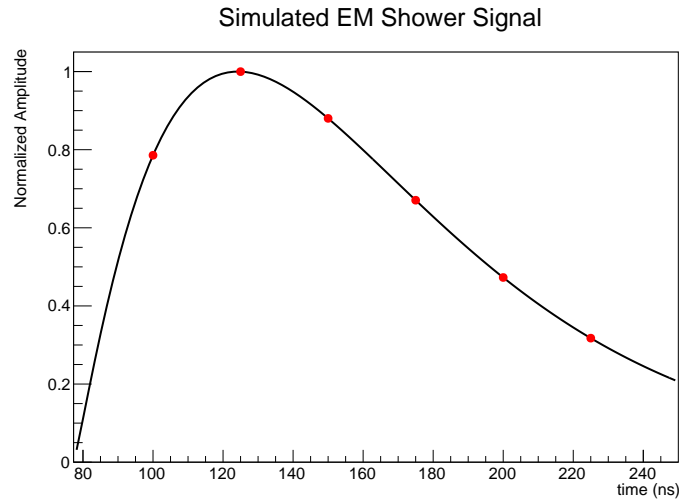
Figure 5.1: ECAL analog pulse shape example, with digitized samples taken every 25ns.

$$E_T = \sum_{i=1}^{10} S_i \times w_i \quad , \quad \sum_{i=1}^{10} w_i = 0 \tag{5.1}$$
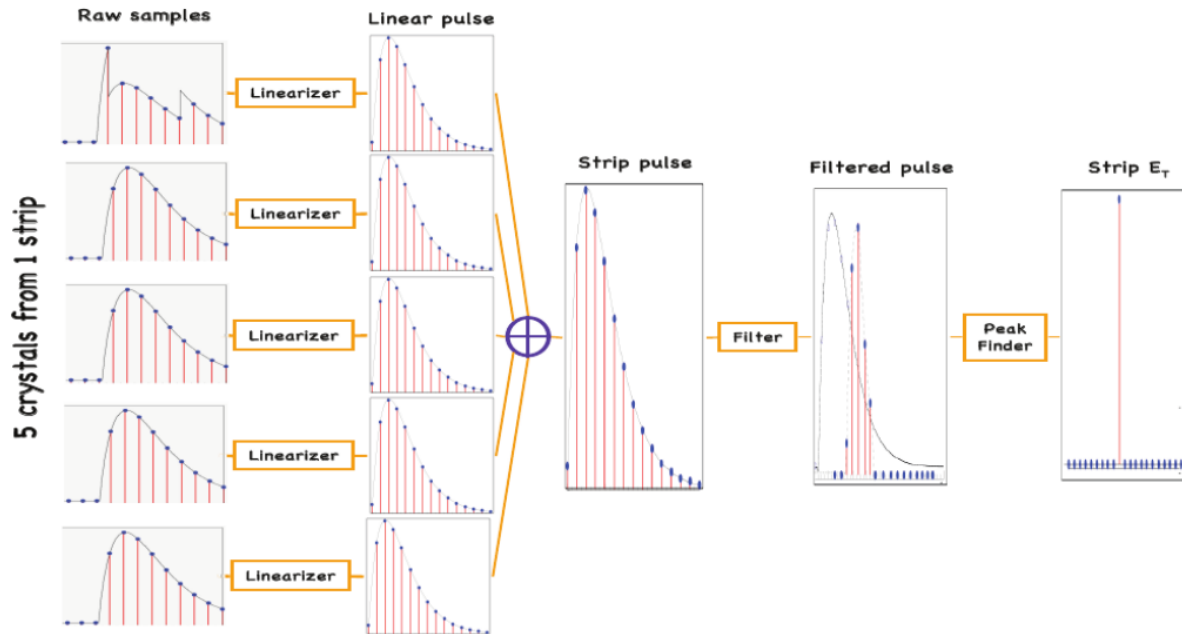
Figure 5.2: ECAL strip E_T formation.

Each ECAL TP in EB and EE is composed of an E_T value computed as the sum of its strip E_T values, information bits, and a BX assignment. ECAL TPs are created on-detector, and are transmitted to the Level-1 trigger at the LHC collisions rate of 40 MHz. Because the transverse momentum of two LHC proton bunches before colliding is 0, the detection of hits with a high E_T or p_T component is a potential sign of an interesting hard interaction between protons, and thus is a quintessential quantity to consider when forming an L1 decision.

5.1.2 PU optimized weights

Throughout Runs 1 and 2, two sets of amplitude weights were used when computing ECAL strip energies and hence TP energies, one for EB and one for EE, shown in Figure 5.3.

sample	1	2	3	4	5	6	7	8	9	10
EB	0	0	-0.5625	-0.546875	0.25	0.484375	0.375	0	0	0
EE	0	0	-0.65625	-0.515625	0.25	0.515625	0.40625	0	0	0

Figure 5.3: Run 1 and 2 ECAL FIR weights

These FIR weight values were obtained from ECAL pulse shapes measured in test beams, as for a given waveform shape, an optimal set of weights can be extracted for measuring the waveform's height.

One way to simulate the photo-detectors' response to crystal scintillation is with an analytic waveform. The function used to simulate the time evolution of the detector response for each crystal is the alpha-beta function defined in Equation 5.2.

$$f(t) = \begin{cases} f(t) = A * \left(1 + \dfrac{(t - t_0)}{(\alpha\beta)}\right)^{\alpha} * e^{\frac{-(t-t_0)}{\beta}} & t > (t_0 - \alpha * \beta) \\ 0 & t \leq (t_0 - \alpha * \beta) \end{cases} \qquad (5.2)$$

In this equation, A is the height of the waveform in ADC counts, t_0 is the time of the waveform's peak in nanoseconds, α describes the behavior of the polynomial term, and β corresponds to the decay time in the exponential term. The pedestal (P) can also be set, giving the full analytic form of the detector response shown in Equation 5.3.

$$G(t; P) = f(t) + P \qquad (5.3)$$

With dedicated fine grain time scans performed on ECAL signals, the parameters A, t_0, α and β were measured for each crystal during Run 2. These scans were performed in October 2017, June 2018, and September 2018, and a variation of the parameters among the crystals can be seen over time due to the ageing of ECAL crystals caused by steady dosages of radiation from LHC collisions.

By producing and sampling these waveforms and applying the Run 2 FIR weights to the samples, one can simulate the reconstructed amplitude of the ECAL TPs as a function of pseudorapidity (η). A fractional amplitude bias, defined as the percent difference between the reconstructed amplitude, $\hat{A}$ and the true amplitude A and shown in Equation 5.4, is shown as a function of η in Figure 5.4 [51; 52].

$$\text{bias} = \frac{\hat{A}}{A} - 1 \tag{5.4}$$
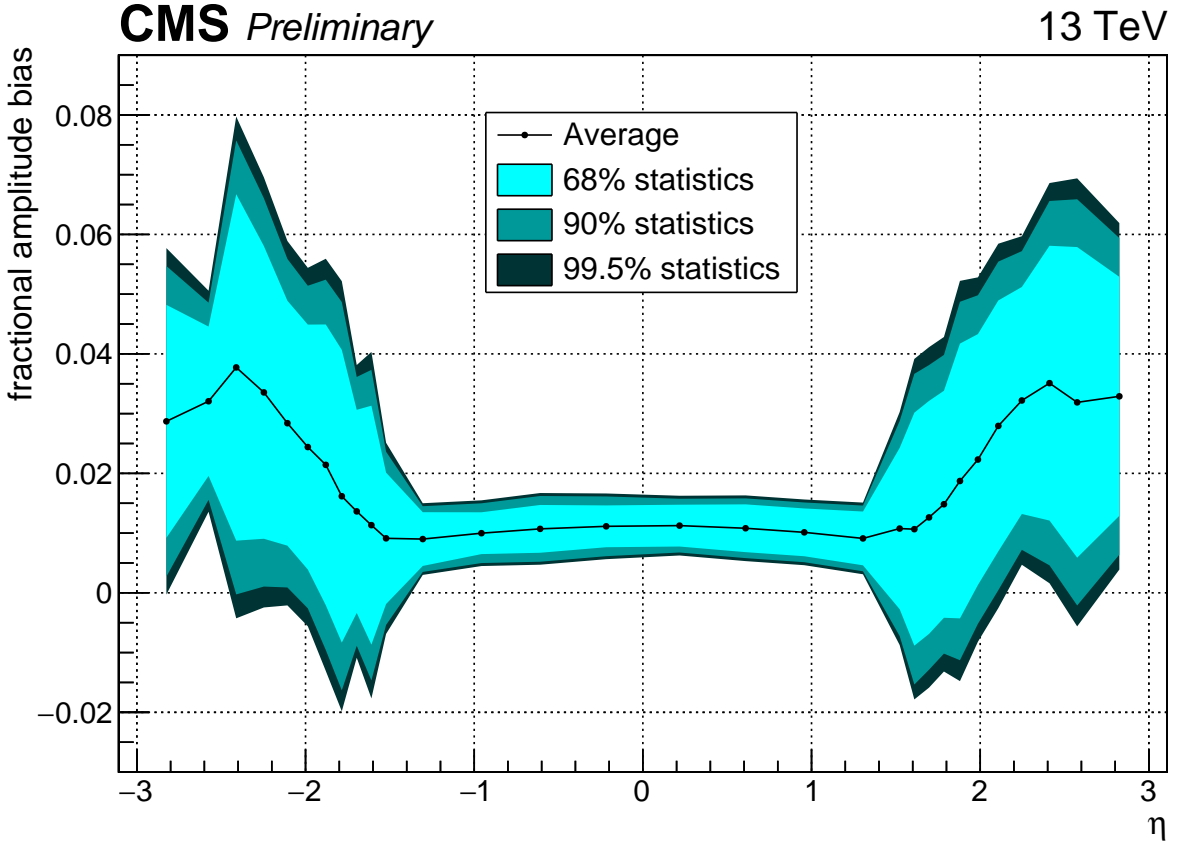
Figure 5.4: Average bias vs. η, with no simulated time shift (ts = 0ns), using September 2018 parameters for detector response and Run 2 weights for reconstruction.

It can be seen from this result that there is a bias in the reconstructed amplitude, particularly in the high-η region where a greater average and spread of bias is present. In the

high-η region occupied by the EE, the average fractional amplitude bias is about a factor of three larger than that in the EB region. This is consistent with the fact that ECAL crystals in the high-η region receive more radiation from LHC collisions, and therefore their crystals and corresponding waveforms are more distorted and stray further from their original shapes use to derive their FIR weights. This indicates that a more ideal set of weights can be produced in order to produce more accurate TPs. This motivates the derivation of new amplitude weights to see if a reduction in bias average and spread can be made.

In order to derive updated amplitude weights, a simulation of ECAL electronics' response to scintillation light was setup from the most recent timing scan data obtained in September 2018, including a realistic PU scenario which depends on η, and distorts the in-time ECAL pulses. Using the alpha-beta analytic waveform to model each crystal's response, and taking a realistic PU energy spectrum and LHC proton bunch train into account (48b7e), the fractional spread of energy biases was computed as a function of signal BX shown in Figure 5.5 for ECAL EB crystals with $|\eta| < 0.7$, and for EE crystals with $2.3 < |\eta| < 3.0$ in Figure 5.6 [53; 54]
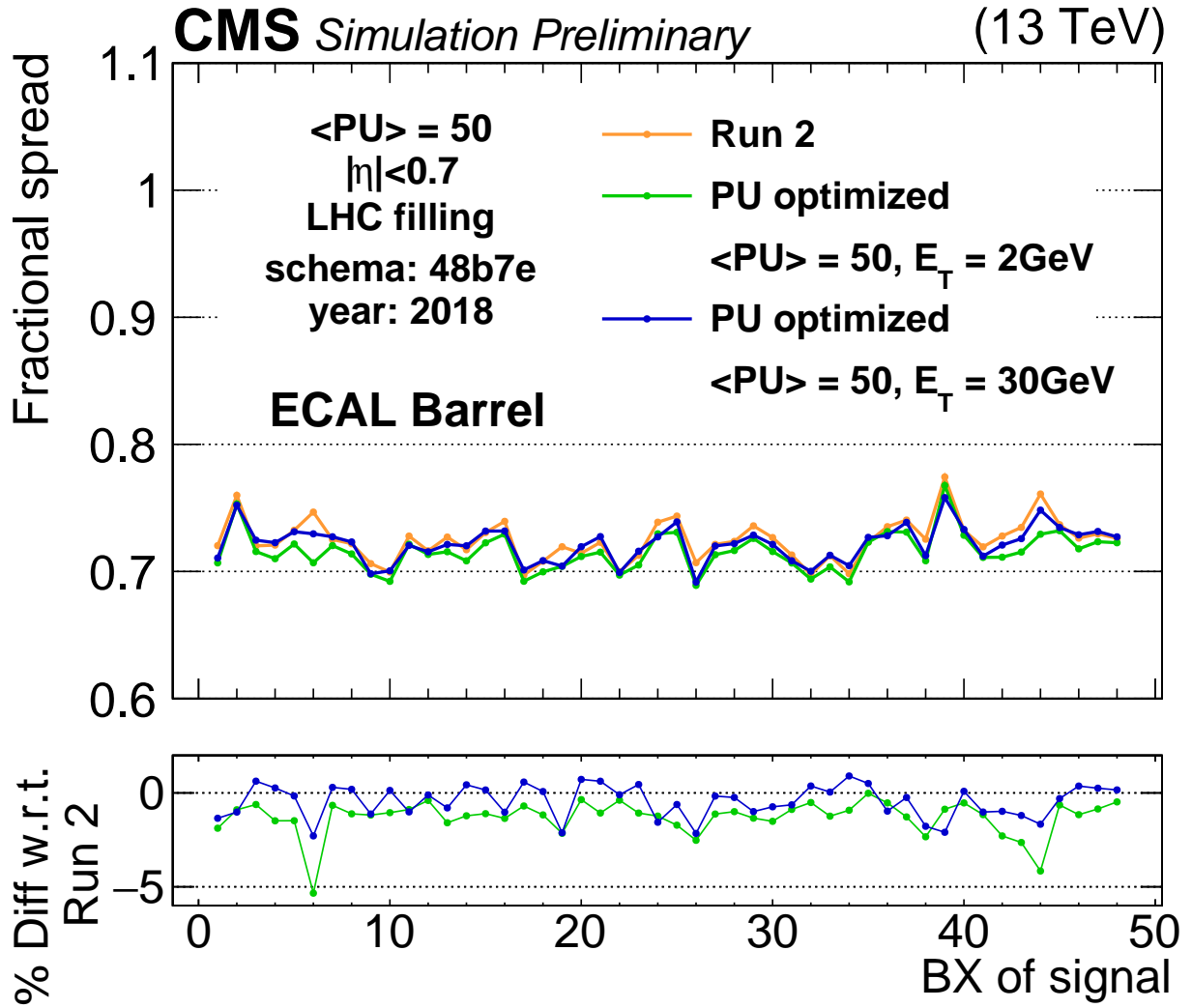
Figure 5.5: Fractional spread of amplitude bias for simulated ECAL crystal responses in the region $|\eta| < 0.7$.
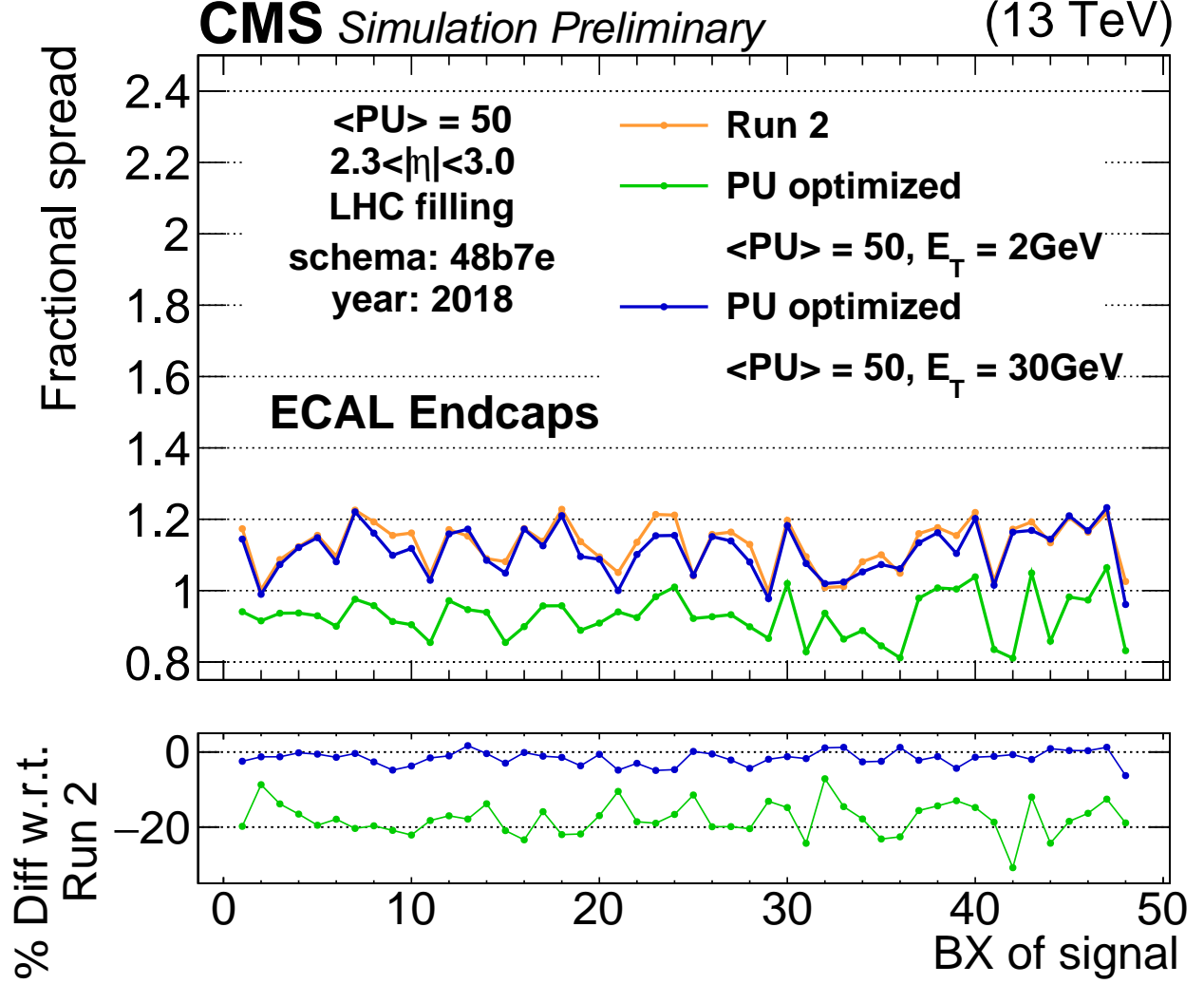
Figure 5.6: Fractional spread of amplitude bias for simulated ECAL crystal responses in the region $2.3 < |\eta| < 3.0$.

For both ECAL regions, fractional spread is shown when reconstructing amplitude with the Run 2 weights, PU optimized weights optimized for a strip E_T of 2 GeV, and for a strip E_T of 30 GeV. In the EB region, an improvement in fractional spread of about 1% is obtained with respect to Run 2 weights when using weights optimized for PU and $E_T = 2$ GeV. In EE, a more drastic improvement of about 15-20% is obtained with respect to Run 2 weights. This is consistent with Figure 5.4, which shows there is more room for improvement in EE compared to EB.

This indicates that updating the existing EB and EE FIR weights may improve the spread

of fractional bias in TP E_T computation. The effect of updated ECAL TP FIR weights on Level-1 quantities, and further evaluation of the potential gain from updating the ECAL L1 amplitude weights to account for changes in ECAL pulse shapes due to ageing and PU is currently being studied and tested in an effort to improve ECAL for Run 3. A potential positive impact of improved ECAL TP resolution is an increase in the L1 tagging efficiency of electron and photon objects, which can potentially increase the efficiency of triggering on HH→WW$\gamma\gamma$ events, and events with similar signatures, at the CMS detector.

In addition to amplitude weights, sets of timing sensitive weights can also be derived. Instead of returning an amplitude when multiplied by waveform samples, these return timing jitter, defined as the time displacement from the expected peak time. These ideal sets of weights are derived to return a bias of 0 when the input waveform is the one they were derived from. Therefore, the effectiveness of these two types of weights can be shown by plotting their bias when different time shifts are applied, defined as a translation of the waveform left or right. For example, a time shift of 5 ns means t_0 would go from t_0 to $t_0 + 5ns$. The average fractional amplitude and time biases as a function of time shift are shown in Figures 5.7a and 5.7b.
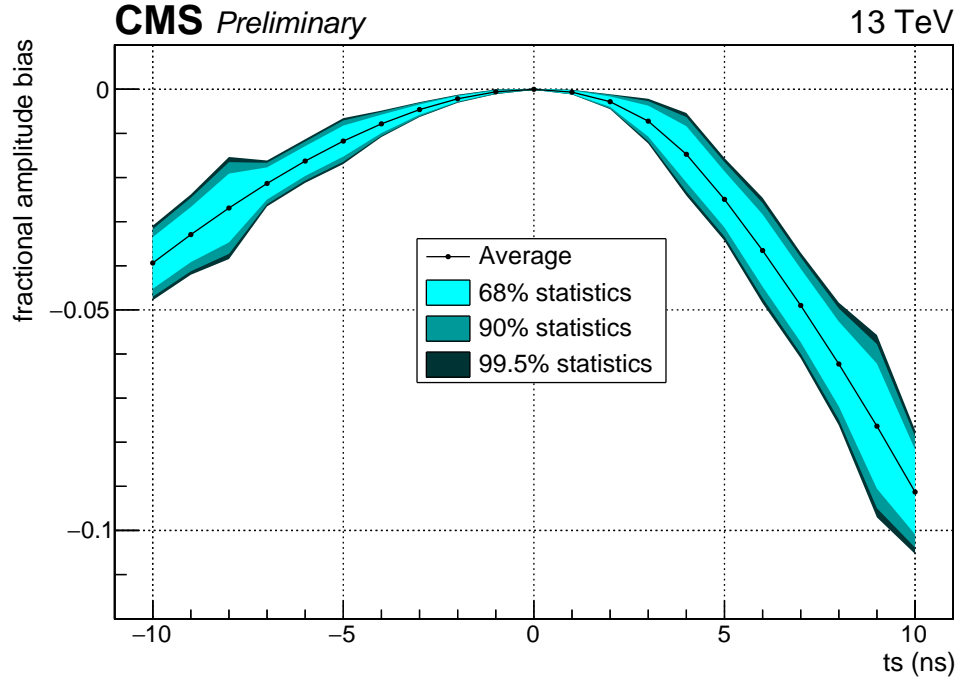
(a) Average amplitude bias vs. time shift
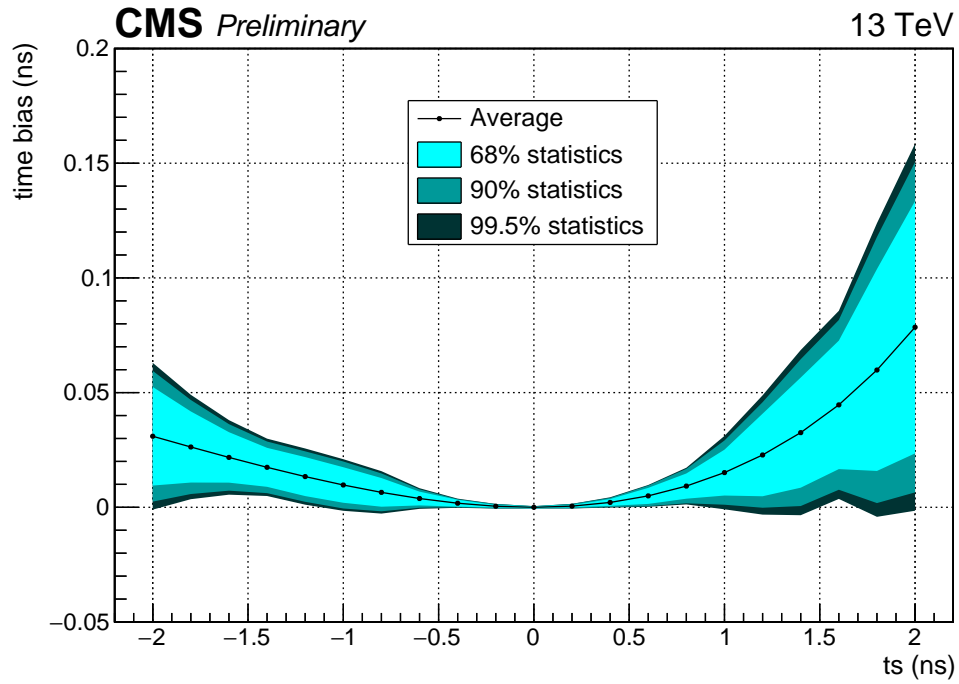
(b) Average timing bias vs. time shift

Figure 5.7: (a) Amplitude and (b) time bias vs time shift for ECAL waveforms, using September 2018 parameters for detector response and ideal weights for reconstruction, for crystals in the η region: $(-3.0, -2.6)$

For time shifts of 0, there is no bias in amplitude or timing weights because the weights were derived for each non-time-shifted waveform. Because the bias is not large for small time shifts, ideal weights can be considered worth investigating.

5.2 Double weights

Throughout LHC Runs 1 and 2, the on-detector ECAL FENIX chip, a custom ASIC, was used for energy reconstruction to form E_T sums for ECAL TPs, multiplying one set of weights by recorded digis as described in Section 5.1.1. During LS2, it was discovered that the ECAL FENIX chip has the capacity to store and use two sets of weights. This essentially duplicates the ECAL FENIX data path, as shown in Figure 5.8, into two electronically equivalent paths, one for each FIR filter named the "EVEN" and "ODD" filters.
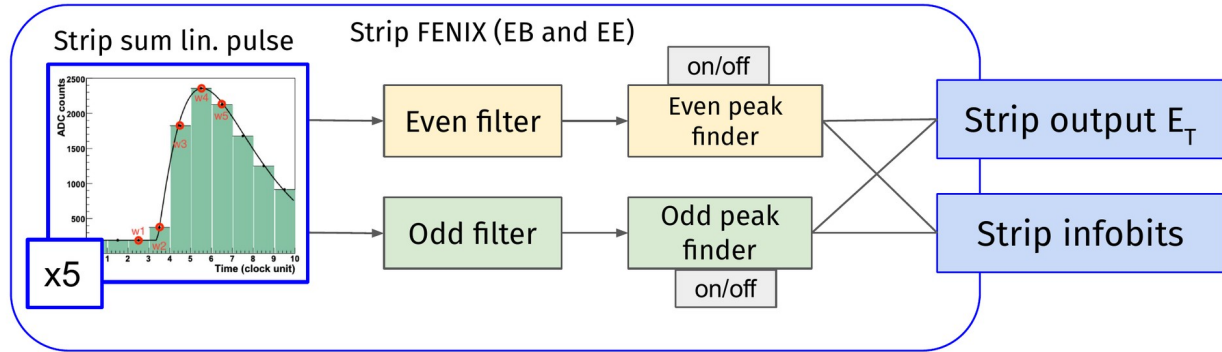
Figure 5.8: ECAL double weights mechanism.

This feature was implemented in the ECAL FENIX chip for potential further use, but was never used during Runs 1 and 2.

5.2.1 Spikes

A commonly observed phenomenon at the ECAL is the direct ionization of the ECAL EB APDs, which produce anomalous signals termed "spikes". Because these signals do not come from electromagnetic showers originating from the hard interactions of LHC collisions, they

must be removed as efficiently as possible to keep trigger rates under control and preserve the quality of the offline reconstruction of electrons, photons and jets. Additionally, spike progenitors often spend time propagating in the CMS detector before directly ionizing the EB APDs, and therefore may be out-of-time with respect to electromagnetic signals.

There is a method in place used to remove spikes at L1 using a topological cut, termed the "spike killer" [55]. This operates by making a topological cut, exploiting the fact that spikes typically deposit all of their energy into a single ECAL crystal as they are due to the direct ionization of APDs, while EM showers are expected to be spread among multiple crystals. A diagram showing the mechanism of the spike killer is shown in Figure 5.9.
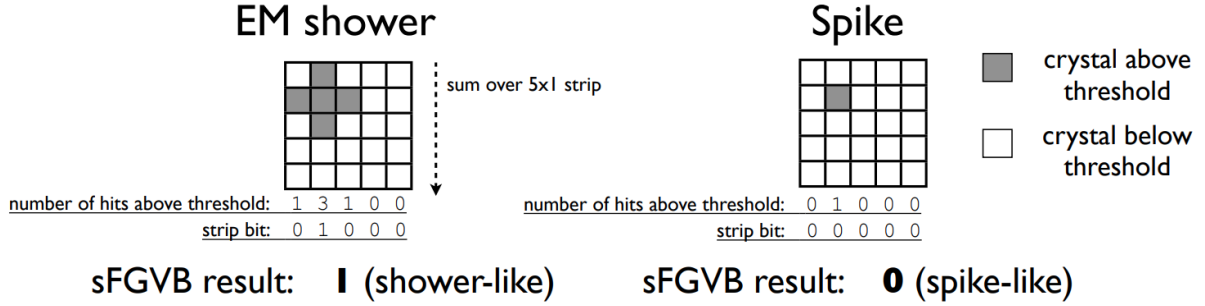
Figure 5.9: Operation of the strip Fine-Grained Veto Bit (sFGVB) on an electromagnetic shower (left) and a spike-like energy deposit (right).

The spike killer makes use of a per-strip bit, the strip Fine-Grained Veto Bit (sFGVB) which is set to 1 if at least 2 crystals in a strip are above a per-crystal energy threshold. If a trigger tower (set of 25 crystals, 5 strips) has at least one strip with a sFGVB equal to 1, it is preserved as it is considered EM shower-like due to its spread in energy. However, if a TT has no strips with at least one sFGVB set to 1, the TP energy is set to 0 if its energy is above the spike killer "killing threshold" of 16 GeV.

In order to optimize the spike killer for Run 3 where higher noise and everage PU is expected, the per-crystal energy threshold was increased, as there will be a higher expected contribution from noise and PU for all crystals. The spike contamination among TPs with the Run 2, and candidate Run 3 working point is shown in Figure 5.10. Notably in this spike

contamination plot, produced using data from a ZeroBias dataset (no triggering on typical physics menus), there is a high spike contamination at high energy. This is because it is more likely to produce a high energy spike, which are high energy due to its direct ionization of the APDs, than a high energy EM shower, which requires the production of a truly high energy particle from proton-proton interactions.
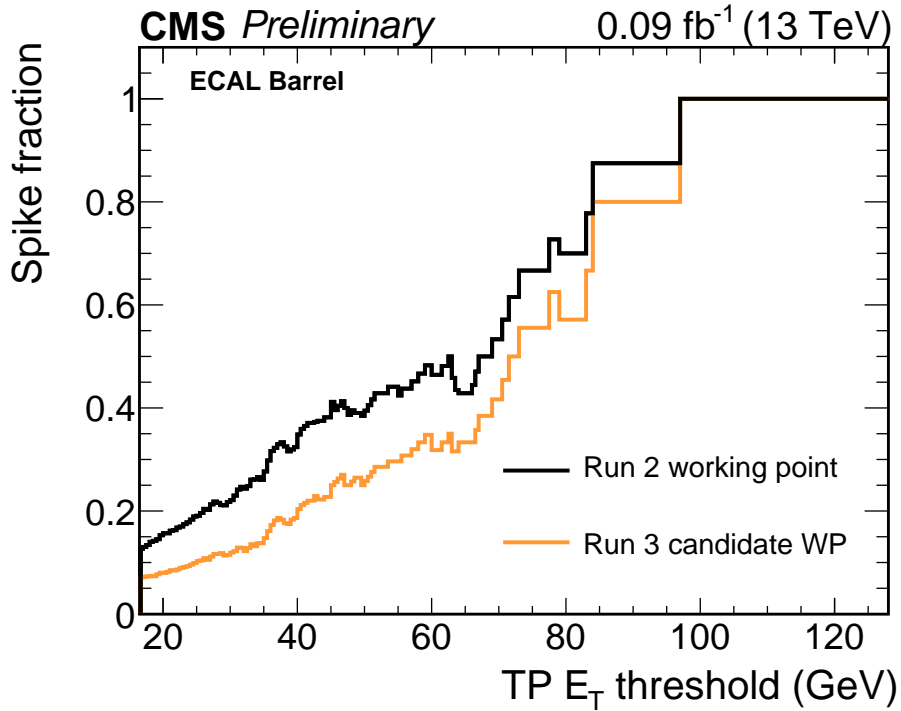
Figure 5.10: Spike fraction vs. TP E_T threshold with a Run 2, and Run 3 candidate working point of the existing ECAL L1 spike killer. The data comes from a ZeroBias dataset recorded in July 2018 with a peak pileup of 50.

This shows that while updating the settings of the existing spike killer to a candidate Run 3 working point removes additional spikes at Level-1, there is much room for improvement, especially in the high energy regime. Additionally, at L1 there is no existing spike killer in the low energy regime 0-16 GeV, as this is below the spike killer threshold.

5.2.2 Timing weights

The initial idea for optimizing ECAL double weights was to keep the original set of amplitude weights in the EVEN filter, and to utilize the second set of weights, the ODD filter, as a set of timing weights in order to compute an on-detector timing value for trigger primitives. These studies showed possible discrimination power, as the timing weights were able to identify out of time signals which came from spikes. Figures 5.11 and 5.12 show the reconstructed amplitude computed as the EVEN weights times signal digis, vs. the reconstructed time as computed by multiplying a set of optimal timing weights occupying the ODD filter by signal digis for signal and spike-like TPs in CMS data.
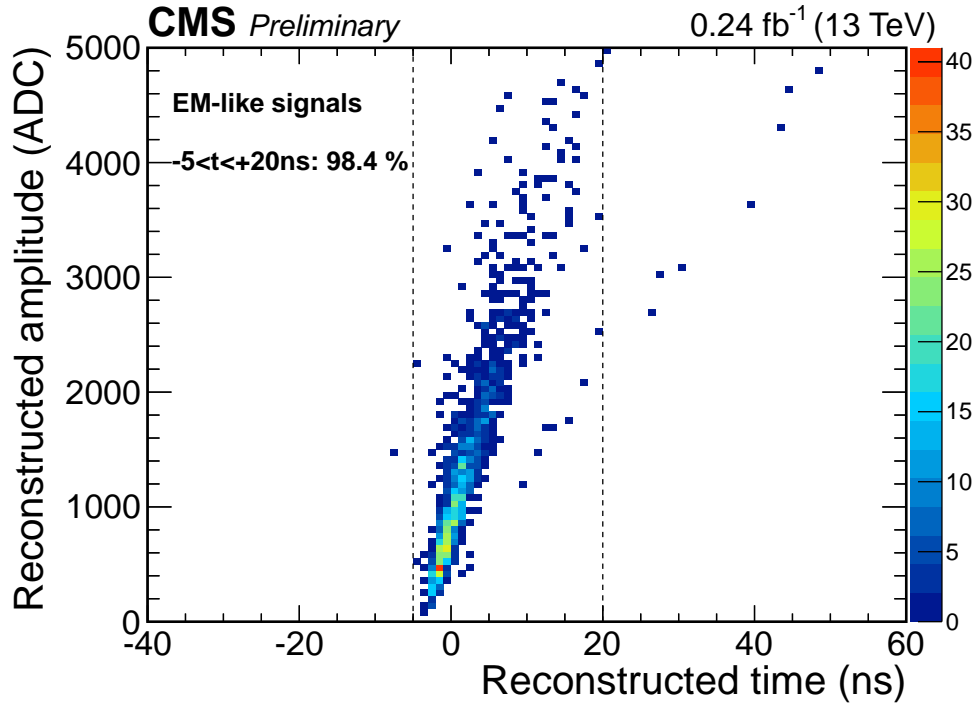
Figure 5.11: Reco amplitude vs. Reco time of EM-like signals in CMS data
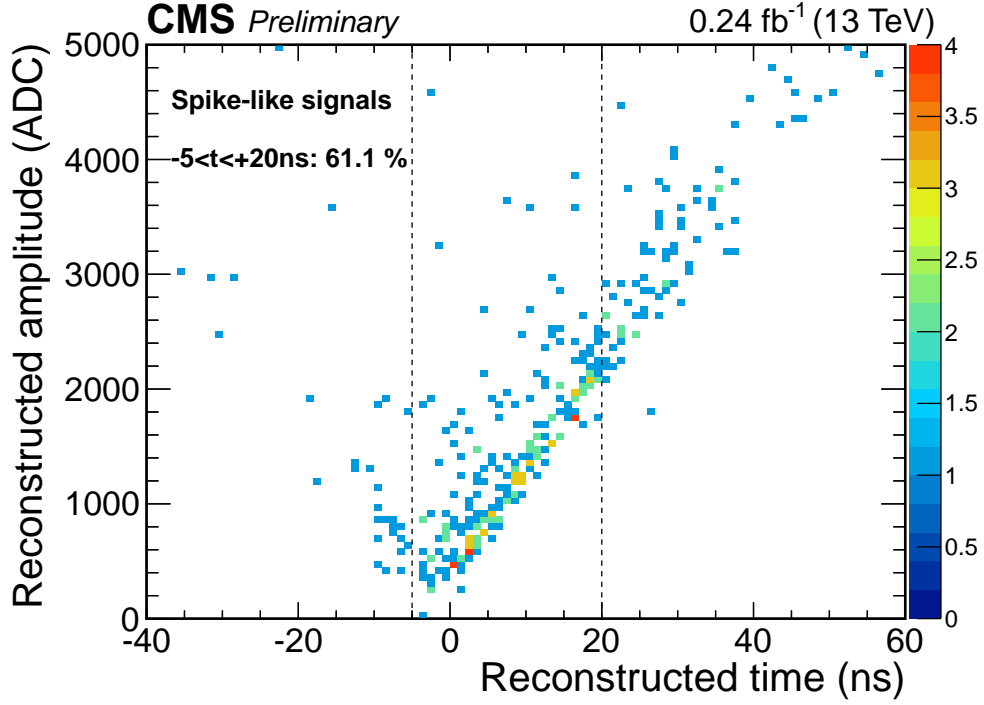
Figure 5.12: Reco amplitude vs. Reco time of spike-like signals in CMS data

By eye, most EM-like signals fall within a reconstructed time window near zero, with a tail going out to around 20 ns for signals with a greater reconstructed amplitude. For spike-like signals, there is a larger time window with some TPs very out-of-time. Interestingly, in the EM-like signals on Figure 5.11 one can see a low population line of entries which appears to follow the trend of the spike-like signals in Figure 5.12, as these are possibly real spikes which are incorrectly tagged offline as signal-like.

For the sake of quantifying the possible discrimination power of ECAL timing weights, a hypothetical timing cut of -5 < t < 20 ns would have been able to drastically reduce the rate of spikes, as shown in Figure 5.13.

(a) Spike Rates

(b) Spike Fractions
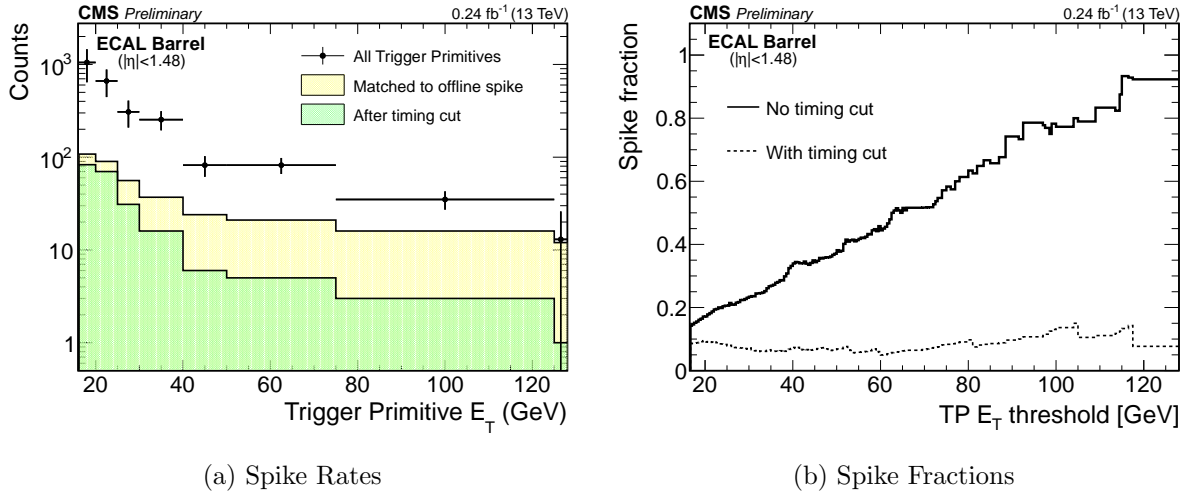
Figure 5.13: Spike quantities with/without timing cut [EcalDPGResults],[CDS]

A timing cut like this is not possible in the ECAL FENIX chip; However this study motivated the idea to use two sets of amplitude weights and a comparator in the FENIX chip in order to identify out-of-time signals with double weights.

5.2.3 Optimization

In the ECAL FENIX chip, it is possible to compute two amplitudes via two sets of weights, and utilize a comparator in the electronics to set a boolean flag if one amplitude output is greater than the other. If an ODD set of weights is optimized to identify out of time signals, it is expected to returns a greater amplitude for out-of-time signals than the Run 2 weights designed for in-time signals. Therefore, the approach is taken to optimize an ODD set of weights for out-of-time signals.

Choosing an odd set of weights for out-of-time signal tagging is a multivariate problem, which must consider a realistic signal energy spectrum, spike energy spectrum, spike timing PDF, and the effects of pileup on signal waveform distortion. Therefore in order to extract ODD weights sets which are optimized to maximize signal efficiency and spike rejection, a numerical optimization was setup in order to derive optimal sets of weights to take the place

of the second FIR filter weights. This optimization makes use of simulated signal waveforms using the alpha-beta analytic representation and simulated pileup described in Section 5.1.2, and the simulation of spike waveforms from a standalone simulation. The optimization is setup as a loss minimization problem which makes use of gradient descent computation and backwards propagation of loss to maximize the amount of spike rejection, while minimizing the amount of signal rejection. This is incorporated in a loss definition, shown in Figure 5.14.

$$L = (\lambda_{Signal} \times L_{SigEff}) +$$
$$(\lambda_{Spike} \times L_{SpikeRej}) +$$
$$(\lambda_{Norm} \times W2LossNorm) +$$
$$W2LossLimit$$

$$L_{SigEff} = \begin{cases} if((A_{w2,d1} - A_{w1,d1}) \geq \delta_{\min}): & (A_{w2,d1} - A_{w1,d1}) \\ if((A_{w2,d1} - A_{w1,d1}) < \delta_{\min}): & 0 \end{cases}$$
$$L_{SpikeRej} = \begin{cases} if((A_{w1,d2} - A_{w2,d2}) \geq \delta_{\min}): & (A_{w1,d2} - A_{w2,d2}) \\ if((A_{w1,d2} - A_{w2,d2}) < \delta_{\min}): & 0 \end{cases}$$

$$W2LossLimit = \begin{cases} if\left(\sum_{i=1}^{5}|w_{2,i}| < 1\right): & 0 \\ if\left(\sum_{i=1}^{5}|w_{2,i}| \geq 1\right): & \sum_{i=1}^{5}|w_{2,i}| \cdot (-100) \end{cases}$$

(a) Loss function   (b) Use of δ_{min} in loss   (c) Definition of ODD weights loss limit.

Figure 5.14: Loss definition used in optimization of ODD set of amplitude weights.

One of the input parameters in the optimization is a minimum separation of the two amplitude values computed by the EVEN (default weights) and ODD (out-of-time sensitive) sets of weights, termed δ_{min}. Varying this parameter results in different working points. The different portions of a simulated spike timing PDF which were tagged as out of time by different working points is shown in Figure 5.15 [56; 57].
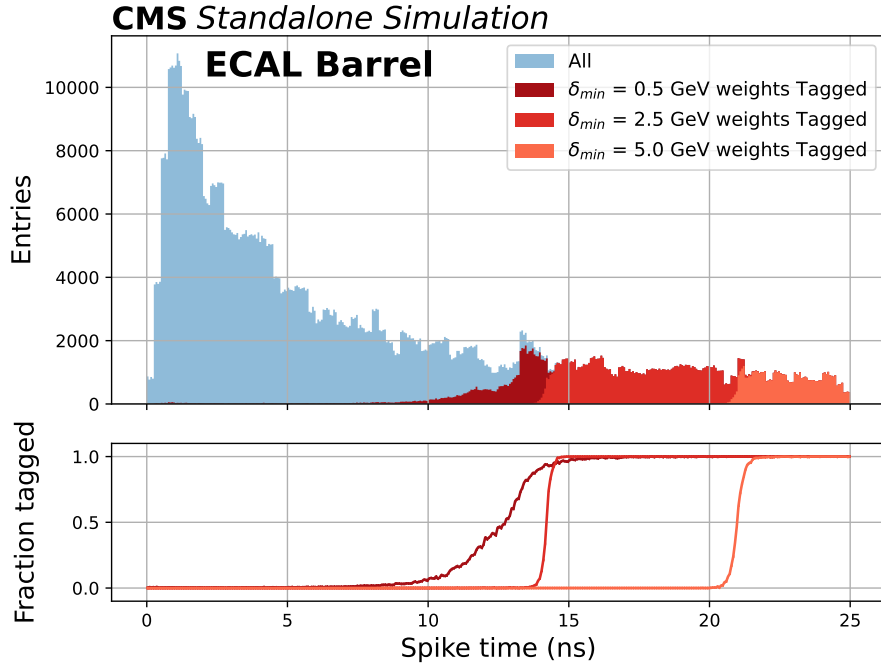
Figure 5.15: Tagging of out of time spikes in a standalone simulation.

In the spike timing PDF, most spikes are relatively in-time with respect to EM signals, while a non-negligible fraction have a late out of time tail. The reason for this is because spike progenitors often spend time propagating in the CMS detector before directly ionizing the EB APDs. It can be seen that increasing the value of the δ_{min} parameter tags later out of time spikes. This is somewhat expected, as a larger δ_{min} value will only use spike examples with larger differences in EVEN and ODD amplitudes in its optimization, which is more likely to come from out-of-time shifted spikes.

While quantifying the expected gain in spike rejection from different δ_{min} working points, it is also important to check their effect on EM shower-like signals, as shown for a standalone simulation in Figure 5.16.
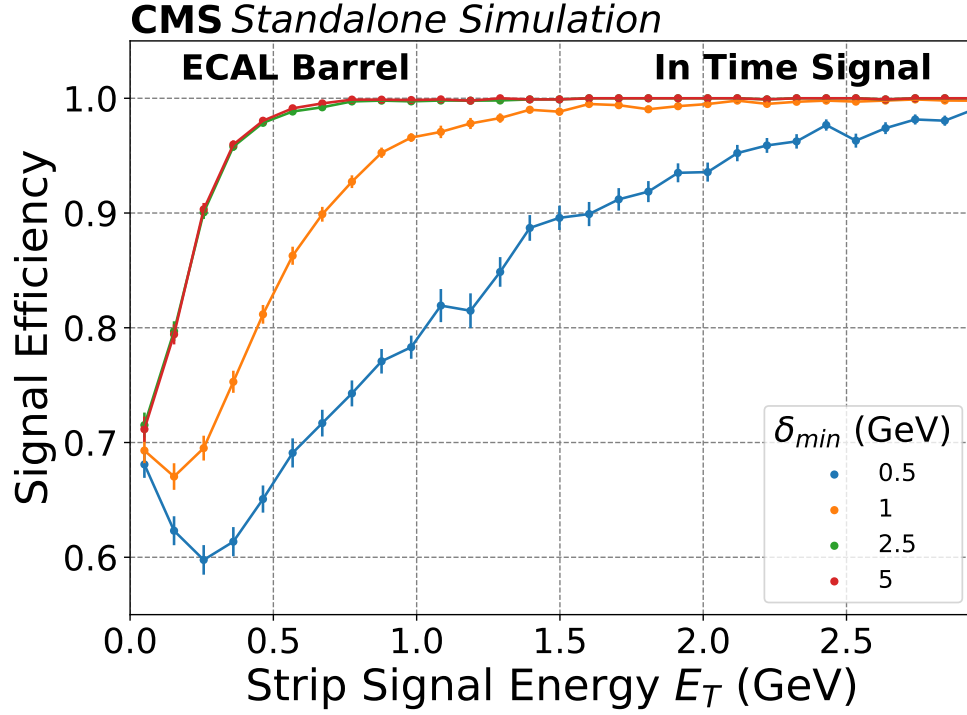
Figure 5.16: Signal efficiency vs. signal energy using a standalone simulation and simulation of ECAL double weights algorithm.

It is observed that increasing the δ_{min} parameter value results in higher signal efficiency, as expected for the same reason that a greater spike rejection is observed for greater δ_{min} values: Only signal and spike waveforms which exhibit larger differences in EVEN and ODD amplitudes are used for weight optimization, leading to weights which are more optimized for very different waveforms and therefore less likely to touch signal waveforms. In order to identify a reasonable trade-off between signal efficiency and spike rejection, the resulting efficiencies are rejections for different δ_{min} working points is shown in Figure 5.17, where only signals with $E_T \leq 3$ GeV are considered as simulated signals with $E_T > 3$ GeV have an efficiency near 100%. Additionally, only spikes with a timing greater than 10 ns are considered, as these working points are not effective at tagging in-time spikes.

It is shown that moving from the $\delta_{min} = 2.5$ GeV to 5.0 GeV working point returns a minimal gain in signal efficiency (0.1%), while a large fraction of spike rejection is lost (43.3%). This indicates that the $\delta_{min} = 2.5$ GeV working point provides a good compromise

δ_{min} (GeV)	Signal efficiency (%)	Spike rejection (%)
0.5	78.2	77.6
2.5	95.6	62.5
5.0	95.7	19.2

Figure 5.17: Signal efficiency and spike rejection for different δ_{min} working points.

between signal efficiency at low E_T and overall spike rejection.

5.2.4 Re-emulation of 2018 data

One of the ways to test new features during a long shutdown period when no new data is being taken is be re-emulating previously recorded data. As double weights were an undiscovered feature, they were not present in the CMS ECAL emulator. After verifying the existence of this feature in hardware through tests at CERN building 904 and at the CMS ECAL itself, the now confirmed second amplitude filter was added as a possible configuration in the CMS emulator [58].

After including this implementation in the centrally used CMS software, 2018 CMS data was re-emulated using ECAL double weights in order to see how this would have affected data-taking. Double weights were run in "Killing mode", meaning that if an ECAL strip has a higher ODD amplitude than EVEN amplitude, its energy is set to zero. The idea behind this is to zero spikes which are often out-of-time, while trying to minimize the zeroing of signals which are in-time.

In order to categorize ECAL TPs in data as signal-like or spike-like, an offline "Severity" assignment is used. Each EB TT (Trigger tower) is composed of 25 ECAL crystals. An offline energy computation is performed for each crystal in highly energetic regions of events with an L1A, called a reconstructed hit or "rec hit". In addition, a timing value is computed for each reconstructed hit, and a "severity" level is assigned. A severity level of 0 corresponds to a reconstructed hit which does not appear problematic in the data. A severity level of 3 means a reconstructed hit is identified as out-of-time based on its reconstructed timing value, and a

severity level of 4 means a reconstructed hit satisfies at least one of the following: Identified as out-of-time based on its reconstructed time value, fails a topological cut, known as a "swiss-cross" cut. Because spikes come from isolated APD hits, rather than from a spread-out EM shower with energy spread over a group of ECAL crystals, spikes usually have their energy fully deposited in one crystal and are identified using a swiss cross variable, shown in Figure 5.18a. Thus, severity zero (four) reconstructed hits typically correspond to signal-like (spike-like) hits shown in its respective region of reconstructed time vs. swiss-cross score in Figure 5.18b [59; 60].
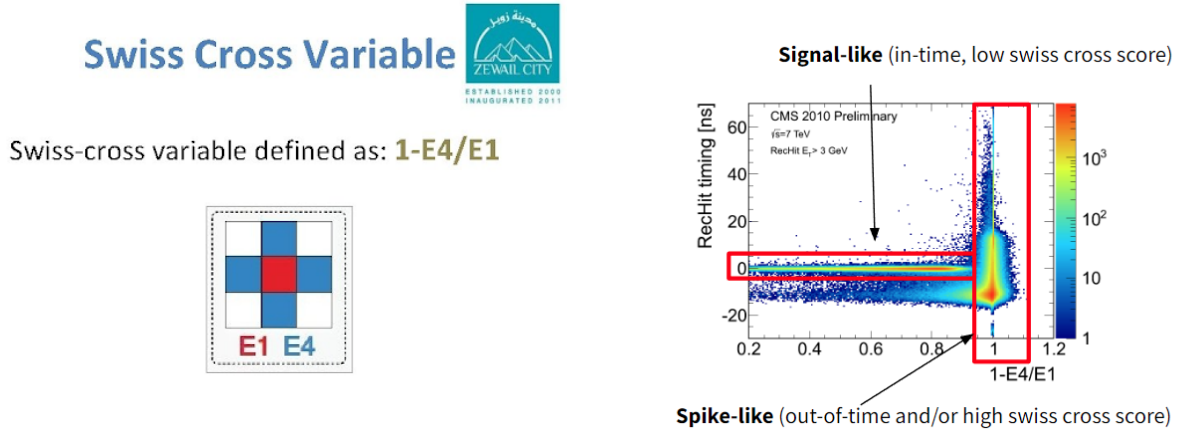
(a) Swiss cross definition, illustrated by the energy hits in a 3x3 ECAL crystal portion. E1 = energy of the central crystal, E4 = sum of the energies of the central crystal's four surrounding neighbors.

(b) Reconstructed time vs. swiss cross score

Figure 5.18: Swiss cross definition, and reconstructed hit timing vs. swiss cross score from a 2010 CMS data sample.

In order to assign a severity level and reconstructed time to an EB TP, the severity level and reconstructed time of the highest energy reconstructed hit in a given TP is assigned to that TP, as shown in Figure 5.19. In this example TP with reconstructed crystal energies in arbitrary units, the highest energy reconstructed hit is in Strip 3, crystal 0 as its value is 201, and thus this TP is assigned the timing and severity of this crystal.

EB Trigger Tower

	XTAL 0	XTAL 1	XTAL 2	XTAL 3	XTAL 4
Strip 0	0	0	5	0	0
Strip 1	1	8	12	0	1
Strip 2	53	20	27	0	0
Strip 3	201	6	15	0	1
Strip 4	0	1	0	1	0

Highest energy recHit in TT
TT assigned offline **time** and **severity** of **this recHit**
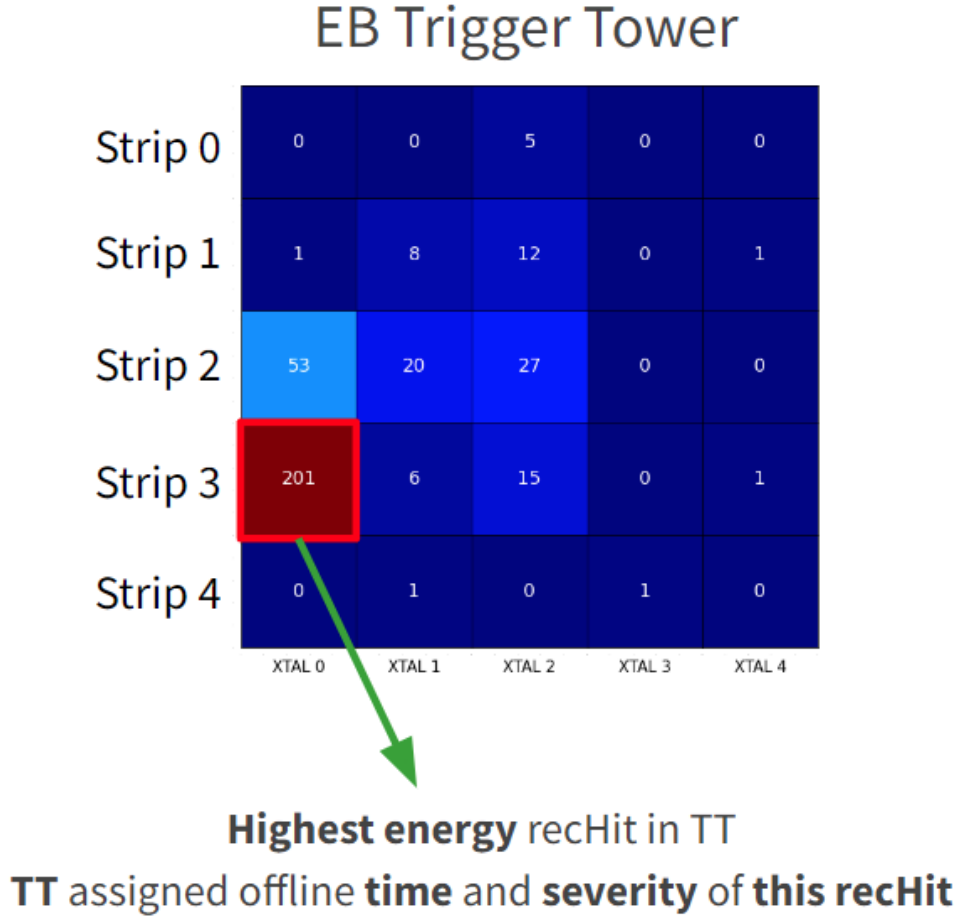
Figure 5.19: Reconstructed hit matching to TP. Crystal energy units are arbitrary.

In the re-emulation of 2018 CMS data, the resulting 1 - emu/real distributions, where emulated energy includes double weights in killing mode, and real energy corresponds to the energy of the TP from data with no double weights applied, are shown in Figure 5.20 for signals (TPs assigned to severity 0 reconstructed hits) which are in time (matched reconstructed crystal hit time $|t| < 3$ns), and spikes (TPs assigned to severity 4 reconstructed hits) which are out-of-time (matched reconstructed crystal hit time $t > 10$ns).
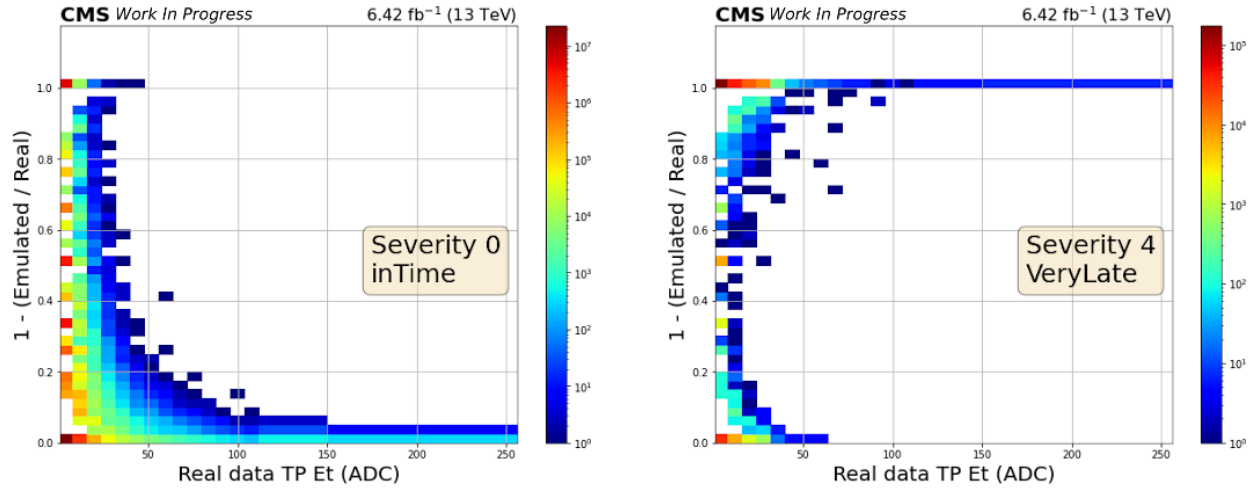
(a) 2018 CMS data re-emulation, in time severity zero energies in killing mode

(b) 2018 CMS data re-emulation, very late severity four energies in killing mode

Figure 5.20: 2018 Data reemulation with double weights in killing mode.

This shows that relatively high energy spikes, greater than about 50 ADC (25 GeV), are being mostly zeroed, shown by the fact that the 1 - emulated / real is close to one, meaning the emulated (TP energy with double weights in killing mode) energy is nearly zeroed. There is also a non-negligible amount of zeroing being applied to in-time signals, as the per y-slice distributions show some entries greater than 0.

To check the timings of TPs which have some energy subtracted by double weights in the full timing range, not just restricted to in time and very later, we can observe the data TP vs. its offline assigned time for all TPs shown in Figures 5.21a and 5.22a, and for TPs in which at least 90% of energy is removed by double weights in killing mode in figures 5.21b and 5.22b. For both severity categories, a line is drawn at 32 ADC, equivalent to 16 GeV for ECAL TPs, as this is the spike killing threshold as defined in Section 5.2.1.
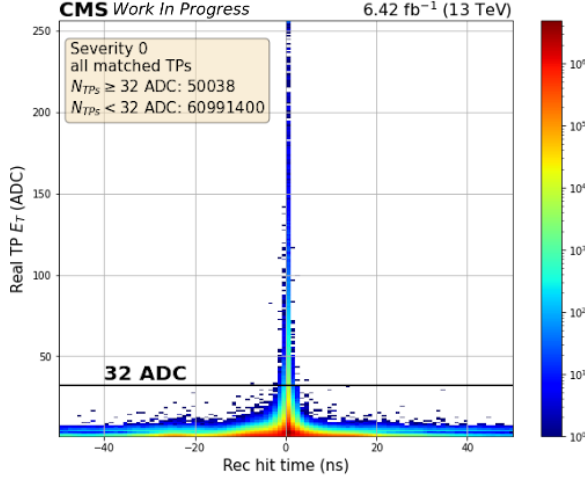
(a) All severity zero TPs
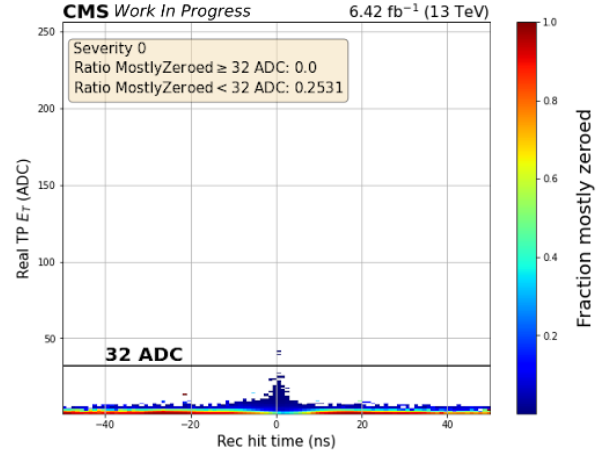
(b) Severity zero TPs mostly zeroed

Figure 5.21: 2018 Data reemulation - severity 0 TPs
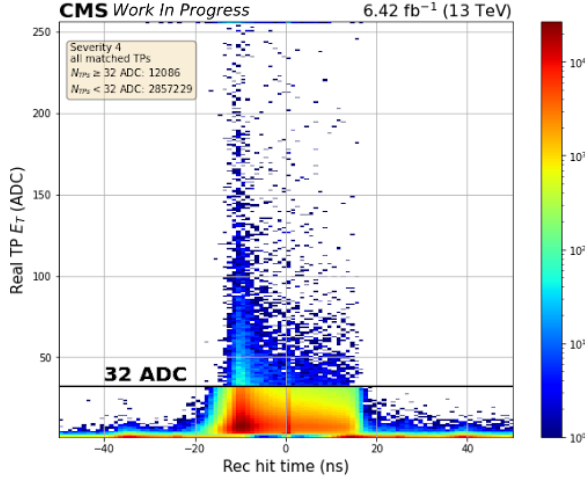
(a) All severity four TPs
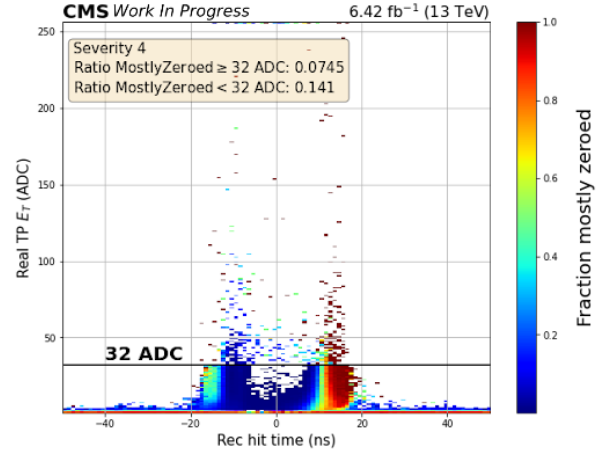
(b) Severity four TPs mostly zeroed

Figure 5.22: 2018 Data reemulation - severity 4 TPs

In the distributions containing all TPs, most signals are in-time as expected. It is also observed that a large portion of spikes are out of time, as expected. It is observed that many spikes have a negative timing around -12.5ns, which is due to a bias in the ECAL offline energy reconstruction, which is optimized for signal waveforms which are slightly different from spike waveforms. Spike waveforms with a negative reconstructed time are generally

expected to really be in time. Additionally, the effect of the spike killer is visible for severity four TPs, as there is a sharp drop-off in the number of TP entries above the spike killer threshold of 32 ADC (16 GeV).

The distributions of TPs which have at least 90% of their energy subtracted by double weights in killing mode show that most signal-like TPs which are mostly zeroed are very low energy and out of time, which are likely coming from noise, and it can be seen that there is a non-zero chance of some in-time signal energy subtraction. For spike TPs, it is seen that the majority of TPs which have their energy mostly subtracted are positively out of time, as expected with double weights based on the standalone simulation shown in Figure 5.15. The spike contamination of ECAL TPs, with and without double weights activated in killing mode, is shown in Figure 5.23.
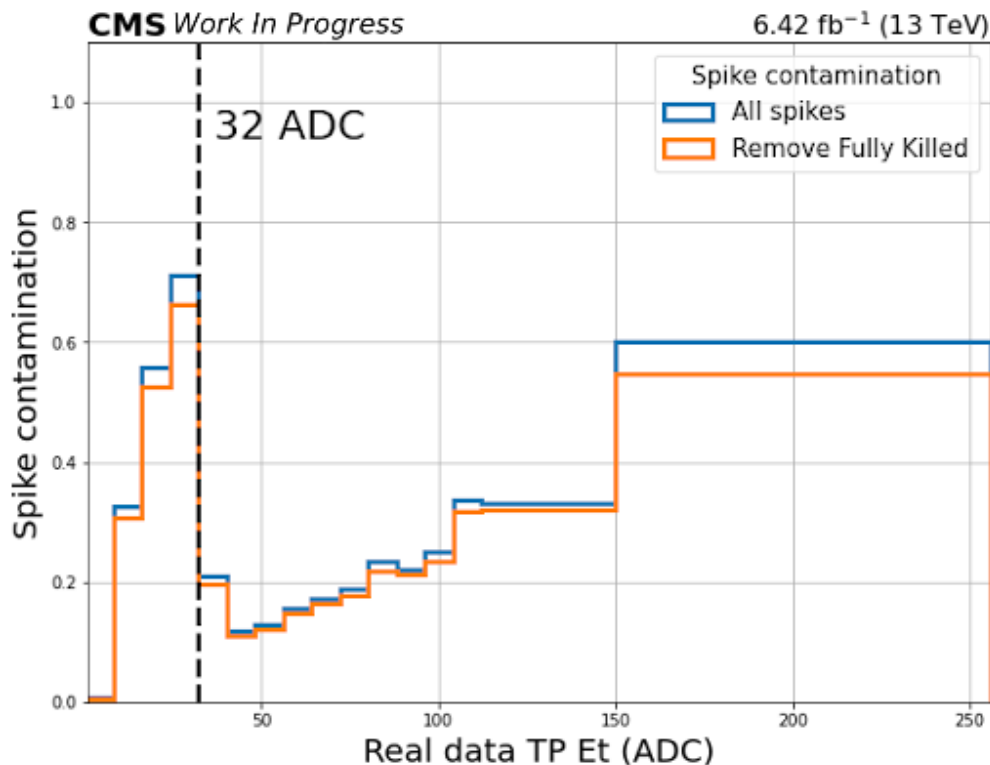
Figure 5.23: 2018 CMS data re-emulation, expected improvement in spike contamination, including below the spike killer threshold.

This shows that with ECAL double weights, there is some potential to lower the spike

contamination rate, including in the high energy regime. This is also true for spikes with energy less than 32 ADC (16 GeV), the existing Level-1 spike killer threshold.

While we see potential for a decrease in spike contamination, this re-emulation of 2018 CMS data also showed we may expect to have the unwanted removal of some signal energy at low TP energies with this double weights working point. In order to further study this, another re-emulation was performed with a full-readout ECAL run. The reason a full-readout run was included in this study is because in full-readout, information from all ECAL crystals is saved. In non full-readout runs, there is a selective readout procedure in which low interest regions are not readout. It is desirable to re-emulate full readout runs when comparing low energy TP energies between data and re-emulation, to ensure that all ECAL information is available for emulation in order to have a proper comparison to data. This re-emulation was performed with two double weights working points: $\delta_{min} = 0.5$ and 2.5 GeV, running with double weights in killing mode. The resulting average energy fractions subtracted from in time signals and out-of-time spikes when re-emulating with these two working points are shown in Figure 5.24.

(a) In time severity zero TPs   (b) Very late severity four TPs
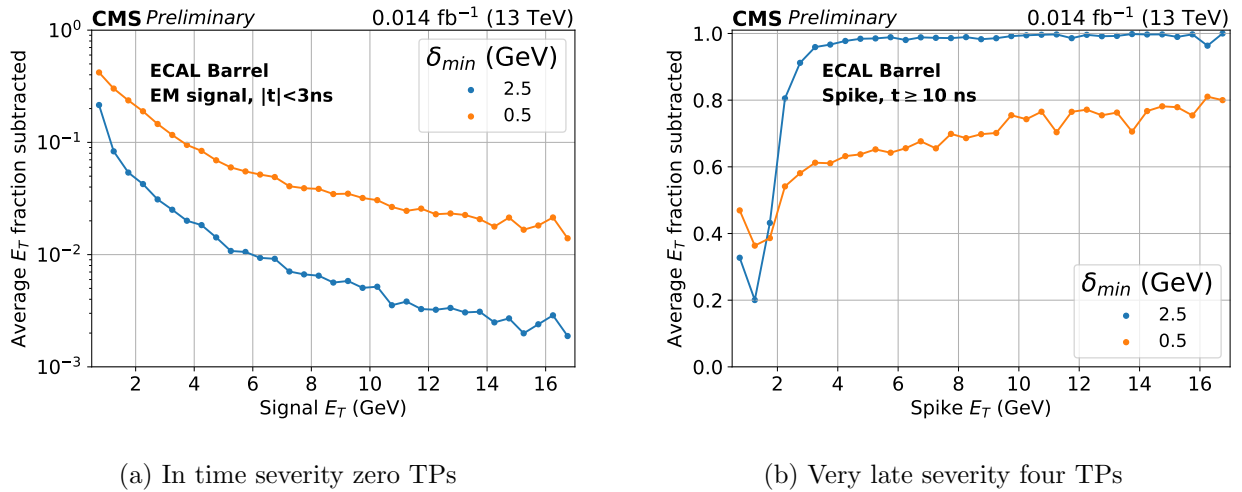
Figure 5.24: 2018 Data reemulation, Full Readout run, with DW in killing mode.

Firstly, this re-emulation with the $\delta_{min} = 0.5$ GeV point shows similar trends observed

in the previous study: Namely that low energy signals have a non-zero probability of having energy subtracted which decreases as the TP energy increases, and that out of time spikes have a large percentage of energy subtracted, which increases as spike energy increases. Secondly, both trends exhibit more desirable behavior with the $\delta_{min} = 2.5$ GeV working point: The amount of signal energy subtraction is decreased, and the amount of spike energy subtraction is increased. These same trends were observed in the standalone simulation results in Figure 5.15 for simulated spikes and Figure 5.16 for simulated signals.

5.2.5 Commissioning for LHC Run 3

During the commissioning of CMS and LHC for Run 3, the accelerator complex provided beam splashes to the experiments, in which an LHC collimator upstream from CMS is closed, resulting in a proton bunch interaction and production of a shower of particles, chiefly muons, which traverse the entire CMS detector. An event display from a 2021 LHC beam splash is shown in Figure 5.25, where red represents ECAL activity and blue represents HCAL activity.

Figure 5.25: 2021 LHC pilot beam: Beam splash

During beam splashes, a broad range of ECAL reconstructed hit timings are returned. This is because a shower of particles arrives at the detector from one direction, where CMS is

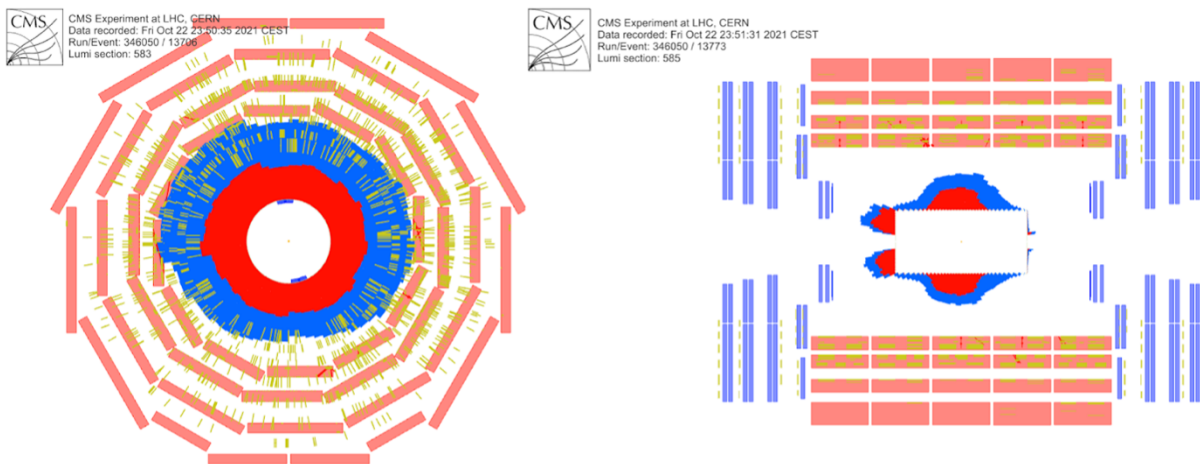configured to trigger the event from ECAL activity in the central region around $\eta = 0$. This defines in-time hits in the detector, akin to the time of a proton-proton bunch collision, and because the shower of particles continues to interact with the rest of ECAL as time passes, all of these hits will be recorded as positively out-of-time. Additionally, all of the hits from the shower of particles which strikes ECAL before the event is triggered will be negatively out-of-time with respect to $\eta = 0$.

As this means a large range of timings for offline ECAL crystal reconstructed hits is expected which can be matched to ECAL TPs in the same fashion performed in 5.2.4, the ECAL operations team used the opportunity to run with double weights in tagging mode, in which no energy is subtracted but a flag is set if a TP is marked as out-of-time by the double weights mechanism. The resulting ECAL TP timings, and the TPs which were tagged are shown in Figure 5.26.

(a) TP timing distribution (b) TPs tagged as out of time
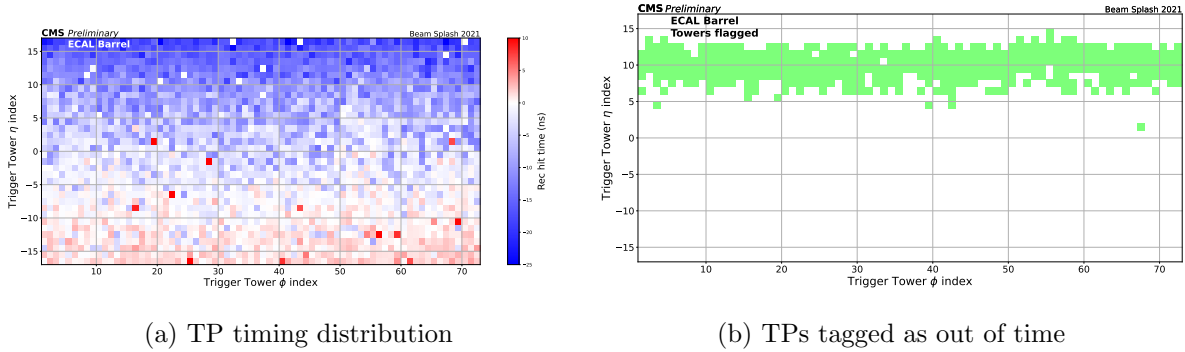
Figure 5.26: TP timing distribution, and TPs which are tagged as out-of-time by the double weights mechanism, from a 2021 CMS beam splash.

It is observed that the TP timings, obtained by assigning the timing of the highest energy reconstructed hit in the TT, range from about -25ns to 10ns. The TPs which are tagged by the double weights mechanism as out-of-time have timings in the largely negative region of about -10 ns to -15 ns, with no tagging of in-time signals. This marked the first instance of out-of-time tagging at the ECAL TP level, and proved the functionality of the double weights mechanism for tagging out-of-time signals in data.

In addition, during the 2021 and 2022 LHC commissioning periods, CMS received low intensity 900 GeV center-of-mass energy collisions. During a 2 hour period, ECAL took data from these collisions in full readout mode running with double weights in tagging mode, in a 2021 run with the $\delta_{min} = 0.5$ GeV working point, and in a 2022 run with the $\delta_{min} = 2.5$ GeV working point. For the 2021 run, the data TP energies vs. offline matched times, and the fraction of TPs tagged over the total are shown in Figure 5.27 for severity zero matched signal-like TPs, and Figure 5.28 for severity 4 matched spike-like TPs.

(a) All severity 0 signal TPs: Data energy vs. time

(b) Signal TPs tagged by double weights with δ_{min} = 0.5 GeV working point
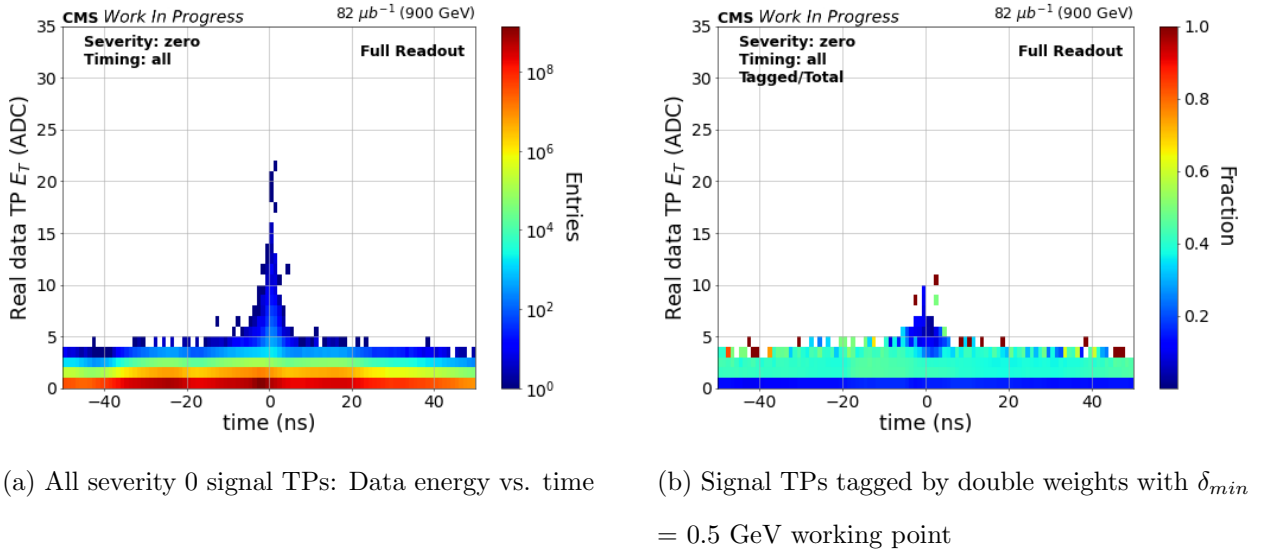
Figure 5.27: 2021 LHC pilot beam severity 0 signal TPs, all and tagged

(a) All severity 4 spike TPs: Data energy vs. time

(b) Spike TPs tagged by double weights with δ_{min} = 0.5 GeV working point
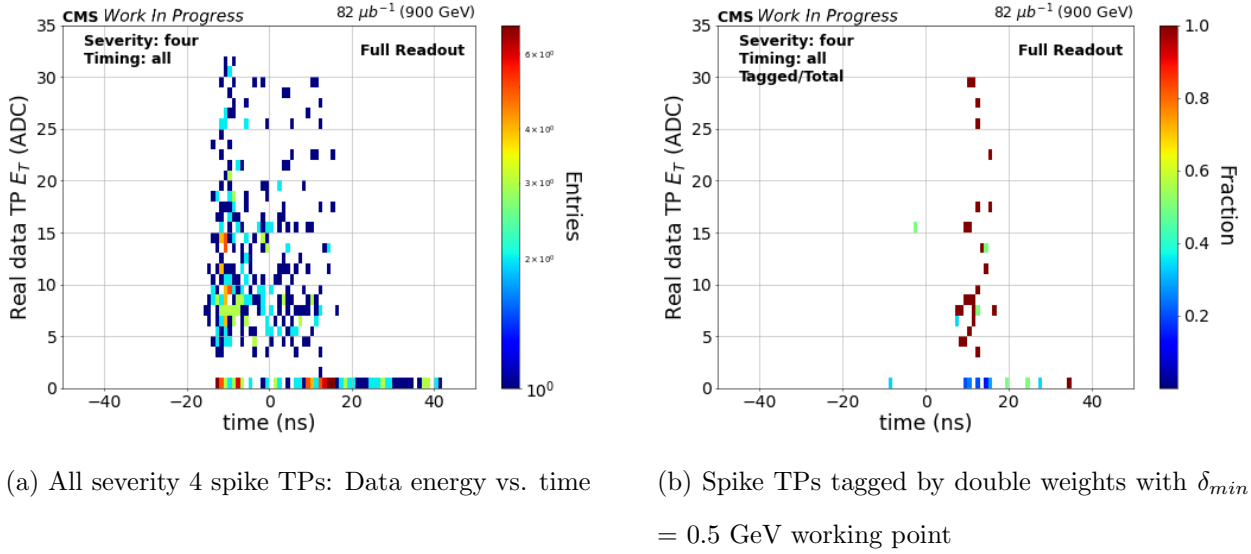
Figure 5.28: 2021 LHC pilot beam severity 4 spike TPs, all and tagged

From these distributions, similar behavior is observed compared to that from the 2018 non full-readout and full-readout data re-emulation: Double weights are able to tag TPs which are positively out-of-time, as well as some spikes which are negatively out of time. For signals, there is a non-negligible amount of tagging seen for in-time signals. As the δ_{min} = 2.5 GeV working point was seen in 2018 re-emulation to have decreased signal tagging and increased spike tagging, the 2022 run with this working point is compared to the 2021 run as shown in Figure 5.29 for in-time severity 0 matched TPs, and Figure 5.30 for very late severity 4 matched TPs.
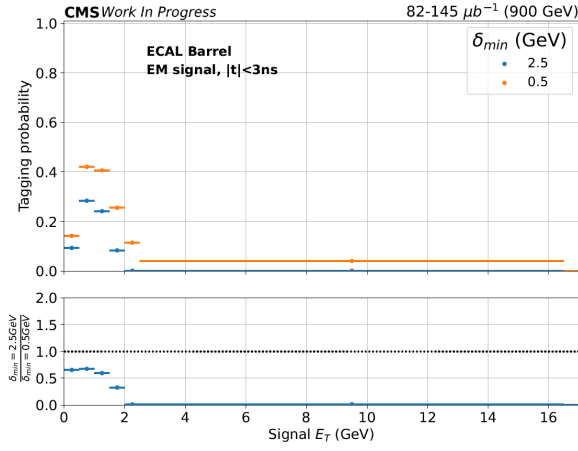
(a) Linear y-scale
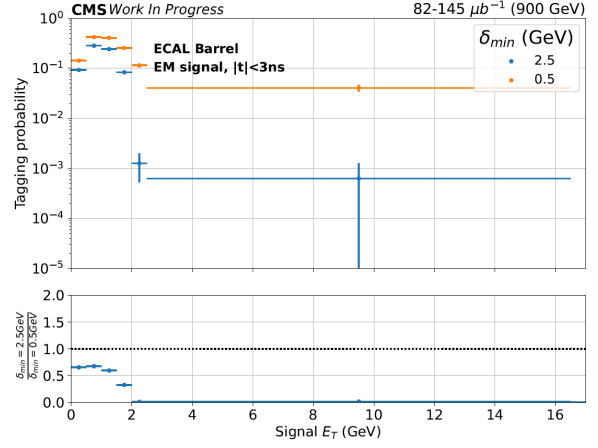
(b) Logarithmic y-scale

Figure 5.29: Tagging probability of in-time signal TPs as a function of TP transverse energy, with two double weights working points, shown in linear and logarithmic y-scale.
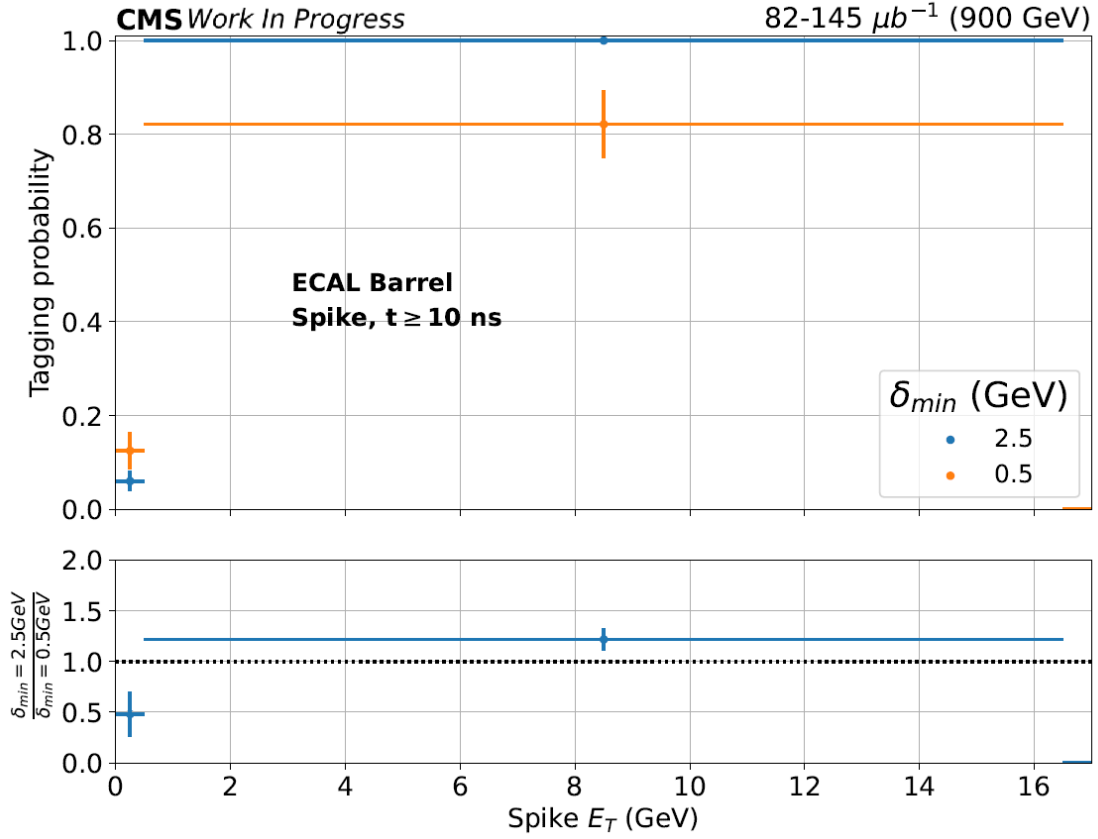
Figure 5.30: Tagging probability of in-time signal TPs as a function of TP transverse energy, with two double weights working points.

191

This comparison returns similar behavior compared to the 2018 full readout re-emualtion shown in Figure 5.24, as the $\delta_{min} = 2.5$ GeV working point has less in time signal tagging which decreases as energy increases, and more late spike tagging which increases as energy increases.

In order to ensure that the emulator is properly simulating the ECAL double weights tagging mechanism as observed in data, a comparison of the tagging by data and the emulator was investigated for these two low energy runs, shown in Figure 5.31 for in-time severity 0 matched TPs, and Figure 5.32 for very late severity 4 matched TPs.

(a) 2021 collisions, $\delta_{min} = 0.5$ GeV working point

(b) 2022 collisions, $\delta_{min} = 2.5$ GeV working point
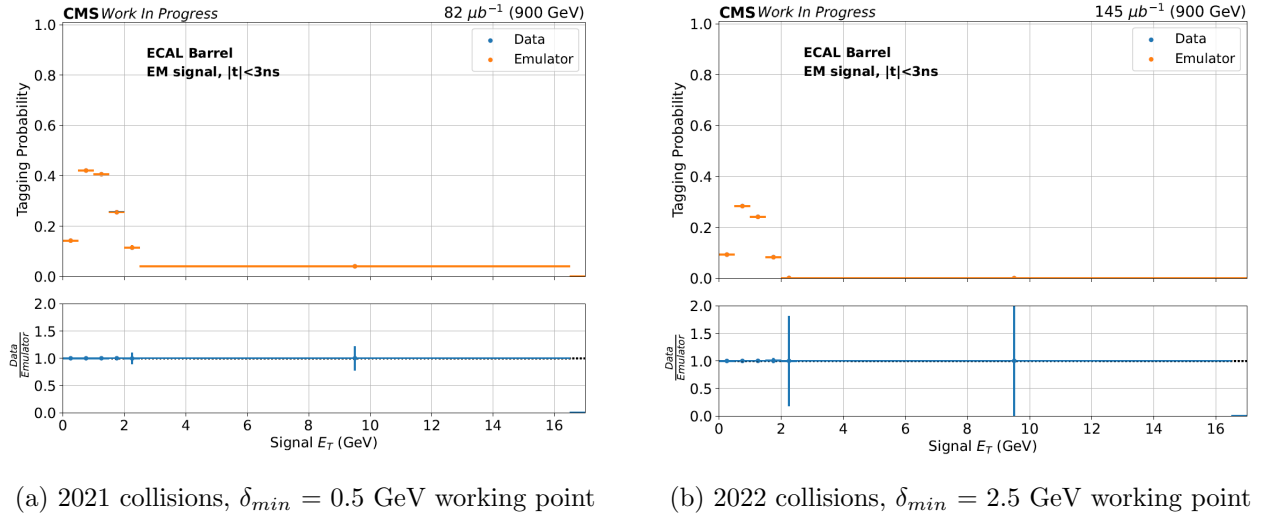
Figure 5.31: Tagging probability in data and as computed by the emulator for Severity 0 matched TPs with offline matched reconstructed times $|t| < 3$ ns.

(a) 2021 collisions, $\delta_{min} = 0.5$ GeV working point

(b) 2022 collisions, $\delta_{min} = 2.5$ GeV working point

Figure 5.32: Tagging probability in data and as computed by the emulator for Severity 4 matched TPs with offline matched reconstructed times > 10 ns.

For the in time severity zero matched TP cases shown in Figure 5.31, the tagging probabilities as evaluated by the data and emulator are in agreement within 0.6%. This indicates that for the most part, the emulat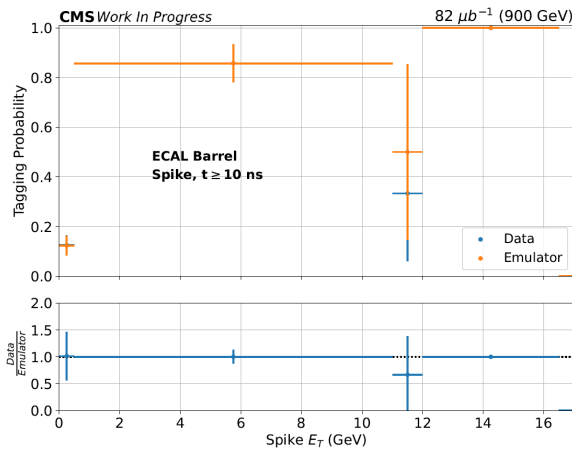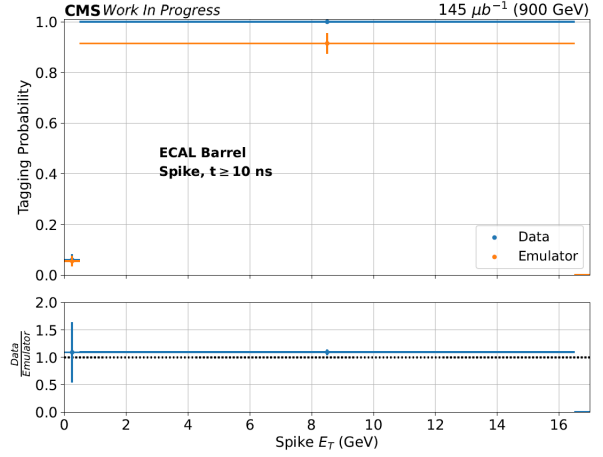or can be trusted for accurately estimating the performance of the double weights mechanism on in-time severity zero matched TPs when re-emulating CMS data.

For the late severity four matched TP cases shown in Figure 5.32, in the 2021 data sample there is one TP with disagreement in data and emulator energy in the 11 GeV bin. This individual TP requires further investigation to understand if this disagreement is due to the double weights mechanism or not. Apart from this TP, the double weights tagging probability as determined by data and the emulator are in agreement within 1.4%, and fully in agreement for highly energetic TPs. In the 2022 data, there are a number of TPs which different data and emulated energies, which may or may not change the tagging probabilities computed in the data and emulator, which disagree by about 10%. These differences require further investigation: They may be found to be due to the double weights in which the algorithm or weight values may need to be updated, or there may be an issue in the emulator which would need to be fixed.

193

Finally, during 2022 the LHC provided further beam splashes to CMS. The ECAL operations teams took this opportunity to run with double weights in "killing + tagging" mode, in which ECAL strips which have a greater ODD amplotide than EVEN amplitude have their energy zeroed (killing), and if there is a large amount of zeroing in a given ECAL TP, a flag is set (tagging). The functionality of this configuration was tested as it may be a potentially useful mode to use in the future, for instance to have the information of which regions of ECAL have their energy at least partially killed by double weights. An event from a 2022 beam splash running with ECAL double weights in killing + tagging mode is shown in Figure 5.33.

(a) TP energy distribution

(b) TPs tagged as out of time
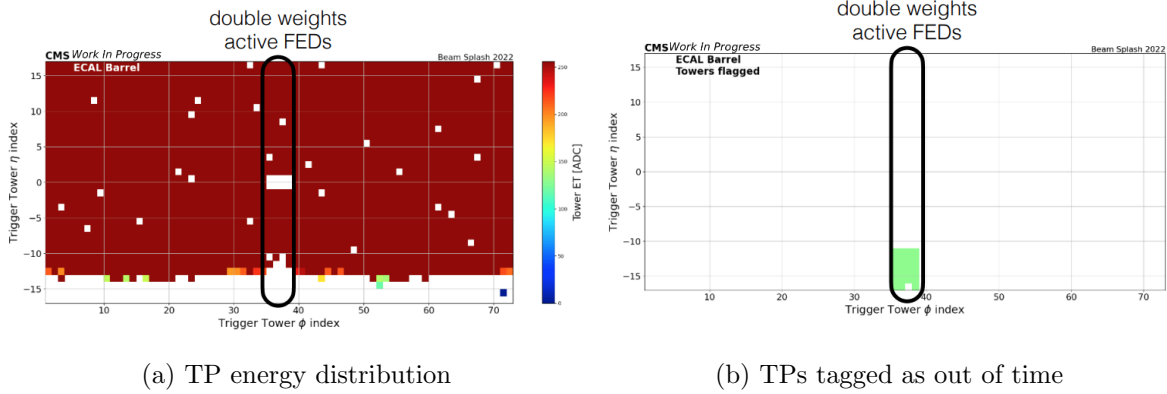
Figure 5.33: ECAL TP energies and TPs tagged as out-of-time by double weights in killing + tagging mode during a 2022 CMS beam splash.

In this configuration, the majority of the ECAL barrel ran with its nominal Run 2 configuration, but killing + tagging mode was set for two supermodules in the center of the detector. In one supermodule in which negatively out-of-time signals are expected, it is observed that there is some amount of killing of energy as the energy in that region is lower than the other supermodules with similar TP times, as the particle from the splash propagate from $-\eta$ to $+\eta$ and are expected to have roughly the same timing per η index, and it can be seen that TPs in the same region are tagged. This is the first instance of ECAL running with double weights in killing + tagging mode, and shows that this previously untested

194

configuration appears to work as expected.

While these initial re-emulation and data checks with double weights show potential gain at the ECAL TP level, as high energy spikes are tagged and removed while there is a minimal impact on low in-time signals and the emulator appears to provide an accurate representation of the double weights mechanism applied to in time signal-like TPs, the next necessary thing to check is the impact of double weights on CMS L1 quantities. This includes the effect on L1 rates, and L1 turn-on curves. A potential gain would be a decrease in the L1 rates due to the removal of spikes, which may allow for a lowering of the L1 seed energy thresholds. This would potentially allow for the collection of more Higgs pair production events in electromagnetic final states, including HH→WW$\gamma\gamma$, which may improve the sensitivity of this and other Higgs pair production analyses to be performed at CMS using the LHC Run 3 dataset.

5.3 Operations

In order to take take quality data at the CMS ECAL and test the re-optimized and new features of the ECAL trigger for LHC Run 3, a variety of operations teams is necessary. The CMS ECAL operations are subdivided into various operations groups, as there is a wide array of areas of technology and expertise required in order to successfully operate the ECAL for data-taking. Each group covers a different aspect of ECAL, all with the goal of minimizing the downtime of the experiment and ensuring quality data is taken. There are many sides to the operation of ECAL, for each of which the corresponding operations team is crucial, and all must remain vigilant for the successful operation and maintenance of ECAL.

5.3.1 Technical Coordination

The purpose of the ECAL Technical Coordination (TC) is to ensure the safe operation of all hardware components of ECAL, both those stored in the Underground Experimental

Cavern (UXC), and Underground Service Cavern (USC). In the event of a major hardware failure, or cooling related issue which may occur and possibly prevent ECAL from running in a safe state, the TC team leads the effort in repairing these components and is responsible for notifying the rest of the ECAL operations group that a particular partition of ECAL is unavailable. During periods of collisions, and especially during long shutdown or technical stop periods, CMS TC coordinates a vast number of physical interventions to repair, upgrade, and service the detector. This large coordination effort requires a deep understanding of the physical architecture and history of ECAL, as well as an understanding of how an intervention on one CMS subdetector may affect another CMS subdetector. The role of the ECAL TC team includes following the planned CMS TC activities, as this may have implications on partitions of ECAL. An example CMS underground plan of the day is shown in Figure 5.34.

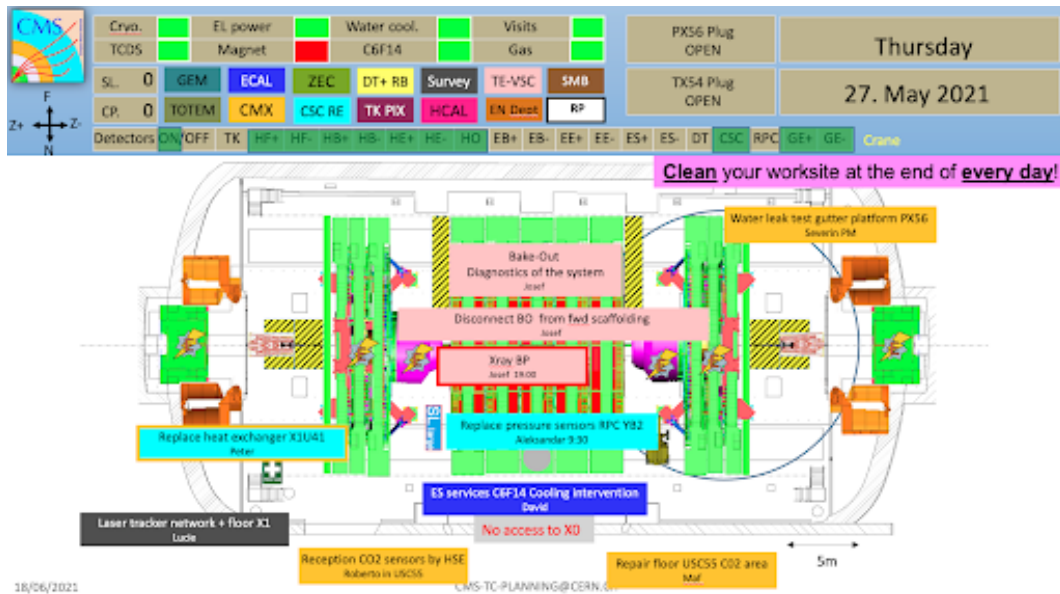Figure 5.34: Example plan of the day in CMS UXC/USC from 27 May 2021.

As an example, during a long LHC shutdown period there may be a day when one of the CMS endcaps must be physically moved in order to allow for an intervention on the inner hardware of another sub-detector which is not accessible when the detector is closed. This has an implication of the ECAL endcaps, as they may need to be powered off during this

196

time to ensure the safety of the electronics. In a case like this, ECAL TC would report this required action of powering off to the rest of the ECAL operations teams in order for all to be aware that one endcap will not be available for a certain period of time. This can then potentially delay planned tests on this endcap, and is therefore essential information for the entire ECAL operations group to be aware of.

5.3.2 Detector Control System

The ECAL Detector Control System (DCS) team maintains, develops, and operates the ECAL DCS in order to ensure the proper control and safety of the detector. An image of the ECAL DCS monitor is shown in Figure 5.35, displaying the powering status of the full ECAL and ES as ON.
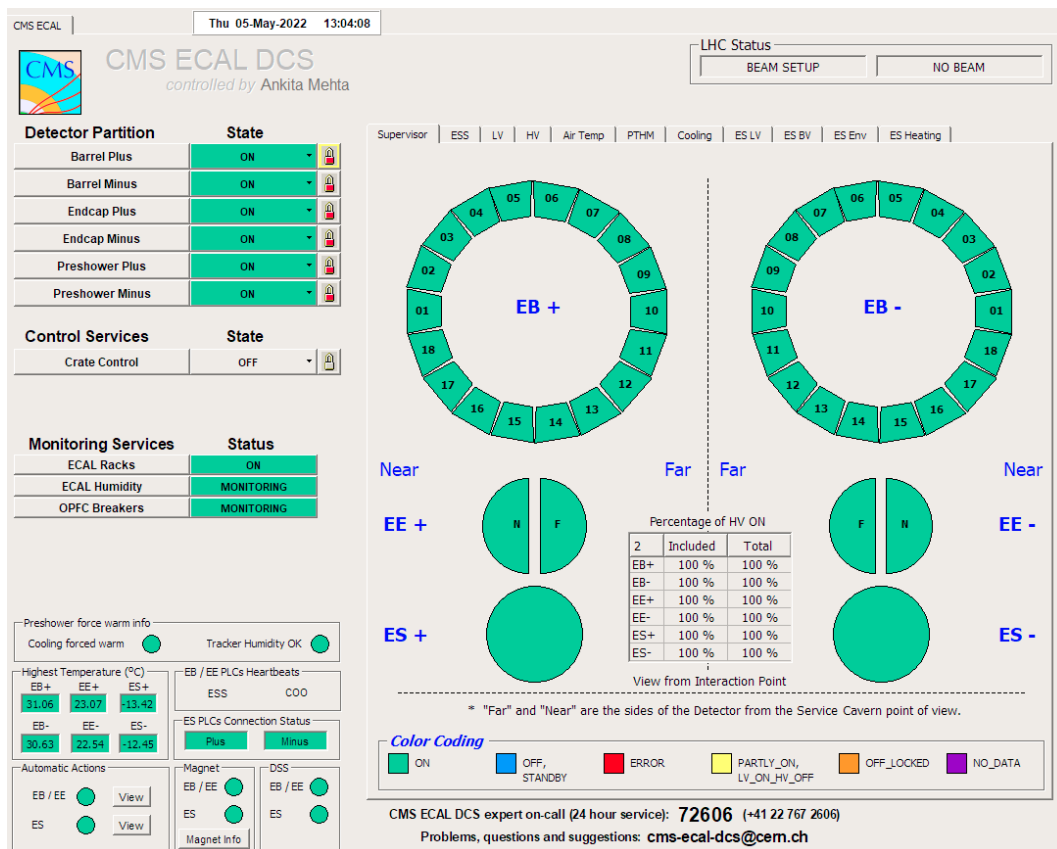

Figure 5.35: ECAL DCS monitor

In the example situation in which there is activity in UXC which requires the powering off of an ECAL Endcap, a request would be made to the ECAL DCS operator to use the DCS in order to power off the desired partition of ECAL. In the event in which issues during this powering off may occur, the operator follows a pre-defined set of protocols in order to safely identify and solve the encountered issue without harming the detector.

5.3.3 Run Coordination

The purpose of ECAL Run Coordination (RC) is to coordinate the running operations of ECAL, including all times during which the detector is powered on. This primarily involves the planning of tests, coordination between ECAL and CMS, and training of on-call ECAL shifters in order to carry out operation plans. A diagram illustrating the paths of communication between ECAL and CMS during running can be seen in Figure 5.36.
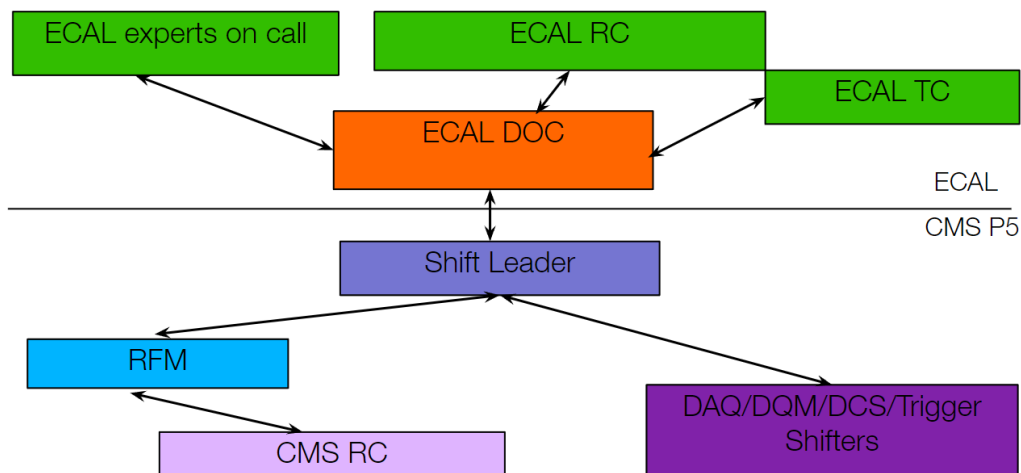
Figure 5.36: ECAL / CMS running communication paths.

On a given day, the CMS run coordinators and Run Field Manager (RFM) make a plan of the day based on the plan of LHC and the requests of the individual subdetectors. It is the job of ECAL RC to make sure the requests made to CMS are consistent with the opinions and availability of the ECAL experts, and to then understand and share the implications of the CMS plan of the day on the ECAL subdetector. This may include planned tests for

ECAL which use the CMS DAQ (Data AcQuisition) system, or the participation of ECAL in the tests of other CMS subsystems. It is essential for all participants in run coordination communications to execute fast and clear communication of information in order to minimize detector downtime, and optimize the use of commissioning and data-taking periods.

5.3.4   Data Acquisition

The ECAL DAQ (Data AcQuisition) team is responsible for ensuring effective data-taking by ECAL. A diagram of the ECAL DAQ path is shown in Figure 5.37.
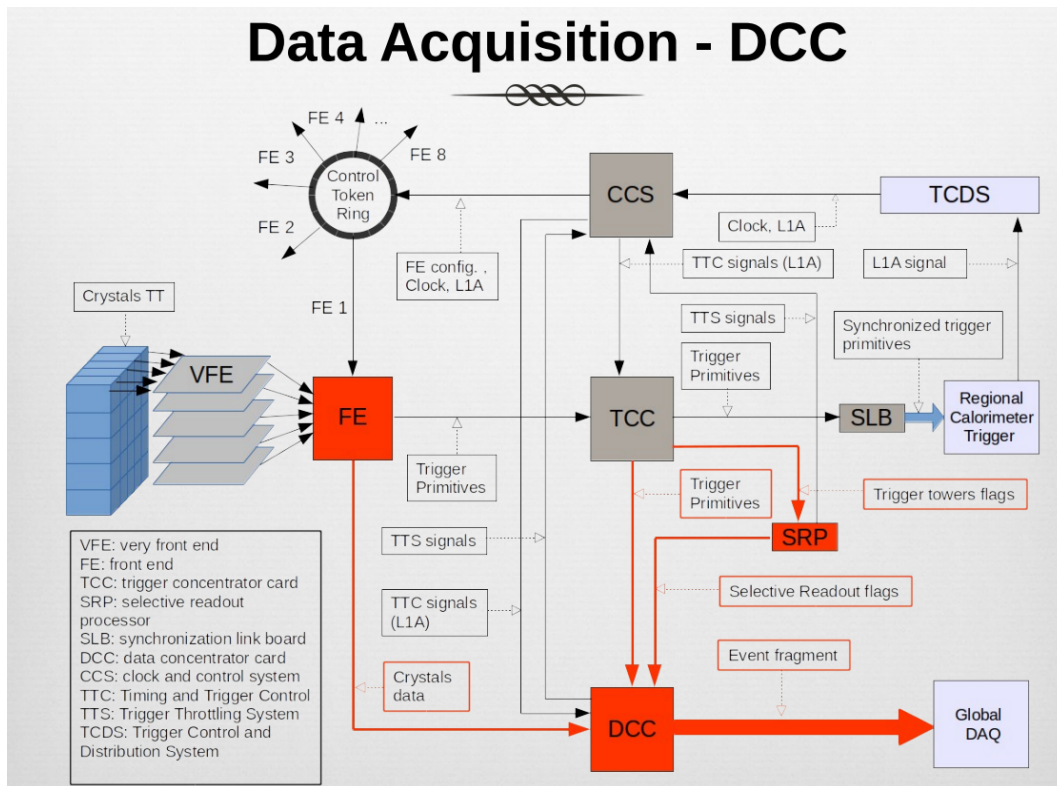

Figure 5.37: ECAL DAQ path

Generally speaking, the data flow which takes place due to an energetic ECAL goes as follows: An energetic electromagnetically interacting particle produces scintillation light in the ECAL crystals (left-most side of Figure 5.37), which reaches the crystals' photo-detectors (or an EB APD may be directly struck, leading to a spike which may fake an energetic ECAL

signal). The signals from the photo-detectors are propagated through the VFE (very front end) cards, where in EB a set of five cards is connected to a single FE (front end card) for a 25 crystal TT, or a range of 1-25 crystals in EE. If an L1A is sent to the FE based on the CMS L1 trigger, the L1A will be received via the control token ring, triggering ECAL to readout its data first sending it to the DCC (data concentrator card), and then to the central CMS DAQ system to be processed at HLT.

The ECAL DAQ team is additionally responsible for maintaining a slew of monitors used for monitoring various DAQ related quantities, to ensure that data acquisition is flowing as expected. An example is the ECAL payload monitor, used to monitor if very large amounts of data are being processed through each ECAL FED (Front end driver), corresponding to different parts of the detector (one supermodule in EB). The contents of this monitor during an ECAL full readout run, during a special run in which ECAL was running with double weights in tagging mode with the $\delta_{min} = 2.5$ GeV working point as described in Section 5.2.5, is shown in Figure 5.38 for ECAL, and 5.39 for the preshower.

Figure 5.38: ECAL payload monitor during a June 2022 full-readout run. On the y-axis, the size of a FED's payload fragment is plotted. On the x-axis, the ECAL FED number is plotted. Each FED number corresponds to an ECAL supermodule, and ranges from 601-654.
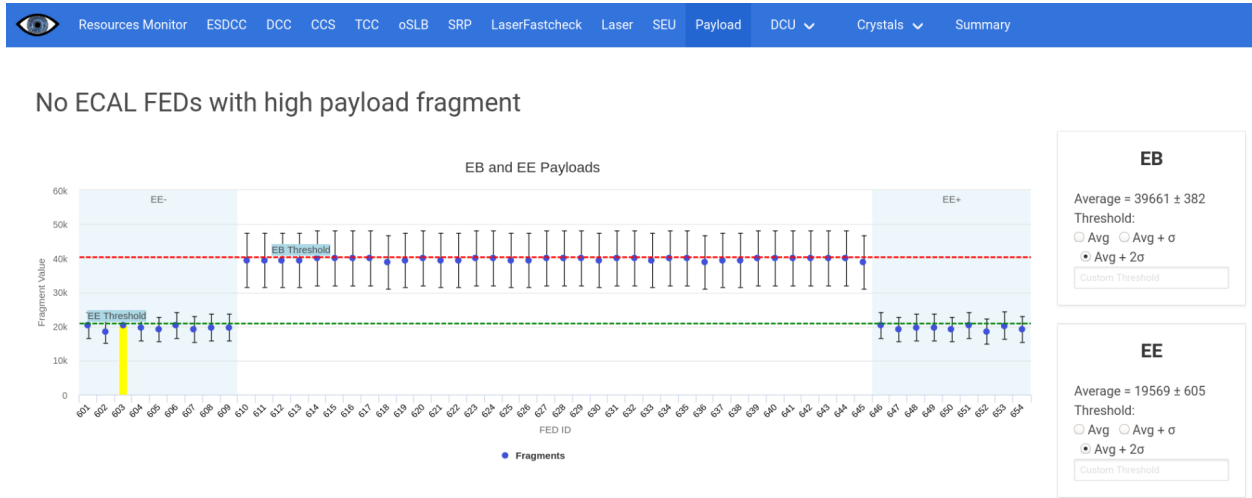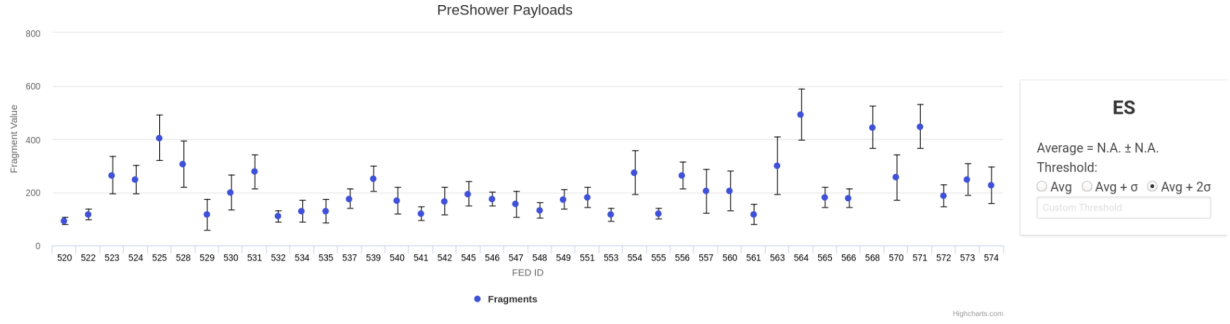
Figure 5.39: ES payload monitor during a June 2022 full-readout run. On the y-axis, the size of a FED's payload fragment is plotted. On the x-axis, the ES FED number is plotted. Each FED number corresponds to a portion of ES.

Notably, the payloads in the ECAL barrel appear to be greater on average than the payloads in the ECAL endcaps. This may potentially be due to the fact that there are more readout channels in the EB (61,200 crystals compared to 14,648).

5.3.5 Trigger

The primary role of the ECAL trigger team is to ensure the smooth operation and proper calibration of ECAL trigger primitive generation. Responsibilities include the identification and masking of noisy or problematic towers, the monitoring of ECAL's contribution to the CMS trigger rate, and the testing and commissioning of new features and protocols for future data-taking periods. A diagram of the ECAL trigger primitive generation path is shown in Figure 5.40.
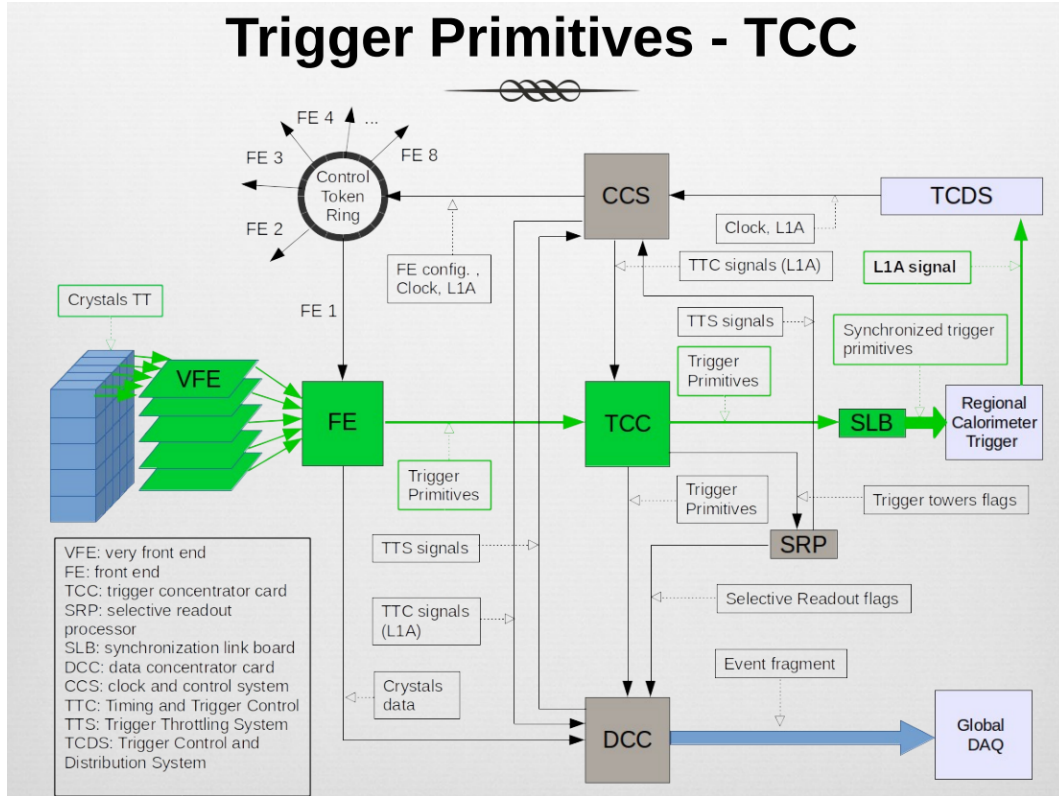
Figure 5.40: ECAL trigger primitive path

While data is first sent to the FE card as described in the previous Section 5.3.4, it is stored on the FE electronics buffers while a trigger primitive is formed and sent to the TCC (Trigger concentrator card). The TCC passes the TPs to the calorimeter layers of L1, while the FE waits to receive, or not receive an L1A.

5.3.6   Electronics

The ECAL electronics team is responsible for the maintenance of the ECAL on- and off-detector electronics. The main off-detector ECAL electronics modules are the TCC (Trigger Concentrator Card), CCS (Clock and Control system), and DCC (Data Concentrator Card). In the ECAL Barrel (EB), there is one TCC, CCS, and DCC per supermodule. By monitoring ECAL electronics, and performing physical maintenance such as the cleaning of electronics fibers or uploading of updated firmware when necessary, the ECAL electronics experts ensure

the robustness and ability of the ECAL electronics to take quality data.

5.3.7   Laser and LED

Due to radiation received by LHC delivered collisions, the transparency of ECAL crystals degrades over time due to radiation damage. A laser correction system is in place in order to measure and correct for losses in ECAL crystal transparency, as shown over the course of LHC Runs 1 and 2 in Figure 5.41. It can also be seen that during long shutdown periods without collisions, the ECAL crystals anneal and recover some transparency, as seen by the slight increases in transparency before and after a shutdown period.
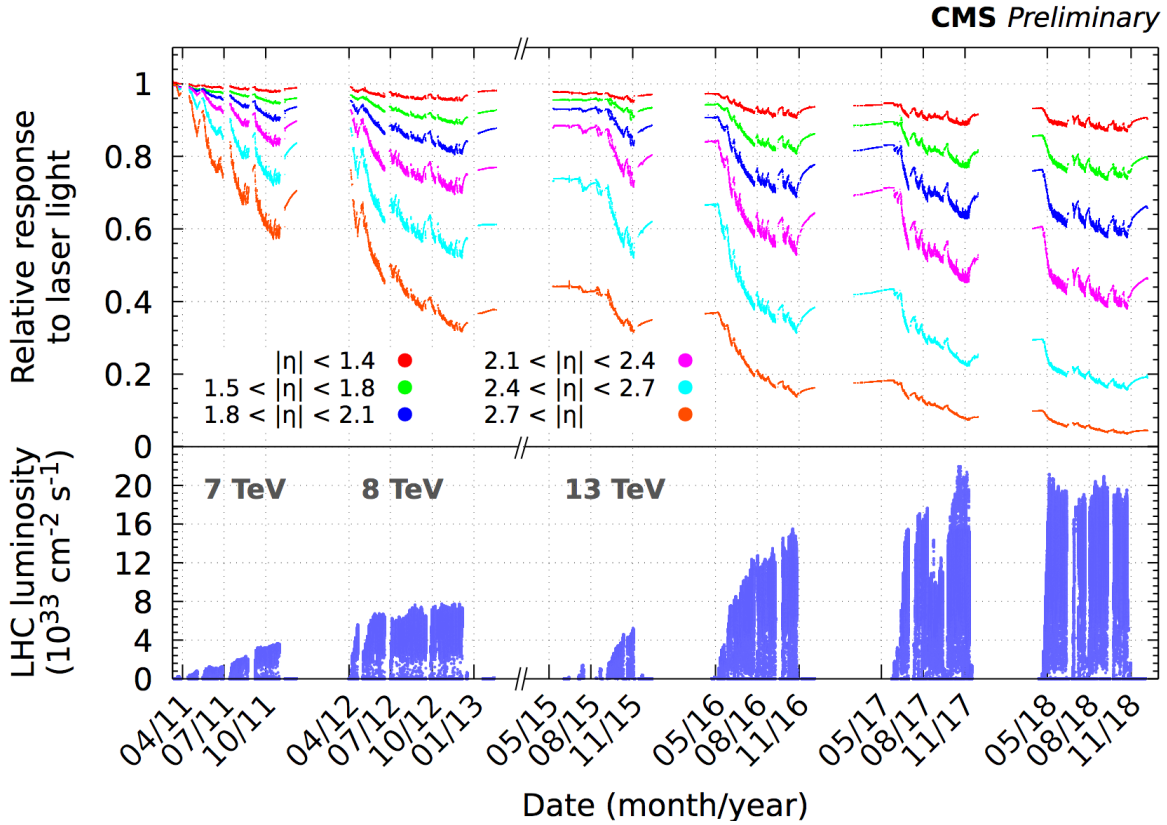

Figure 5.41: ECAL crystal transparency history during LHC Runs 1 and 2.

While similar shapes are observed for different η regions of the detector, more radiation is received at higher η regions, leading to lower transparency with respect to that from the start of LHC Run 1. In the highest pseudo-rapidity region in the last EE rings 2.7

$< \eta$, the crystals have an average transparency down to $\approx 4\%$ with respect to their original transparency. The high levels of radiation damage in the high η regions are consistent with the higher amplitude fractional bias shown in Figure 5.4, and is one of the motivations for replacing the ECAL EE for the Phase-II CMS detector in favor of a new endcap detector called HGCAL (High granularity calorimeter).

An additional transparency measurement is taken by the LED for the ECAL endcaps. The ECAL laser team is responsible for ensuring the smooth operation of the ECAL laser and LED systems, which take crucial measurements to monitor the ECAL crystals and calibrate their outputs.

5.3.8 Data quality monitor

The purpose of the ECAL Data Quality Monitor (DQM) group is to maintain and develop the ECAL DQM plots used by both the central CMS DQM monitoring page, and the local version used privately by ECAL. An example set of DQM plots is shown in Figure 5.42.
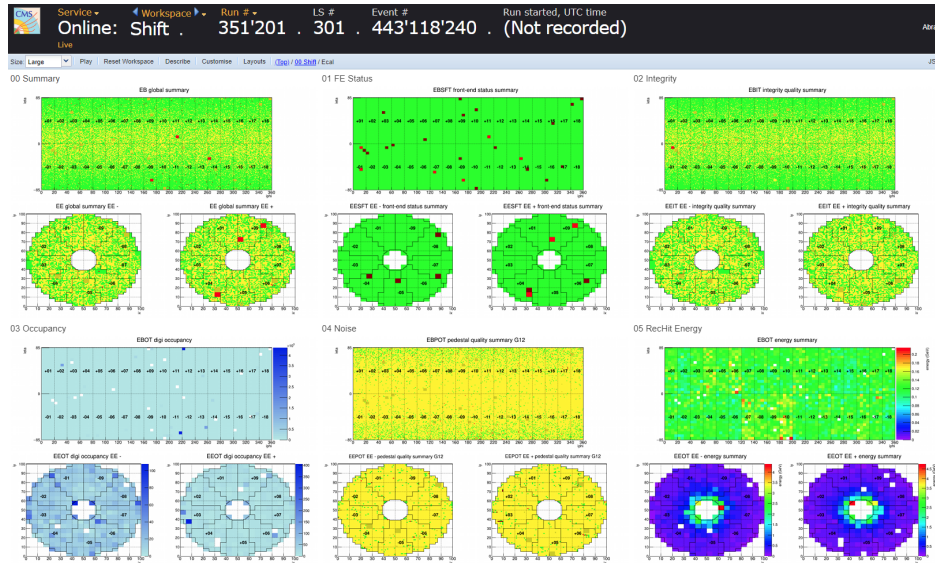

Figure 5.42: Example ECAL DQM plots

These plots are essential for monitoring the quality of data being taken by ECAL. If large sections of ECAL DQM plots show issues, typically colored red, it may hint at a problem

which can be confirmed by going through additional DQM plots in order to better understand the underlying issue. This information would then be propagated to the appropriate ECAL experts in order to take the necessary action, such as fixing a certain piece of hardware or software. It is then checked if a problem has been solved by starting a new run, and confirming that the DQM plots no longer indicate an issue.

5.3.9   Prompt feedback group

The role of the ECAL Prompt Feedback Group (PFG) is the provide prompt feedback regarding the quality of ECAL data. One of the main roles of the PFG group is to provide daily reports to the entire ECAL operations team, notifying everyone of the general status of ECAL based on a variety of monitoring plots, largely from the DQM previously described in Section 5.3.8. This daily report is crucial for catching any clear issues in ECAL data-taking, which may affect large portions of CMS data if left un-noticed.

5.3.10   Detector performance group

The role of the ECAL Detector Performance Group (DPG) includes the maintenance, and improvement in quality of calibration applied to ECAL data. This also includes the tracking of physics performance of the ECAL detector, which can for instance be checked by analyzing the reconstruction of expected physics processes such as $\pi_0 \to \gamma\gamma$, shown for runs from a 2022 commissioning period in black and a 2018 data taking period in blue in Figure 5.43.
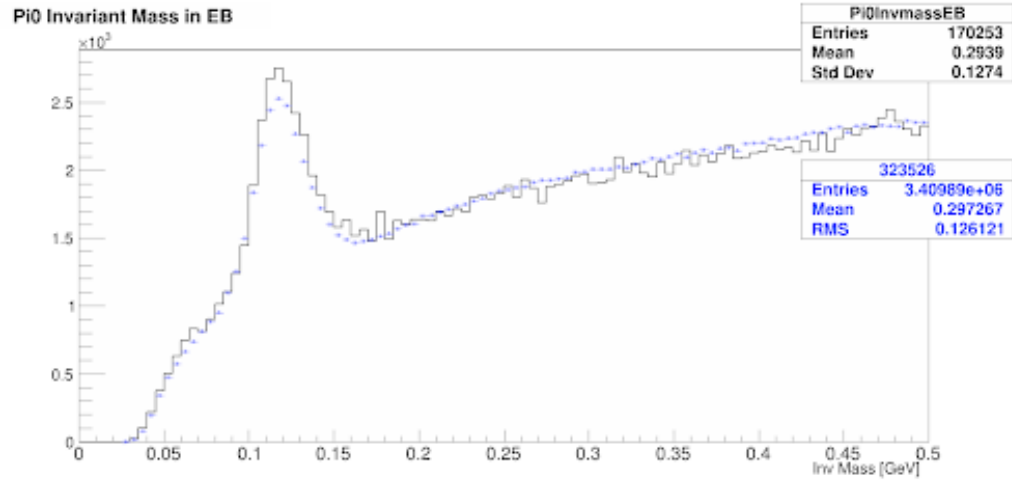
Figure 5.43: Invariant mass of a diphoton pair from a π_0 candidate in EB during a 2022 commissioning run (black) and 2018 data-taking run (blue).

Chapter 6

Future: Prospects for HH measurements in the WW$\gamma\gamma$ and $\tau\tau\gamma\gamma$ final states at the High Luminosity LHC

In addition to analyzing data already taken by the CMS detector during LHC Run 2, and further developing the detector's data-taking features to improve physics sensitivity during LHC Run 3, it is important to perform projection studies in order to estimate the expected sensitivity to physics processes with future particle accelerators and upgraded detectors. These studies provide physicists with initial insight of what to expect when performing future measurements and searches, and can motivate which analyses to perform in the future.

Through the results of the search for di-Higgs production in the WW$\gamma\gamma$ final state using the LHC Run 2 dataset, it is difficult to obtain an accurate estimate of the analysis sensitivity at the future HL-LHC with the upgraded CMS detector. In order to perform this projection, a separate simulation-only analysis is performed. In addition, the $\tau\tau\gamma\gamma$ HH final state is added to this search as it has a similar final state topology to $WW\gamma\gamma$.

The structure of this chapter is as follows: The strategy of the analysis will be described in Section 6.1. The phase II CMS detector will be described in Section 6.2. The simulated samples used in this analysis will be described in Section 6.3. Object selection is described in Section 6.4. Event selection and categorization will be described in Section 6.5. A description of the systematic uncertainties considered is described in Section 6.6. The results of the analysis are presented in Section 6.7, and the analysis is summarized in Section 6.8.

6.1 Strategy

For the $WW\gamma\gamma$ portion of this analysis, the strategy is very similar to that of the Run 2 analysis. For the $\tau\tau\gamma\gamma$ portion of the analysis, a similar analysis strategy is followed with respect to the semi-leptonic final state of the Run 2 analysis, namely through the use of a DNN.

For both HH final states, the signal and background topologies are the same as for the Run 2 analysis as the upgrade in the LHC and CMS detector will not dramatically change the signal and background signatures. In this analysis, a simulation template is formed for HH, H and a continuum of background process. As there is not yet a Phase II dataset to use for a statistical interpretation via a fitting of the simulation templates to the data, a projection is made by fitting the background-only hypothesis simulation templates to the signal + background simulation templates in order to estimate how clear of an HH signature is expected to be seen in the Phase II CMS dataset. This is performed in a signal region defined as the diphoton invariant mass, in the window $115 < m_{\gamma\gamma} < 135$. This region is chosen due to the expectation that the H$\rightarrow \gamma\gamma$ leg of the HH$\rightarrow$(WW+$\tau\tau$) $\gamma\gamma$ processes should provide a peak in this region.

As was the case for the Run 2 analysis, there are two background signatures present in this analysis: A resonant background from the single Higgs to $\gamma\gamma$ process, and a continuum background formed by a combination of background processes which do not contain a prompt diphoton. An illustration of signal and background signatures is shown in Figure 4.2.

In order to optimize the sensitivity of this analysis, a DNN (Deep Neural Network) is employed for the Semi-Leptonic WW$\gamma\gamma$ final state and one Tau $\tau\tau\gamma\gamma$ final state. These final states are expected to be the most sensitive due to the increase in branching ratio from their hadronic decays, but with the benefit of maintaining a clean signature due to the presence of a lepton in their leptonic decays.

For the Fully-Leptonic $WW\gamma\gamma$ and two Tau $\tau\tau\gamma\gamma$ channels, cut based strategies are

performed due to a lack of number of events.

In order to combine all final state categories in order to extract a more sensitive final result, it is imperative to apply orthogonal selections to simulation events in order to avoid including the same events in multiple background categories. This is done via the event's number of leptons, namely the number of electrons and muons in the $WW\gamma\gamma$ categories, and number of τ particles in the $\tau\tau\gamma\gamma$ categories. Each lepton must pass a common set of selections applied for all final state tags. After a set of lepton objects is selected for each simulation event, events fall into the Semi-leptonic $WW\gamma\gamma$ category if they contain exactly one lepton, the Fully-leptonic $WW\gamma\gamma$ category if they contain at least two leptons, and the one (two) τ $\tau\tau\gamma\gamma$ category if they contain exactly one (two) hadronically decaying τ particles.

Further event selections are made for the each final state category, but by requiring an orthogonal separation of the number of electrons, muons and τ particles, it is guaranteed no one event can fall into more than one category. Thus, background and signal models in different final state categories can be simultaneously fit to pseudo-data in order to obtain a final result which benefits from a combination of the physics signatures of all final states.

6.2   The Phase-2 CMS detector

The CMS detector [61] will be substantially upgraded in order to fully exploit the physics potential offered by the increase in luminosity, and to cope with the demanding operational conditions at the HL-LHC [62; 63; 64; 65; 66]. The upgrade of the first level hardware trigger (L1) will allow for an increase of L1 rate and latency to about 750kHz and 12.5 μs, respectively, and the high-level software trigger (HLT) is expected to reduce the rate by about a factor of 100 to 7.5kHz. The entire pixel and strip tracker detectors will be replaced to increase the granularity, reduce the material budget in the tracking volume, improve the radiation hardness, and extend the geometrical coverage and provide efficient tracking up

to pseudorapidities of about $|\eta| = 4$. The muon system will be enhanced by upgrading the electronics of the existing cathode strip chambers (CSC), resistive plate chambers (RPC) and drift tubes (DT). New muon detectors based on improved RPC and gas electron multiplier (GEM) technologies will be installed to add redundancy, increase the geometrical coverage up to about $|\eta| = 2.8$, and improve the trigger and reconstruction performance in the forward region. The barrel electromagnetic calorimeter (ECAL) will feature the upgraded front-end electronics that will be able to exploit the information from single crystals at the L1 trigger level, to accommodate trigger latency and bandwidth requirements, and to provide 160MHz sampling allowing high precision timing capability for photons. The hadronic calorimeter (HCAL), consisting in the barrel region of brass absorber plates and plastic scintillator layers, will be read out by silicon photomultipliers (SiPMs). The endcap electromagnetic and hadron calorimeters will be replaced with a new combined sampling calorimeter (HGCal) that will provide highly-segmented spatial information in both transverse and longitudinal directions, as well as high-precision timing information. Finally, the addition of a new timing detector for minimum ionizing particles (MTD) in both barrel and endcap regions is envisaged to provide the capability for 4-dimensional reconstruction of interaction vertices that will significantly offset the CMS performance degradation due to high PU rates.

A detailed overview of the CMS detector upgrade program is presented in Ref. [62; 63; 64; 65; 66; 67; 68; 69], while the expected performance of the reconstruction algorithms and pile-up mitigation with the CMS detector is summarised in Ref. [70].

6.3   Simulated samples

Because this analysis is a projection study of the prospects for $WW\gamma\gamma$ and $\tau\tau\gamma\gamma$ searches as the future HL-LHC and upgraded CMS detector, the samples used in the analysis are exclusively simulation.

As was done for the Run 2 analysis, signal Monte Carlo $gg \rightarrow HH$ samples are generated

using PowHEG v2 [20; 21; 22; 23] at next-to-leading order (NLO) in QCD including the full top quark mass dependence with the SM parameters.

Subsequent decays of the Higgs boson pairs into WW or $\tau\tau$ and a pair of photons are implemented using PYTHIA 8.212 [27]. $WW\gamma\gamma$ samples are generated separately for each final state in $WW\gamma\gamma$. For $\tau\tau\gamma\gamma$ signal samples, all possible decays for taus are allowed.

As the process signature remains the same for both the Run 2 and Phase II analyses, the expected background signatures also remain the same. The analysis is affected by backgrounds from single Higgs boson production and by non-resonant backgrounds with continuum $m_{\gamma\gamma}$ spectra. The event generator MADGRAPH5_AMCATNLO [24; 25] with the FxFx merging scheme [26] was used for the generation of the background from SM single Higgs boson production, including gluon-gluon fusion (ggH), vector-boson fusion (VBFH), associated production with a Z or W boson (VH) and associated production with a top quark pair (ttH). The additional single Higgs production mode of top quark associated production (tHq) is also included, and was generated using MADGRAPH version-2.7 at LO.

The continuum background contribution comes from various SM processes. Most of the dominant backgrounds across all the final states are due to the $\gamma\gamma$+jets processes that are modeled with the SHERPA v.2.2.1 generator [28]. γ+jets, QCD-induced processes and WW processes are modeled with the PYTHIA 8 [27] generator.

Drell Yan and W production processes in association with photons and jets are modeled using MADGRAPH5 version-2.7 at LO. Finally, the $t\bar{t}$ process is generated using PowHEG v2, and $t\bar{t}W$, $t\bar{t}\gamma$, $t\bar{t}\gamma\gamma$, $Z\gamma$ are modeled using MADGRAPH5_AMCATNLO [24; 25; 26].

For these simulation samples, all are simulated with the Phase-2 upgraded CMS detector geometry using DELPHES fast simulation with average pile-up of 200 interactions and at $\sqrt{s} = 14$ TeV, the expected data-taking conditions at the HL-LHC.

6.4 Objects

Before applying final-state specific category selections, a common set of object selections is required for the various physics objects reconstructed event-by-event for each simulation sample. In order to maximize the number HH events saved, each simulation event is required to have at least one pair of photons, called a diphoton.

Photons used in this analysis are required to have a transverse momentum (p_T) above 25 GeV, and at least one photon with a p_T of 35 GeV within $|\eta| < 2.5$.

The relative isolation of the photon candidate, defined as sum of the p_T of all particles within a cone $(\Delta R = \sqrt{(\Delta \eta)^2 + (\Delta \phi)^2})$ of size 0.3 around the photon and divided the sum by the photon p_T, is required to be less than 0.3 and must pass a loose identification criteria corresponding to 90% signal efficiency.

Electrons are required to have p_T above 10 GeV within $|\eta| < 2.5$ excluding the ECAL transition region and must be isolated from photon candidates with an angular separation in the $\eta - \phi$ plane greater than $\Delta R = 0.4$. The transverse momenta of muons are required to be above 10 GeV and within $|\eta| < 2.5$, and they are required to be isolated from photon and electron candidates with an angular separation greater than $\Delta R = 0.4$. Hadronically decaying taus are required to have $p_T > 20$ GeV within $|\eta| < 2.5$, and are required to be separated from photon, electron and muon candidates with an angular separation greater than $\Delta R = 0.2$. The relative isolation of the electrons (muons) is required to be less than 0.3 (0.1).

Jets are reconstructed using the anti-k_T clustering method with a distance parameter of 0.4. They are required to have $p_T > 30$ GeV, be within $|\eta| < 5$ and to be well separated from the photon and lepton candidates with an angular separation greater than $\Delta R = 0.4$. The likelihood that a jet comes from b-quark hadronization, termed a b-tagging score, is computed using a deep neural network (DNN) based secondary vertex algorithm, DEEP-JET [71; 72].

6.5 Event Selections and Categorization

All events are required to have exactly two photons with an invariant mass in the range $100 < m_{\gamma\gamma} < 180$. The analysis is performed in mutually exclusive final states targeting decays of the vector bosons referred to as 1L (Semi-leptonic) and 2L (Fully-leptonic) final states for $WW\gamma\gamma$, and 1 τ or 2 τ final states for $\tau\tau\gamma\gamma$.

Here, lepton (L) refers to either an electron ($e^{\pm}$) or muon ($\mu^{\pm}$).

6.5.1 Semi-leptonic final state

Events fall into the Semi-leptonic (1L) analysis category if they contain at least one pre-selected diphoton pair, and contain exactly one electron or muon passing the selection criteria described in Section 6.4. This final state is expected to be the most sensitive of the three $WW\gamma\gamma$ channels due to the combination of a relatively large $W \rightarrow qq$ branching ratio, and the presence of a highly energy lepton from the $W \rightarrow \ell\nu$ decay.

In order to maximize the sensitivity of this final state, two multiclass DNNs are trained to separate the di-Higgs signal from the resonant single Higgs boson background and continuum background where the di-Higgs processes are labelled as HH, single Higgs backgrounds as H and all other background samples as continuum background.

During training, each class has a weight applied which scales the event loss such that the effective importance's of each of the three classes are equalized. This ensures that the network focuses on categorising all classes with an equal importance.

Two multiclass DNNs are trained, one which trains on one half of simulation events, and a second which trains on the other half of simulation events. This separation on simulation datasets allows one to apply the training performed with "even" events on the "odd" data set, and vice versa, to avoid any training bias.

The simulation sample variables used as inputs for the DNN trainings include the kine-matic variables such as p_T, η, ϕ and energy values of photons, jets, electrons and muons.

For photons, p_T and energy values are scaled by the diphoton mass in order to avoid the creation of an artificial resonance among continuum background processes. Additionally, the jet multiplicity, missing transverse energy and the invariant mass of the leading and subleading jets are utilized in the trainings.

The multiclass DNN outputs three DNN scores, one for each class, but only the HH output DNN score is used in the analysis. The HH DNN score distribution is shown in Figure 6.1.
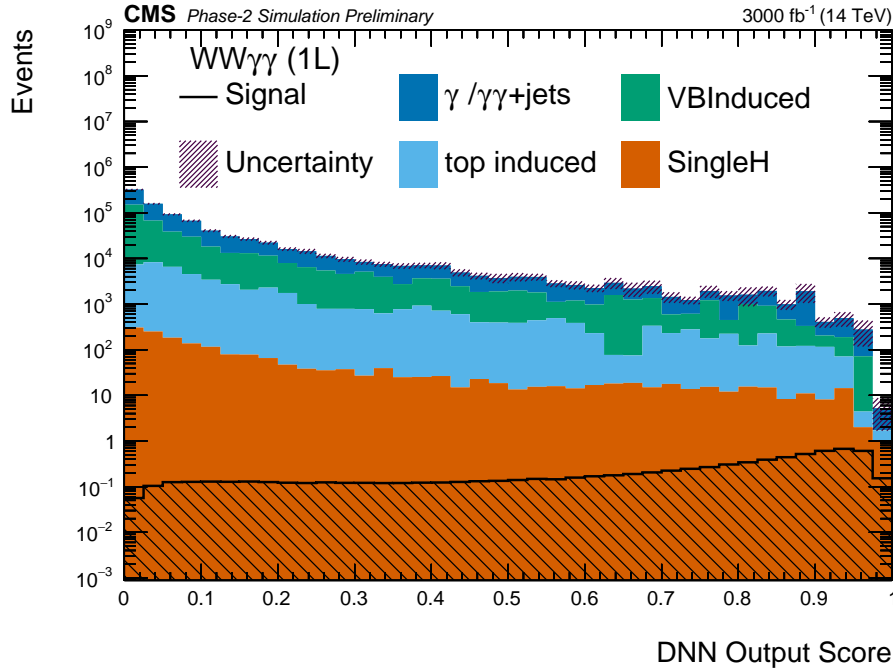

Figure 6.1: Semi-leptonic DNN output score distribution.

In order to further optimize the analysis sensitivity, events are partitioned into four categories making use of the *HH* node output score. The category boundaries are chosen such that the expected significance is maximized, and are shown in Table 6.1.

This categorization leads to an improved combined significance as opposed to using a single category, as multiple regions with reasonable signal sensitivities can be combined. Category four is the category with the highest signal purity and significance.

Categories	Definition
Category 1	$0.1 < $ DNN score $ < 0.6$
Category 2	$0.6 < $ DNN score $ < 0.8$
Category 3	$0.8 < $ DNN score $ < 0.92$
Category 4	DNN score $ > 0.92$

Table 6.1: Semi-leptonic final state DNN score categories.

6.5.2 Fully-leptonic final state

For events to fall into the Fully-leptonic category, they must contain at least one diphoton candidate, and at least two oppositely charged leptons (e^+e^-, $\mu^+\mu^-$, $e^\pm\mu^\mp$) passing the electron and muon object selections described in Section 6.4.

In order to save events with two leptonically decaying W bosons, events fall into the fully-leptonic category if they satisfy the selections listed in Table 6.2, where $\Delta R(l,l)$ is the ΔR between two leptons, m_{ll} is the mass of dilepton system and $m_{e\gamma}$ is the invariant mass of the leading electron and the leading photon in the events that have at least one electron.

Variable	Selection
$\Delta R(l,l)$	> 0.4
p_{T} of leading lepton	> 20
p_{T} of subleading lepton	> 10
E_T^{miss}	> 20
$p_T^{\gamma\gamma}$	> 91
m_{ll}	< 80 or > 100
number of medium-tagged b-jets	$= 0$
$|m_{e\gamma} - m_z|$	> 5

Table 6.2: Selection criteria of the Fully-leptonic Channel.

6.5.3 One Tau lepton final state

Events fall into the one τ category if they contain at least one diphoton candidate, exactly one hadronically decaying tau lepton, and exactly zero electrons and muons.

In order to maximize the sensitivity of this final state, a similar method to that of the

semi-leptonic final state described in Section 6.5.1 is followed. Namely, two multiclass deep neural networks (DNNs) are trained. In this case, the structure of the DNNs are the same as those from the semi-leptonic analysis, with the electron and muon input features replaced by the τ candidate's input features. The multiclass DNNs output three scores, but only the one which estimates the likelihood that an event is HH like is used in this analysis. The distribution of this DNN score is shown in Figure 6.2.
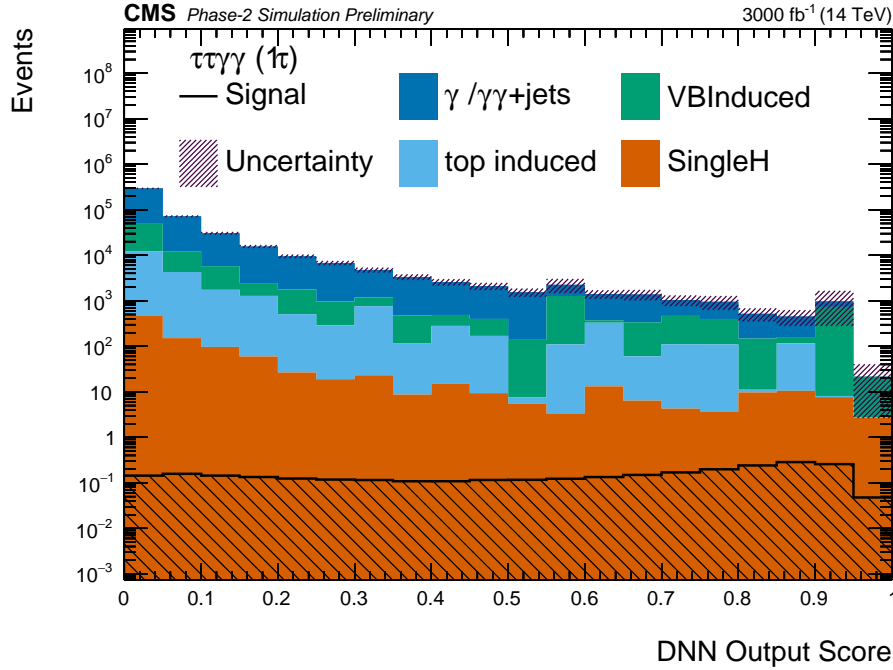

Figure 6.2: One tau DNN output score distribution.

Events are partitioned into two categories based on the DNN score. Category one corresponds to events where the DNN score lies between 0.1 and 0.65, while events with a DNN score higher than 0.65 are placed into category 2.

6.5.4 Two Tau leptons final state

Events fall into the two τ final state if they contain at least one diphoton candidate, at least two hadronically decaying taus, and zero electrons and photons. For the taus, it is required that they be oppositely charged because they are expected to come from a neutral Higgs

boson. In this final state category, no additional selections are required.

6.6   Systematic uncertainties

The contribution of systematic uncertainties have been divided in experimental and theoretical uncertainties. Because the samples in this analysis are exclusively simulation based, experimental uncertainties are estimated from simulation. The experimental uncertainties are shown in Table 6.3, and follow the common Phase II projection uncertainties folloiwing the Yellow Report recommendation described in Ref.[73]. Theoretical uncertainties are added on the ggHH signal and single Higgs boson processes, as described in Table 6.4.

Uncertainty Source	Input (%)
Luminosity	1
Diphoton trigger	2
$m_{\gamma\gamma}$ resolution	5
PhotonID	0.5/photon
electronID	0.5/electron
muonID	0.5/muon
tauID	2.5/tau
Tau energy scale	3
Jet energy Scale	3
b-tagging veto	3

Table 6.3: Experimental uncertainties considered in this study.

Process	Uncertainty Source		
	PDF $+\alpha_s$ (%)	QCD Scale (%)	m_{top} (%)
ggHH	± 3	+2.1/-4.9	+4.0/-18
ggH	+4.6/-6.7	± 3.2	-
VBFH	+0.5/-0.3	± 2.1	-
VH	+0.4/-0.7	± 1.8	-
ttH	+6/-9.2	± 3.5	-
tHq	+6.4/-14.7	± 3.6	-

Table 6.4: Theoretical uncertainties considered on the ggHH signal and single Higgs processes.

6.7 Results

The expected Phase-2 $m_{\gamma\gamma}$ distributions are shown in Figure 6.3 for the semi-leptonic $WW\gamma\gamma$ final state, and one tau $\tau\tau\gamma\gamma$ final state.

(a) Semi-leptonic final state   (b) One tau final state
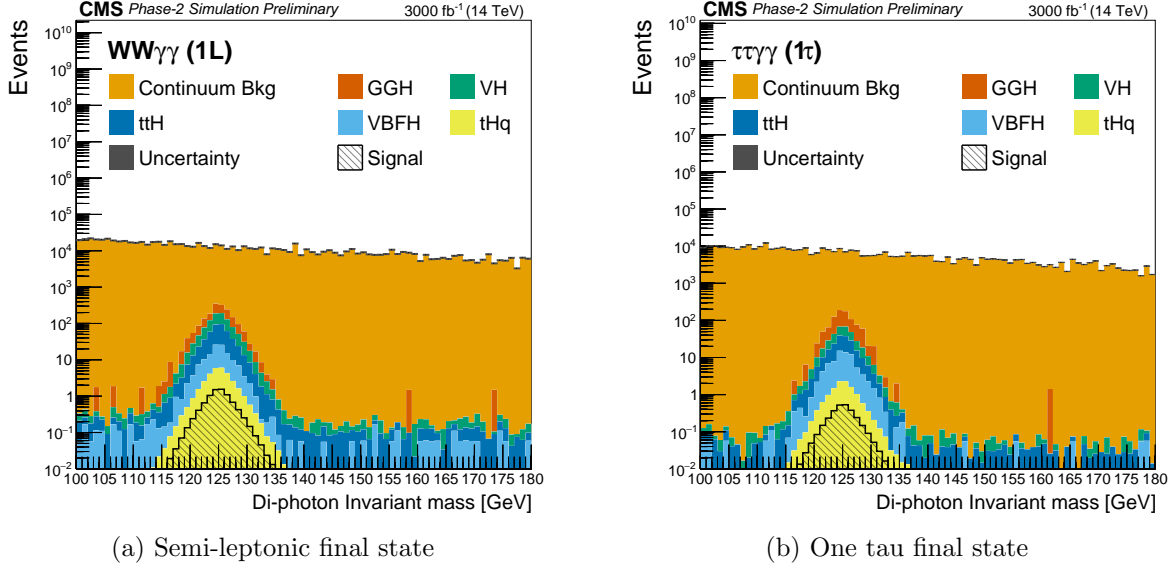
Figure 6.3: $m_{\gamma\gamma}$ distributions in the $WW\gamma\gamma$, Semi-leptonic (left) and $\tau\tau\gamma\gamma$, 1τ (right) final states.

Given the presence of high fluctuations in the $m_{\gamma\gamma}$ distribution of the continuum background across different categories, a falling exponential function is fit to the continuum background templates and used as the final background template for each category. After applying this exponential fit, and a gaussian fit to each HH and H template, the diphoton invariant mass distributions for the Semi-leptonic final state in its most sensitive category, the single fully-leptonic category and in the single 2τ final state category are shown in Figure 6.4, where signal HH and single Higgs templates are modelled as Gaussian functions fit to the diphoton mass distributions, and the continuum background is modelled by exponential functions. The (pseudo-)data are generated according to the fitted signal, single Higgs and continuum background contributions.

The expected signal significance is extracted by fitting the background-only $m_{\gamma\gamma}$ template
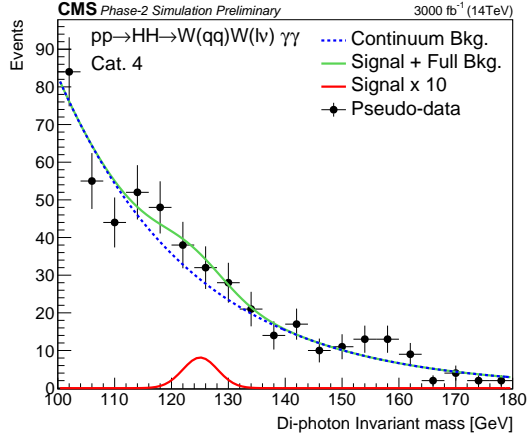
(a) Semi-leptonic final state, Category 4
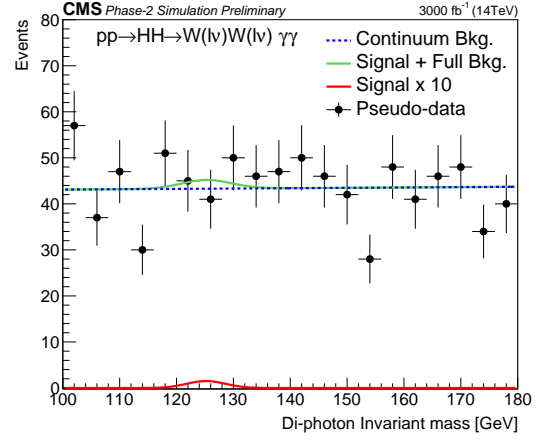
(b) Fully-leptonic final state
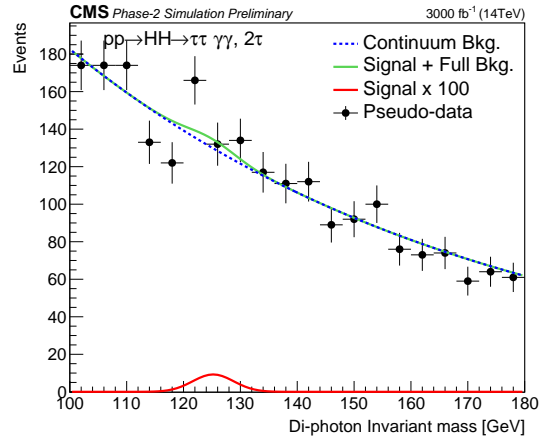
(c) Two taus final state

Figure 6.4: $m_{\gamma\gamma}$ distributions in the $WW\gamma\gamma$, Semi-leptonic (top left), Fully-leptonic (top right) and $\tau\tau\gamma\gamma$, 2τs (bottom) final states.

to the signal + background template simultaneously in all categories, following a binned maximum likelihood approach, with all systematic uncertainties treated as nuisance parameters with log-normal distributions. The correlations among different sources of uncertainties are taken into account while the different final states are considered as independent channels in the fit.

The significance values obtained are shown in Table 6.5 for the WW$\gamma\gamma$ and $\tau\tau\gamma\gamma$ final states along with their combination.

Final State	Significance (stat+exp+theory)
$WW\gamma\gamma$	0.21
$\tau\tau\gamma\gamma$	0.08
Combination	0.22

Table 6.5: Expected HL-LHC significances (σ) results of the WW$\gamma\gamma$ and $\tau\tau\gamma\gamma$ processes with their combination.

A combined significance of 0.22σ is extracted, combining the $WW\gamma\gamma$ and $\tau\tau\gamma\gamma$ categories.

6.8 Summary

A projection of the sensitivity of non-resonant Higgs boson pair production in the WW$\gamma\gamma$ and $\tau\tau\gamma\gamma$ final states has been performed, using simulated proton-proton collision events at a center-of-mass energy of 14 TeV and integrated luminosity of 3000 fb^{-1} at the future HL-LHC. Additionally, the response of the future Phase II CMS detector has been simulated. For the $WW\gamma\gamma$ and one tau $\tau\tau\gamma\gamma$ final states of this analysis, the analysis strategy and techniques from the Run 2 $WW\gamma\gamma$ analysis are used.

Combining all final state categories and including systematic uncertainties, a combined expected significance of 0.22 σ is measured.

When considering a projection analysis, it is important consider a few caveats to the result. The first is that because the analysis is simulation only, it is not possible to make

the use of data-driven techniques, such as the one used for the Fully-hadronic final state of the Run 2 $WW\gamma\gamma$ analysis. Additionally, as the HL-LHC and Phase II CMS detector have not yet been assembled, physicists have not yet had a chance to study this new detector's response to new data-taking conditions. Such studies can often include the optimization of the detector's ability to identify particles, and thus can lead to improved identification and analysis sensitivity.

Chapter 7

Conclusions and outlook

The Standard Model of particle physics, while widely successful and consistent with the majority of physical observations, does not account for all observed phenomena. Through the ongoing physics studies by the experiments at the CERN LHC, physicists continue to attempt to answer questions about the fundamental nature of the universe, and test the standard model by searching for and measuring new processes. Part of this analysis program includes the search for Higgs pair production, as it provides direct access to one of the unmeasured parameters of the SM: The Higgs self-coupling. As Higgs pair production is a rare process, it is vital to include as many di-Higgs decay channels as possible to maximize the chances for discovery at the future HL-LHC, and an eventual precise measurement of the Higgs self-coupling.

To this end, the first search for Higgs pair production in the WW$\gamma\gamma$ final state has been performed by the CMS experiment. The analysis made use of data collected by the CMS detector from 2016-2018, corresponding to an integrated luminosity of 138 fb^{-1}, from proton-proton collisions at a center-of-mass energy of 13 TeV. The analysis resulted in an observed (expected) 95% CL_s upper limit on the di-Higgs production cross-section of 3.0 (1.7) pb, corresponding to about 97 (53) times the standard model prediction. In addition to the search for the SM interpretation of di-Higgs, scans of modified SM and purely BSM coupling parameters in an EFT framework result in an observed (expected) constraint on the Higgs self-coupling of -25.9 (-14.5) to 24.1 (18.4) times its standard model value, and a constraint on the magnitude of the direct coupling of two top quarks to two Higgs bosons of -2.4 (-1.7) to 2.9 (2.2) at a 95% CL_s. Additionally, observed (expected) 95% CL_s upper limits are placed on twenty EFT benchmark scenarios ranging from 1.7 - 6.2 (1.0 - 3.9) pb.

As it is not yet possible to experimentally observe Higgs pair production with the Run 2 dataset due to its low production cross section, the optimization of the CMS detector for LHC Run 3 will be crucial for improving the detector's efficiency at triggering on Higgs pair production events. For this analysis and similar analyses, the use of the CMS electromagnetic calorimeter is of vital importance for the detection and accurate reconstruction of photons. In order to maintain and improve the sensitivity of this and other analyses using photons and electrons, during LS2, several optimizations of the CMS ECAL were investigated. This included updating the parameters of the on-detector energy reconstruction algorithm to account for updated ECAL signal signature shapes, and the preliminary investigation of a new feature to be used for out-of-time signal tagging. The re-optimization of the energy reconstruction parameters is expected to improve the accuracy of ECAL energy measurements used as input to the CMS level-1 trigger, which can potentially increase the detector's efficiency at triggering on di-Higgs events. Additionally, during LS2, the existence of a second amplitude filter in the on-detector ECAL electronics was discovered, which combines with the standard amplitude filter to form "double weights". Its existence and functionality was proven through tests at a test electronics setup, and at the CMS ECAL itself. Its functionality was then added to the CMS ECAL emulator in order to test its impact on previously taken CMS data. Since then, emulator and data studies have been performed in order to test the potential removal of anomalous signals called ECAL spikes. Initial studies show that double weights may be able to remove some ECAL spikes via out-of-time tagging, with a minimal effect on ECAL signals. The potential gain of this feature may include the removal of ECAL spikes at L1, allowing CMS to trigger on more physics events including di-Higgs events, which may improve the sensitivity of di-Higgs analyses using the LHC Run 3 dataset. The possibility of using double weights to tag out-of-time physics signatures may also be investigated in the future, which may potentially improve the sensitivity of analyses targeting BSM scenarios, including those which include the Higgs boson as a bridge to BSM physics.

As LS2 has ended, so has the commissioning of the CMS detector for LHC Run 3. During this commissioning period, the CMS ECAL operations teams all performed well and are in good shape for operating the CMS ECAL and ES for LHC Run 3. During commissioning, the ECAL and preshower detectors were turned on, various tests on electronics were performed, and the commissioning of new features including double weights was performed.

While the past Run 2 dataset has been analyzed, and the CMS ECAL is continuing to optimize its features for the Run 3 dataset, the first Phase II projection of the search for Higgs pair production in the $WW\gamma\gamma$ and $\tau\tau\gamma\gamma$ final states with the Phase-II CMS detector has been performed. The analysis strategy makes use of the Run 2 analysis strategy, including the use of deep neural networks in order to improve expected sensitivity, resulting in an expected significance of 0.22 σ.

During LHC Run 3 and at the future HL-LHC, the multitude of expertise's in the field of particle physics will continue their endeavors: Engineers and technicians will continue to maintain the LHC accelerator and CMS detector, computing experts and maintainers will continue to keep the CERN offline computing resources alive, and particle physicists will continue to develop novel analysis techniques in order to perform statistical interpretations of the newly collected datasets in order to continue answering questions about the fundamental nature of the universe.

Bibliography

[1] Georges Aad et al. Observation of a new particle in the search for the Standard Model Higgs boson with the ATLAS detector at the LHC. *Phys. Lett. B*, 716:1–29, 2012.

[2] Serguei Chatrchyan et al. Observation of a New Boson at a Mass of 125 GeV with the CMS Experiment at the LHC. *Phys. Lett. B*, 716:30–61, 2012.

[3] Serguei Chatrchyan et al. Observation of a New Boson with Mass Near 125 GeV in pp Collisions at $\sqrt{s} = 7$ and 8 TeV. *JHEP*, 06:081, 2013.

[4] The Tracker Group of the CMS Collaboration. The CMS Phase-1 Pixel Detector Upgrade. Technical report, CERN, Geneva, Mar 2020.

[5] A.M. Sirunyan et al. Performance of the CMS level-1 trigger in proton-proton collisions at $\sqrt{s} = 13$ tev, journal = Journal of Instrumentation. 15(10):P10017–P10017, oct 2020.

[6] Tommi Markkanen, Arttu Rajantie, and Stephen Stopyra. Cosmological aspects of higgs vacuum metastability. *Frontiers in Astronomy and Space Sciences*, 5, 2018.

[7] D. de Florian et al. Handbook of LHC Higgs Cross Sections: 4. Deciphering the Nature of the Higgs Sector. 2016.

[8] Koji Nakamura, Kenji Nishiwaki, Kin-ya Oda, Seong Chan Park, and Yasuhiro Yamamoto. Di-higgs enhancement by neutral scalar as probe of new colored sector. *Eur. Phys. J.*, C77(5):273, 2017.

[9] Christoph Englert and Joerg Jaeckel. Probing the Symmetric Higgs Portal with Di-Higgs Production. 2019.

[10] Tania Robens, Tim Stefaniak, and Jonas Wittbrodt. Two-real-scalar-singlet extension of the SM: LHC phenomenology and benchmark scenarios. 2019.

[11] Yong Tang. Implications of LHC Searches for Massive Graviton. *JHEP*, 08:078, 2012.

[12] Alexandra Carvalho, Martino Dall'Osso, Tommaso Dorigo, Florian Goertz, Carlo A. Gottardo, and Mia Tosi. Higgs Pair Production: Choosing Benchmarks With Cluster Analysis. *JHEP*, 04:126, 2016.

[13] G. Buchalla, M. Capozi, A. Celis, G. Heinrich, and L. Scyboz. Higgs boson pair production in non-linear Effective Field Theory with full m_t-dependence at NLO QCD. *JHEP*, 09:057, 2018.

[14] Matteo Capozi and Gudrun Heinrich. Exploring anomalous couplings in Higgs boson pair production through shape analysis. *JHEP*, 03:091, 2020.

[15] M. Aaboud et al. Search for higgs boson pair production in the $\gamma\gamma WW^*$ channel using pp collision data recorded at $\sqrt{s} = 13$ TeV with the atlas detector. *The European Physical Journal C*, 78(12):1007, Dec 2018.

[16] Alexandra Carvalho, Martino Dall'Osso, Pablo De Castro Manzano, Tommaso Dorigo, Florian Goertz, Maxime Gouzevich, and Mia Tosi. Analytical parametrization and shape classification of anomalous HH production in the EFT approach. 7 2016.

[17] Giuseppe Degrassi, Pier Paolo Giardino, Fabio Maltoni, and Davide Pagani. Probing the Higgs self coupling via single Higgs production at the LHC. *JHEP*, 12:080, 2016.

[18] Fabio Maltoni, Davide Pagani, Ambresh Shivaji, and Xiaoran Zhao. Trilinear Higgs coupling determination via single-Higgs differential measurements at the LHC. *Eur. Phys. J. C*, 77:887, 2017.

[19] A. M. Sirunyan et al. Measurements of Higgs boson properties in the diphoton decay channel in proton-proton collisions at $\sqrt{s} = 13$ TeV. *JHEP*, 11:185, 2018.

[20] Paolo Nason. A New method for combining NLO QCD with shower Monte Carlo algorithms. *JHEP*, 11:040, 2004.

[21] Stefano Frixione, Paolo Nason, and Carlo Oleari. Matching NLO QCD computations with Parton Shower simulations: the POWHEG method. *JHEP*, 11:070, 2007.

[22] Simone Alioli, Paolo Nason, Carlo Oleari, and Emanuele Re. A general framework for implementing NLO calculations in shower Monte Carlo programs: the POWHEG BOX. *JHEP*, 06:043, 2010.

[23] G. Heinrich, S.P. Jones, M. Kerner, G. Luisoni, and L. Scyboz. Probing the trilinear Higgs boson coupling in di-Higgs production at NLO QCD including parton shower effects. *JHEP*, 06:066, 2019.

[24] J. Alwall, R. Frederix, S. Frixione, V. Hirschi, F. Maltoni, O. Mattelaer, H. S. Shao, T. Stelzer, P. Torrielli, and M. Zaro. The automated computation of tree-level and next-to-leading order differential cross sections, and their matching to parton shower simulations. *JHEP*, 07:079, 2014.

[25] Pierre Artoisenet, Rikkert Frederix, Olivier Mattelaer, and Robbert Rietkerk. Automatic spin-entangled decays of heavy resonances in Monte Carlo simulations. *JHEP*, 03:015, 2013.

[26] Rikkert Frederix and Stefano Frixione. Merging meets matching in MC@NLO. *JHEP*, 12:061, 2012.

[27] Torbjörn Sjöstrand, Stefan Ask, Jesper R. Christiansen, Richard Corke, Nishita Desai, Philip Ilten, Stephen Mrenna, Stefan Prestel, Christine O. Rasmussen, and Peter Z.

Skands. An Introduction to PYTHIA 8.2. *Comput. Phys. Commun.*, 191:159–177, 2015.

[28] Enrico Bothmann et al. Event Generation with Sherpa 2.2. *SciPost Phys.*, 7(3):034, 2019.

[29] Vardan Khachatryan et al. Event generator tunes obtained from underlying event and multiparton scattering measurements. *Eur. Phys. J.*, C76(3):155, 2016.

[30] Albert M Sirunyan et al. Extraction and validation of a new set of CMS PYTHIA8 tunes from underlying-event measurements. 2019.

[31] Richard D. Ball et al. Parton distributions for the LHC Run II. *JHEP*, 04:040, 2015.

[32] S. Agostinelli et al. Geant4a simulation toolkit. *Nuclear Instruments and Methods in Physics Research Section A: Accelerators, Spectrometers, Detectors and Associated Equipment*, 506(3):250–303, 2003.

[33] A. M. Sirunyan et al. Particle-flow reconstruction and global event description with the CMS detector. *JINST*, 12:P10003, 2017.

[34] Eleftherios Spyromitros-Xioufis, William Groves, Grigorios Tsoumakas, and Ioannis Vlahavas. Multi-target regression via input space expansion: treating targets as inputs. *Mach Learn*, 104, 2016.

[35] A.M. Sirunyan et al. Identification of heavy-flavour jets with the CMS detector in pp collisions at 13 TeV. *JINST*, 13(05):P05011, 2018.

[36] Lloyd S. Shapley. *A Value for n-Person Games*. RAND Corporation, Santa Monica, CA, 1952.

[37] Glen Cowan, Kyle Cranmer, Eilam Gross, and Ofer Vitells. Asymptotic formulae for likelihood-based tests of new physics. *The European Physical Journal C*, 71(2), Feb 2011.

[38] Albert M Sirunyan et al. Measurements of $t\bar{t}H$ Production and the CP Structure of the Yukawa Interaction between the Higgs Boson and Top Quark in the Diphoton Decay Channel. *Phys. Rev. Lett.*, 125(6):061801, 2020.

[39] A. M. et al. Sirunyan. Measurements of $t\bar{t}h$ production and the cp structure of the yukawa interaction between the higgs boson and top quark in the diphoton decay channel. *Phys. Rev. Lett.*, 125:061801, Aug 2020.

[40] P.D. Dauncey, M. Kenzie, N. Wardle, and G.J. Davies. Handling uncertainties in background shapes: the discrete profiling method. *Journal of Instrumentation*, 10(04):P04015–P04015, Apr 2015.

[41] Massimiliano Grazzini, Gudrun Heinrich, Stephen Jones, Stefan Kallweit, Matthias Kerner, Jonas M. Lindert, and Javier Mazzitelli. Higgs boson pair production at NNLO with top quark mass effects. *JHEP*, 05:059, 2018.

[42] Albert M Sirunyan et al. Precision luminosity measurement in proton-proton collisions at $\sqrt{s} = 13$ TeV in 2015 and 2016 at CMS. *Eur. Phys. J. C*, 81:800, 2021.

[43] CMS Collaboration. CMS luminosity measurement for the 2017 data-taking period at $\sqrt{s} = 13$ TeV. CMS Physics Analysis Summary CMS-PAS-LUM-17-004, 2018.

[44] CMS Collaboration. CMS luminosity measurement for the 2018 data-taking period at $\sqrt{s} = 13$ TeV. CMS Physics Analysis Summary CMS-PAS-LUM-18-002, 2019.

[45] Vardan Khachatryan et al. Performance of Electron Reconstruction and Selection with the CMS Detector in Proton-Proton Collisions at $\sqrt{s} = 8$ TeV. *JINST*, 10(06):P06005, 2015.

[46] A. M. Sirunyan et al. Performance of the CMS muon detector and muon reconstruction with proton-proton collisions at $\sqrt{s} = 13$ TeV. *JINST*, 13:P06015, 2018.

[47] Vardan Khachatryan et al. Jet energy scale and resolution in the CMS experiment in pp collisions at 8 TeV. *JINST*, 12(02):P02014, 2017.

[48] Alexander L. Read. Presentation of search results: The CL_s technique. *J. Phys. G*, 28:2693, 2002.

[49] Thomas Junk. Confidence level computation for combining searches with small statistics. *Nucl. Instrum. Meth. A*, 434:435, 1999.

[50] Glen Cowan, Kyle Cranmer, Eilam Gross, and Ofer Vitells. Asymptotic formulae for likelihood-based tests of new physics. *Eur. Phys. J. C*, 71:1554, 2011. [Erratum: Eur.Phys.J.C 73, 2501 (2013)].

[51] CMS-DP-2019-031: CMS ECAL trigger plots. https://cds.cern.ch/record/2690933, Sep 2019.

[52] CMS ECAL public plots: CMS-DP-2019-031. https://cmsdpgplots.web.cern.ch/#/ecalapproved/CMS-DP-2019_031, 2019.

[53] CMS-DP-2022-016: ECAL trigger for Run 3:. https://cds.cern.ch/record/2812785, Jun 2022.

[54] CMS ECAL public plots: CMS-DP-2022-016. https://cmsdpgplots.web.cern.ch/#/ecalapproved/CMS-DP-2022_016, Jun 2022.

[55] D A Petyt and. Mitigation of anomalous APD signals in the CMS electromagnetic calorimeter. *Journal of Physics: Conference Series*, 404:012043, dec 2012.

[56] CMS-DP-2022-007: ECAL trigger for Run 3. https://cds.cern.ch/record/2808229, Apr 2022.

[57] CMS ECAL public plots: CMS-DP-2022-007. https://cmsdpgplots.web.cern.ch/#/ecalapproved/CMS-DP-2022_007, Apr 2022.

[58] ECAL emulator development in CMSSW. `https://github.com/cms-sw/cmssw/pull/33349`, 2021.

[59] CMS-DP-2012-008: ECAL Detector Performance Plots: more on 2011 data. `http://cds.cern.ch/record/1457923`, Jun 2012.

[60] CMS ECAL public plots: CMS-DP-2012-008. `https://cmsdpgplots.web.cern.ch/#/ecalapproved/CMS-DP-2012_008`, Jun 2012.

[61] S. Chatrchyan et al. The CMS Experiment at the CERN LHC. *JINST*, 3:S08004, 2008.

[62] Technical Proposal for the Phase-II Upgrade of the CMS Detector. CMS Technical Proposal CERN-LHCC-2015-010. LHCC-P-008. CMS-TDR-15-02, 2015.

[63] CMS Collaboration. The Phase-2 Upgrade of the CMS Tracker. CMS Technical Design Report CERN-LHCC-2017-009. CMS-TDR-014, 2017.

[64] CMS Collaboration. The Phase-2 Upgrade of the CMS Barrel Calorimeters Technical Design Report. CMS Technical Design Report CERN-LHCC-2017-011. CMS-TDR-015, 2017.

[65] CMS Collaboration. The Phase-2 Upgrade of the CMS Endcap Calorimeter. CMS Technical Design Report CERN-LHCC-2017-023. CMS-TDR-019, 2017.

[66] CMS Collaboration. The Phase-2 Upgrade of the CMS Muon Detectors. CMS Technical Design Report CERN-LHCC-2017-012. CMS-TDR-016, 2017.

[67] Collaboration CMS. A MIP Timing Detector for the CMS Phase-2 Upgrade. Technical report, CERN, Geneva, Mar 2019.

[68] The Phase-2 Upgrade of the CMS Level-1 Trigger. Technical report, CERN, Geneva, Apr 2020. Final version.

[69] CMS Collaboration. The Phase-2 Upgrade of the CMS Data Acquisition and High Level Trigger. Technical report, CERN, Geneva, Mar 2021. This is a temporary submission, just to get the LHCC reference number, to be used in this and other CMS documents.

[70] CMS Collaboration. Expected performance of the physics objects with the upgraded CMS detector at the HL-LHC. Technical Report CMS-NOTE-2018-006. CERN-CMS-NOTE-2018-006, 2018.

[71] Performance of the DeepJet b tagging algorithm using 41.9/fb of data from proton-proton collisions at 13TeV with Phase 1 CMS detector. Technical Report CMS-DP-2018-058, Nov 2018.

[72] Emil Bols, Jan Kieseler, Mauro Verzetti, Markus Stoye, and Anna Stakia. Jet Flavour Classification Using DeepJet. *JINST*, 15(12):P12012, 2020.

[73] Andrea Dainese, Michelangelo Mangano, Andreas B Meyer, Aleandro Nisati, Gavin Salam, and Mika Anton Vesterinen. Report on the Physics at the HL-LHC, and Perspectives for the HE-LHC. Technical report, Geneva, Switzerland, 2019.

[74] Pierre Baldi, Peter Sadowski, and Daniel Whiteson. Searching for exotic particles in high-energy physics with deep learning. *Nature communications*, 5:4308, 07 2014.

APPENDIX A

Deep Neural Network Employment

A deep neural network (DNN) is a multi-layered network of inter-connected mathematical functions that performs a transformation between a set of input values and a set of output values. The coefficients (weights) within these functions can be varied (trained) to obtain the desired output. Typically, these are varied in an iterative procedure in which a loss-function is used as a metric of the performance and weights are adapted in order to minimise this metric. There are many applications for deep neural networks thus, there are several types of problems they can be used to solve and infinite variations in the implementation. In this analysis supervised trainings of deep neural networks are performed which means the training dataset is fully-labelled. We use the information on the final state physics objects recorded by the CMS detector as input values where each event is labelled as either "signal" or "background". The aim of the network is to use the input features to predict whether an event is from the signal or background process.

Deep neural networks are very adept at uncovering small signals amongst much larger backgrounds. From very basic features, the network can learn how they (and their correlations) can be used to distinguish signal from background. This is usually much more powerful than the cut-based approach which optimises cut values sequentially to maximise signal acceptance and background rejection simultaneously. Furthermore, one does not need to hand-craft complicated input features with large discriminatory power. If such a feature can be constructed using low-level information (e.g. four-vectors of physics objects), then it is deducible provided the network is given the required low-level information [74].

In this analysis, a deep neural network is used to distinguish between the di-Higgs $WW\gamma\gamma$, signal process and the major backgrounds. The signal signature varies depending on the

targeted decay of the W bosons and therefore so do the dominant backgrounds. As a result, networks are trained separately, each targeting a specific final state. Once trained, the neural network should predict values close to one for signal-like events and zero for background-like events. The distribution output by the DNN is used to further categorise events in a way that maximises the signal significance in the categories most sensitive to the signal. The $m_{\gamma\gamma}$ distribution of events within these categories make up independent templates that are used as input to the maximum likelihood fit. All networks have been trained using Keras 2.3.1 with the TensorFlow backend.

APPENDIX B

DNN Input Variables LO to NLO Reweighting

This section contains ratio plots for each Semi-Leptonic DNN input variable between the sum of 12 LO Benchmarks plus the SM LO point, and the 2017 SM at NLO sample. The LO samples all have LO to NLO reweighting applied as described in Section 4.2. There is slight disagreement observed, indicating the network is suboptimal, but because these events are only used for training there is no bias introduced in the analysis from any disagreement in these ratios. In addition, the amount of disagreement observed is not expected to have a detrimental effect on the performance of the network.
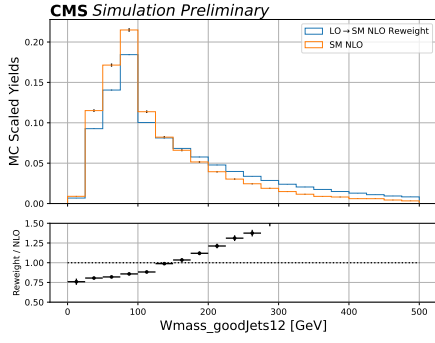
(a) m_{jj}
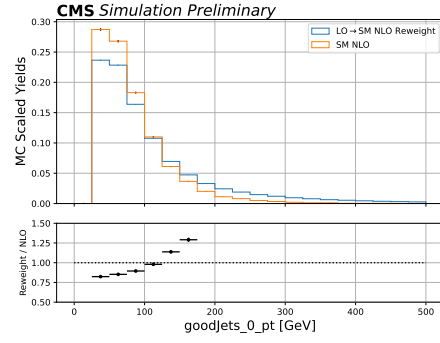
(b) Leading Jet p_T

Figure B.1: Invariant mass of the two leading jets, leading jet p_{T}
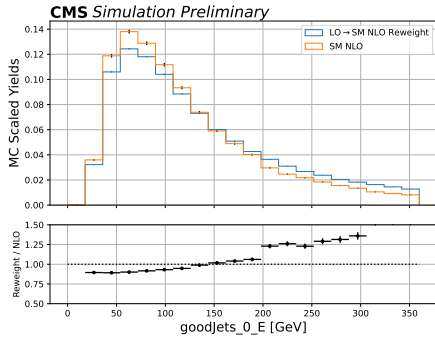
(a) Leading jet Energy
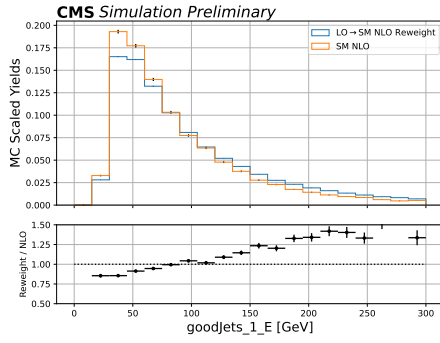
(b) Subleading Jet Energy

Figure B.2: Leading and subleading jet energy
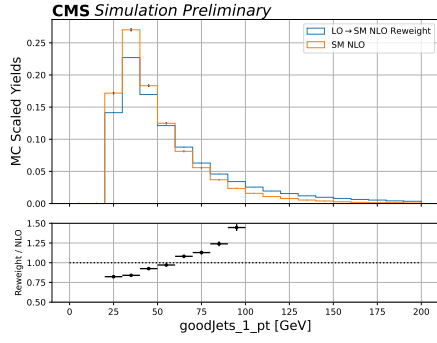
(a) Subleading Jet p_T
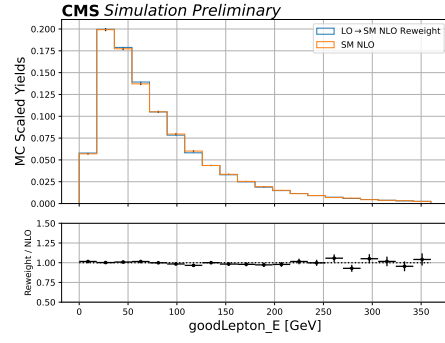
(b) Lepton Energy

Figure B.3: Subleading jet p_T, lepton energy
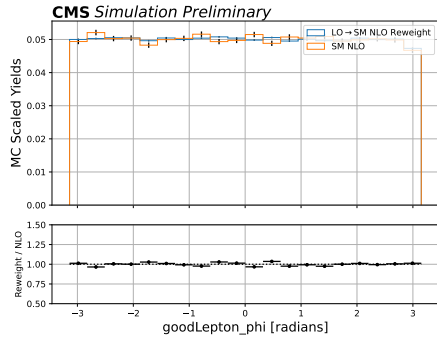
(a) Good Lepton ϕ
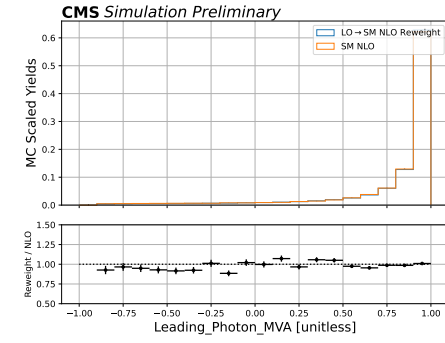
(b) Leading Photon MVA

Figure B.4: Lepton ϕ, leading photon MVA
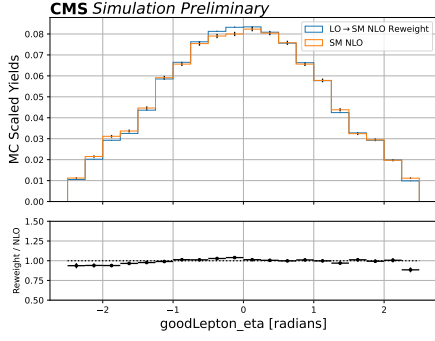
(a) Good Lepton η (b) Subleading Jet η
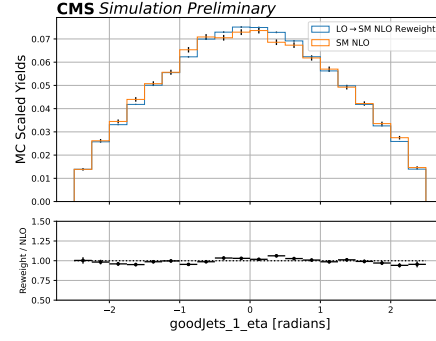
Figure B.5: Lepton η, subleading jet η
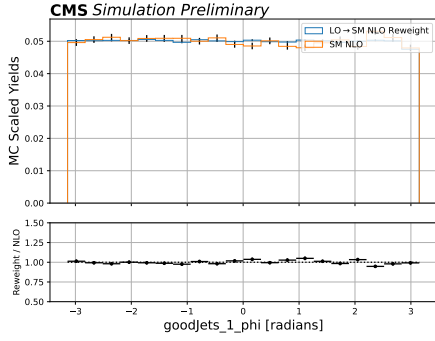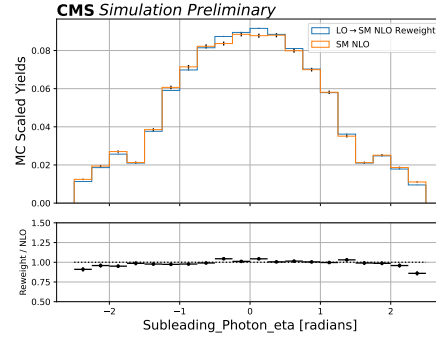
(a) Subleading Jet ϕ (b) Subleading Photon η

Figure B.6: Subleading jet ϕ, subleading photon η
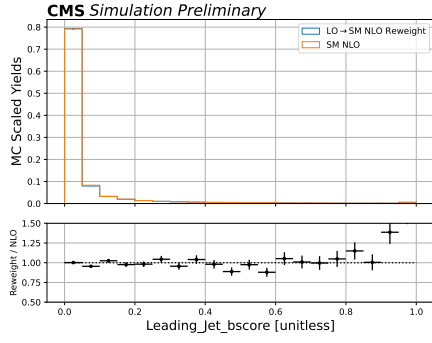
(a) Leading Jet b-tagging score
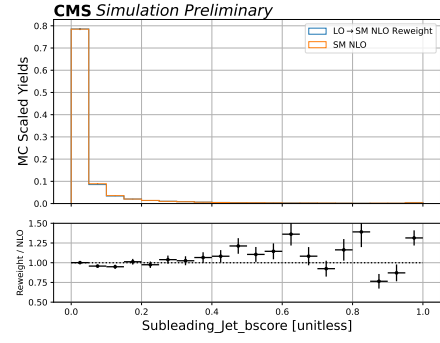
(b) Subleading Jet b-tagging score

Figure B.7: Leading and subleading jet b-tagging score
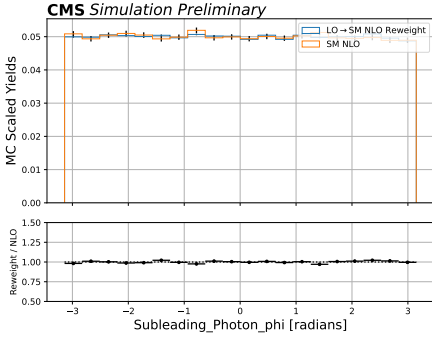
(a) Subleading Photon ϕ
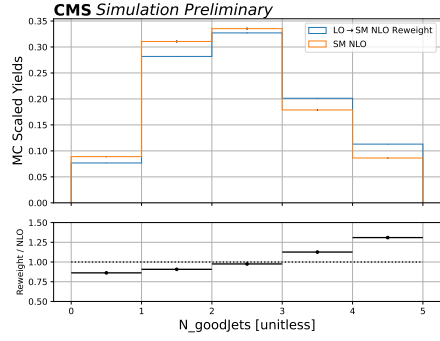
(b) Number of jets

Figure B.8: Subleading photon ϕ, number of jets
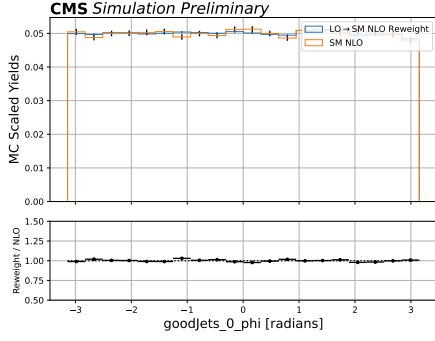
(a) Leading Jet ϕ
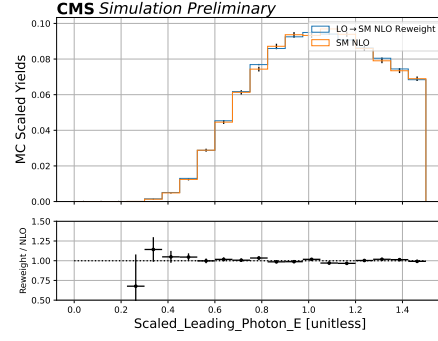
(b) Scaling Leading Photon E

Figure B.9: Leading jet ϕ, leading photon energy over $m_{\gamma\gamma}$
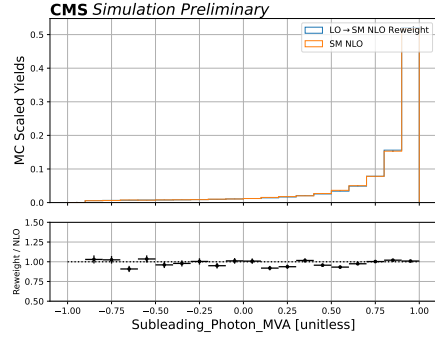
(a) Subleading Photon MVA
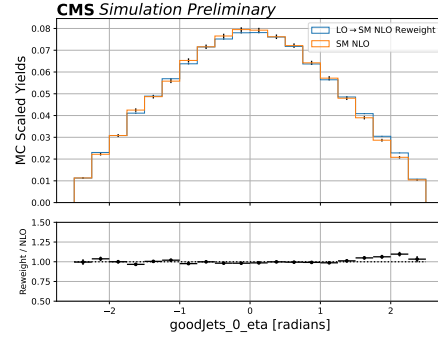
(b) Leading Jet η

Figure B.10: Subleading photon MVA, leading jet η
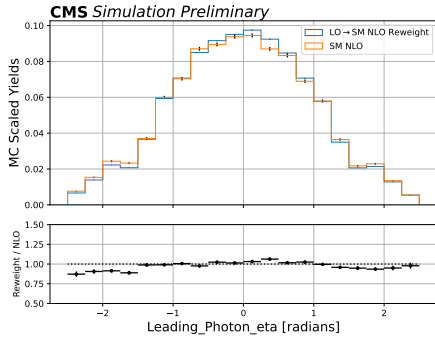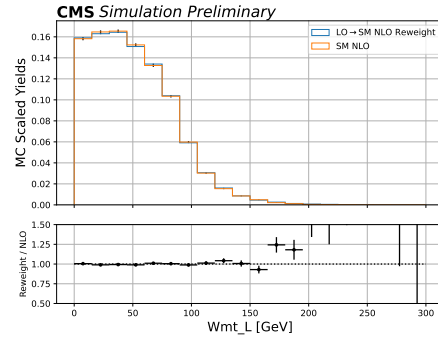
(a) Leading Photon η

(b) Transverse Mass of lepton and MET

Figure B.11: Leading photon η, transverse W mass

B.1   Systematic Impacts

The systematic impacts for the Run 2 combination of the Semi-Leptonic, Fully-Hadronic and Fully-Leptonic categories combined with Single Higgs processes modeled in all categories are shown in Figures B.12 , B.13 , B.14 , B.15 , where signal strength is set to the expected limit.

Note: unconstrained systematics have been removed from these impact plots in order to be able to view the impacts of other systematics.

In addition, the largest impact in all cases due to the HH theory uncertainty, including the ggHH QCD scale uncertainty and top mass uncertainty amounting to a log normal uncertainty of +6% / -23%, has been removed so that the other impacts are more visible.
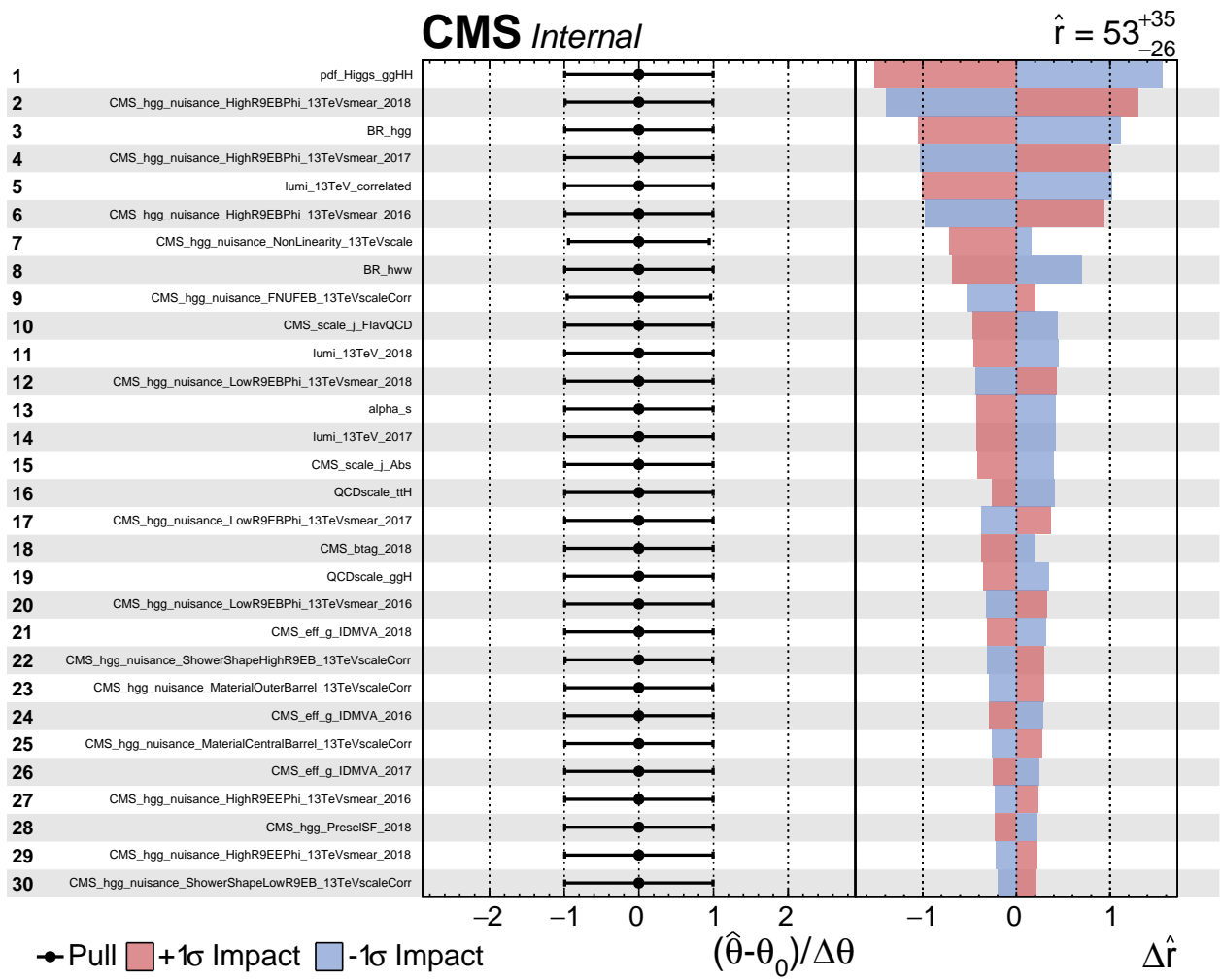
Figure B.12: Combined Run2 Expected Systematic Impacts: Page 1
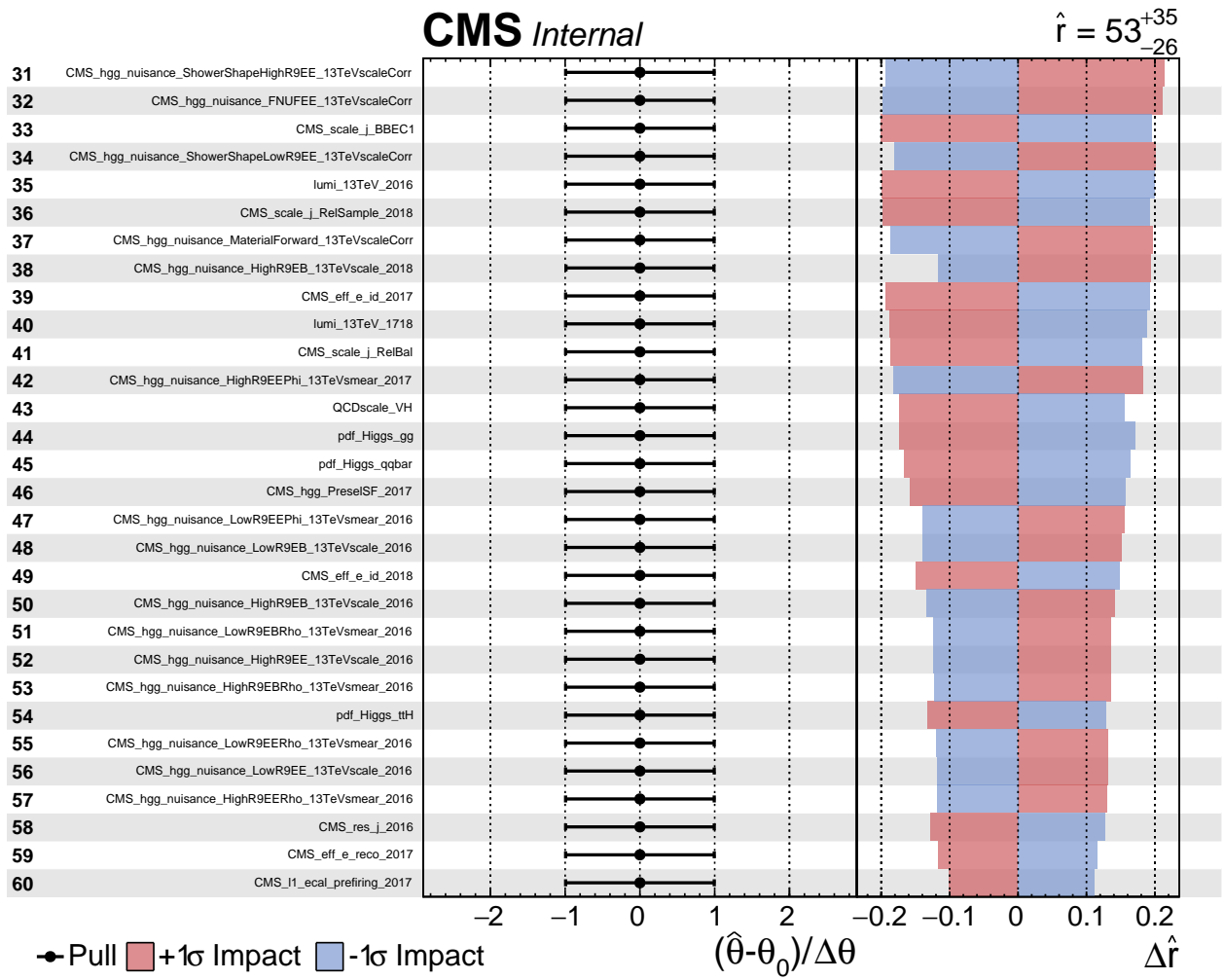
Figure B.13: Combined Run2 Expected Systematic Impacts: Page 2
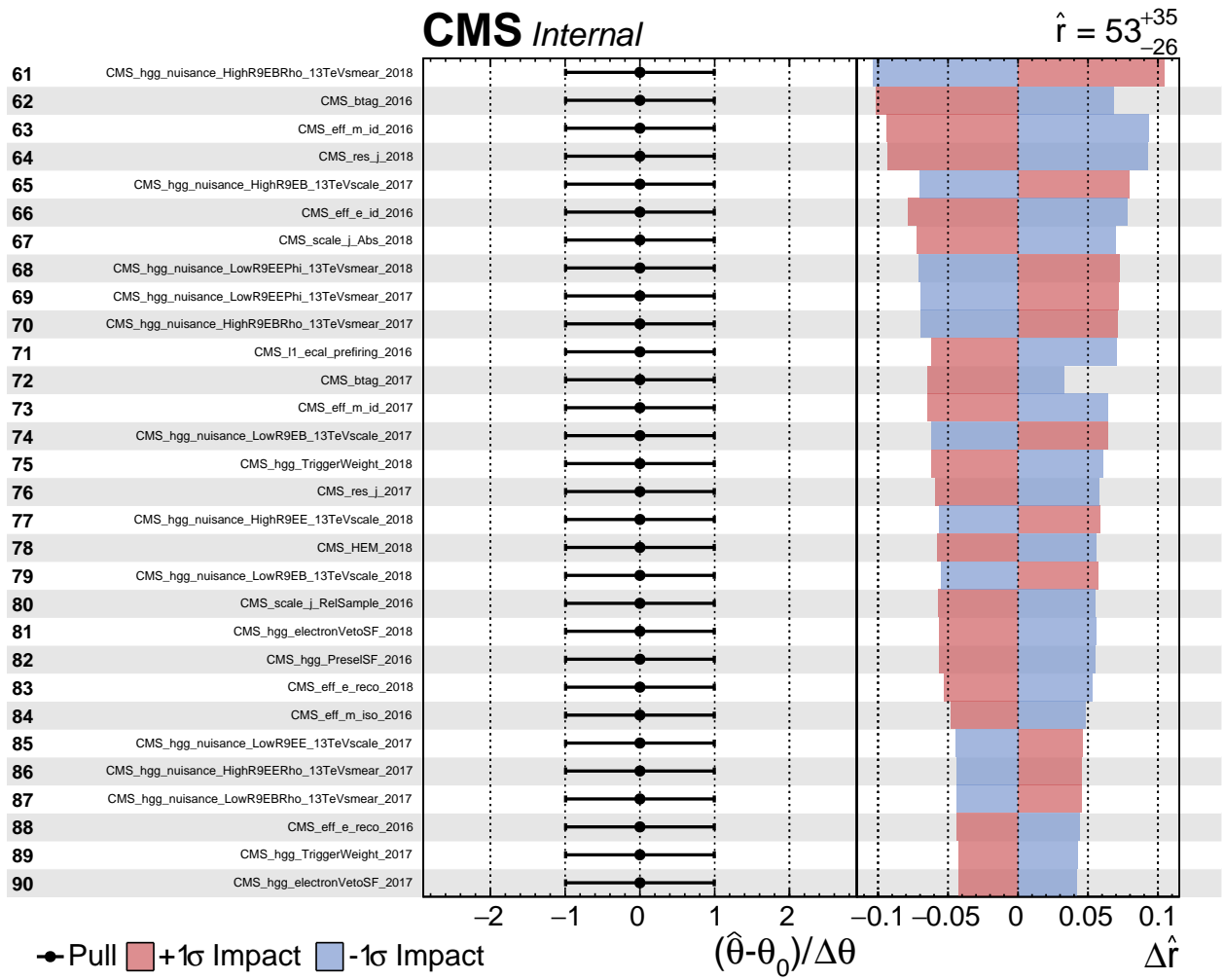
Figure B.14: Combined Run2 Expected Systematic Impacts: Page 3
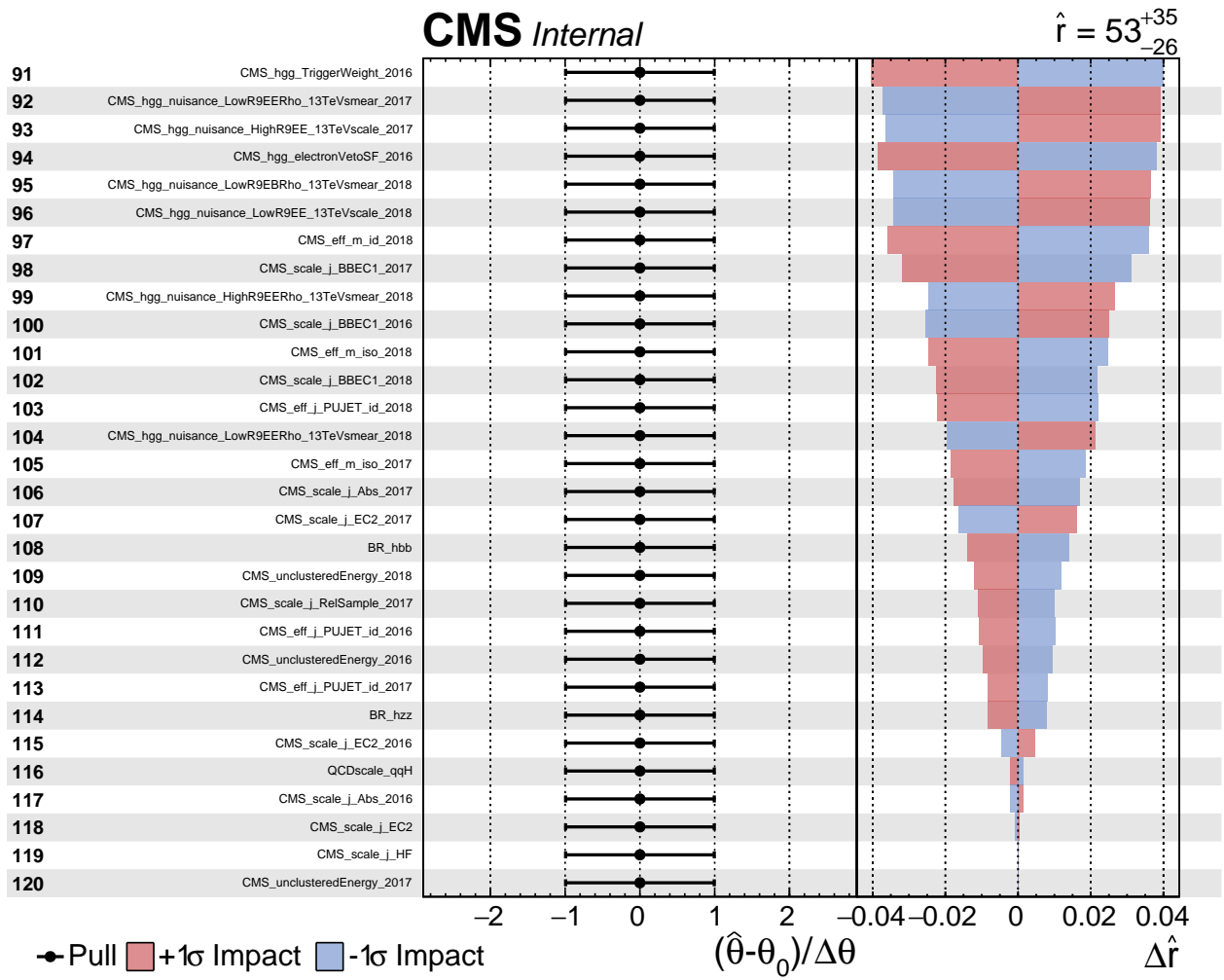
Figure B.15: Combined Run2 Expected Systematic Impacts: Page 4

APPENDIX C

Semileptonic DNN Data sideband and MC Signal Region Checks

To ensure the diphoton mass is not shaped by the semileptonic multiclass DNN, the sidebands of the diphoton mass distribution are shown for different selections made on the DNN output score, shown in the figures below. No evident shaping is seen, and therefore no bias is expected from the DNN.

(a) DNN score > 0.0
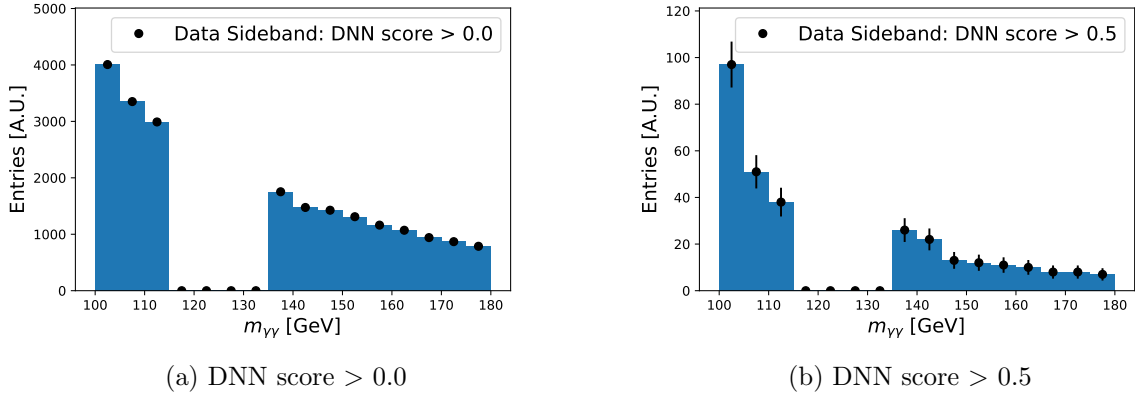
(b) DNN score > 0.5

Figure C.1: Di-photon mass data sideband: Taken from Run 2 data.
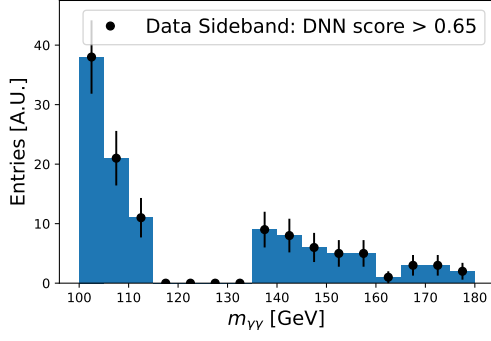
(a) DNN score > 0.65
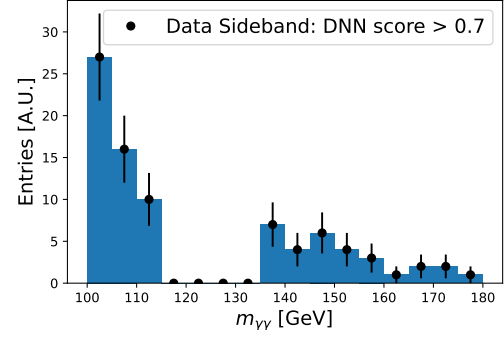
(b) DNN score > 0.7

Figure C.2: Di-photon mass data sideband: Taken from Run 2 data.
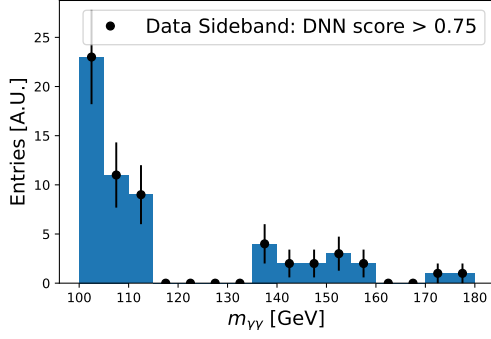
(a) DNN score > 0.75
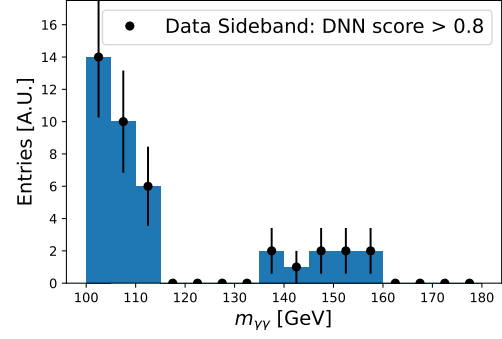
(b) DNN score > 0.8

Figure C.3: Di-photon mass data sideband: Taken from Run 2 data.
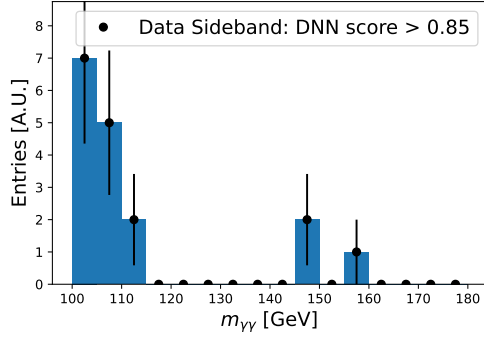
(a) DNN score > 0.85
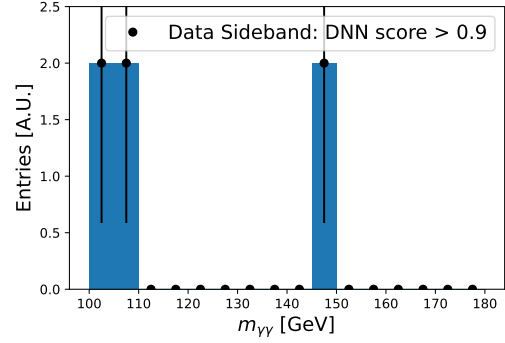
(b) DNN score > 0.9

Figure C.4: Di-photon mass data sideband: Taken from Run 2 data.

In addition, the diphoton mass of the background MC which the DNN trains on is plotted in the mass range 100 to 180 GeV, including the signal region, for different DNN selections, shown in the figured below. No evident shaping is seen within the statistical uncertainty of the check, and therefore no bias is expected from the DNN.
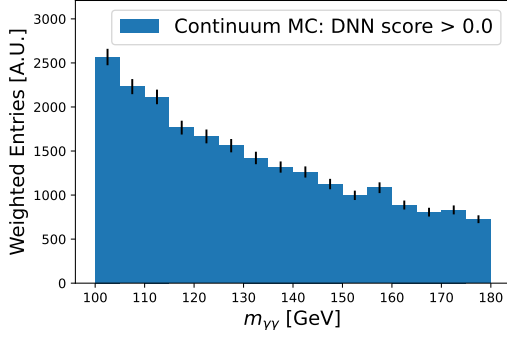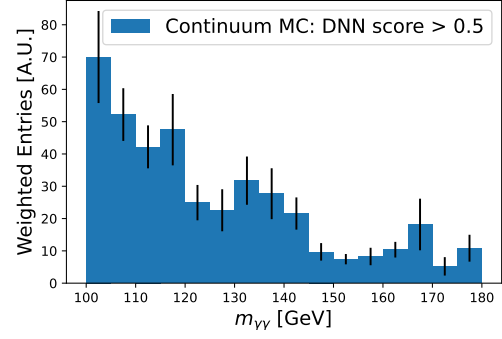
(a) DNN score > 0.0

(b) DNN score > 0.5

Figure C.5: Di-photon mass of MC in the data sideband and signal region: Taken from MC used for DNN training.
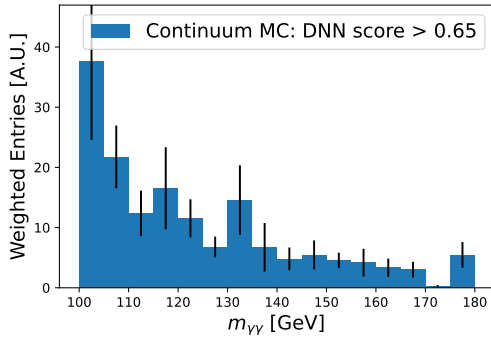
(a) DNN score > 0.65
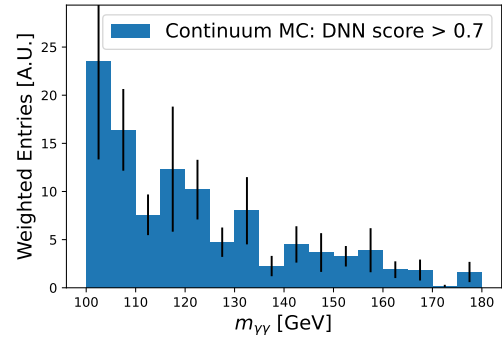
(b) DNN score > 0.7

Figure C.6: Di-photon mass of MC in the data sideband and signal region: Taken from MC used for DNN training.
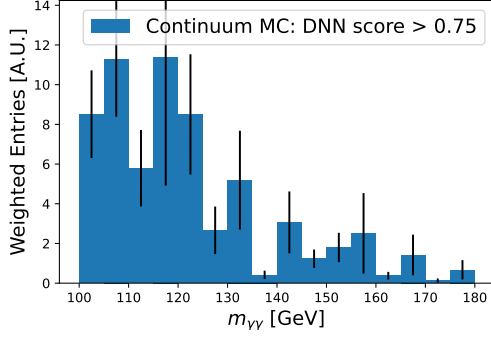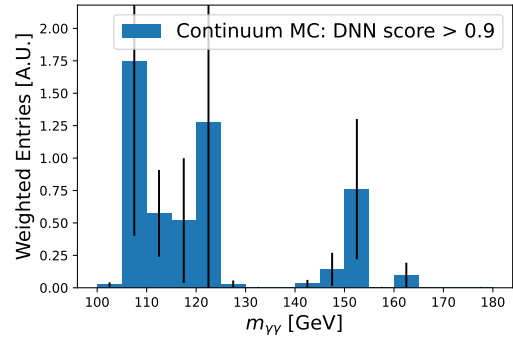
(a) DNN score > 0.75
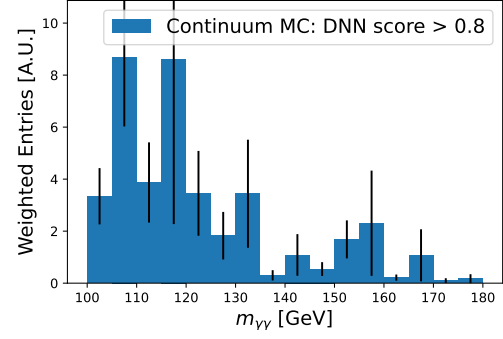
(b) DNN score > 0.8

Figure C.7: Di-photon mass of MC in the data sideband and signal region: Taken from MC used for DNN training.
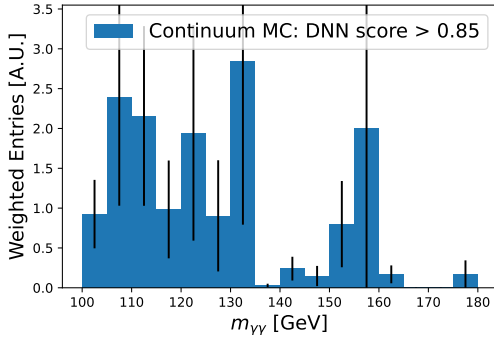
(a) DNN score > 0.85

(b) DNN score > 0.9

Figure C.8: Di-photon mass of MC in the data sideband and signal region: Taken from MC used for DNN training.

APPENDIX D

DNN and signal validation

In order to verify that the DNNs used for the semileptonic and fullhadronic categories is behaving as expected and not introducing a large bias in yields, a control region is defined to check that:

1) There is relatively good agreement between data and the MC sum, which would validate S + B. Given that background (B) has been validated, this could imply a signal validation.

2) There is not a large difference in data and MC acceptance in a control region similar to the signal region

3) The DNN behaves as expected in a control region on a signal with a similar topology to HH→WW$\gamma\gamma$.

The signal used to mimic the HH→WW$\gamma\gamma$ signal topology is the WWZ process. This is used as the process contains two real W bosons, and contains Z→ee which can fake H→ $\gamma\gamma$.

In order to obtain a control region, the diphoton preselections outlined in 4.4.2 are used, but the electron veto requirement is inverted. This means, rather than tagging a diphoton, it is expected that these preselections will tag a di-electron pair. With this applied, a selection on the invariant diphoton object mass (corresponding to a di-electron mass) of 80 < mass < 100 (85 < mass < 95 for the category) in order to defined a Z boson peak phase space. In addition, after DNN score evaluation of data and backgrounds with the main analysis DNNs, events with a DNN output score below 0.1 are not used, as low score events are not use in the main analysis.

Note that there is no retraining done. The DNNs used in the main analysis are used for this control region check.

When running on data, the SingleElectron datasets shown in Tab.D.1 are used. No HLT paths are applied when running on MC, but the HLT paths applied to data are:

`HLT_Ele32_WPTight_Gsf*`

Dataset
/SingleElectron/Run2017B-31Mar2018-v1/MINIAOD
/SingleElectron/Run2017C-31Mar2018-v1/MINIAOD
/SingleElectron/Run2017D-31Mar2018-v1/MINIAOD
/SingleElectron/Run2017E-31Mar2018-v1/MINIAOD
/SingleElectron/Run2017F-31Mar2018-v1/MINIAOD

Table D.1: Data MiniAODs used for the DNN and signal control region check

The data-MC distributions in the Z mass control region and evaluated by the semileptonic DNN and shown in Figures D.1, D.2, D.3 and D.4, and for the fullyhadronic DNN in Figures D.5, D.6 and D.7.

The conclusions are that the data-MC agreement is reasonable, as the disagreements appear to be mainly due to statistical uncertainty, and therefore there is not a large difference in acceptance between data and MC. It is also concluded that the DNNs behave as expected when evaluated on WWZ, as a di-electron peak near 90 GeV is observed, and high DNN scores are observed for this process, and therefore the DNNs are expected to behave properly on the HH→WW$\gamma\gamma$ signal topology.

(a) Linear y scale   (b) Logarithmic y scale
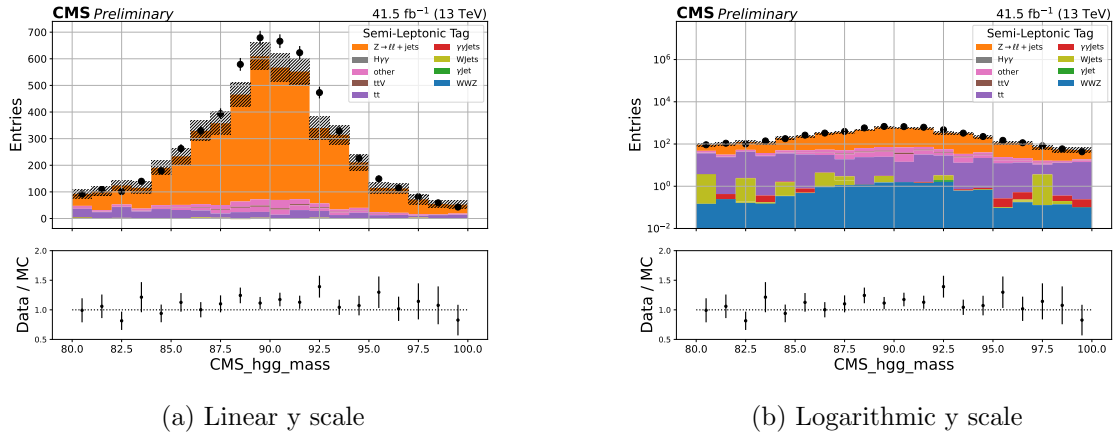
Figure D.1: Semileptonic category: Di-electron mass in the above defined control region, shown in linear and logarithmic y scale.
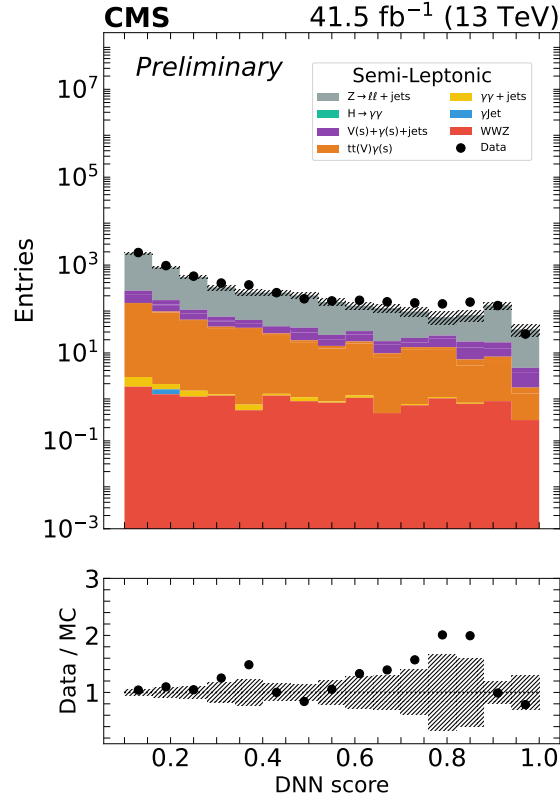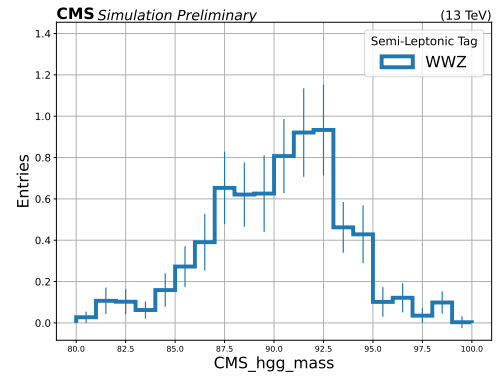
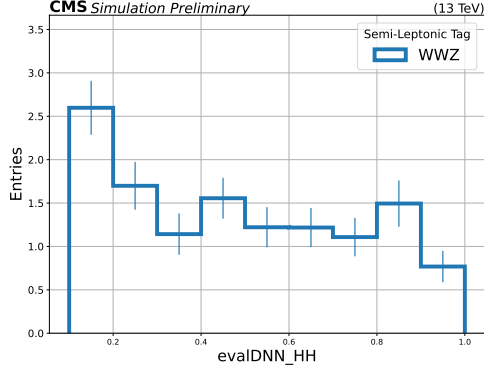Figure D.2: Semileptonic category: Semileptonic DNN score in the above defined control region.
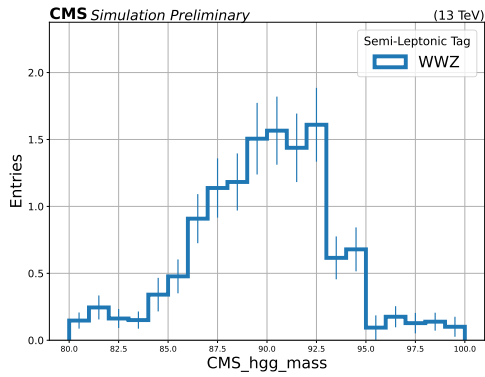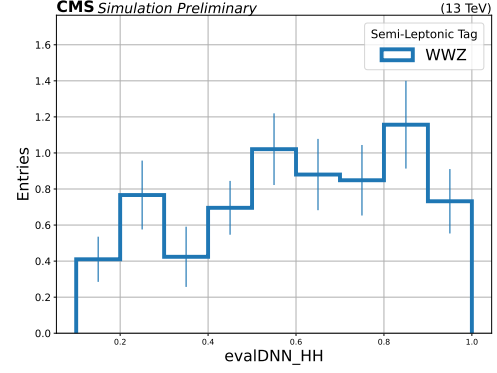

(a) Scaled Leading Photon pt > 0

(b) Scaled Leading Photon pt > 1.0

Figure D.3: Semileptonic category: Di-electron mass of the WWZ process with and without a scaled leading photon pt selection of 1.0 applied.
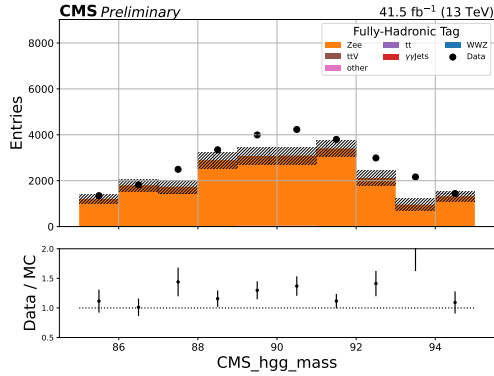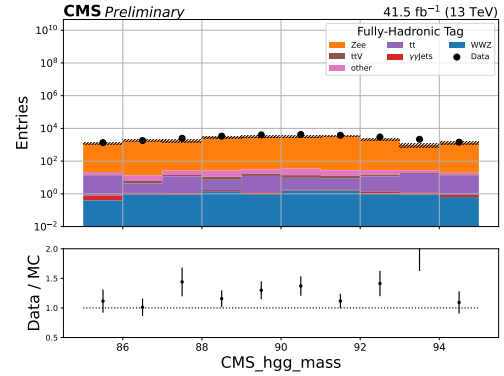
(a) Scaled Leading Photon pt > 0

(b) Scaled Leading Photon pt > 1.0

Figure D.4: Semileptonic category: DNN score of the WWZ process with and without a scaled leading photon pt selection of 1.0 applied.

(a) Linear y scale

(b) Logarithmic y scale

Figure D.5: Fullyhadronic category: Di-electron mass in the above defined control region, shown in linear and logarithmic y scale.
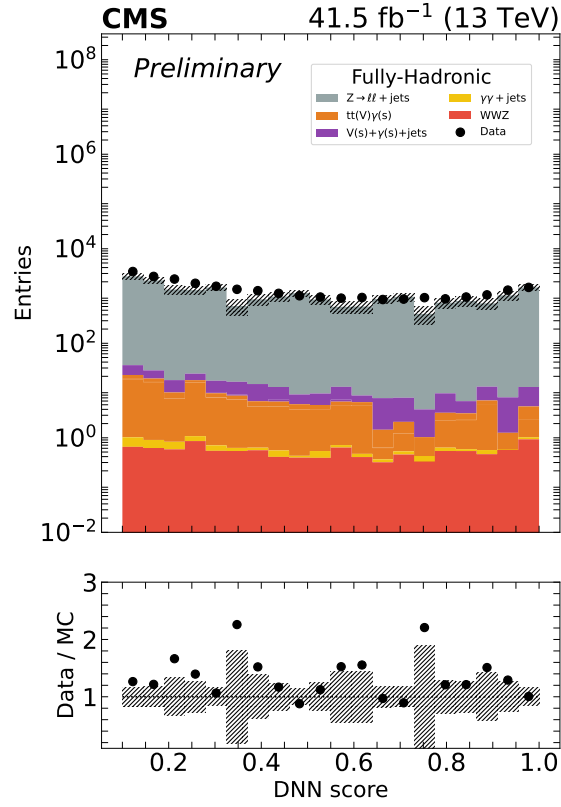
Figure D.6: Fullyhadronic category: Fullyhadronic DNN score in the above defined control region.

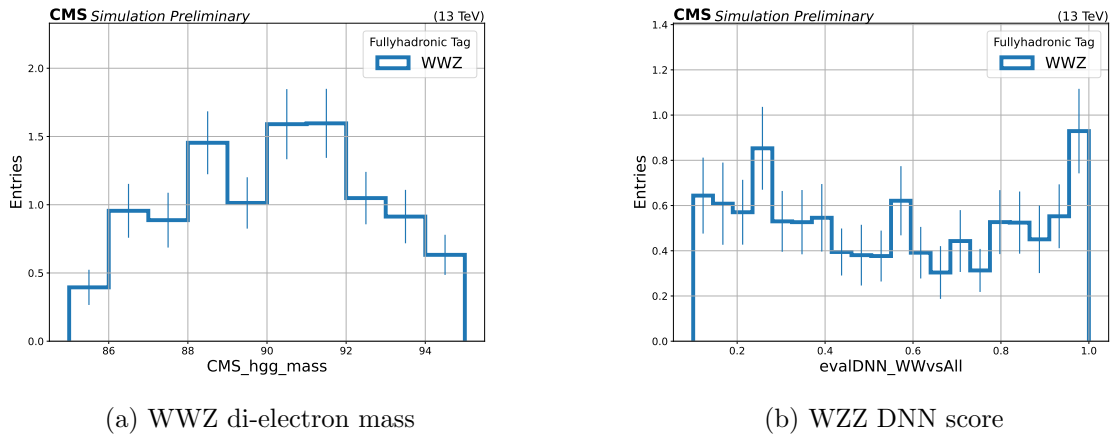(a) WWZ di-electron mass

(b) WZZ DNN score

Figure D.7: Fullyhadronic category: Di-electron mass and fullyhadronic DNN score of the WWZ process.